

**Development of a Digital Microfluidic Toolkit: Alternative Fabrication Technologies for
Chemical and Biological Assay Platforms**

By

Eli Nadia Abdul Latip

A thesis submitted to the University of Hertfordshire in partial fulfilment of the requirements
of the degree of Doctor of Philosophy

School of Engineering and Technology

February 2019

Abstract

This thesis proposes the development of a digital microfluidics (DMF) device using alternative fabrication methods and materials for application in chemical and biological assays. DMF technology which relies on electrowetting-on-dielectric (EWOD) mechanism, offers several advantages such as reduced sample volume, faster analysis, device flexibility, and portability. It is however not without shortcomings as the fabrication of DMF devices is expensive while the reliability of such devices is reduced due to surface contamination when highly concentrated biomolecular samples (e.g. protein and cells) are used.

The first experimental work in this thesis aims to reduce the cost of electrode patterning of DMF devices by investigating the use of inkjet printing method in conjunction with several combinations of conductive ink and substrate. It has been found that EWOD device made of PEDOT:PSS, a type of conductive polymer ink printed on *Melinex*®, a polyethylene terephthalate substrate presents the most reliable droplet actuation performance with velocity comparable to the standard chrome-on-glass device. Two types of inkjet-printed *PEDOT:PSS-on-Melinex*® device have been fabricated; one is a 3D 4 × 4 electrode array device and the other is a magnetic micro-immunoassay device establishing the feasibility of the proposed method. The 3D 4 × 4 electrode array device which utilises both sides of the substrate (i.e. top and bottom surfaces) for electrode patterning allows for future construction of multi-level DMF devices with large functional area. Implementation of such electrode design increases throughput as it made multiple parallel assays possible. The second inkjet-printed device demonstrates the possibility of employing the *PEDOT:PSS-on-Melinex*® device in heterogeneous immunoassay by successfully performing mixing and

merging of two droplets and more importantly the magnetic beads separation operation.

The second experimental investigation concerns the search for substitute materials for the dielectric and hydrophobic components of EWOD device using off-the-shelf products. For the dielectric component, the best performing material in terms of electrowetting reversibility is *Rust-Oleum® Polyurethane Finish* while for the hydrophobic surface is Top Coating of *NeverWet®* superhydrophobic material. Both are low-cost materials which employ a very simple spraying technique as their fabrication method. The *NeverWet®* superhydrophobic material has been selected for detailed investigation due to its other potential function as an anti-biofouling surface to either eliminate or minimise the biomolecules adsorption problem. The superhydrophobic material has shown great potential by demonstrating droplet contact angle reversibility and low roll-off angle for highly concentrated protein solution indicating low adsorption of protein on its surface. A superhydrophobic EWOD device has been fabricated using the Top Coating of *NeverWet®* as the actuating surface and the device has reliably transported concentrated protein droplets across its surface.

It is hoped that the findings in the thesis will assist towards the future realisation of low-cost and robust DMF devices for a wide range of biological and chemical assays applications outside of conventional laboratory environment.

Acknowledgements

I would like to thank both of my supervisors, Dr Loic Coudron and Prof. Mark Tracey for their guidance, advices and kind support while I was working here. I would also like to thank all members of the Microfluidics and Micro-engineering Research Group who have helped me greatly during my time working in the laboratory. I am very grateful to Tan Sri Dr. Azmil Khalili Dato' Khalid who has provided me with the financial support for my research project through his generous scholarship. I am also thankful to my university in Malaysia, Universiti Teknologi MARA for approving my study leave, allowing me to pursue my PhD study. Finally, I would like to thank my family and friends. Without their support and encouragement I would not be able to complete this.

Table of Contents

| | |
|--|-----|
| Abstract | ii |
| Acknowledgements | iv |
| List of figures | x |
| List of tables | xix |
| Introduction | 1 |
| Digital microfluidics as a platform for biological and chemical assays | 1 |
| Problem statement | 2 |
| Aims and objectives | 2 |
| Outline of thesis | 3 |
| Explanation of work done by the author | 4 |
| 1 Fundamentals and components of digital microfluidics | 5 |
| 1.1 Actuating mechanisms in digital microfluidics | 5 |
| 1.2 Electrowetting-on-dielectric and its applications | 8 |
| 1.2.1 Liquid lens | 9 |
| 1.2.2 Electronic display technology | 11 |
| 1.2.3 EWOD-based DMF device in lab-on-a-chip technology | 12 |
| 1.2.3.1 Immunoassay | 15 |
| 1.2.4 Summary | 17 |
| 1.3 Principles of electrowetting-on-dielectric | 17 |
| 1.3.1 Contact angle and the Young-Lippmann equation | 18 |
| 1.3.2 Droplet transportation and calculation of actuation force | 24 |
| 1.3.3 EWOD-based DMF device format | 30 |
| 1.4 Dielectric material in EWOD | 32 |
| 1.5 EWOD actuating surface | 37 |
| 1.5.1 Contamination of hydrophobic surface and the problem of biofouling .. | 38 |
| 1.5.2 Superhydrophobic materials as actuating surface in EWOD devices ... | 40 |
| 1.6 Fabrication of EWOD device | 43 |
| 1.6.1 Microfabrication techniques of EWOD plates | 43 |
| 1.6.2 Printed electronics in EWOD device fabrication | 48 |
| 1.6.2.1 Inkjet printing technology | 52 |
| 1.6.2.2 Conductive polymer PEDOT:PSS ink | 54 |
| 1.7 Summary | 57 |
| 2 Inkjet printing as EWOD electrodes patterning method | 59 |
| 2.1 Introduction | 59 |

| | | |
|---------|---|-----|
| 2.2 | Electrode patterning using desktop inkjet printer Hewlett Packard Deskjet 1000 J110 | 60 |
| 2.2.1 | Experimental..... | 61 |
| 2.2.1.1 | The HP Deskjet 1000 J110 printer setting..... | 61 |
| 2.2.1.2 | The HP Deskjet 1000 J110 cartridge preparation and maintenance | 61 |
| 2.2.1.3 | Conductive inks..... | 62 |
| 2.2.1.4 | Types of substrate and plasma treatment of substrate | 64 |
| 2.2.1.5 | Conductivity measurements of the printed pattern..... | 65 |
| 2.2.1.6 | Fabrication of EWOD plates and droplet actuation in the parallel-plate EWOD devices | 66 |
| 2.2.1.7 | Parylene-C deposition method..... | 68 |
| 2.2.2 | Continuity and reliability of the printed tracks | 69 |
| 2.2.3 | Minimum allowable electrode spacing | 76 |
| 2.2.4 | Reliability of the inkjet-printed EWOD plates | 78 |
| 2.2.5 | EWOD performance of the inkjet-printed parallel-plate devices | 81 |
| 2.2.6 | Conclusions | 84 |
| 2.3 | Electrode patterning using Fujifilm Dimatix DMP-2850 | 86 |
| 2.3.1 | Experimental..... | 92 |
| 2.3.1.1 | Conductive inks..... | 93 |
| 2.3.1.2 | The Fujifilm Dimatix DMP-2850 printer setting..... | 93 |
| 2.3.1.3 | Cartridge maintenance..... | 94 |
| 2.3.1.4 | Types of substrate and surface treatment..... | 95 |
| 2.3.1.5 | Conductivity measurements of the printed pattern..... | 96 |
| 2.3.1.6 | Contact angle measurements | 97 |
| 2.3.1.7 | Fabrication of EWOD plates and evaluation of droplet actuation in the parallel-plate EWOD devices | 97 |
| 2.3.2 | Drop spacing and electrical conductivity of the printed tracks | 98 |
| 2.3.3 | Minimum allowable nominal electrode spacing to produce electrical separation..... | 104 |
| 2.3.4 | EWOD performance of the printed base plate | 105 |
| 2.3.5 | Process details and problems encountered during fabrication of EWOD plates | 110 |
| 2.3.6 | Conclusions | 112 |
| 3 | Off-the-shelf products as alternative low-cost component materials in DMF device | 116 |
| 3.1 | Introduction | 116 |

| | | |
|---------|---|-----|
| 3.2 | Preliminary study on dielectric materials | 117 |
| 3.2.1 | Methodology | 119 |
| 3.2.1.1 | Preparation of dielectric material samples | 120 |
| 3.2.1.2 | Contact angle measurements | 122 |
| 3.2.1.3 | Surface characterisation | 124 |
| 3.2.1.4 | Design and fabrication of EWOD plates and actuation of DI water droplet..... | 124 |
| 3.2.2 | Contact angle measurements..... | 125 |
| 3.2.3 | Droplet actuation | 132 |
| 3.2.4 | Conclusions | 134 |
| 3.3 | Preliminary study on superhydrophobic and hydrophobic materials | 136 |
| 3.3.1 | Methodology | 139 |
| 3.3.1.1 | Preparation of the superhydrophobic/hydrophobic surfaces | 139 |
| 3.3.1.2 | Contact angle measurements | 142 |
| 3.3.1.3 | Surface characterisation | 142 |
| 3.3.1.4 | Design and fabrication of EWOD plates and actuation of water droplets | 142 |
| 3.3.2 | Contact angle measurements..... | 143 |
| 3.3.3 | Droplet actuation | 147 |
| 3.3.4 | Conclusions | 149 |
| 3.4 | Superhydrophobic NeverWet top coating material as EWOD actuating surface | 150 |
| 3.4.1 | Experimental..... | 151 |
| 3.4.1.1 | Types of substrates and deposition of dielectric layer..... | 151 |
| 3.4.1.2 | Hydrophobic and superhydrophobic surface preparation..... | 152 |
| 3.4.1.3 | Surface characterisation | 154 |
| 3.4.1.4 | Contact angle measurements | 154 |
| 3.4.1.5 | Roll-off angle measurements | 156 |
| 3.4.1.6 | Evaluation of the biofouling rate..... | 157 |
| 3.4.2 | Surface characterisation | 158 |
| 3.4.3 | Contact angle measurements..... | 162 |
| 3.4.4 | Electrowetting-number of the surfaces | 167 |
| 3.4.5 | Effect of maximum DC voltage magnitude on CA reversibility and hysteresis on TNW surface..... | 169 |
| 3.4.6 | Effect of maximum DC voltage duration on CA reversibility and hysteresis on Cytop® surface..... | 171 |

| | | |
|---------|---|-----|
| 3.4.7 | Saturation angle of the surfaces | 172 |
| 3.4.8 | Roll-off angle measurements | 174 |
| 3.4.9 | Biofouling rate evaluation | 180 |
| 3.4.10 | Conclusions | 181 |
| 4 | Application prospect of the low-cost EWOD devices | 185 |
| 4.1 | Introduction | 185 |
| 4.2 | Three-dimensional 4 × 4 electrode array EWOD device | 186 |
| 4.2.1 | Design and fabrication of the 3D 4 × 4 electrode array devices | 188 |
| 4.2.1.1 | Printer setting and types of ink and substrate | 189 |
| 4.2.1.2 | The fabrication process of the base plate | 190 |
| 4.2.1.3 | Assembly of the 3D 4 × 4 electrode array device | 192 |
| 4.2.2 | Vias fabrication | 192 |
| 4.2.3 | Electrode characterisation and identification | 195 |
| 4.2.4 | Droplet transportation across vias in 3D 4 × 4 electrode array device | 196 |
| 4.2.5 | Conclusions | 203 |
| 4.3 | Magnetic micro-immunoassay EWOD device | 204 |
| 4.3.1 | EWOD-based DMF magnetic immunoassay platform | 205 |
| 4.3.2 | Design and fabrication of magnetic micro-immunoassay EWOD plates | 207 |
| 4.3.2.1 | Printer setting and types of ink and substrate | 208 |
| 4.3.2.2 | The fabrication process of the base plate and assembly of the device | 208 |
| 4.3.2.3 | Reagents and samples of the micro-immunoassay | 209 |
| 4.3.3 | Protocol of the direct ELISA | 210 |
| 4.3.4 | Reliability of the inkjet-printing method to fabricate immunoassay plate | 212 |
| 4.3.5 | Separation of magnetic beads | 212 |
| 4.3.6 | Mixing of magnetic beads and droplet | 213 |
| 4.3.7 | Photodetection of the immunoassay | 215 |
| 4.3.8 | Conclusions | 218 |
| 4.4 | Superhydrophobic NeverWet top coating as EWOD anti-biofouling surface | 219 |
| 4.4.1 | Design, fabrication and testing of superhydrophobic EWOD device ... | 220 |
| 4.4.2 | Linear transportation of droplet | 223 |
| 4.4.3 | Merging, mixing and splitting of droplets | 228 |
| 4.4.4 | Conclusions | 230 |

| | | |
|-----|--|-----|
| 5 | Conclusions and future works..... | 232 |
| 5.1 | Summary of achievements..... | 232 |
| 5.2 | Future works | 234 |
| 5.3 | Conclusions..... | 235 |
| | Bibliography | 237 |
| | Appendix A: The HP Deskjet 1000 J110 printer setting..... | 248 |
| | Appendix B: Effect of IPA on the wetting of silver ink..... | 249 |
| | Appendix C: Down selection of polymer transparency substrate | 251 |
| | Appendix D: Effect of plasma treatment on the tracks conductivity..... | 253 |

List of figures

Figure 1.1: (a) Thousands of yeast cells manipulated to form the text ‘Lab on a Chip’ using dielectrophoretic force [39]. (b) Surface acoustic wave device with interdigitated electrodes (shown in lower left inset) patterned on top of a lithium niobate (LiNbO_3) piezoelectric substrate [40]. (c) Merging and mixing (frame 1-5) and splitting (frame 6-10) of droplets containing magnetic particles in a magnetic-based DMF device [29]. (d) A droplet of PDMS moving on top of an array of micro heaters (the thin dark lines) in a thermocapillary-based device [32]. 6

Figure 1.2: Electrowetting and EWOD mechanisms. In electrowetting, the liquid droplet sits on a conductive layer while in EWOD a layer of insulator is added on top of the conductive layer to avoid electrolytic decomposition of the droplet. The surfaces are in non-wetting state when no voltage is applied. The dashed lines represent the wetting state of the droplets when voltage is applied across them..... 8

Figure 1.3: Electrowetting in liquid lens. (a) A typical structure of a liquid lens. (b) The liquid lens changes from convex to concave when voltage is applied to the electrode. (c) At 0 V, the lens is convex, (d) at 100 V the lens is completely flat, and (e) at 120 V the lens is concave [49]. (f) Attachment to a mouse skull containing electrowetting tuneable liquid lens employed in a microscope system. (g) A microscopic image of the mouse’s brain neurons captured using the electrowetting tuneable liquid lens [50]. 10

Figure 1.4: Electrowetting in display technology. (a) A basic structure of an electrowetting display. (b) The coloured oil film contracts to the side when voltage is applied due to the imbalance in electrostatic energy. (c) and (d) The states perceived by an observer when look from above for condition described in (a) and (b) respectively [51]. (e) Amazon’s Liquavista electrowetting display [56]. 11

Figure 1.5: Configurations of DMF device: single-plate (left) and parallel-plate (right) configurations. The base plate of the device contains rows of electrode which can be individually addressed. 13

Figure 1.6: The top image (a) shows the schematic of Ng et al.’s [64] DMF device for cell-based assay. Virtual micro wells (shown in the right side of the image) as the site for cell culture by creating hydrophilic regions in the EWOD device. The bottom image (b) displays the DMF device for DNA amplification using loop-mediated isothermal amplification (LAMP) method. The sequence of events on the right represent the merging and mixing operations of the reagents and the DNA sample, where the red-coloured droplet is the DNA sample while the blue-coloured sample is the LAMP reagents. 14

Figure 1.7: a) Sessile droplet on a solid surface. The surface tensions acting between the three phases at the contact line are indicated by the red arrows and θ is the contact angle. b) Droplet contact line movement due to a change in droplet size. 18

Figure 1.8: The variation of contact angle with applied voltage of a liquid droplet sitting on a silicon dioxide surface. The dashed lines represent the contact angle evolution based on the Young-Lippmann equation which predicts that the contact angle reduces to less than 60° as the voltage is increased. Experimental data (black and white squares) show otherwise where the contact angle stop decreasing at approximately 79° and this angle is called saturation angle [83]......23

Figure 1.9: Transportation of droplet in parallel-plate DMF device. The state of the droplet just after a voltage is applied to the third electrode. The front meniscus of the droplet spread towards the activated electrode.25

Figure 1.10: Transportation of droplet in a single-plate DMF device.....27

Figure 1.11: Failure in the dielectric layer causes electrolysis as indicated by the bubble formation in the left figure. The right figure shows normal EWOD of droplet without any failure [120].34

Figure 1.12: The left graph shows breakdown voltage and necessary voltage to change CA from 120° to 80° as a function of Teflon™ AF thickness. The graph on the right display the relationship between the voltage change CA from 120° to 80° and the dielectric constant of the material [102]......35

Figure 1.13: Biofouling of EWOD actuation surface. On the right side of the figure are the fluorescence micrographs of the EWOD surface before and after the droplet transportation. The after image shows protein (FITC-BSA) adsorption that occurred after moving on the surface four times [24]......39

Figure 1.14: Nanostructure of the EWOD actuating surface made by SiO₂ coated with perfluorodecyltrichlorosilane developed by Yun & Kim. The surface is capable of producing very high CA of approximately 169° [129]......41

Figure 1.15: Layer by layer fabrication process of EWOD device.....44

Figure 1.16: Steps involved in photolithography process. Photolithography is a technique employed to pattern material using exposure of UV light and photoresist material.....45

Figure 1.17: EWOD device fabricated using printed electronics fabrication method. From left to right: 1) graphite-on-paper EWOD plate using spray painting [119], 2) silver-on-paper EWOD plates using screen printing method [118], 3) silver-on-paper EWOD plate using inkjet printing [61], 4) silver-on-PET EWOD plate using inkjet printing [117].49

Figure 1.18: Formation of ink droplet in inkjet printing. Top) single droplet ejection where Z is between 1 and 10, bottom) satellite drop formation when Z is larger than 10 [156]......53

Figure 1.19: Inkjet printing of PEDOT:PSS as organic electronic component. Clockwise from top left: 1) micrograph of TFT (S, source; D, drain; and G, gate) [160], 2)

PEDOT:PSS/polyaniline electrode for pH sensor [159], 3) OLED on glass substrate [150], 4) logical NOR-gate printed on glossy photo paper [161]. 55

Figure 2.1: The pattern of the control electrode for the base plate of the parallel-plate EWOD devices..... 66

Figure 2.2: The PMMA frame used to hold the EWOD device in place. Only the base plate is mounted in this figure and it is connected to the control electronics (not shown here) by 16 spring-loaded pin connectors. 67

Figure 2.3: Parylene deposition system. (Top left) The chemical structure of Parylene dimer, monomer, and polymer. (Middle and bottom left) The Parylene deposition process. It begins in the vaporiser where the solid dimer is turned into gas under vacuum and temperature of 175 °C for Parylene-C, then the gas is split into monomer inside the pyrolysis furnace at temperature of 690 °C and finally deposited as a thin film inside the deposition chamber at ambient temperature [179]. (Right) The SCS Labcoater® 2 Parylene Deposition System equipment..... 69

Figure 2.4: Test pattern to determine the minimum allowable track width and electrode spacing. The smallest width of the track is 10 μm and the largest width is 250 μm . For the electrode spacing, the smallest gap is 80 μm and the largest gap is 340 μm 70

Figure 2.5: The left and middle tracks are made of Ag ink while the right track is made of Ag/IPA ink. The left and right tracks were printed on untreated substrate while the middle track was printed on substrate treated at 30 W for 60 s. All tracks were printed in two layers. 73

Figure 2.6: Average resistance in 15 mm long and 250 μm wide horizontal tracks and the reliability of the printing process to produce conductivity in the tracks. The standard deviations are given in the labels..... 75

Figure 2.7: The first (blue outline) and second (yellow outline) printing pass did not align precisely which can cause overlapping between adjacent electrodes, indicated in the red-dashed circle, reducing the resolution of the inkjet printing method for silver inks..... 78

Figure 2.8: The sequence of images in the left show the droplet while in transportation (from electrode no. 2 to electrode no. 4) in the PP/T20 device while the right images is for the Ag/IPA device. The PP/T20 electrodes are harder to identify than the Ag/IPA electrodes because of the PEDOT:PSS transparency. The still images were taken from videos recorded using Canon PowerShot at 29 frame per second and camera phone Samsung Galaxy Ace 4 Neo at 25 frame per second for the Ag/IPA and PP/T20 devices respectively. 82

Figure 2.9: The Fujifilm Dimatix DMP-2850 printer (left). Some of the important components such as the printer carriage is shown in the figure. The printer cartridge (right) is consisted of a fluid model and a jetting module. The fluid model contains the ink while the jetting module contains the nozzles and the electrical connection to the printer. 87

Figure 2.10: The printer cartridge carriage, without cartridge attach to it. The vernier scale is used to set the mounting angle which determine the drop spacing. The cleaning pad on the left is used to absorb ink from the nozzles during cleaning cycles..... 88

Figure 2.11: The simplified diagram of the chamber, PZT element, and the nozzle. The jetting waveform applied to the PZT element will cause its deflection and relaxation which controls the flow of the ink fluid inside the chamber. A meniscus pressure is applied to avoid the ink from flooding the nozzle while the PZT element is in its relaxation mode. 89

Figure 2.12: An example of jetting waveform and non-jetting waveform applied to the piezoelectric element of the DMP print head. The jetting waveform is composed of four segments. The user can edit the amplitude, the slope, and the duration of each segment in the waveform [183]. 90

Figure 2.13: The Drop Watcher camera displays the droplet ejection from the nozzles, allowing the user to evaluate in real-time the performance of the droplet with the changing of the printing parameter. The image above shows good formation of ink droplets with no long tails or satellite drops trailing behind [183]. 92

Figure 2.14: Contact angle measurements of DI water droplet on the substrates employed in this investigation..... 99

Figure 2.15: The left image shows a silver track printed on Melinex® substrate without any heat applied to the platen and the right image is a silver track printed on the same substrate while the platen temperature was raised to 60 °C. There is a disconnection (shown in the red circle) in the left track due the non-uniform spreading of the silver ink when the substrate was not heated. 102

Figure 2.16: PP/T20 tracks on PP60 paper substrate using 15 µm drop spacing. The left tracks are horizontal tracks, printed parallel to the printing direction while the tracks in the right are vertical tracks, printed in perpendicular direction to the printing direction..... 103

Figure 2.17: The silver-on-HPA (left) and the PP/T20-on-hPET devices..... 105

Figure 2.18: The displacement and velocity of water droplets across five electrodes and back to the original position in four EWOD devices. One of the device is a chrome-on-glass device with the electrodes fabricated using photolithography method. The other three are inkjet-printed devices. The water droplets were actuated using 150 V and 100 ms pulse signal.. 108

Figure 3.1: Experimental set up for the CA measurement using optical tensiometer. The droplet was connected to the positive output terminal of the power supply via a wire while the silicon wafer was connected to the negative output terminal..... 123

Figure 3.2: The design of electrode pattern for the EWOD plates comprises three rows of 16 square electrodes, 1.7 mm in nominal size with 200 µm nominal inter-electrode spacing (left),

and the actual inkjet-printed plate made of PEDOT:PSS electrode on PET substrate (right).
..... 125

Figure 3.3: The electrowetting behaviour of the BF (yellow lines), RO-CC (blue lines), and RO-PU (green lines) dielectric materials. The solid lines represent the one-layer squeegee and spray-coated samples of the BF and both RO-CC and RO-PU materials respectively. The dashed lines represent the two-layer squeegee and spray-coated samples of the BF and both RO-CC and RO-PU materials respectively. The small dotted lines represent the spin-coated samples which underwent electrolysis once voltage is applied across the droplet. 128

Figure 3.4: Bubble formation due to dielectric layer failure in one-layer Blackfriar varnish sample. The first figure shows the initial condition of a DI water droplet before any voltage was applied. In the second figure, tiny bubbles started to form during the voltage application. The relatively thin insulating layer of the BF sample underwent breakdown, causing electrolysis of the water as current ran through it. The third and the fourth figures illustrate the bubbles progressive formation as the voltage was increased to the maximum value of 250 V. 129

Figure 3.5: Evolution of contact angle of one-layer spray-coated RO-PU during repeated cycle of electrowetting. 131

Figure 3.6: Different in microstructures between the spin-coated (above) and spray-coated (below) for Drywired® superhydrophobic material. Striations can be seen in the spin-coated surface due to solvent evaporation of the volatile superhydrophobic solution while the spray-coated surface exhibits a more homogenous microstructure..... 141

Figure 3.7: The EWOD plate employing superhydrophobic/hydrophobic materials for the evaluation of droplet transportation. The electrode design pattern comprising three rows of 16 square electrodes, 1.7 mm in nominal size with 200 µm nominal inter-electrode gap (left), and the actual inkjet-printed plate made of PEDOT:PSS electrode on PET substrate (right). This plate employed Rain-X as its actuating surface. The red dots are markers to help aligning the contact pads with the pin connectors since the PEDOT:PSS ink is transparent. 143

Figure 3.8: The changes in CA when 250 V of DC voltage is applied across a 20 µl of DI water sitting on the superhydrophobic/hydrophobic surfaces. The solid lines represent the spin-coated surfaces, the dashed line represent spray-coated surface, and the dotted line represent surface deposited using cloth..... 146

Figure 3.9: Preparation steps of the three types of superhydrophobic/hydrophobic surfaces for CA angle and roll-off angle measurements. All three surfaces were deposited with Parylene C dielectric layer before coated with either Cytop®, TNW, or BTNW. (Top right) The Cytop® hydrophobic material and its solvent; (bottom right) the Top coat and Base coat materials of the NW superhydrophobic product..... 153

Figure 3.10: Effect of droplet volume on the CA measurement for superhydrophobic surface. The droplets in the figure are DI water sitting on TNW superhydrophobic surface. There is a large difference in the mean CA (more than 10°) between the 2 µl and 15 µl droplets while the difference between the 5 µl and 20 µl droplets is quite small ($\pm 2^\circ$ to $\pm 3^\circ$). 155

Figure 3.11: SEM microstructure images of BTNW (left) and TNW (right) superhydrophobic surfaces at different magnifications (increasing from top to bottom); $\times 40$ (a and d), $\times 200$ (b and e), and $\times 15,000$ (c and f). 159

Figure 3.12: Droplets of DI water on Cytop® (left), BTNW (middle), and TNW (right) surfaces. The images were captured using the optical tensiometer. The baseline for the estimation of the CA is represented by the dash line. 160

Figure 3.13: Contact angle changes with applied DC voltage for different droplet solutions on three types of surface: TNW (top), BTNW (middle), and Cytop® (bottom). Note that left to right, the plots are from zero to maximum voltage and back to zero voltage – for clarity this is an ‘unfolded’ hysteresis curve plot. 163

Figure 3.14: Electrowetting hysteresis curves for different droplet solutions (clockwise from top left) DI water, 0.01, 1, and 0.1 mg ml⁻¹ ovalbumin on three types of surface: TNW (blue triangles), BTNW (orange circles) and Cytop® (grey crosses). Each curve starts at the higher initial point and the difference between the initial and the final CA is the hysteresis. Red arrows indicate the increasing or the decreasing voltage segment of the curve. 165

Figure 3.15: Fittings of Young-Lippmann equation for experimental data below saturation point (clockwise from top left) DI water, 0.01, 1, and 0.1 mg ml⁻¹ ovalbumin on different types of surface. Square markers for Cytop®, round markers for TNW, triangle markers for BTNW, and straight lines for Young-Lippmann fittings. 168

Figure 3.16: Electrowetting hysteresis curves for different droplet solutions (clockwise from top left) DI water, 0.01, 1, and 0.1 mg/ml ovalbumin on TNW surface comparing between 150 V and 250 V maximum voltage. Each curve starts at the higher initial point and the difference between the initial and the final CA is the hysteresis. 170

Figure 3.17: Hysteresis of different solutions on TNW for 150 V and 250 V maximum applied voltage (column graphs) and on Cytop® for long and short duration application of 250 V (line graphs). 171

Figure 3.18: Hysteresis of different solutions on TNW for 150 V and 250 V maximum applied voltage (column graphs) and on Cytop® for long and short duration application of 250 V (line graphs). 172

Figure 3.19: Biofouling rate of Alexa Fluor 647 human fibrinogen on Cytop® and TNW surfaces (Left) Mean fluorescence intensity of 0.1 mg ml⁻¹ fluorescent-tagged fibrinogen after different electrowetting treatments. (Right) The fluorescence image of the TNW surface after

exposure to the 0.1 mg ml^{-1} fluorescent-tagged fibrinogen where protein adsorption is indicated by the red spots [220]..... 181

Figure 4.1: Side view of the simplified 3D 4×4 electrode array device structure. The yellow component represents the inkjet-printed conductive ink while the blue component is the PET substrate. In this structure, both sides of the substrate, top and bottom surfaces are deposited with the ink to form the interconnection between the inner electrode and the contact pad. Pinholes are fabricated at the relevant contact pad and inner electrode to connect between the top surface electrode and contact pad with the bottom surface track..... 187

Figure 4.2: The design of the 3D 4×4 electrode array. The first and second images are the top and bottom pattern respectively. The squares at the top corners in each image are the markers for alignment on the printer platen. The third image shows the location of the laser-cut pinholes. The pinholes size is exaggerated here for illustration purpose wherein the actual drawing the size is $10 \mu\text{m}$ (the smallest possible dot size for the laser cutter software). The last image is the superposition of the top, bottom, and the laser-cut pinholes images. 189

Figure 4.3: The process flow of the 3D 4×4 electrode array device base plate fabrication. 191

Figure 4.4: The effect of laser power and speed on the diameter of via. Five laser power levels, 10%, 15%, 20%, 50%, and 100% were used while for the cutting speed, four settings were used, 0.5%, 10%, 50%, and 100%. The diameter decreased as the laser speed increased and the laser power decreased. 193

Figure 4.5: A via fabricated with laser cutter using 10% power and 100% speed. The average diameter of the hole where the substrate is fully removed is $105 \mu\text{m}$ and the average diameter including the lips around the hole is $270 \mu\text{m}$ 194

Figure 4.6: The identification number for the 16 electrodes in the 3D 4×4 electrode array device..... 196

Figure 4.7: Droplet movement across inner electrodes, from electrode 13 to electrode 7 using $225 V_{\text{RMS}}$ in the first configuration. There are four inner electrodes with the vias located in the middle of each electrodes. In the first image, the droplet is indicated in the blue circle while the four vias are indicated inside the dashed red circles. The red arrow indicates the direction of droplet movement..... 200

Figure 4.8: Droplet movement across inner electrodes, from electrode 6 to electrode 11. There are four inner electrodes with the vias located on the top left corner of each electrodes. In the first image, the droplet is indicated in the blue circle while the four vias are indicated inside the dashed red circles. Initially, the droplet was positioned on electrode 6 (the bottom left electrode of the four inner electrodes). The second image shows the elongation of the droplet during its transportation to the next electrode as electrode 11 was activated. The red

arrow indicates the direction of droplet movement. The third image shows the droplet in its final position, on electrode 11. 202

Figure 4.9: Front view (left) and top view (right) of the EWOD-based DMF magnetic immunoassay platform developed by the UH's MMRG. The images show the system without the black box cover and also without the photodetector connected to it. The magnet assembly for the magnetic beads separation operation is contained in the 3D-printed black cylinder located below the EWOD plates. 206

Figure 4.10: The design of the assay plate contains 47 electrodes. The size of the control electrode is 1.7 mm and the reservoir electrode size is 5 mm. The enlarged inset shows the mixing region and the locations of magnetic separation and photodetection. 208

Figure 4.11: Flow process of the micro-immunoassay antibody antigen. 211

Figure 4.12: The images show the sequence of events during the separation of the magnetic beads from the supernatant. In the first image, the magnet is already engaged below the plate and the beads started moving towards the location with the highest magnetic field. The beads begin to cluster together into a pellet after some time. The last two images show the beads pellet is finally detached from the supernatant as the next electrode is activated. 213

Figure 4.13: The sequence of events during merging and mixing between the magnetic beads and a droplet solution. The first image shows the droplet and the pellet of separated magnetic beads right before the merging happened. The red-dotted circles represent the previous positions of the droplet. The first two rows of images show the sequence of electrode activation during the mixing operation. The third, fourth, and fifth rows images display the condition of the droplet at the end of a mixing cycle. 214

Figure 4.14: The intensity histogram of the droplet image for each cycle. The 10th cycle image pixel intensity closely matched with the 18th cycle image indicating well-mixed droplet after the 10th cycle. 215

Figure 4.15: Signals from the PEDOT:PSS-on-Melinex® and chrome-on-glass devices using 2 mg/ml of Protein A/G-coated magnetic beads and 2 µg/ml of HRP-conjugated IgG antibody. 216

Figure 4.16: The photodetector signals produced by a 5 µl of 0.5 µg/ml HRP-conjugated IgG droplet added with luminol sitting on different types of electrode and substrate. 217

Figure 4.17: Designs of the superhydrophobic EWOD device, (left) single-plate configuration, (middle) parallel-plate configuration. (Right) The base plate of the superhydrophobic EWOD device was made of glass with ten rows of sixteen chromium control electrodes. Each electrode in the same column is electrically connected by thin chromium lines [220]. 221

Figure 4.18: Displacements of 35 μl (single-plate) and 5 μl (parallel-plate) of DI water, ovalbumin and fibrinogen droplets for one cycle (across seven electrodes and back) using 150 V_{RMS} and 100 ms pulse rate [220]..... 224

Figure 4.19: The rolling mechanism observed in droplet actuated using single-plate configuration. The droplet moves or rolls in lateral direction as indicated by the red markers which represent the previous locations of the droplet. The markers track the position of the top edge of the droplet frame by frame. 225

Figure 4.20: The timed video frames show the sequence of the merging of two 5 μl droplets followed by the mixing operation in the parallel-plate superhydrophobic device. One droplet is DI water while the other droplet is 5 mg ml^{-1} New Coccine dye solution (red coloured droplet). The activated electrode pad is represented with white-dash outline. The first row of images display the frame-by-frame merging of the two droplets while the second row show the stabilisation of the merged droplet by actuation to the next electrode. The third and final rows demonstrate the mixing operation which occurred by moving the droplet in a circular fashion [220]..... 229

List of tables

| | |
|---|-----|
| Table 1.1: Dielectric materials employed in EWOD device..... | 33 |
| Table 2.1: The minimum nominal track width required to produce measurable electrical conductivity for different type of inks and substrate treatment..... | 71 |
| Table 2.2: The minimum allowable spacing between electrodes for different types of ink.... | 77 |
| Table 2.3: Reliability of plates printed using the PP/T20 ink. The tracks' width is 250 μm while the electrode spacing is 360 μm . Only one layer of printing was applied for this ink..... | 79 |
| Table 2.4: Reliability of plates printed using the silver inks. The tracks width is 250 μm while the electrode spacing is 320 μm . Two layers of printing were applied for this ink and 2+1 indicates two layer of printing with additional printing pass just for the tracks connecting the electrodes excluding the square electrodes..... | 79 |
| Table 2.5: The printer setting applied for the silver and PEDOT:PSS inks printing..... | 94 |
| Table 2.6: Substrates employed in the Fujifilm Dimatix DMP-2850 printer investigation with the required surface treatment..... | 96 |
| Table 2.7: Droplet spacing used for printing of the silver and PEDOT:PSS inks on different types of substrate. Electrical resistance and the minimum track width for different combination of ink and substrate..... | 100 |
| Table 2.8: The minimum allowable spacing between electrodes for different combination of ink and substrate..... | 104 |
| Table 2.9: EWOD performance of devices made from the inkjet-printed base plate..... | 106 |
| Table 2.10: Summary of the problems in fabrication of the inkjet-printed EWOD base plates..... | 112 |
| Table 3.1: List of commercially available dielectric materials for the EWOD investigation.. | 118 |
| Table 3.2: Fabrication method for commercial dielectric materials | 121 |
| Table 3.3: Initial CA, electrowetting hysteresis, and average thickness of the dielectric materials samples | 127 |
| Table 3.4: Droplet transportation performance of EWOD plates with difference types of dielectric layer..... | 133 |
| Table 3.5: List of superhydrophobic and hydrophobic materials..... | 137 |
| Table 3.6: Deposition method for the commercial superhydrophobic and hydrophobic materials..... | 139 |
| Table 3.7: Summary of contact angle measurements of the SH/H materials..... | 145 |
| Table 3.8: Droplet transportation performance of EWOD plates with difference types of dielectric layer..... | 148 |
| Table 3.9: Summary of the CA measurement results..... | 166 |

Table 3.10: *The roll-off angles for different types of solution on TNW and Cytop® surfaces*
..... 176

Table 4.1: *The nominal and measured size of the inkjet-printed PEDOT:PSS electrodes in the 3D 4 × 4 electrode array device*..... 195

Table 4.2: *Summary of the droplet movement in the 3D 4 × 4 array device for different types of configuration. The first column represent the design employed for the four inner electrodes while the second column depict the droplet transportation across the 3D 4 × 4 array device. The red dashed circles represent the position where the droplet became stuck in each device.*
..... 197

Table 4.3: *Droplet actuation performance of the device using the fourth configuration.*..... 202

Table 4.4: *The peak and mean velocities of different types of solution in the parallel-plate (grounded and ungrounded) and single-plate superhydrophobic EWOD devices*..... 223

Introduction

Digital microfluidics as a platform for biological and chemical assays

Biological and chemical assays are very useful analytical tools widely used in the medical, military, food, and environmental sectors for diagnostic and bio-detection purposes [1-3]. Integration of biological and chemical assays with lab-on-a-chip (LoC) technology began in the early 1990s and since then it has undergone tremendous transformation [3-5]. LoC is a device that integrates multiple laboratory functions into one single chip of only few square millimetres to few square centimetres in area [6]. In order to miniaturise conventional large-scale laboratory processes, LoC devices apply microfluidics technology to manipulate liquid samples and reagents at micro scale level. Miniaturisation of biological and chemical assays brings many advantages such as fast reaction time and minimal waste as a result of drastic reduction of the sample and the reagent consumption [1, 6, 7].

Due to their small size, LoC devices can be made portable which allows for rapid on-site analysis. This is beneficial for applications in the developing countries and remote regions or during disaster situations where access to laboratory tests is very limited and costly [8]. Recently, promise for further improvement of LoC devices was demonstrated by implementing fully automated assays using a technique called digital microfluidics (DMF). DMF allows multiple small droplets (in the microlitre range) to be precisely manipulated on a planar substrate. Apart from requiring only small volume of reagents, DMF devices are also reconfigurable due to their open architecture, not constricted by features such as micro-channels, valves or pumps as in conventional flow microfluidics [1, 9, 10]. Several research groups [11-14] have developed devices capable of performing assays such as heterogeneous

immunoassays, DNA-based tests and cell-based tests [1, 9] using the DMF technology. DMF technology has also been employed to perform other functions such as particle sampling [15, 16] and electronic cooling systems [17, 18].

Problem statement

Despite its enormous potential, improvements are still needed to some areas of DMF technology before it can become more universally adopted. Some of the key features that should be taken into consideration while developing a LoC device are affordability, simple operation, user-friendliness, rapidity, robustness, and transportability [6, 8, 11, 19]. Most DMF devices developed to-date have fulfilled some but not all of the aforementioned features. The main challenge is its affordability - the potentially high fabrication cost [9, 20-22] of the device. Since DMF device was first presented by Pollack et al. in 2000 [23], most of the methods employed for the device fabrication involved clean-room processes and equipment [10]. Apart from being expensive, these microfabrication methods are not easily available in every research facility. Another drawback in DMF technology is the robustness of the device, which can be compromised when samples containing biomolecules are used. The biomolecules when in contact with the device contaminate the DMF device surface, compromising its performance and sometimes rendering it unusable [24, 25].

Aims and objectives

This thesis seeks to address these challenges by investigating and employing alternative fabrication methods and materials for DMF devices. Generally, there are three main aims in this project, though these aims will be found to overlap often throughout this thesis:

- To develop a low-cost DMF device using alternative fabrication methods.

- To develop a low-cost DMF device using alternative materials.
- To research novel techniques to improve the robustness of DMF devices in respect to surface contamination by biomolecules.

In order to achieve the above aims, research has been conducted to attain the following objectives:

- To test the feasibility of employing the inkjet printing technique as a method to pattern electrodes in DMF device.
- To test the feasibility of using conductive polymer and polymer sheet as the DMF device's electrode and substrate materials respectively.
- To investigate the suitability of inexpensive off-the-shelf products as the dielectric and hydrophobic components of the DMF device.
- To investigate the electrowetting behaviour of a commercial superhydrophobic material as the actuating surface in DMF device to overcome the biomolecule contamination problem.
- To fabricate DMF devices using the resulting alternative methods and materials to demonstrate their applicability to real-world applications.

Outline of thesis

This thesis is divided into five main chapters. The first chapter provides the literature review of the topics involved in this thesis where the physical principles and state-of-the-art of each aspect will be discussed. Chapter 2 and Chapter 3 report investigations of alternative fabrication technologies and materials for DMF devices. Chapter 2 focuses on the substrate and electrode components of the DMF device while Chapter 3 covers the dielectric and hydrophobic layers of the device. Chapter 4 describes prospect of application of the EWOD devices fabricated using selected methods and

materials based on the investigations conducted in the previous chapters. The final chapter, Chapter 5, summarises the findings of the investigations in this thesis and discusses future work that could be conducted to improve the reported outcomes.

Explanation of work done by the author

All the experimental works described in this thesis were conducted by the author. The electronics and software of the EWOD devices employed in the investigations preceded the PhD research project and has been built and designed by Mr. Ian Munro of the Microfluidics and Micro-engineering Research Group (MMRG), University of Hertfordshire (UH). The supporting frame for the EWOD devices was also built by the members of MMRG. The magnetic micro-immunoassay DMF platform employed in **Section 4.3** was designed and built by the MMRG group. The EWOD chrome-on-glass plates used in **Sections 4.3** and **4.4** were designed and fabricated by the MMRG group. All the designs for the EWOD control electrodes were designed and drawn by the author except for the one used in **Sections 4.3** and **4.4**. Pre-existing design was used for the control electrodes in the immunoassay plates. The design was redrawn by the author so that it can be adapted for the inkjet printing method to fabricate the conductive polymer EWOD on polymer substrate devices.

1 Fundamentals and components of digital microfluidics

This chapter reviews the fundamentals of digital microfluidics (DMF), a technology used to control the movement of individual droplet in a microfluidics device. The first part discusses the physical mechanisms and theories involved in the droplet's motion, the applications of this technology, and the essential components comprised in a DMF device. The later part of the chapter discusses the state-of-the-art materials and fabrication techniques required to fabricate a DMF device. Specifically, a review of the potential of printed electronics methods as DMF device fabrication techniques is also included.

1.1 Actuating mechanisms in digital microfluidics

DMF is the name given to a set of techniques that allow the precise handling of liquid movements in discrete droplet form. There are different mechanisms that can be employed to achieve droplet actuation in a DMF device; dielectrophoresis (DEP) [26, 27], surface acoustic wave (SAW) [28], magnetic manipulation [29-31], thermocapillary effect [32-34], and electrowetting-on-dielectric (EWOD) [1, 6, 7, 9]. However, of these mechanisms, EWOD has been the most commonly applied thus far. Accordingly, this section briefly discusses all of the above mechanisms except for EWOD, which is thoroughly examined in **Section 1.2** and subsequently.

In a dielectrophoretic-based device, dielectric particles suspended in a polarisable medium, such as water, are mobilised when subjected to a non-uniform electric field. The non-uniform electric field can be generated by either DC or AC voltage (frequency typically in the 10 kHz to 100 MHz range) but AC voltage is more widely used due to lower voltage requirement and very low heat generation [26, 35]. There are few types of electrode that can be used to generate the non-uniform electric field such as pin-and-plate electrodes and parallel rectangular electrode array [36, 37].

The non-uniform electric field polarises both the dielectric particle and the medium into dipoles and due to the field inhomogeneity, there is a net force resulting in the movement of the particle either towards or away region of higher field intensity. In positive DEP, where the polarisability of particle is larger than the surrounding medium, the particle moves towards region of high field intensity. Negative DEP occurs when the particle has lower polarisability than the surrounding medium. The particle moves away from region of high field intensity in negative DEP [27, 38].

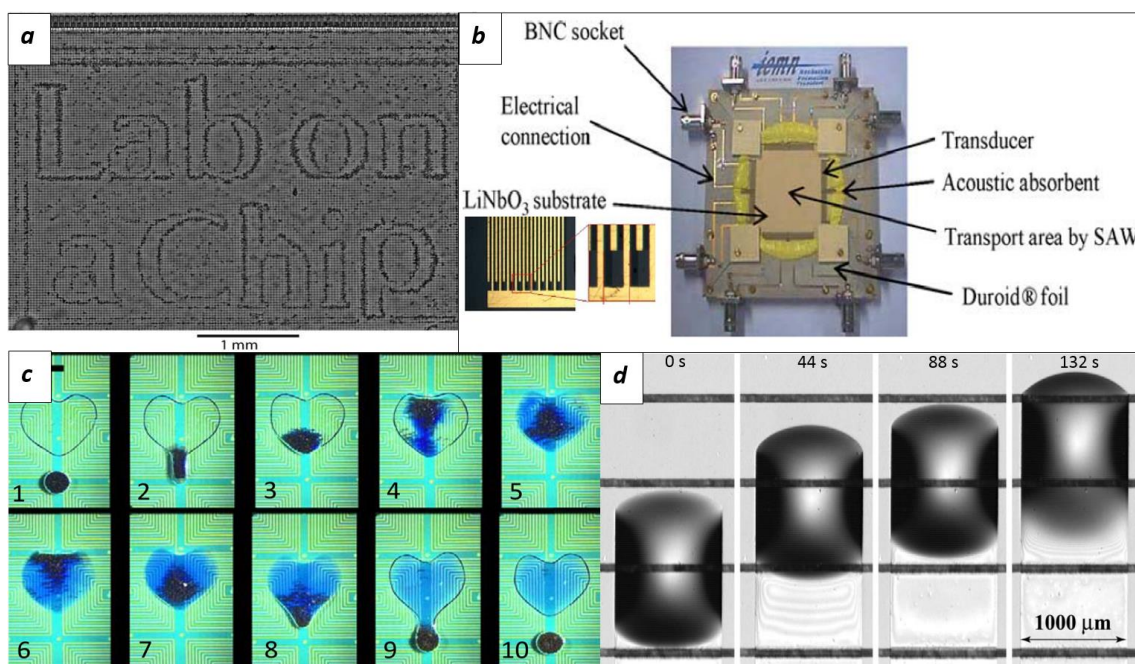


Figure 1.1: (a) Thousands of yeast cells manipulated to form the text ‘Lab on a Chip’ using dielectrophoretic force [39]. (b) Surface acoustic wave device with interdigitated electrodes (shown in lower left inset) patterned on top of a lithium niobate (LiNbO_3) piezoelectric substrate [40]. (c) Merging and mixing (frame 1-5) and splitting (frame 6-10) of droplets containing magnetic particles in a magnetic-based DMF device [29]. (d) A droplet of PDMS moving on top of an array of micro heaters (the thin dark lines) in a thermocapillary-based device [32].

A hybrid integrated circuit (IC)/microfluidic chip device with a programmable two dimensional array of pixels employing the DEP mechanism has been used to trap and move thousands of yeast cells suspended in an oil medium (**Figure 1.1 a**) [39]. A

limitation of the DEP method is the effect of Joule heating when a highly conductive droplet sample is used due to the strong electric field generated within such devices [12, 39].

SAW devices operate by propagating acoustic waves along an elastic surface to cause droplet motion. As the acoustic waves propagate through the droplet, they are attenuated due to the droplet's viscosity. The attenuation of waves creates a pressure gradient that moves the droplet along the acoustic waves' direction. The SAWs are generated using interdigitated microelectrodes patterned on top of a piezoelectric substrate applied with high frequency voltage (**Figure 1.1 b**) [41]. A SAW device capable of performing DNA amplification by polymerase chain reaction (PCR) has been reported by Guttenberg et al. [42].

Magnetic actuation methods are based on controlling the movement of the droplet containing magnetic beads by using a magnet located beneath the device substrate. While electrodes are not required, magnetic beads are necessary for droplet manipulation [43]. **Figure 1.1 (c)** shows a microfluidics device used to perform an enzyme-linked immunosorbent assay (ELISA) of rabbit anti-mouse immunoglobulin that utilised magnetic manipulation for droplet movement [29]. The device creates a magnetic field gradient to move droplets using magnetic coils on a printed circuit board (PCB) substrate. To facilitate operations such as splitting and merging of droplets, the actuating surface was patterned with hydrophilic and hydrophobic regions using oxygen plasma treatment.

The thermocapillary effect takes advantage of a temperature gradient across the actuating surface to instigate droplet movement by altering the surface tension around the droplet perimeter. The difference in the surface tensions between the advancing

and receding ends of the droplet creates a capillary pressure which pulls the droplet to migrate from the warmer to the cooler region [44]. The thermocapillary device contains arrays of micro heaters to generate the temperature gradient. An insulator layer is deposited above the heater arrays and is chemically patterned into wetting and non-wetting regions (**Figure 1.1 d**) [32]. Previously, Valentino et al. [34] have performed β -galactosidase enzyme assay and measured the effect of temperature on its reaction rate using a thermocapillary-based microfluidics device.

1.2 Electrowetting-on-dielectric and its applications

The most basic form of electrowetting that had been demonstrated consisted of a liquid droplet sitting on top of a conductive layer with a voltage applied between them (shown in **Figure 1.2**). Typical structures of EWOD devices (shown in **Figure 1.5**) evolved from this basic setup. Electrowetting induces the movement of the droplet due to electrostatic forces generated when voltage is applied across the solid-liquid interface of the liquid droplet [45, 46]. The observable effect of electrowetting is the significant reduction of the droplet contact angle (CA) as the droplet transition into the wetting state, hence the name [1].

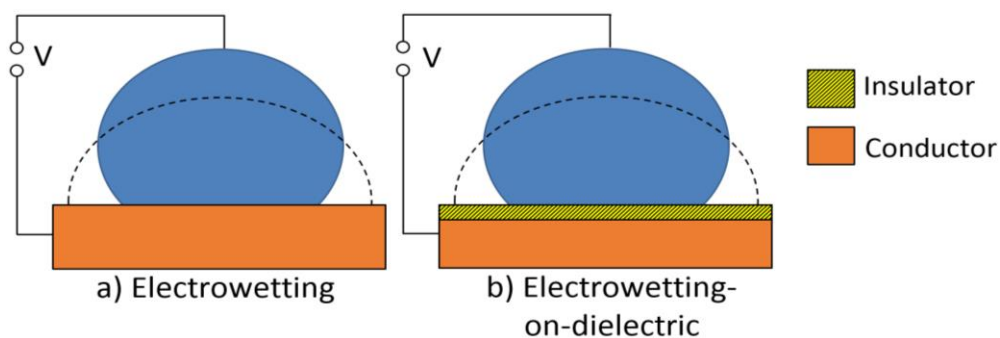


Figure 1.2: *Electrowetting and EWOD mechanisms. In electrowetting, the liquid droplet sits on a conductive layer while in EWOD a layer of insulator is added on top of the conductive layer to avoid electrolytic decomposition of the droplet. The surfaces are in non-wetting state when no voltage is applied. The dashed lines represent the wetting state of the droplets when voltage is applied across them.*

The voltage applied to the droplet is however limited to about hundreds of millivolts, which correspond to the onset of electrolytic decomposition. To overcome the electron transfer across the solid-liquid interface, a layer of insulator is added on top of the electrode and this technique is called electrowetting-on-dielectric or EWOD. This results in wider range of operating voltage and improves the ability of a droplet CA to return to its initial value after applied voltage is removed, i.e. electrowetting reversibility [45, 46]. Due to its ability to control the CA changes electrically, electrowetting has found its applications in liquid lens [47-50], electronic display technology [51], and lab-on-a-chip [11-14]. The following sections will describe the applications of EWOD in the aforementioned technologies.

Another mechanism that can change the wetting of a droplet on a surface using electric fields is dielectrowetting or DEWOD [52, 53]. While the effect of DEWOD on liquid droplet is similar to EWOD where the CA decreases with electric fields, the governing mechanism of DEWOD is the same as liquid dielectrophoresis. DEWOD controls the movement of droplet using non-uniform electric fields acting on dipoles within the droplet [52, 54]. Recently, Geng et al. [55] have fabricated a DEWOD device capable of demonstrating all the fundamental fluidic operations; droplet transportation, merging, mixing, dispensing, and splitting using a single-plate device.

1.2.1 Liquid lens

Figure 1.3 shows a variable liquid lens capable of changing its focal length by electrowetting principle. The lens is made of two immiscible liquids, one conductive and one insulating, with dissimilar refractive indices, contained inside a cylindrical glass tube coated with electrode material. When voltage is applied to the electrode, it will lower the surface tension between the conductive and insulating liquids thus moving the meniscus from convex to concave position and changing the focal length

of the lens. As shown in **Figure 1.3 (c), (d), and (e)**, the liquid lens changes from convex to concave when voltage is applied to the electrode. Different voltage levels produce different conditions of the lens; at 0 V, the lens is in convex condition (**Figure 1.3 c**), at 100 V the lens is completely flat (**Figure 1.3 d**), and at 120 V the lens is in concave condition (**Figure 1.3 e**) [49].

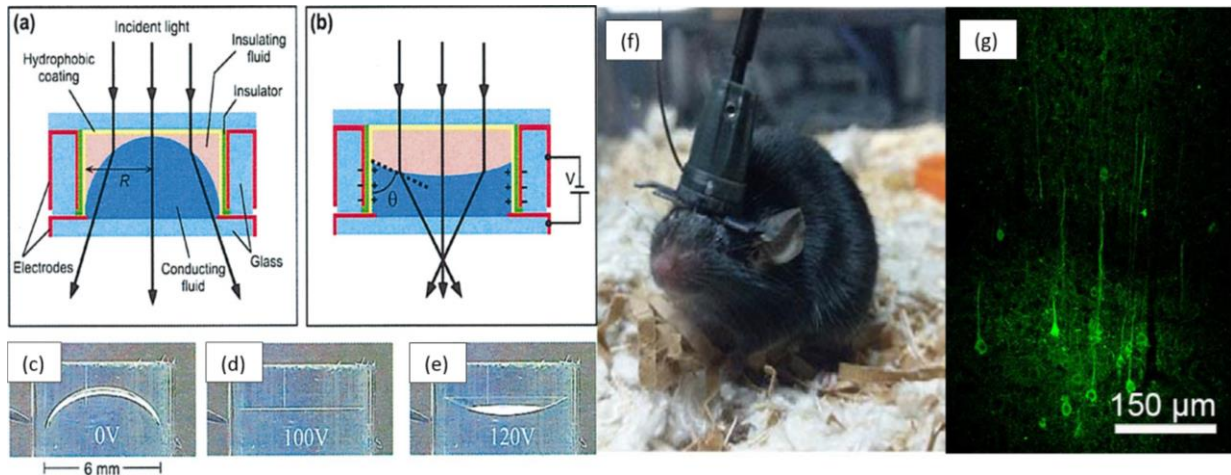


Figure 1.3: Electrowetting in liquid lens. (a) A typical structure of a liquid lens. (b) The liquid lens changes from convex to concave when voltage is applied to the electrode. (c) At 0 V, the lens is convex, (d) at 100 V the lens is completely flat, and (e) at 120 V the lens is concave [49]. (f) Attachment to a mouse skull containing electrowetting tuneable liquid lens employed in a microscope system. (g) A microscopic image of the mouse's brain neurons captured using the electrowetting tuneable liquid lens [50].

Electrowetting tuneable liquid lens have been employed in a two-photon excitation fibre-coupled microscope capable of carrying out active axial-scanning for 3D-neuronal imaging of a freely-moving mouse. The focal length of the liquid lens corresponding to optical power range of -16 to 36 dioptres can be adjusted using AC voltage between 25 and 60 V_{RMS} . Apart from its simplicity in design and easy miniaturisation, the electrowetting tuneable liquid lens also has the advantage of not being affected significantly by motion and orientation when compared to the other conventional optical lens. This can be achieved by employing liquids with the same

density for the conductive and insulating liquids. This will result in a perfectly spherical meniscus that is minimally affected by external vibrations and orientation [49, 50].

1.2.2 Electronic display technology

In electronic display technology, two immiscible liquids, water and coloured oil, are contained on top of a white substrate, transparent electrode, and hydrophobic layer (**Figure 1.4**). Without any voltage application, the coloured oil covers the surface continuously; once voltage is applied between the electrodes and water, the oil film displaces to the side due to the electrostatic energy imbalance. When this phenomenon is viewed from above, two states can be perceived by the observer: a coloured state (no voltage is applied) and a transparent state (voltage is applied) [51]. An example of this technology is the Amazon Liquavista's display shown in **Figure 1.4** [56].

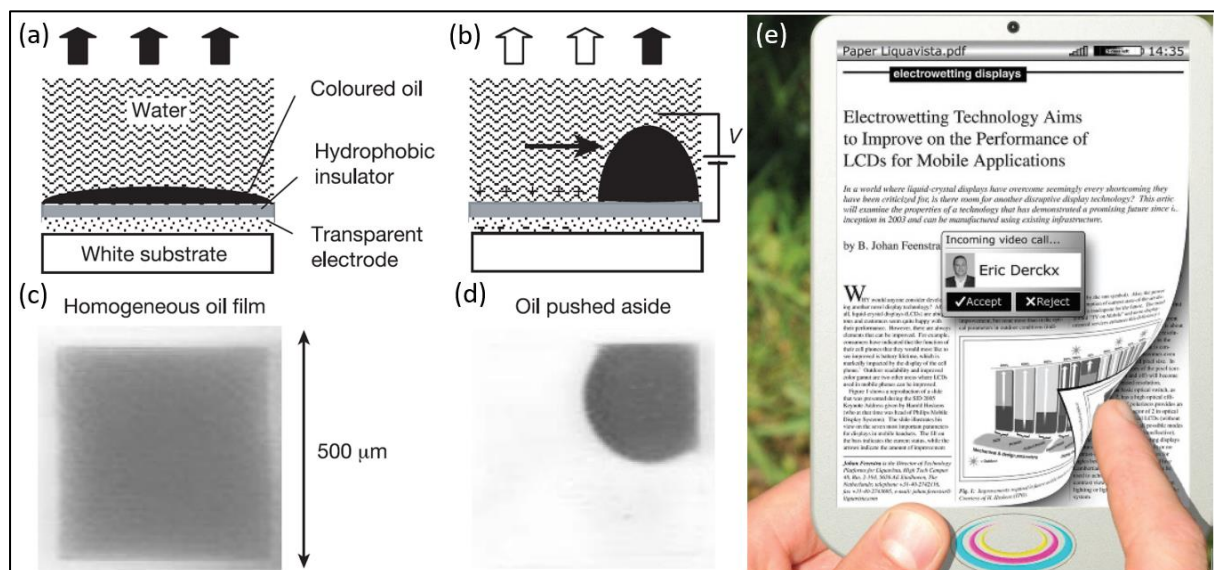


Figure 1.4: Electrowetting in display technology. (a) A basic structure of an electrowetting display. (b) The coloured oil film contracts to the side when voltage is applied due to the imbalance in electrostatic energy. (c) and (d) The states perceived by an observer when look from above for condition described in (a) and (b) respectively [51]. (e) Amazon's Liquavista electrowetting display [56].

Comparing between the available electronic display technologies such as liquid crystal display (LCD), the electrowetting display offers lower power consumption, better performance in high lighting condition, e.g. for outdoor utilisation, and faster response which allows for colourful video on an electronic paper device [52].

1.2.3 EWOD-based DMF device in lab-on-a-chip technology

One of the most reported applications of EWOD is DMF based lab-on-a-chip (LoC) technology. LoC technology is concerned with miniaturising laboratory operations to reduce the reagent volumes thus minimising the time taken to analyse a product [57]. To achieve this, LoC employs microfluidics principles to control the behaviour of the liquid at the microscale. Continuous flow microfluidics have been implemented extensively in LoC but digital microfluidics has gained increasing attention since the Duke Microfluidics Laboratory pioneered the movement of liquid droplets using EWOD mechanism in 2000 [23].

One of the advantages that DMF offers over the continuous flow microfluidics is reconfigurability from one type of application to another due to its simple design and not requiring physical channels, pumps, valves or mixers. The use of suspended phase solid samples is also feasible, within limits, without the risk of clogging. Apart from miniaturising the volume and processes, DMF technology also strongly facilitates the full implementation of automated process as droplet actuation is purely electrically controlled [1, 9].

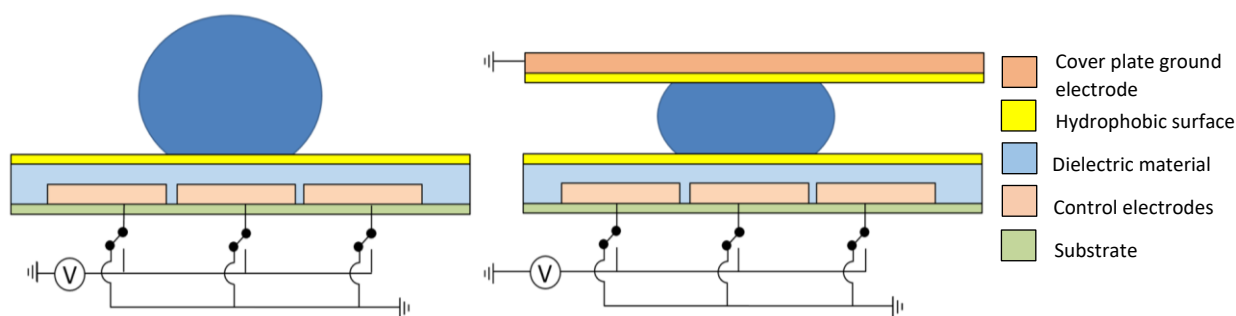


Figure 1.5: Configurations of DMF device: single-plate (left) and parallel-plate (right) configurations. The base plate of the device contains rows of electrode which can be individually addressed.

Typically, an EWOD-based DMF device can assume either a single-plate or a parallel-plate configuration (**Figure 1.5**) however the parallel-plate is more commonly found in the literature. The base plates of both configurations are comprised of the same components, from bottom to top layers: substrate, control electrodes, dielectric material, and hydrophobic surface. The cover plate in the parallel-plate configuration is composed of ground electrode coated with a hydrophobic surface. Fundamentally, the droplet moves forward due to an imbalance of opposing meniscus forces due to the action of electrostatic forces when a control electrode is activated by application of voltage. Movement of an individual droplet across the plate is thus controlled by activating the control electrodes in programmed sequence. The details of the physical mechanism involved in the droplet movement are described in **Section 1.3.2**.

There are many laboratory procedures especially in the biochemistry and biomedical fields that have been demonstrated successfully on EWOD-based DMF platforms, for example, chemical and enzymatic assays [58], sample processing [59], immunoassays [12, 13, 60-63], cell-based assays [14, 64], proteomics [65, 66], tissue engineering [67], and DNA-based applications [68, 69]. Recently, an EWOD-based DMF device was developed by Wang et al. [63] to carry out immunoassay of avian

influenza H5N1 virus. The immunoassay employed magnetic particles as antibody carrier and the device is integrated with Raman system for signal detection using surface enhanced Raman scattering (SERS) method. When compared to the standard enzyme-linked immunosorbent assay method, the integrated DMF-SERS device has shorter assay time (less than one hour), and lower reagent consumption while demonstrating excellent sensitivity and selectivity for the virus detection [63].

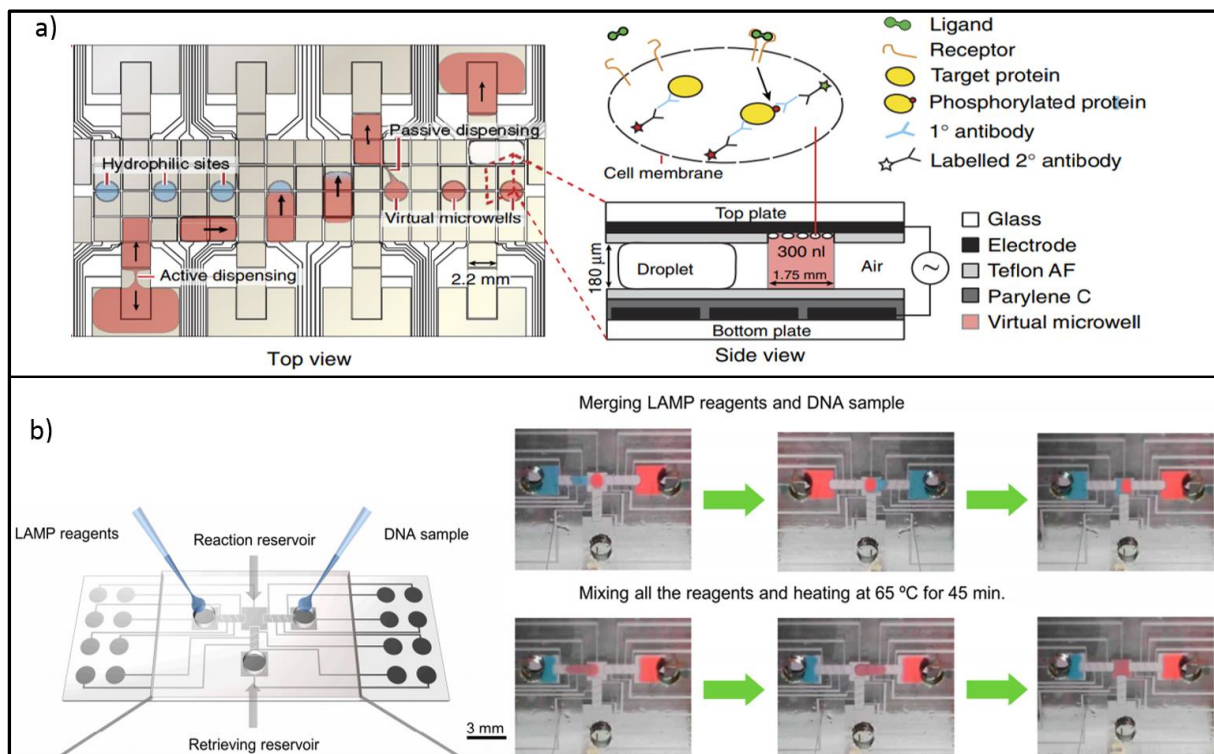


Figure 1.6: The top image (a) shows the schematic of Ng et al.'s [64] DMF device for cell-based assay. Virtual micro wells (shown in the right side of the image) as the site for cell culture by creating hydrophilic regions in the EWOD device. The bottom image (b) displays the DMF device for DNA amplification using loop-mediated isothermal amplification (LAMP) method. The sequence of events on the right represent the merging and mixing operations of the reagents and the DNA sample, where the red-coloured droplet is the DNA sample while the blue-coloured sample is the LAMP reagents.

Figure 1.6 shows another EWOD-based parallel-plate DMF device developed by Ng et al. which was used to perform cell-based assay capable of implementing cell

culture, cell stimulation, and immunocytochemistry of fibroblast cell, a type of cell found in connective tissue of animals [64]. This device employs hydrophilic sites on its cover plate surface to create virtual micro wells for the cell culture when droplets of cell suspension are passed across the hydrophilic regions. The cells are stimulated by transporting droplets of reagents through the virtual micro wells and finally the cells are labelled with antibodies for signal detection [64].

Another application of DMF devices is in DNA-based assays, for example, DNA sequencing and DNA amplification. Coelho et al. [70] conducted loop-mediated isothermal amplification (LAMP) which is relatively a new amplification method compared to the more common polymerase chain reaction (PCR) on EWOD-based DMF platform. LAMP is an isothermal method which is more favourable to the conventional method such as PCR that requires thermal cycling, increasing the complexity and the cost of the device. The device base plate, shown in **Figure 1.6**, is capable of inducing temperature of 65 °C for the DNA reaction using thin ITO film resistor located beneath it [70].

1.2.3.1 Immunoassay

One of the objectives of this thesis is to demonstrate the usability of alternative fabrication technique for the realisation of a low-cost device capable of performing real-life applications such as immunoassay. Immunoassay is a laboratory test to detect the minute presence of a target analyte, usually an antigen, by capturing it using an antibody which only binds to that specific antigen [71]. An antibody, sometimes called an immunoglobulin (Ig), is a large Y-shaped glycoprotein produced by plasma cells, a type of white blood cell, as part of the body's immune response to pathogens such as viruses and bacteria [72]. There are five classes of immunoglobulin that can be found in mammals: IgA, IgD, IgE, IgG, and IgM, each differing in their biological properties

and the antigens that bind to them. In immunoassay, the antibody or sometimes the antigen, is immobilised by attaching it onto a solid phase such as the plastic surface of a microtiter plate. To measure the concentration of the target analyte, either the antibody or the antigen is labelled with a tracer (e.g. radioactive isotope) to generate the signal for detection. The concentration of the target analyte would then be proportional to the intensity of the generated signal. The formats of the immunoassay can be based on the types of label used for the signal detection or the steps involved in its implementation (i.e. the assays protocol) [71].

The immunoassay type (partially) ran in this thesis (**Section 4.3**) was enzyme-linked immunosorbent assay, commonly known as ELISA. ELISA uses enzyme linked to either the antibody or the antigen as the detection method and the protocol used was the direct method where only one type of antibody is used. The capture antibody/antigen which is immobilised to a solid phase, is used to bind to the specific analyte [71]. For the implementation in a DMF platform, magnetic particles are usually employed as the solid phase instead of the microtiter plate surface used in the standard bench-top procedure. In the context of Lab on a Chip, DMF devices are well suited for the utilisation of magnetic particles and any other solid micro-suspensions as they are much less susceptible to clogging compared to conventional flow microfluidics [43].

In assays, after the analyte has bound to the capture antibody/antigen, wash steps are performed with buffer solution to remove the unbound labelled-analyte. ELISA uses an enzyme as the label for the signal detection purpose, for example, horseradish peroxidase (HRP). When a substrate (e.g. luminol) and an oxidising agent (e.g. hydrogen peroxide) are introduced, the peroxide ion oxidises the substrate with

the presence of HRP as the catalyser and as a result photon is emitted. This method of detection is called chemiluminescence and the intensity of the light emission can be measured using photodetector such as a photomultiplier tube [71, 73].

1.2.4 Summary

Comparing the mechanisms employed in DMF devices that have been discussed, EWOD is distinguished by its capability to perform all fundamental fluidic operations (i.e. transport, merging, mixing, splitting, and dispensing of droplets) on-chip using the parallel-plate configuration [74]. Furthermore, EWOD as DMF actuating mechanism is not subject to some of the problems of other techniques. Unlike DEP and thermocapillary techniques, EWOD does not generate heat which is beneficial for temperature sensitive applications [9]. Most of reported DEP [27, 39, 75] and magnetics-based devices [29-31] employ suspending liquid such as silicone oil and 1-bromododecane to facilitate the droplet movement. While the use of suspending medium lowers the voltage required for droplet actuation (in both DEP and EWOD-based systems) and eliminates the problem of droplet evaporation, there is the risk of dissolved species within the immiscible solvent due to partitioning of the sample and reagent droplets into the suspending medium [24]. In an EWOD system, suspending medium is not necessary and the use of air medium reduce the complexity of the device [10, 76]. In this thesis, only air-medium, EWOD-based DMF devices will be researched and employed in the investigations.

1.3 Principles of electrowetting-on-dielectric

This section describes in details the physical principles involved in the EWOD mechanism. Firstly, the forces that govern a static water droplet are described followed by a discussion of the changed conditions when electrostatic forces are introduced.

The latter part consists of explanation on the dynamics of droplet transportation and the formats of EWOD devices.

1.3.1 Contact angle and the Young-Lippmann equation

The shape of a liquid droplet sitting on a solid surface is determined by the surface tension of the liquid. Surface tension or the interfacial energy per unit area between the liquid and gas phases is the inward pulling experienced by the liquid molecules at the liquid-gas boundary due to unbalanced cohesive forces. The unbalanced forces exist because of the absence of liquid molecules above the liquid surface to counter the downward forces exerted by the neighbouring molecules. Surface tension is responsible for the spherical shape of droplets and bubbles as the liquid contracts to maintain the lowest surface energy [77].

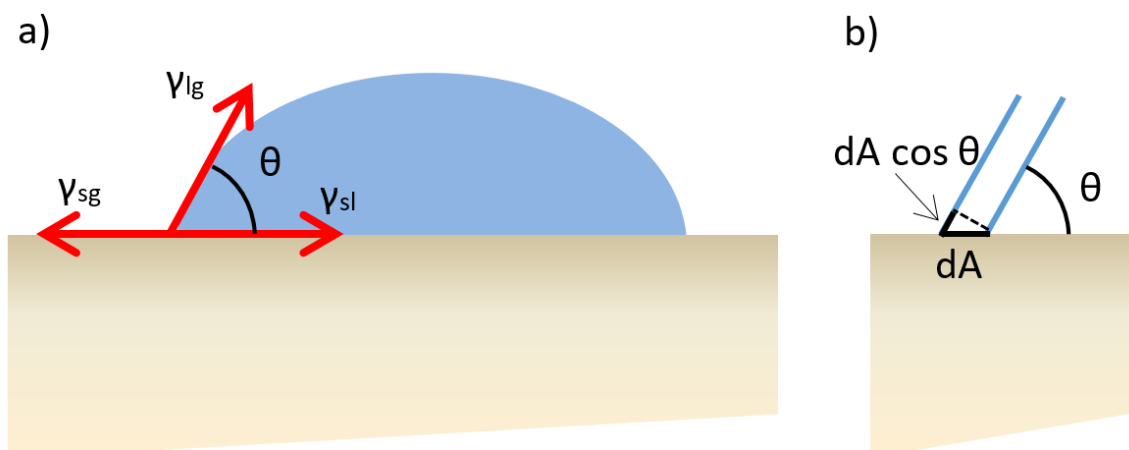


Figure 1.7: a) Sessile droplet on a solid surface. The surface tensions acting between the three phases at the contact line are indicated by the red arrows and θ is the contact angle. b) Droplet contact line movement due to a change in droplet size.

The contact angle (CA), sometimes called the Young's angle, θ of a liquid droplet resting on a solid surface, as shown in **Figure 1.7(a)**, is the angle formed at the intersection of liquid-solid and liquid-gas interfaces when under mechanical equilibrium. The CA is used as a measure of wettability of a surface; a surface is

considered hydrophobic if the CA is larger than 90° and it is said hydrophilic when it is less than 90°. If the CA is larger than 150°, the surface is considered as superhydrophobic [78].

The interfacial energies per unit area, γ between the different phases of the system shown in **Figure 1.7(a)** are represented as γ_{sl} for the solid-liquid interface, γ_{sg} for the solid-gas interface, and γ_{lg} for the liquid-gas interface. The free energy, W of the droplet which is equal to the surface energy of the system, W_s is given by **equation (1.1)** [46, 79, 80]:

$$(1.1) \quad W = W_s = \sum \gamma A$$

where A is the droplet surface area. The work required to make an infinitesimal increase in the surface area is represented by the following **equation (1.2)**:

$$(1.2) \quad dW = \gamma dA$$

The total work done to displace the surface is then obtained by adding the work done by the pressure gradient to change the volume, v . The pressures in the two phases, inside the droplet and outside the droplet are P_1 and P_2 respectively. This is shown in the following equation, **equation (1.3)** [80]:

$$(1.3) \quad dW = \int P_2 - P_1 dv + \gamma dA$$

The volume change, dv is equal to $d\zeta \cdot dA$, where $d\zeta$ is the displacement of the surface between the two phases. The infinitesimal change in area, dA can be expressed in terms of the principal radii of the droplet curvature, r_1 and r_2 . Applying the equilibrium condition where dW is zero and the geometrical conditions of dv and dA to **equation**

(1.3), we obtained the following **equation (1.4)** (full derivation shown in Skjaeveland (2015) [80]):

$$(1.4) \quad \Delta p = \gamma_{lg} \left(\frac{1}{r_1} + \frac{1}{r_2} \right)$$

Equation (1.4) is called Young-Laplace equation where ΔP is the pressure drop across the liquid-gas interface ($P_2 - P_1$). The implication of this equation is that a droplet sitting on a homogenous surface will adopt a spherical cap shape when in equilibrium [46, 79, 80].

Another commonly encountered equation called Young equation which describes the CA of a sessile droplet on a surface can also be derived from **equation (1.1)**. Expanding **equation (1.1)** to describe the total energy of the system shown in **Figure 1.7** in terms of the surface tensions of the three different phases it becomes **equation (1.5)** [46, 79]:

$$(1.5) \quad W_s = \gamma_{lg} A_{lg} + \gamma_{sl} A_{sl} + \gamma_{sg} A_{sg}$$

where A_{lg} is the spherical surface area, A_{sl} is the contact area of the droplet, and A_{sg} is the solid-gas surface area. Young's equation can be derived by implementing free energy minimisation to **equation (1.5)**. Based on **Figure 1.7(b)**, where $dA_{lg} = dA_{sl} \cos \theta$, the change of free energy due to infinitesimal change in droplet size can be represented as following **equation (1.6)** and **equation (1.7)** [46, 81]:

$$(1.6) \quad dW_s = \gamma_{lg} dA_{lg} + \gamma_{sl} dA_{sl} + \gamma_{sg} dA_{sg}$$

$$(1.7) \quad dW_s = (\gamma_{sl} - \gamma_{sg} + \gamma_{lg} \cos \theta) dA_{sl}$$

At equilibrium condition where dW_s equal to zero, **equation (1.7)** becomes the following **equation (1.8)** called Young equation [46, 81]:

$$(1.8) \quad \gamma_{sl} = \gamma_{sg} - \gamma_{lg} \cos \theta$$

which describes the relationship between the Young's CA, θ with the interfacial energies per unit area. The same Young's equation can be derived by obtaining the horizontal component of the forces acting at the three-phase contact line in **Figure 1.7** [46, 79].

The wetting property of the surface, represented by the CA parameter, can be changed by introducing electrostatic force to the system. The solid surface where the droplet is sitting on is comprised of dielectrically coated electrode, similar to the surface shown in **Figure 1.2**. The total energy of the system is now contributed by the interfacial energies described by **equation (1.1)** and by the electrostatic energy, W_{el} given by the following **equation (1.9)** [46, 79]:

$$(1.9) \quad W_{el} = \frac{1}{2} \int \vec{E}(\vec{r}) \cdot \vec{D}(\vec{r}) dv$$

where $\vec{E}(\vec{r})$ is the electric field and $\vec{D}(\vec{r}) = \epsilon_o \epsilon_r(\vec{r}) \vec{E}(\vec{r})$ is the electric displacement at location \vec{r} . The total free energy, W of a droplet in an EWOD setting is then contributed by the interfacial and electrostatic energies [46, 79]:

$$(1.10) \quad W = W_s + W_{el} = \sum \gamma A - \frac{1}{2} \int \vec{E}(\vec{r}) \cdot \vec{D}(\vec{r}) dv$$

Two simplifications can be made on the electrostatic energy; the capacitor formed by the droplet and electrode, C is $= c_d A_{sl}$ (c_d is the capacitance per unit area for the dielectric layer) and the droplet is sufficiently large so that the fringe fields at

the edge of the droplet is negligible. Capacitance per unit area, c_d is equivalent to $\frac{\epsilon_0 \epsilon_r}{d}$ where ϵ_0 is the permittivity of vacuum, ϵ_r is the dielectric material constant, and d is the dielectric layer thickness. These assumptions resulted in the following **equation (1.11)** [46, 79]:

$$(1.11) W_{el} \approx \frac{CV^2}{2} = \frac{\epsilon_0 \epsilon_r V^2 A_{sl}}{2d}$$

where V is the applied voltage. Considering **equation (1.10)** and **equation (1.11)**, the total free energy for EWOD electrodes is [46, 79]:

$$(1.12) W = \gamma_{lg} A_{lg} + \gamma_{sg} A_{sg} + A_{sl} \left(\gamma_{sl} - \frac{\epsilon_0 \epsilon_r V^2}{2d} \right)$$

The above **equation (1.12)** have the same structure with **equation (1.5)**. Comparing the coefficients and combining with Young's equation, **equation (1.8)**, the following **equation (1.13)** called Young-Lippmann's equation is obtained [46, 79]:

$$(1.13) \quad \cos \theta_v = \cos \theta + \frac{1}{2\gamma_{lg}} cV^2$$

Thus the wettability of the droplet, represented by the contact angle at applied voltage, θ_v can be controlled by varying the applied voltage; the higher the voltage, the larger the difference between the initial and final CA. **Figure 1.8** shows the evolution of CA of a droplet sitting on a dielectric surface with applied voltage. As shown in the graphs, the CA decreases as the applied voltage is increased for both the experimental data and the Young-Lippmann prediction. In practice however, the CA diminution predicted by the Young-Lippmann equation is limited to a certain value beyond which it cannot be further reduced as demonstrated by the experimental data in **Figure 1.8**. The CA at which no further decrease is obtainable is called the saturation angle [46, 82, 83].

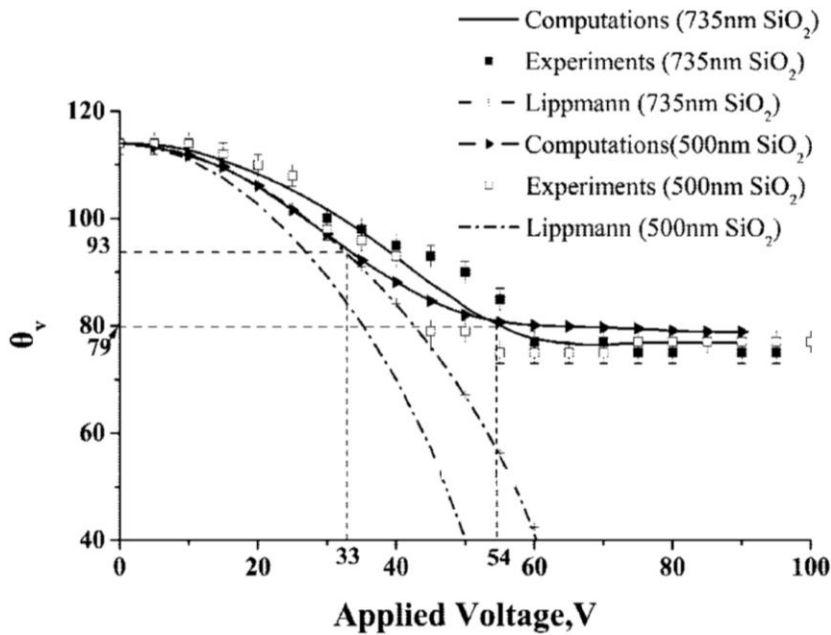


Figure 1.8: The variation of contact angle with applied voltage of a liquid droplet sitting on a silicon dioxide surface. The dashed lines represent the contact angle evolution based on the Young-Lippmann equation which predicts that the contact angle reduces to less than 60° as the voltage is increased. Experimental data (black and white squares) show otherwise where the contact angle stop decreasing at approximately 79° and this angle is called saturation angle [83].

Studies [82-85] have suggested that the saturation angle is approximately $60^\circ - 80^\circ$ for any electrowetting systems. Currently, a universal theory in predicting the mechanism of the contact angle saturation is lacking [83] but some studies suggested that this phenomenon occurs due to micro-droplet ejection and charge injection [85, 86]. Physical interpretation of the droplet actuation using electromechanical approach (described in the next **Section 1.3.2**) suggests that the occurrence of CA saturation is due to the equilibrium reached between the electrostatic and surface tensions. Chevalliot et al. [85] proposed some of the factors that could influence the value of saturation angle: the type of applied voltage (i.e. DC or AC) and the type of hydrophobic surface. Both Chevalliot et al. and Quinn et al. have clearly demonstrated

that CA saturation is also highly time-dependent: the longer the duration of voltage application, the higher the saturation angle [84, 85].

There is a difference in CA value at a given potential depending upon whether the applied voltage is being increased or being decreased during an electrowetting cycle. The CA when the droplet spreads as the voltage is increased is called the advancing angle while the CA when the droplet recedes as the voltage is decreased is called the receding angle. CA hysteresis is the difference between the advancing and receding angles. It exists due to the pinning of the droplet at the triple contact line caused by the presence of roughness and heterogeneity on the solid surface. The higher the pinning force, the higher the CA hysteresis which means the lower the CA reversibility of the surface after an electrowetting cycle [87].

1.3.2 Droplet transportation and calculation of actuation force

As briefly discussed in **Section 1.2**, the driving force behind the droplet motion is the electrostatic force that originates from the electrical energy stored in the dielectric material when a voltage is applied across the droplet sitting on the electrode. There are three interpretations of the physical mechanism of the droplet's movement: thermodynamic, electromechanical, and energy minimisation. All three interpretations result in the same Young-Lippmann **equation (1.13)** which governs the change in droplet CA [45].

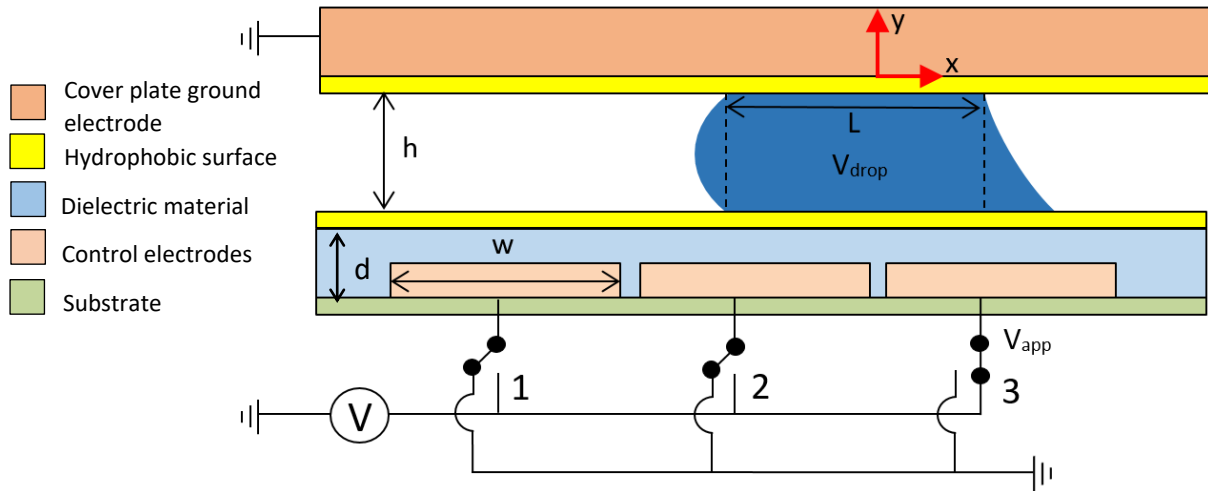


Figure 1.9: Transportation of droplet in parallel-plate DMF device. The state of the droplet just after a voltage is applied to the third electrode. The front meniscus of the droplet spread towards the activated electrode.

Using the thermodynamic interpretation, the changes in CA are the cause of the droplet motion rather than the consequence of it, thus making it inadequate in explaining the motion of dielectric liquids and low surface tension liquids which have very small CA changes when subject to electric fields [10]. Using the electromechanical interpretation, which predicts the same CA changes, provides insight that electrostatic energy rather than surface tension is the driving force behind the EWOD actuation. For example, in **Figure 1.9** the droplet was sitting on top of the second electrode. When the third control electrode is activated, the polarised charges in the dielectric layer will attract the free charges or dipoles inside the droplet to move forward. This will result in the CA change at the bottom front of the droplet as predicted by the Young-Lippmann equation [1, 6, 7, 9]. The actuation forces in an EWOD system, for example the one shown in **Figure 1.9** can be calculated by integrating the horizontal component of the following Maxwell stress tensor, T_{ij} , **equation (1.14)** [10, 46] over a distance $\geq d$ (dielectric layer thickness):

$$(1.14) \quad T_{ij} = \varepsilon_0 \varepsilon_r \left(E_i E_j - \frac{1}{2} \delta_{ij} E^2 \right)$$

where E is the electric field, δ_{ij} is the Kronecker delta function, and i and j represent the x , y , and z axes. The resulting actuation force in the x direction, F_x by the integration of the Maxwell stress tensor will give the following **equation (1.15)**, where w is the width of the electrode:

$$(1.15) F_x = \frac{1}{2} \frac{w \epsilon_0 \epsilon_r V^2}{d}$$

In practise [88, 89], the CA changes due to the voltage application occur only at the macroscopic level; if we were to observe microscopically at the intersection of the three phase contact lines, the local CA remain constant. Due to this phenomenon, the CA value corresponding to the change in voltage level is sometimes referred to as apparent CA [46]. The change in the apparent CA is due to the action of the Laplace pressure to balance the divergence in the Maxwell stress at the three phase contact line. The higher density of electrostatic charges at the three phase contact line generates fringe fields and divergence of the Maxwell stress. The electric fringe fields which is localised within a distance on the order of d from the contact line does not change or affect the local CA [88, 89].

The electrical forces that drive the droplet forward can also be calculated using an energy-based model. The total capacitive energy of the system, U depicted in **Figure 1.9** is given by the following **equation (1.16)** [90]:

$$(1.16) U = \frac{1}{2} c_u w L V_{drop}^2 + \frac{1}{2} c_l w \left(x + \frac{L}{2} \right) (V_{app} - V_{drop})^2 + \frac{1}{2} c_l w \left(\frac{L}{2} - x \right) (-V_{drop})^2$$

where V_{drop} is the droplet potential, V_{app} is the applied voltage, c_u and c_l are the capacitances per unit area of the top hydrophobic layer, and bottom dielectric and hydrophobic layers respectively. The electrostatic force acting on the droplet in the horizontal direction is obtained by differentiating the total energy of the system with

respect to the x coordinate. The above equation reduces to the following **equation (1.17)**, which is the same as the **equation (1.15)** derived using the electromechanical approach [90-93]:

$$(1.17) \quad F_x = \frac{1}{2} w c_l V_{app}^2 = \frac{1}{2} \frac{w \epsilon_0 \epsilon_r V_{app}^2}{d}$$

The electrostatic force above is derived from the parallel-plate system shows in **Figure 1.9** but a similar force equation can be arrived if we consider an open or single-plate system. The single-plate system is shown in **Figure 1.10** where a droplet undergoes contactless electrowetting as the droplet is not in direct contact with the electrodes. There is no top-plate in this configuration [79].

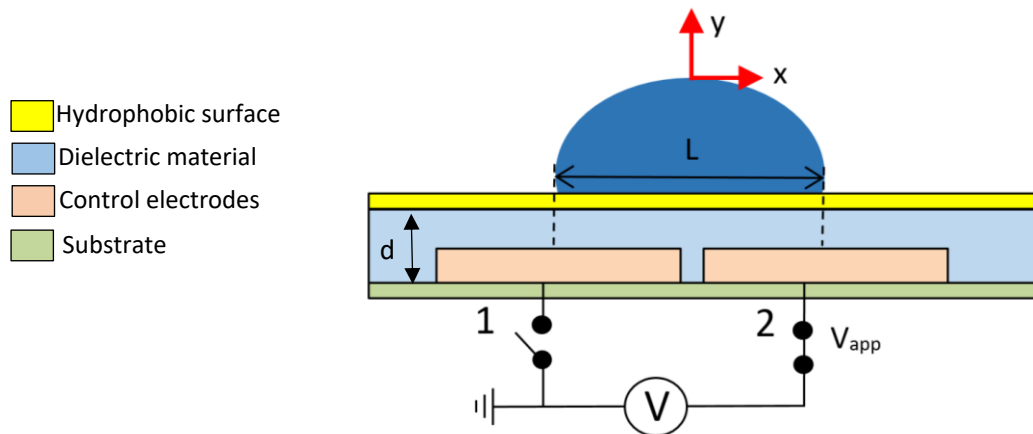


Figure 1.10: Transportation of droplet in a single-plate DMF device.

Neglecting the effect of fringing fields, the capacitances per unit width on the left side (C_1) and the right side (C_2) of the droplet are given by the following **equations (1.18)** [79]:

$$(1.18) \quad C_1(x) = \frac{\epsilon_0 \epsilon_r}{d} (L - x) \quad \text{and} \quad C_2(x) = \frac{\epsilon_0 \epsilon_r}{d} (L + x)$$

The series combination of the capacitance, $C(x)$ gives the following **equation (1.19)**:

$$(1.19) \quad C(x) = \frac{C_1 C_2}{C_1 + C_2} = \frac{\epsilon_0 \epsilon_r}{2Ld} (L^2 - x^2)$$

The total electrostatic energy per unit width, f_x of the system is the sum of the capacitance energy contributed by the left and right sides of the droplet and is given by the following **equation (1.20)**:

$$(1.20) \quad f_x = -\frac{1}{2} \frac{\epsilon_0 \epsilon_r V_1^2}{d} + \frac{1}{2} \frac{\epsilon_0 \epsilon_r V_2^2}{d}$$

The voltage drop on the left side (V_1) and the right side (V_2) of the droplet can be determined using capacitive voltage dimension and expressed in terms of L and x (full equations shown in Jones (2009) [79]). Substituting the voltage drop equations into **equation (1.20)**, we obtained the following electrostatic energy per unit width **equation (1.21)** which is similar to **equation (1.17)** [79]:

$$(1.21) \quad f_x = -\frac{1}{2} \frac{\epsilon_0 \epsilon_r x V^2}{Ld}$$

In order for the droplet to move forward, the actuation force generated by the electrical energy needs to be larger than the opposing forces. At the initiation of the droplet's movement, the actuation force needs to overcome the static friction force, F_s contributed by the CA hysteresis and/or any other friction. The threshold voltage to initiate the droplet movement is highly influenced by the liquid-surface interaction characterised by the CA, rather than the droplet viscosity or the geometry of the electrodes [94]. As the droplet begins to move, there are three main forces opposing its motion: the viscous dissipation occurring inside the fluid droplet, F_d , the contact line friction, F_f , and the viscous friction between the droplet and the suspending medium, F_v . Considering all the significant forces acting on the droplet during an electrowetting actuation, the following **equation (1.22)**, governs the dynamics of the droplet motion [87, 90, 94-96]:

$$(1.22) F_x - F_s = F_d + F_f + F_v$$

The viscous flow within the droplet is a function of capillary number, $Ca = \frac{\mu_d v}{\gamma_{lm}}$ and liquid-medium surface tension, γ_{lm} where μ_d is the droplet viscosity and v is the droplet average velocity. The following **equation (1.23)** represents the viscous dissipation force due to the viscous flow within the droplet, where B is a dimensional coefficient, whose value is obtained by fitting to experimental data [87, 90, 94-96]:

$$(1.23) F_d = B \left(\frac{\mu_d v}{\gamma_{lm}} \right)^{0.3} \gamma_{lm}$$

The contact line friction is contributed by molecular adsorption and desorption around the contact line. At low and intermediate velocities, this friction force is linearly dependent with the velocity and is given by **equation (1.24)**:

$$(1.24) F_f = (\zeta v) 4\pi r$$

where ζ is the friction coefficient. The effect of the viscous flow of the medium on the droplet's motion is highly dependent on the density of the medium, ρ_m and the droplet's average velocity. It is also dependent on the radius of the droplet, r and the spacing between the top and bottom plates, h . An estimation of the viscous resistance on the droplet due to the medium is given by **equation (1.25)** [96]:

$$(1.25) F_v = \left(\frac{1}{2} C \rho_m v^2 \right) 2rd$$

where C is the drag coefficient for a cylinder in a cross flow. The viscous drag is especially significant if the EWOD system uses oil as the suspending medium [97, 98]. In this thesis, air is used as the suspending medium for droplet transportation making the effect of the viscous drag negligible.

1.3.3 EWOD-based DMF device format

There are four key components in a typical EWOD-based DMF device: substrate, electrodes, a dielectric layer, and hydrophobic surfaces. As previously mentioned in **Section 1.2.3**, there are two configurations that can be implemented in DMF devices: the single-plate (or ‘open’) and the parallel-plate (or ‘closed’) formats, as shown in **Figure 1.5**. Both configurations have a base plate that contains an array of control electrodes underneath a dielectric layer. The parallel-plate configuration consists of two plates that sandwich the droplet and the suspending medium which can either be air or immiscible fluid [23, 94, 99]. Implementation of immiscible fluid such as silicone oil results in lower threshold and breakdown voltages, lower operating voltage and improvement in reversibility due to lower CA hysteresis than in air medium [23, 92, 99]. It also prevents from droplet evaporation [9, 100].

However, there are a few drawbacks of employing oil medium; walls are required to contain the medium from leaking [100] and it is difficult to fill the chip reservoir with the oil medium without introducing air bubbles [6]. Apart from that, there is the risk of dissolved species from the droplet into the oil medium as mentioned previously [24]. The use of oil medium also limited the use some types of reagents, for example ethanol, due to their miscibility with oil [9]. Certain on-chip detection techniques are also incompatible with the oil medium [101]. To reduce the complexity of the device fabrication process, air medium has been chosen as the device format in this thesis.

Both the base and the cover plates are coated with hydrophobic material as the actuating surface to facilitate droplet motion and to provide a wider range of CA modulation [23, 46, 91]. The top cover plate comprises one contiguous grounded electrode. Most of the reported devices [12, 13, 23, 58, 60-62, 68, 69, 92-94, 102, 103]

use the parallel-plate configuration, both because it provides reliable droplet volumes by protecting droplets from evaporation and because droplets in parallel-plate devices are less affected by gravity than in single-plate devices [104]. One disadvantage of the parallel-plate configuration is the difficulty of incorporating additional functions such as sensing devices without affecting the electrode design and arrangement [104]. The single-plate devices [105, 106], while simpler in design are not capable of performing droplet splitting operation as yet. An example of single-plate device is an all-terrain actuation EWOD device developed by Abdelgawad [107] capable of transporting a droplet across wide range of surface topography such as inclined, vertical, and inverted using polyimide as a flexible substrate.

There are also reports [104, 108-110] of parallel-plate devices with a passive/ungrounded top cover plate but this configuration requires a specific design of bottom plate control electrodes. The benefit of employing a parallel-plate configuration with a passive top plate is that the top plate can be used for other functions while still maintaining the advantageous aspects of having two plates rather than single plate. However Pollack et al. [94] have suggested that this configuration is unworkable if the typical square electrode designs previously used in [12, 13, 23, 58, 60-62, 68, 69, 92, 94, 102, 103] are employed due to diminishing of surface energy gradient once the droplet reaches halfway between two electrodes. Several suggestions to overcome this include using a much smaller electrode size (100 μm) than droplet size such as Washizu's [108] device or by adding thin coplanar ground electrodes in between the control electrodes [94]. Several studies [104, 109, 110] accomplished droplet transportation using a passive top plate by using actuation electrodes comprising of 2, 4 or 6 sub-electrodes. Pressure difference to move the

droplet forward is achieved by applying potentials among the sub-electrodes within an actuation pad.

Subsequent chapters of this thesis describe both single-plate and parallel-plate devices fabricated to test the feasibility of the proposed materials and methods. The parallel-plate with passive cover plate configuration was also developed in the later section, employing commercial superhydrophobic actuating surfaces as a novel technique to achieve droplet actuation using this configuration.

1.4 Dielectric material in EWOD

The dielectric layer in an EWOD device functions to sustain large electrostatic energy across the capacitor, formed by the dielectric layer and droplet, by preventing electron transfer from the electrodes to the droplet. The introduction of the dielectric layer to the electrowetting process has improved the reversibility and modulation of the droplet CA [22, 45, 46]. **Table 1.1** lists some of dielectric materials that have been employed previously in EWOD devices. The most commonly reported material in recent literature is Parylene-C [22]. Other dielectric materials include silicon dioxide (SiO_2), aluminium dioxide, and *Teflon*TM *AF* [92, 99, 102, 111].

There are several important factors to consider in choosing a dielectric material for EWOD device application: high dielectric constant, high dielectric strength, and good adhesion with substrate, electrode and hydrophobic layer. High dielectric constant increases the capacity of the material to store electrostatic energy, thus making it more effective for droplet actuation at lower voltage [99, 102]. It also provides large CA tunability [22]. High dielectric strength is desirable to prevent the breakdown of the insulating layer which in turn can cause the electrolysis of the droplet [22, 111].

Table 1.1: Dielectric materials employed in EWOD device

| Dielectric materials | Dielectric constant, ϵ_r | Fabrication method | Authors |
|--|-----------------------------------|---|------------------------------|
| Teflon™ AF | 1.93 | Spin coating | [99, 102] |
| Cytop® | 2.1-2.2 | Spin coating | [111] |
| Polydimethylsiloxane (PDMS) | 2.3-2.8 | Spin coating | [107, 112] |
| Parylene-C | 3.15 | Chemical vapour deposition (CVD) | [9, 23, 61, 62, 94, 99, 102] |
| SU-8 (epoxy based photoresist) | 3.2 | Spin coating | [15, 113] |
| Silicon dioxide (SiO ₂) | 3.9 | Plasma-enhanced chemical vapour deposition (PECVD), wet oxidation process | [92, 99, 102] |
| Silicon nitride (Si ₃ N ₄) | 7.8 | PECVD, low pressure chemical vapour deposition (LPCVD) | [102] |
| Aluminium oxide (Al ₂ O ₃) | 9.5 | Atomic layer deposition | [114] |
| Other unconventional dielectric materials | | | |
| Tantalum pentoxide (Ta ₂ O ₅) | 20-25 | Sputtering, dry or plasma etching, anodising | [115, 116] |
| Barium strontium titanate (BST) | 180 | Metal organic chemical vapour deposition (MOCVD) | [92, 102] |
| Ion gel poly(vinylidene fluoride-co-hexafluoropropylene) (P(VDF-HFP) + 1-ethyl-3-methylimidazolium bis(trifluoromethylsulfonyl)imide (EMIM)(TFSI)) | 12 | Spin coating | [22] |
| Cyanoresin CR-S cyanoethyl pullulan (CEP) | N/A | Roller coating | [117] |
| Saran™ wrap (polyethylene film) | N/A | Applied manually | [20] |
| Parafilm | N/A | Applied manually | [118] |
| Adhesive tape | N/A | Applied manually | [119] |

Good adhesion between the dielectric material and the substrate and electrode materials is important to prevent detachment of the layer which again can result in electrolysis. The left image in **Figure 1.11** shows bubble formation in a droplet due to improper adhesion of *Teflon*TM *AF* dielectric layer to gold electrode. The right image displays no dielectric failure indicating better interaction between *Teflon*TM *AF* and graphene material [120].

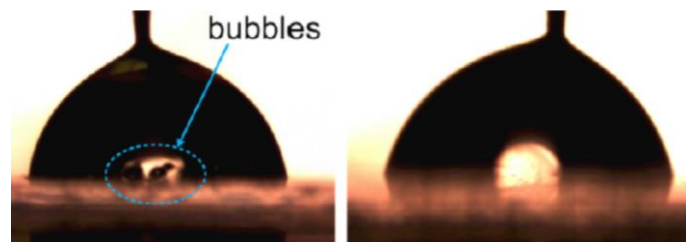


Figure 1.11: Failure in the dielectric layer causes electrolysis as indicated by the bubble formation in the left figure. The right figure shows normal EWOD of droplet without any failure [120].

The magnitude of operating voltage required to produce adequate electrostatic forces to transport droplet forward in an EWOD device depends on the thickness of the dielectric material and the dielectric constant [99, 102]. Operating voltage can be reduced by using a thinner dielectric layer but at the same time the thickness must be able to withstand the applied voltage without breaking down which then leads to leakage current and electrolysis. The left graphs in **Figure 1.12** show the relationship between the thickness of *Teflon*TM *AF* dielectric layer with the breakdown voltage and the voltage to induce CA change from 120° to 80°. Both the breakdown voltage and the voltage to induce the CA change increase with the thickness of the dielectric material. For *Teflon*TM *AF*, the minimum thickness required to avoid dielectric failure upon voltage application is approximately 0.2 μm [102]. Reported thickness of dielectric material in EWOD can range from 0.07 μm [102] up to 16 μm [117] depending on types of material and fabrication method.

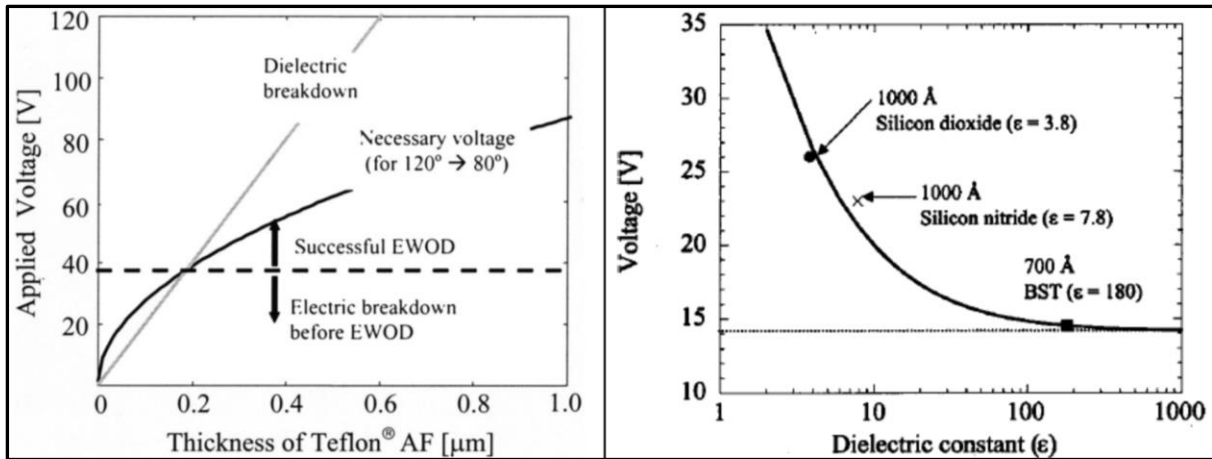


Figure 1.12: The left graph shows breakdown voltage and necessary voltage to change CA from 120° to 80° as a function of Teflon™ AF thickness. The graph on the right display the relationship between the voltage change CA from 120° to 80° and the dielectric constant of the material [102].

Threshold voltage is the voltage required to initiate droplet movement across electrodes. The earlier DMF devices built by the Duke Microfluidics Laboratory in Duke University employed $\sim 0.9 \mu\text{m}$ of insulating layer (Parylene-C and Teflon™ AF) which resulted in 15 V to 40 V in threshold voltage [23, 94]. The reversibility of Teflon™ AF with low thickness however shows dependency on the voltage polarity. The CA is irreversible when negative potential is applied to the droplet. It is suggested that this is due to hydroxide ion, OH^- preferential adsorption to the Teflon™ AF surface as the same effect was not observed on SiO_2 with the same thickness [99, 102].

Despite reducing the operating voltage, a thicker dielectric layer is preferable in cases where a higher voltage range is employed. A thicker dielectric layer also protected against failure mechanisms such as dielectric breakdown and liquid infiltration [101]. Another advantage of using a thicker layer is that it diminishes the effect of local defects caused by the presence of trenches (between two adjacent electrodes) or contaminating particles during the fabrication process [20].

The right graph in **Figure 1.12** represents the voltage required to induce CA change from 120° to 80° as a function of dielectric constant. Materials with high dielectric constant could also lower the operating voltage though not as effectively as using thinner dielectric. For the same thickness of 1.65 μm , Parylene-C which has a higher dielectric constant than *Teflon*TM *AF* does not lower the threshold voltage significantly (from 46 V to 45 V) which indicates that a higher dielectric constant is required to lower the voltage significantly [99]. Moon et al. [102] demonstrated that barium strontium titanate (BST) which has $\epsilon_r = 180$ is capable of inducing 40° contact angle change using just 15 V. For material with dielectric constant more than 100, the Young-Lippmann equation predicts that a further reduction in its thickness will not reduce the operating voltage by much if a certain CA modulation is to be achieved [102].

One study [22] has developed a new material, an ion gel with high dielectric constant of 12, which can be deposited using spin coating procedure. The ion gel was made of a structuring polymer and ionic liquid which is the component that contributes the most to the capacitance property of the ion gel. The capacitance of the dielectric layer was found to be independent of the thickness of the ion gel where thicknesses ranged from 5-18 μm gave the similar CA modulation with respect to the same applied voltage. The ion gel and *Teflon*TM *AF* combination produced the largest CA change for a certain applied voltage when compared with the other dielectric materials with the same or lower thicknesses. However, due to the ion gel's high capacitance, a thicker hydrophobic *Teflon*TM *AF* layer is required to avoid the dielectric breakdown of the *Teflon*TM *AF* layer.

There are also studies which employ readily available non-specialist products such as SaranTM wrap [20], parafilm [118], and adhesive tape [119] as the dielectric

layer. Off-the-shelf products are inexpensive and employ very simple fabrication methods which makes them very good candidate materials for the studies detailed in this thesis whose aim is to develop a low-cost EWOD device. The preliminary results of the feasibility of using commercial dielectric material as an EWOD component is reported in **Section 3.2**.

1.5 EWOD actuating surface

The main function of the hydrophobic layer in an EWOD device is to facilitate droplet movement by providing a low surface energy, hence a low CA hysteresis to oppose the droplet motion [76]. The hydrophobic surface is also impermeable to liquid, providing a barrier from water infiltration. *Teflon™ AF* [23, 60-62, 92-94, 102], *FluoroPel™* [17, 121], and *Cytop®* [15, 104, 122] have been employed for the realisation of hydrophobic surfaces in EWOD devices because they produce high CA of $\sim 110^\circ$ or larger. They also demonstrate high reversibility with low hysteresis for most types of aqueous droplet solutions after an electrowetting cycle. However these materials are prone to molecular adsorption when solutions with a high concentration of biomolecules are used [123]. Surface contamination by the biomolecules causes low durability of the EWOD devices. Another drawback of these hydrophobic materials is their quite high cost; both *Teflon™ AF* and *Cytop®* are inherently expensive perfluoropolymers coatings due to their multistep monomer preparation processes [124]. In response to this, some studies have investigated low-cost, commercial 'rain repellent' materials such as *Rain-X*, [118] *Nevosil Si-7100*, [119] and *Avam* [119]. While the results from these studies are promising where droplets have been actuated on the off-the-shelf hydrophobic surfaces, thorough investigation of the electrowetting response of these products has not been conducted. Their robustness with 'real-world' samples has also yet to be reported.

1.5.1 Contamination of hydrophobic surface and the problem of biofouling

Despite its many advantages, the full potential of DMF for bioassay applications will not be achieved without successfully addressing the question of device reliability and usability when 'real-world' samples are used. 'Real-world' samples, often containing high concentrations of biomolecules, can cause contamination of the actuation surface, generally referred to as biofouling, by the adsorption of biomolecules (e.g. proteins). The residue left on the surface can cause two issues. Firstly, the impediment of the subsequent droplet motion as it becomes stuck at the contaminated location. This compromises the device's reliability and ability to function, thus limiting its lifetime. The second problem is cross-contamination if the same device were to be used for multiple experiments [9, 24, 62].

Berthier & Brakke [91] postulated that the inhomogeneity of the hydrophobic surface resulting from biomolecules' adsorption may lead to dielectric layer breakdown due to anomalous localized electric field maxima causing the dielectric strength of the material to be exceeded. **Figure 1.13** shows an example of biofouling on *Teflon™ AF* surface in an EWOD device caused by protein adsorption. The microscopic images illustrate the contamination that occurred after a droplet containing conjugate of fluorescein isothiocyanate (FITC) with bovine serum albumin (BSA) at concentration of 7 µg/ml was transported across the electrodes four times. [24]. This indicates how rapid the adsorption process is as the droplet was in contact with the surface for only a short period of time.

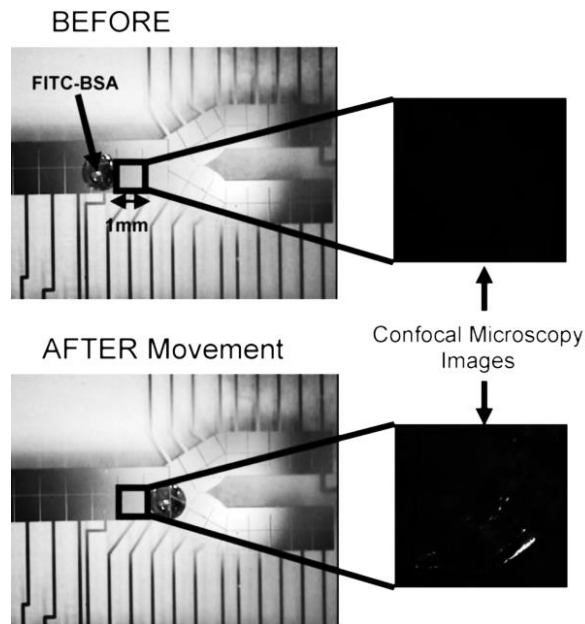


Figure 1.13: Biofouling of EWOD actuation surface. On the right side of the figure are the fluorescence micrographs of the EWOD surface before and after the droplet transportation. The after image shows protein (FITC-BSA) adsorption that occurred after moving on the surface four times [24].

Several strategies have been employed to address the biofouling problem. The first approach is by using a silicone oil medium [92, 94, 99] to reduce biofouling apart from reason to reduce the hysteresis and voltage requirement by forming a barrier between the droplet and the hydrophobic surface. However this approach requires specific device packaging to avoid leakage and is challenging in terms of transportability and connectivity with other microfluidic devices [62]. There is also the risk of droplet components diffusing into the oil phase or the oil infiltrating the droplet thus interfering with the droplet's chemistry [125]. The second technique to reducing biomolecular adsorption involves adding an amphiphilic component such as *Pluronic*® non-ionic surfactant [24] to the droplet. This method has successfully allowed actuation of foetal bovine serum, a very 'sticky' solution back and forth across four electrodes for two cycles [24]. The use of surfactant however has the drawback of not being compatible with all types of reagent [24, 25].

The third approach is by adding graphene oxide, which has a very high protein binding capacity, to the droplet as the nano-carrier for the protein molecules preventing them from adsorbing to the actuating surface [25]. Similar to the surfactant additive, this method might not be suitable with all types of sample and reagent. The fourth method that has been employed to prevent biofouling is by using removable 'skin' so that it can be replaced once the surface is contaminated [24]. The hydrophobic material, *Teflon*[™] *AF* was coated onto polyethylene food wrap, *Saran*[™] instead of directly onto the device. The easily replaceable skin acts as both the dielectric and hydrophobic components of the device. While this technique prevents the biofouling from cross-contaminating the subsequent experiments and also from directly polluting the EWOD plate, it still does not solve the biomolecules adsorption that occurs within a given experiment [9, 24].

The fifth technique that has been developed involves electrostatically repelling the protein molecules from the surface through droplet solution pH and electrode polarity regulation. However employing this method with real-life samples is difficult as more than one type of protein with different charges and polarity can be present in the sample [9, 125]. The final reported approach to address biofouling is by using superhydrophobic surfaces [9, 15, 126]. The presence of nanostructures in the superhydrophobic surface reduces the contact area between the droplet and the surface, thus suppressing the biofouling effect. Superhydrophobic surface as an EWOD actuating surface will be discussed in significant detail in the next section as this approach is employed in this thesis to address the biofouling problem.

1.5.2 Superhydrophobic materials as actuating surface in EWOD devices

A surface is characterised as superhydrophobic when its static CA is larger than 150° [126]. This property is produced by combining micro and nanostructures with low

surface energy. A key component in the development of superhydrophobic surfaces is the introduction of surface roughness by the micro and nanostructures, a feature that is also present in naturally occurring superhydrophobic surfaces (e.g. butterfly wings, colocasia leaves and lotus leaves) [127-129]. Wang & Jiang [129] described five possible states of superhydrophobic surfaces: Wenzel state, Cassie-Baxter state, Lotus state (special case of Cassie-Baxter state), transitional state between Wenzel and Cassie-Baxter states, and 'Gecko' state. In both the Cassie-Baxter state and the Lotus state, the superhydrophobic surfaces gain a self-cleaning property due to the high CA which reduces liquid droplet contact area with the surface and provides almost frictionless droplet movement [128, 129].

There are only a few reported applications of superhydrophobic surfaces in DMF devices. Jonsson-Niedziolka et.al [15] described the partial use of a superhydrophobic surface in a DMF device applied only to the ground (cover) electrode plate instead of the control electrode (base) plate in a 'closed' EWOD configuration. This device demonstrated almost complete removal of four types of pre-deposited particles: MS2 bacteriophage, BG (*Bacillus atrophaeus*) spores, ovalbumin protein, and polystyrene latex micro beads, indicating a very efficient self-cleaning property.

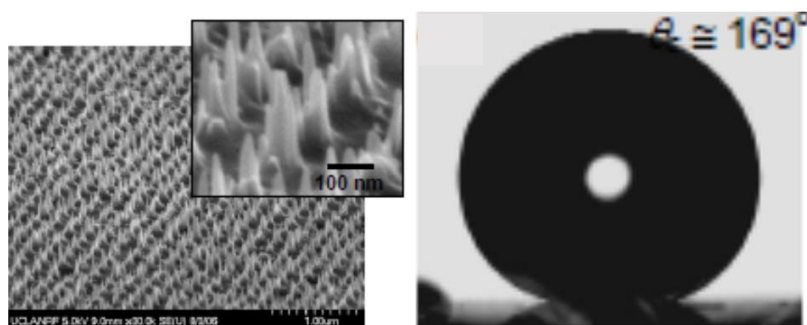


Figure 1.14: Nanostructure of the EWOD actuating surface made by SiO₂ coated with perfluorodecyltrichlorosilane developed by Yun & Kim. The surface is capable of producing very high CA of approximately 169° [129].

Only one study reports the fabrication of a fully superhydrophobic (both base and cover plates) EWOD device [129]. This device comprises a nanostructured SiO₂ layer coated with perfluorodecyltrichlorosilane that acts both as the dielectric layer and the superhydrophobic actuating surface (**Figure 1.14**). Displacement of a water droplet across very short distances at a low voltage of 24 V was demonstrated but it is unclear from the reported evidence that the device allowed reliable actuation across an operationally relevant distance. Other studies [130-135] concerning EWOD superhydrophobic surfaces only investigated the electrowetting reversibility of CA but did not demonstrate fully functional EWOD transportation devices.

Mats et al. [127] investigated some aspects of the application of the commercial superhydrophobic material *Ultra-Ever Dry*® in a non-EWOD magnetic actuation based DMF device but only reported the roll-off angle required to move magnetic particle suspension droplets. The superhydrophobic surface was prepared by the simple spray-deposition process using a chromatography sprayer. Freire & Tanner [136] employed a superamphiphobic (repels both water and oil) surface to develop a DMF device capable of moving bovine serum albumin at a concentration 2000 times higher than previously reported without using any additives. This device, termed field dewetting device, however relies on rolling mechanism and DEP forces for droplet motion where no wetting of droplet on the device surface is involved.

While offering a solution to the biofouling problem [9], all of the reported superhydrophobic EWOD surfaces require elaborate and complex processes such as various chemical reagents for surface modifications [15, 131], and expensive equipment such as LPCVD [130], thermal evaporation [130, 133], PECVD [129, 135], atomic layer deposition (ALD) [135], radio frequency sputtering [131] and laser interference lithography [129]. For the realisation of cheap and potentially disposable

EWOD bioassay devices, these techniques imply high ultimate production costs [129-132].

To address this issue, this thesis proposes the application of commercially available materials as the EWOD actuating surface. **Sections 3.4** and **4.4** are dedicated to investigations of the electrowetting properties of these superhydrophobic materials and actuation of protein-laden droplets on superhydrophobic surfaces respectively.

1.6 Fabrication of EWOD device

There are generally three main processes in creating an EWOD device: patterning of control electrodes onto the substrate, deposition of a dielectric material, and finally, deposition of a hydrophobic layer. This section will review the conventional methods that have been used for the fabrication of EWOD devices. Later in this section, there is a discussion of non-traditional technique for the electrode patterning using printed electronics technology.

1.6.1 Microfabrication techniques of EWOD plates

Microfabrication techniques of EWOD plates usually involve conventional clean-room processes used in the production of integrated circuits (IC) [61, 118, 119]. **Figure 1.15** shows the main steps required in the fabrication of EWOD plates. The fabrication process involves blanket deposition of each of the EWOD device component materials layer by layer. Patterning of each material is performed before the next layer is deposited if required [68, 115, 137].

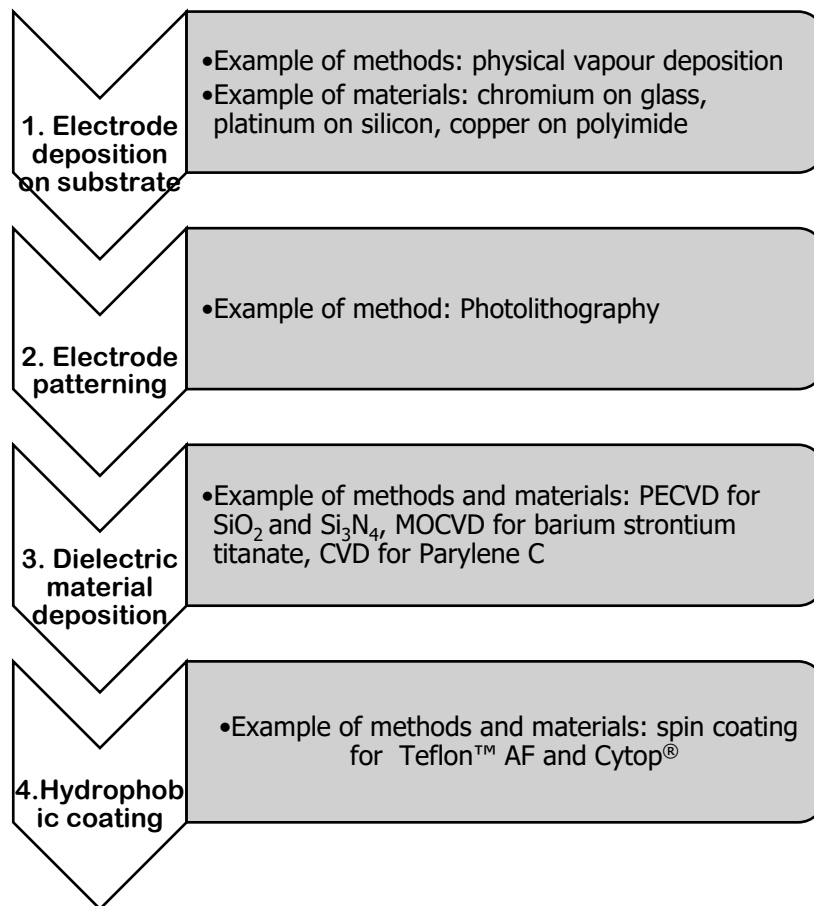


Figure 1.15: Layer by layer fabrication process of EWOD device.

The process starts by the deposition of electrode material onto the substrate. Common materials for the substrate are glass and silicon due to their chemical inertness [9]. The choice of substrate is very important as it determines the geometry of the EWOD device as well as the methods that can be used for the fabrication process. The conductive material for the electrode is usually metal such as chromium, gold, aluminium, copper, and platinum [68, 102, 105, 115, 137] which uses physical vapour deposition (PVD) as the fabrication method. The most reported PVD method employed in EWOD device fabrication are electron beam evaporation and sputter coating [68, 102, 105, 115, 137].

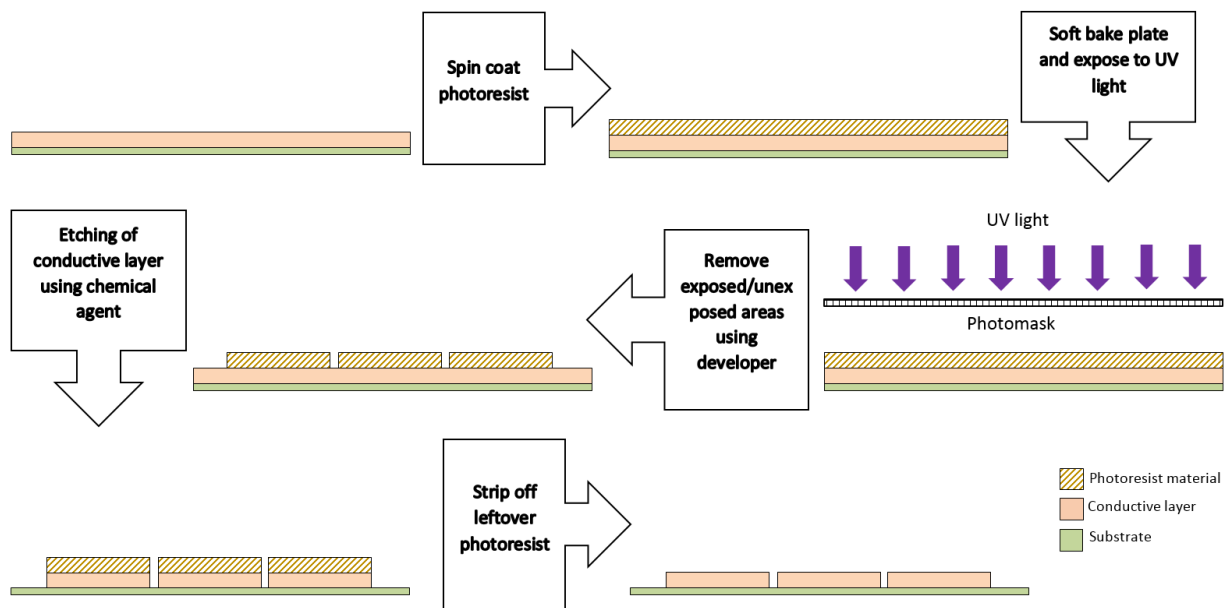


Figure 1.16: Steps involved in photolithography process. Photolithography is a technique employed to pattern material using exposure of UV light and photoresist material.

The second stage of the fabrication process involves the patterning of the deposited conductive material into individual electrodes. Photolithography is the most widely used method to pattern the thin metal film [68, 102, 105, 115, 137]. **Figure 1.16** depicts the photolithography process. Firstly, a photoresist material is deposited on top of the conductive layer. There are two types of photoresist material, a negative type which crosslinks or polymerises upon exposure to UV light and a positive type which becomes soluble to developer solution once exposed to UV light. A photomask with the desired electrode pattern is aligned above the photoresist layer prior to the UV light exposure. The exposed or non-exposed area of the photoresist layer (depending on the type of the photoresist material) is then removed using developer solution. The next step is the etching of the conductive layer areas that are unprotected by the photoresist material using chemical agent and it can either be a wet (liquid solution) or dry (plasma) process. Finally, the leftover photoresist material is stripped off chemically leaving the patterned conductive layer on the plate [68, 115, 137].

Photolithography is a well-established process capable of producing very high resolution pattern; state-of-the-art equipment resolution can be as small as 50 nm [138]. This technology however is expensive and is not easily accessible and available in every laboratory [9, 20].

Apart from the traditional electrode patterning method described above, there are also studies [139-141] that utilise printed circuit boards (PCB) technology for the manufacture of the EWOD plates, exploiting the electrodes and electrical connections available within their standard production process. The advantage of using PCB technique is the low cost and batch production of the fabrication process. The PCB technique has also made the realisation of EWOD devices with large electrode array sizes possible as the connections between the contact pads and the electrodes are multi-layered [9]. The voltage requirement for droplet actuation is however very high ~500 V due to the roughness and topography (e.g. trenches) of the PCB surface [140]. The third step of the EWOD plate fabrication process is the dielectric layer deposition. The deposition method depends on the type of material and, as listed in **Table 1.1** some of the dielectric materials are deposited using methods such as PVD and chemical vapour deposition (CVD). SiO₂ is fabricated using plasma-enhanced chemical vapour deposition (PECVD), silicon nitride (Si₃N₄) uses either PECVD or low-pressure chemical vapour deposition (LPCVD) [68, 93, 104] while BST uses metal-organic chemical vapour deposition (MOCVD) [102], all are variants of the CVD methods.

All of the aforementioned CVD methods operate at a very high temperature of more than 200°C, for example, MOCVD at 700°C, which limits the range of options for the substrate material [122, 137]. Parylene-C uses PVD method while tantalum pentoxide (Ta₂O₅) is fabricated by sputter coating a layer of tantalum and then

anodised with a gel form of citric acid solution to produce tantalum pentoxide [99, 115, 137]. Both of these material deposition methods offer an alternative to the high temperature CVD techniques by operating at room temperature [122].

Another disadvantage of the methods that have been discussed so far is their high fabrication cost due to requirement of well-equipped setup and facilities. In addition, these conventional integrated circuit (IC) fabrication processes are time consuming [22, 61, 118, 119]. Several studies [15, 107, 112, 113] attempted to overcome the high fabrication cost by employing materials such as SU-8 photoresist and polydimethylsiloxane (PDMS) due to their simpler fabrication method involving spin coating. For the SU-8 material, there is an issue of pin holes formation inside the layer deposited using the spin coating method [142]. This fabrication defect can cause device failure by the electrochemical etching of the metal electrode due to direct contact with liquid droplet which infiltrates through the pin holes [142].

The final layer of the EWOD plates is the hydrophobic actuating surface which is applied to both the base and cover plates. Most reported EWOD devices employ either *Teflon™ AF* (The Chemours Company, Delaware, US), or *Cytop®* (Asahi Glass Co. Ltd., Japan), for which the most common fabrication method is spin coating [15, 23, 60-63, 104, 122]. If a superhydrophobic surface is employed instead, the fabrication method increases in complexity as microfabrication technologies such as wet etching, laser interference lithography, LPCVD, plasma deposition and thermal evaporation are needed [129-132]. The base and cover plates are finally assembled together using a conventionally machined spacer of precise thickness as the separator.

1.6.2 Printed electronics in EWOD device fabrication

As discussed in the previous section, the high fabrication cost of EWOD devices is one of the main obstacles in DMF technology. Several studies [61, 117-119, 143] have ventured into other techniques such as printed electronics as an alternative to the conventional electrode patterning methods using PVD, photolithography and etching. Printed electronics is the adaptation of conventional printing technology, for example, inkjet printing, to manufacture electronics devices [144]. It is an emerging research area, but it is not widely used yet for EWOD device fabrication. In the electronics manufacturing, both screen printing and inkjet printing techniques are employed in the production of solar cells. Another example is the used of gravure printing and screen printing to manufacture ceramic passive components such as capacitors and resistors [145].

Printed electronics methods that have been employed for EWOD electrode patterning are: inkjet printing [11, 61, 117, 143], laser printing [20], screen printing [118], micro-contact printing [146], and spray painting [119]. These methods are cheaper, faster and simpler than the traditional cleanroom processes [117]. Printed electronics fabrication methods are also easily adaptable for a wide variety of substrates and ink to be used. For example, inkjet printing has been used in tissue engineering to pattern biomolecules and cells on to substrates such as agar and collagen [147, 148].

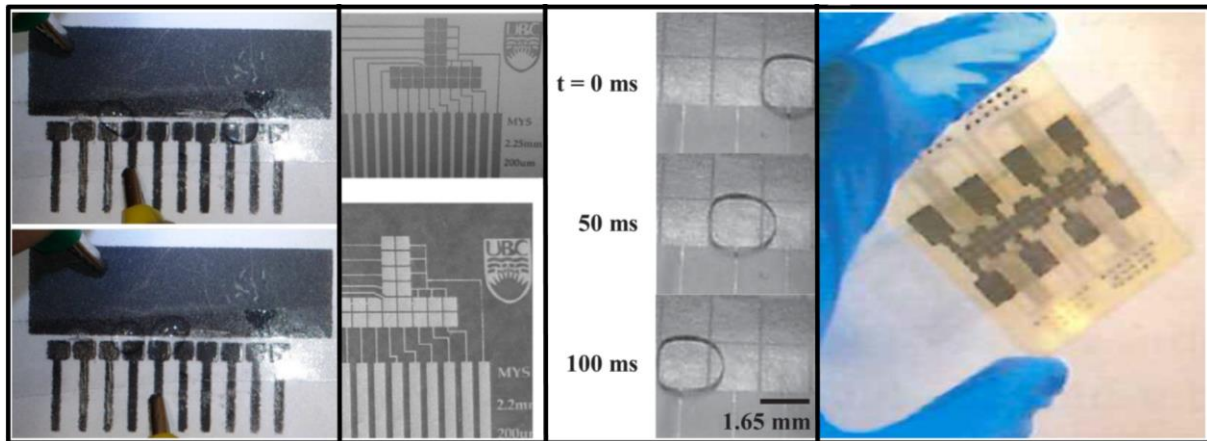


Figure 1.17: EWOD device fabricated using printed electronics fabrication method. From left to right: 1) graphite-on-paper EWOD plate using spray painting [119], 2) silver-on-paper EWOD plates using screen printing method [118], 3) silver-on-paper EWOD plate using inkjet printing [61], 4) silver-on-PET EWOD plate using inkjet printing [117].

Figure 1.17 shows examples of EWOD devices fabricated using printed electronics techniques. Abadian et al. [119] propose the use of graphite spray painting and laser-cut templates as an electrode patterning method. The electrodes were spray-painted on a standard A4 size paper for the fabrication of a single-plate configuration EWOD device shown in the first image of **Figure 1.17**. Serendipitously, it was found that graphite leakage into the inter-electrode gaps, which was initially considered undesirable, can perform as interdigitated electrodes similar to designs in [4-5,11] thus improving the droplet motion [37].

Screen printing as a method to print electrodes in EWOD devices was introduced by Yafia et al. [118]. In screen printing, patterning is performed by squeezing ink or paste through a screen mesh, designed with the desired pattern, using a squeegee [145]. Silver, carbon, and Bare conductive (commercial ink made of carbon) inks were used as the electrodes while paper, glass and wax paper were all employed as substrates. The silver-on-paper device is shown in the second image of **Figure 1.17**. The time spent to fabricate the patterns on the stainless steel screen

mesh was approximately 20 minutes and once this patterned screen was prepared, only few seconds were needed to apply ink into the substrate by passing squeegee across the patterned screen mesh [118].

Using the screen printing technique, Yafia et al. [118] found that resolution down to 50 μm for both electrode spacing and line width, and around 10 μm for thickness can be produced. They however recommended the electrode spacing of 200 μm as it has shown more reliability. Results from the same study [118] have shown that the wax paper device produced a wider spacing than the screen pattern due to the hydrophobic nature of the paper while ink spreads easily on the normal paper due to capillarity causing the spacing to shrink. The silver ink has a better conductivity than the carbon ink on all types of substrate and the highest conductivity was produced by the silver-on-glass [118].

Two groups [61, 117, 143] have utilised inkjet printing method to pattern EWOD control electrodes on specialist paper (third image in **Figure 1.17**) and polyethylene terephthalate (PET) (fourth image in **Figure 1.17**) substrates. Fobel et al. [61] utilised a laboratory inkjet printer, Fujifilm Dimatix DMP-2800 (Fujifilm Dimatix, Inc., Santa Clara, US) to pattern silver nanoparticle ink as EWOD device control electrodes on paper substrates. The reported cost for one device was less than US \$0.65 and took approximately one minute to print. The inkjet printer was able to produce features as small as 30 μm width and with spacings of 30 μm [61].

Another inkjet-printed device [117] was fabricated using an inexpensive desktop inkjet printer commonly found in homes and offices for low volume printing tasks. The reported inkjet printer, Epson C88+ (Seiko Epson Corporation, Tokyo, Japan) was capable of producing average electrode spacings of 55 μm and 148 μm

average line width using silver ink on transparent PET substrate coated with porous coating. The average thickness of the electrode is 1 μm . Previously, this type of inkjet printer has been used to deposit conductive layers in organic electronics for electronic components such as organic light emitting diode (OLED) or thin film transistor (TFT) [149, 150].

Abdelgawad & Wheeler [20] developed an EWOD electrode patterning method using desktop laser printer. In this study, instead of using the printer to deposit the electrode material, it was used to pattern a photomask directly onto a copper-clad (acts subsequently as the electrode material) PCB laminate. The substrate then underwent an etching process to remove the exposed part of the copper material and the printed photomask was removed using acetone-dampened tissue. This method can potentially be useful if access to photolithography equipment is unavailable [20].

The same research group [146] developed another method of electrode patterning using micro-contact printing technique. A poly(dimethylsiloxane) or PDMS stamp, fabricated using photolithography, is used to deposit either masking material on a gold-on-glass substrate for later etching, or to print colloid patterns on glass substrate to seed electroless deposition of copper. In addition to being cheaper, the micro-contact printing method is approximately 2.5 times faster (to fabricate a batch of 10 devices) than photolithography. However, while no clean-room facilities are needed for the patterning of the electrodes, they are still necessary to create the initial PDMS stamp [146].

Among the printed electronics fabrication methods that have been discussed, ink jet printing is the most attractive due to its reliability, high throughput, and minimal waste, which is particularly important if an expensive ink is used [61, 117]. The EWOD

devices produced using the other printed electronics methods have been shown to demonstrate a limited performance when compared with the inkjet-printed ones [117]. The inkjet printing method is also scalable for mass production and the existing printing equipment can be adapted easily for EWOD device fabrication without the need for major modifications [117, 118]. For these reasons, inkjet printing was selected as the electrode patterning technique to be investigated in Chapter 2.

1.6.2.1 Inkjet printing technology

A print head of an inkjet printer contains multiple nozzles and transducers which can be either of two types: thermal or piezoelectric transducers. Commercial inkjet printers employ 'drop-on-demand' printing technology where an ink droplet from a reservoir is ejected through a nozzle when a signal pulse is transmitted to the transducer [151]. A thermal print head contains a resistor inside each nozzle, which heats up when current passes through it. The increase in temperature causes the ink to vaporise and increase in pressure. The current is then cut off abruptly, resulting in ejection of an ink droplet from the nozzle [151]. A piezoelectric print head contains piezoelectric material inside each nozzle which deflects under application of voltage. The deformation and relaxation cycle of the piezoelectric element pressurises and depressurises the fluid forcing the ink droplet out from the nozzle [152, 153].

One of the most vital components of the inkjet printing technology is the ink and its physical properties. In order for the ink to be ejected efficiently from the inkjet printer nozzles, its surface tension and viscosity have to be within a certain range, 28 mN/m – 36 mN/m and below 20 mPa s respectively [154, 155]. The dimensionless number which represents the ratio between the viscous force to the surface tension and inertial forces is called Ohnesorge number (Oh), **equation (1.26)** [155]:

$$(1.26) Oh = Z^{-1} = \frac{\eta}{\sqrt{\rho D \sigma}} \quad (7)$$

where η is the ink viscosity, ρ is the ink density, D is the characteristic length parameter, usually the nozzle diameter, and γ is the ink's surface tension. To ensure the formation of typical Newtonian fluid ink droplet from the nozzle, the value of Z (inverse of Oh), needs to range between 1 and 10 [154, 155]. For $Z < 1$ where the ink has relatively high viscosity, viscous dissipation dominates and will prevent the ejection of an ink droplet. For $Z > 10$ where the ink has low viscosity, it will cause formation of long tail behind the ink drop or, in some cases, formation of satellite drops. A satellite drop is an additional unwanted droplet formed during the intended ejection of a single droplet. **Figure 1.18** shows the formation of both single and satellite droplets due to varying values of Z [154, 155].

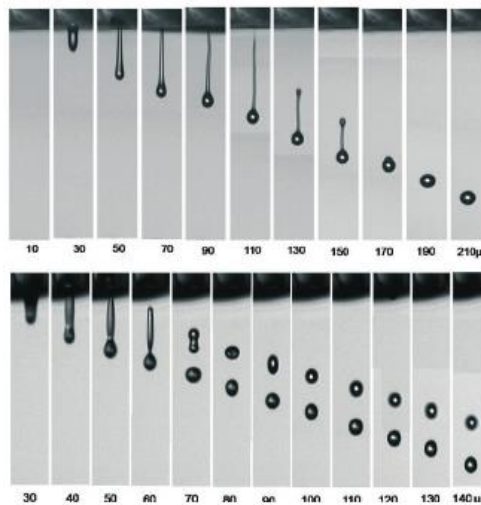


Figure 1.18: Formation of ink droplet in inkjet printing. Top) single droplet ejection where Z is between 1 and 10, bottom) satellite drop formation when Z is larger than 10 [156].

Inkjet printers produce better resolution and sharper edges when smaller print head volumes are used. Their resolution also depends on the type of substrate and ink used. Substrates with low surface energy and inks with high surface tension

produce smaller ink droplets and hence higher resolution. In the case of electrode patterning, it is important however that these ink droplets are not too small so that they fail to overlap and connect with each other to produce a contiguous, electrically conductive feature [149].

Inkjet printing method allows for the implementation of paper and polymer substrates as it does not operate at high temperature, unlike some of the clean room processes discussed in previous section. Transparent polymer sheets are very attractive due to the low cost of material, their structural flexibility, their disposability, their transparency, and their mass producibility [61]. Previously, Abdelgawad et al. [107] have utilised polyimide sheet as an DMF device substrate capable of actuating droplet on all types of surface geometry due to the substrate flexibility.

The main challenge of using polymer substrates is the low wetting of the ink droplets due to the polymer's low surface energy [157]. Low wetting and spreading of the ink droplet causes disconnections in the electrode patterns due to the discontinuity between the ink droplets. Usually polymer substrates are treated with gas plasma, UV or ozone irradiation before printing to modify their surface chemistry and, change contact angles and hence increase the ink's spreading and wetting [157]. In the Chapter 2, transparent polymer sheet is selected as the substrate component to be investigated in combination with the inkjet printing method.

1.6.2.2 Conductive polymer PEDOT:PSS ink

Inkjet printing technology allows for variety of conductive materials to be implemented as EWOD electrodes due to the adaptability of the method to wide range of ink materials. Apart from the more common silver ink, the conductive polymer poly(3,4-ethylenedioxythiophene) doped with polystyrene sulfonic (PEDOT:PSS) has the

potential to be widely used as EWOD electrode due to the following benefits. Conductive polymer is lower in cost when compared to metal such as silver and chromium [158]. PEDOT:PSS has the advantage of being transparent which allows for easy integration with optical sensing functions. The material is also flexible compared to the more brittle conventional metal [157, 159].

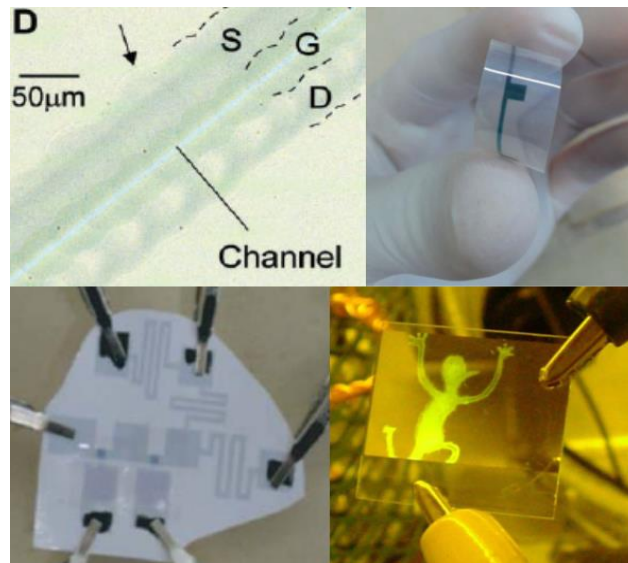


Figure 1.19: Inkjet printing of PEDOT:PSS as organic electronic component. Clockwise from top left: 1) micrograph of TFT (S, source; D, drain; and G, gate) [160], 2) PEDOT:PSS/polyaniline electrode for pH sensor [159], 3) OLED on glass substrate [150], 4) logical NOR-gate printed on glossy photo paper [161].

Other than inkjet printing [149, 150, 157, 159-162], fabrication methods such as spin coating [163, 164], negative mould transfer printing [165], spray coating [158], and screen printing [166] have been previously employed to deposit thin layer of PEDOT:PSS film. This conductive polymer received increased attention in printed electronics when Sirringhaus et al. [160] inkjet-printed this material on glass substrate to fabricate a polymer transistor circuit. Since then, PEDOT:PSS has been inkjet-printed to fabricate devices such as: 1) TFT on glass substrate using a custom-made piezoelectric inkjet printer [160], 2) pH sensors on polyethylene naphthalene (PEN)

using laboratory-grade piezoelectric inkjet printer [159], 3) OLED on glass substrate using thermal desktop inkjet printer [150], 4) a logic circuit on glossy photo paper using thermal desktop inkjet printer [161], 5) photovoltaic cells on an ITO-coated glass substrate using a laboratory-grade piezoelectric inkjet printer [167]. **Figure 1.19** shows few of the devices listed here.

PEDOT:PSS have been deposited on various substrates such as glass [149, 150, 157, 160, 162, 165], polyether sulfone [165], PET [157], polyethylene naphthalene (PEN) [157, 159], ITO-coated PET foil [157] using ink jet printing [149, 150, 157, 159, 160, 162] or negative polydimethylsiloxane (PDMS) mould transfer printing [165] techniques. After treatment with UV/ozone radiation, the glass substrate produced the thinnest and smoothest PEDOT:PSS electrode while on PEN the ink spread too much causing an unintentionally interconnected pattern. Both PET and ITO-coated PET foil substrates display uneven spreading of ink [157]. Substrate temperature can also affect the quality of the printed electrode. A higher temperature of 60°C compared to 25°C produced low homogeneity electrodes due to bubble forming which burst later on. Ink droplets also tend to dry too quickly on high temperature substrates preventing mutual flow connection between droplets [157, 165].

One study has reported resolution down to 40 µm pattern width and 50 µm gap spacing [157] for PEDOT:PSS ink printed using laboratory inkjet printer. Previously, high resolution of 5 µm was achieved by creating a polyimide hydrophobic pattern (using photolithography and oxygen plasma etching) to prevent the PEDOT:PSS ink from spreading [160]. In some of these studies, electrical conductivity of the PEDOT:PSS was improved by adding glycerol and surfactant to the ink [149, 150,

165]. When a piezoelectric inkjet print head is used, firing voltage is one of the important parameters that affects the quality of the PEDOT:PSS printing. Higher firing voltage produces stronger pressure pulses, resulting in higher ink deposition and thus greater electrode thickness. Low firing voltage causes lower spreading of the polymer ink [157]. Better resolution can also be achieved if the electrode or pattern longitudinal orientation is in parallel with the printing direction (print head movement) compared to the perpendicular direction [157]. For the investigation on the inkjet printing technology as electrode patterning method in the Chapter 2, PEDOT:PSS ink was chosen as the electrode material to be deposited on the polymer substrate.

1.7 Summary

Based on the literature review that has been conducted in this chapter, some of the key points are:

- Among the mechanisms that have been employed to actuate droplets in a DMF device, EWOD has the best performance in terms of the ability to perform droplet transportation, mixing, merging, dispensing, and splitting efficiently. Its operation also does not generate heat or necessarily require liquid suspending medium which could affect the droplet condition.
- There are a wide range of biochemical assays that can be applied in DMF devices such as immunoassay, DNA-based assay, and cell-based assay. For the preliminary testing of the EWOD device developed in this project, a well-established ELISA immunoassay has been selected.
- Another challenge in DMF technology is the biofouling problem where the hydrophobic actuating surface of the device is contaminated when in contact with biomolecules such as protein. A superhydrophobic surface has the

potential to be an effective method to suppress this problem but the existing fabrication processes are costly.

- The fabrication methods for EWOD electrode and dielectric components such as the PECVD and photolithography techniques require expensive and well-equipped facilities which increase the cost of the EWOD device.
- Off-the-shelf products can be the low-cost alternatives to the conventional dielectric and hydrophobic materials.
- Inkjet printing technology is a good alternative to the conventional method of electrode patterning. This technique is simpler, cheaper and faster compared to the former. A few research groups have developed EWOD devices utilising inkjet printing method.
- Conductive polymer PEDOT:PSS is a possible candidate as a substitute to the traditional metal electrode in EWOD devices. This material has been inkjet-printed to produce devices such OLED and solar cells.

The next two chapters attempt to address the challenges discussed in the key points here. The Chapter 2 focuses on the investigation of inkjet printing using PEDOT:PSS ink as an alternative electrode patterning method while the Chapter 3 examines the suitability of commercial products intended for other markets as dielectric and hydrophobic components of EWOD devices.

2 Inkjet printing as EWOD electrodes patterning method

2.1 Introduction

One of DMF research's many challenges is to find a simple, inexpensive, and reliable electrode patterning technique as an alternative to the microfabrication techniques [61] which are whilst robust and reliable due to years of development for semiconductor and integrated circuit manufacturing [168], involve time consuming processes and require expensive clean room equipment [22]. A few groups have ventured into printed electronics technology such as inkjet printing, screen printing, and spray painting to pattern EWOD electrodes [61, 117, 119, 143]. Apart from being lower in cost than the standard microfabrication processes, printed electronics also provides simplification of the process by combining the two procedures, i.e. material deposition and photolithography into just one. Using this technology, the electrode material is deposited onto the substrate directly into the desired pattern.

This chapter aims to overcome the problem of high fabrication cost by proposing inkjet printing technique in combination with new ink and substrate materials. The following sections describe the investigations on the feasibility of using two types of inkjet printer for EWOD electrodes patterning: a low-cost desktop inkjet printer and a specialised laboratory inkjet printer. The general principle behind inkjet printing technology such as the ink requirement for inkjet printing and the ink droplet ejection mechanism has been discussed in **Section 1.6.2.1**. Two types of ink were employed in the investigations. In addition to the more common silver ink, the investigations in this chapter also included conductive polymer poly(3,4-ethylenedioxythiophene) doped with polystyrene sulfonic, known as PEDOT:PSS as the EWOD electrode material. Such polymer material has the dual advantage over metal such as silver and chrome to being flexible [157, 159] as well as lower in cost [158]. Another vastly

beneficial feature of using PEDOT:PSS electrode is its transparency which allows for integration of optical detection and monitoring system into the EWOD device [169]. For the substrates, several types of polymer film and paper were used instead of the traditional glass slides. These substrates are flexible and also inexpensive [170], making them very suitable if low-cost and disposable EWOD devices were to be realised.

2.2 Electrode patterning using desktop inkjet printer Hewlett Packard Deskjet 1000 J110

The first investigation in this chapter utilised a low-cost desktop inkjet printer, the Hewlett Packard (HP) Deskjet 1000 J110, suitable for low-volume printing as a tool for a preliminary investigation of inkjet printing technology as an EWOD electrode patterning method. This desktop printer is a drop-on-demand thermal inkjet printer with maximum resolution of 1200 × 1200 dots per inch (dpi). The print head can move only in one direction (in the lateral direction) and during the printing process the substrate is moved forward by printer rollers to provide the second axis of patterning.

There are two types of cartridge for the printer, a black ink cartridge and a tri-colour ink cartridge. The black cartridge contains only one reservoir while the colour ink cartridge has three reservoirs for cyan, yellow, and magenta inks. The ink, in each reservoir, is contained in sponges, which allows controlled flow of the ink into the nozzle. Without the sponges, the ink would flood the print head nozzles. For a large size cartridge, the reservoirs can hold up to 8.5 ml and 7.5 ml maximum ink volume for the black and tri-colour ink reservoirs respectively. The cartridges can be cleaned and refilled with other types of ink once empty.

2.2.1 Experimental

In order to investigate the feasibility of using the desktop inkjet printer as an EWOD electrodes patterning method, the capability of the printer to produce micro-feature size patterns was assessed. The conductivity of narrow tracks of varying width and the electrical separation of electrodes of different spacing patterned using the printer were evaluated. Several combinations of ink formulation and substrate treatment were tested to determine which one was the most reliable in producing fully interconnected tracks without any shorted electrodes. The chosen ink and substrate treatment combinations were then employed to fabricate EWOD plates for water droplet actuation evaluation.

2.2.1.1 *The HP Deskjet 1000 J110 printer setting*

Since the pattern of the electrodes used in this study has features as small as ten microns, the printer setting was set to its maximum printing resolution (steps described in **Appendix A**). The electrode patterns for the investigation were drawn using Adobe Illustrator® (Adobe Inc., San Jose, US) software. All the patterns were applied with rich black fill colour to increase the ink density and to ensure the contiguity between the ink droplets.

2.2.1.2 *The HP Deskjet 1000 J110 cartridge preparation and maintenance*

The ink cartridges used for the investigation were empty, used ink cartridges. Only the black cartridge was used for electrode printing while the colour cartridge was not mounted to the cartridge carrier during the printing process. Prior to filling the reservoir with the ink formulation, the cartridge was first thoroughly cleaned using DI water and isopropyl alcohol (IPA). It was dried using compressed air afterwards. After the nozzles were completely dried, the ink was filled into the reservoir. Because filling the sponge requires a large quantity of ink (1 ml) the ink was directly pipetted into the cartridge

without any sponge to allow small quantity to be used at each refill. By using only a small amount of 85 μl , the problem of flooded nozzles due to the absence of a sponge can be avoided while avoiding ink waste at the same time. This volume can print about 8 plates with the design shown in **Figure 2.1**. After each printing session, the cartridges were cleaned using DI water and IPA. For storage, the nozzles were immersed in a DI water bath to keep them from drying and clogging in case there was any ink residue left after cleaning.

2.2.1.3 Conductive inks

Two types of ink were separately evaluated to fabricate the electrode patterns; PEDOT:PSS (739316, Sigma Aldrich, St. Louis, US) and reactive silver (745707, Sigma Aldrich, St. Louis, US) inks. From the manufacturer's specifications, the surface tension, γ of the PEDOT:PSS and silver ink are 31 - 34 mNm^{-1} and 20 - 50 mNm^{-1} respectively, while the viscosities, η are 7 -12 mPa s and 10 -12 mPa s respectively. Both types of ink were agitated in an ultrasonic water bath for 15 minutes prior to usage to re-disperse the ink particles. For the PEDOT:PSS ink, the following formulation was used: 86 % PEDOT:PSS, 9.5 % DI water, 4.5 % glycerol (Boots, Nottingham, UK) and ~0.045% Tween 20 surfactant (Sigma Aldrich, St. Louis, US) [150]. Henceforth, this formulation will be referred to as PP/T20 ink. Glycerol was added to increase the electrical conductivity of the ink while the surfactant was added to increase the droplet wetting on the substrate [150, 165]. Apart from this formulation, the PEDOT:PSS (PP) ink was also used as-is but the PP/T20 ink was preferred due to less occurrences of nozzles clogging, thus longer cartridge lifetime. To avoid nozzles clogging, both the PP/T20 and PP inks were filtered with a 0.45 μm syringe filter before filling the cartridge. After printing of the pattern on the polymer substrate, the PEDOT:PSS electrodes were dried for 5 minutes at a temperature of 110 $^{\circ}\text{C}$ on a hot plate [169].

For the reactive silver ink, two types were prepared: one was mixed with IPA ($\gamma = 23 \text{ mNm}^{-1}$ [171]), which will be referred to as Ag/IPA ink while the other one was used as-is referred to simply as Ag. The volume ratio of 5:8 for IPA to the silver ink was used after evaluation of few different ratios to determine the one that produced the best quality of ink wetting (results available in **Appendix B**). To remove the residual acetate groups (ink stabilising agent) that inhibit the ink conductivity, the silver electrodes were annealed at a temperature of 120 °C for 5 minutes on hot plate after printing as suggested by the manufacturer [172]. However, it has been found from preliminary investigation on the transparency polymer substrates (results available in **Appendix C**) that the silver ink required at least two layers of printing on the polymer substrate used in this investigation to produce measurable film conductivity. After the first printing pass, the ink was annealed using lower temperature of 90 °C for about 2 minutes. This was to ensure the ink dried and did not smear when going through the printer rollers during printing of the second layer. A lower temperature was used to reduce the bending of the polymer substrate due to high heat. The bending of the polymer substrate increased the error in the alignment of the pattern after each printing passes.

For the PP/T20 ink, conductive film was produced after just one layer of printing, while the PP ink required more than one layer of printing to attain a measurable conductivity. In comparison both the Ag and Ag/IPA inks, required at least two printing passes to make all the silver ink droplets fully connected. Fewer requirement of printing passes for the PP/T20 ink than the PP and both of the silver inks indicates better wetting property resulting in a fully-interconnected film on the transparency substrate [149, 150].

In order for the films to be conductive, the deposited ink droplets need to be connected or overlapped with each other. The droplet spreading and the shape of the ink droplets upon impact with the substrate are highly dependent on the ink surface tension, substrate surface energy, and surface roughness [149, 173]. Ink with higher surface tension produces smaller ink droplets causing discontinuity between the deposited ink droplets on the substrate [149]. To increase the spreading of ink droplet on the substrate used in this investigation, two other side studies have been conducted. One study attempted to lower the silver ink (aqueous solution) surface tension by adding IPA (mentioned previously, results in **Appendix B**). Alcohol such as IPA reduces the surface tension of an aqueous solution by introducing surface excess through the formation of a monolayer of the IPA molecules at the liquid-gas interface. The IPA molecules then begin to aggregate due to the attraction forces between the molecules which consequently disrupt the intermolecular interactions of the bulk water molecules [174, 175]. Studies have shown that there is a decrease in water surface tension with the addition of alcohols [175]. Another study lower the surface energy of the substrate by introducing plasma treatment (discussed briefly in the next section, results in **Appendix D**).

2.2.1.4 Types of substrate and plasma treatment of substrate

Initially, eight types of transparent sheet used for overhead projector polymer sheets with different surface roughness made of cellulose acetate were evaluated (**Appendix C**). Only one was selected for further investigation and device fabrication based on the conductivity performance of the deposited films on that substrate. An initial trial with a standard A4 paper substrate showed no measurable conductivity for either silver inks after six printing passes while a conductive layer was produced after two layers of printing for the PP/T20 ink.

In order to further improve the wetting of the inks, the substrates were cleaned using radio frequency (RF) plasma asher (Emitech K1050X, Quorum Technologies). Specific process gases can be used for the treatment but in this investigation, ambient air from the class 1000 cleanroom was used to feed the plasma equipment. The plasma asher modifies the surface chemistry of the substrate by generating RF-induced discharges such as ions, electrons, and radicals. These excited species then interact with the substrate surface either by breaking any organic bonds of contaminants on the surface, binding to the substrate surface or combining with contaminants to form new molecules such as water [176].

While the preliminary investigation on the substrates has shown that the best performing cellulose acetate substrate was capable of producing conductive film (6 mm square in size) for PP/T20 and silver inks, this result was harder to reproduce when narrow tracks (less than 250 μm wide) were printed on the substrate. To overcome this, plasma treatment was introduced to increase the surface energy of the cellulose acetate substrate. The wetting of droplet on substrate is highly influenced by the substrate surface energy; the higher the surface energy, the lower the CA and the wetting of the ink droplet [149, 173]. To determine the power intensity of the plasma treatment and its duration for each type of ink, a short investigation was conducted and the results are available in **Appendix D**. The settings applied were 10 W for 10 s and 50 W for 120 s for the PP/T20 and PP inks respectively. Meanwhile, the Ag ink required 30 W of power for the duration of 1 minute.

2.2.1.5 Conductivity measurements of the printed pattern

The conductivity measurements of the electrode patterns and tracks deposited using the inkjet printer were conducted using a handheld digital multimeter (72-7745, Tenma).

2.2.1.6 Fabrication of EWOD plates and droplet actuation in the parallel-plate EWOD devices

Three types of parallel-plate EWOD devices, PP/T20, Ag, and Ag/IPA-on-cellulose acetate, were fabricated using the HP inkjet printer to create the conductive pattern of the control electrodes. The design of the control electrode printed on the base plate is shown in **Figure 2.1**. It comprises three rows of 16 square electrodes, 1.7 mm in nominal size with the corresponding contact pads for connection with the electronics located at the top of the design. Nominal size is defined as the size of the electrode or pattern in the software drawing, not the measured size of the inkjet-printed electrode. The nominal gap size for the electrode is 360 μm for the PP/T20 device and 320 μm for both Ag and Ag/IPA devices.

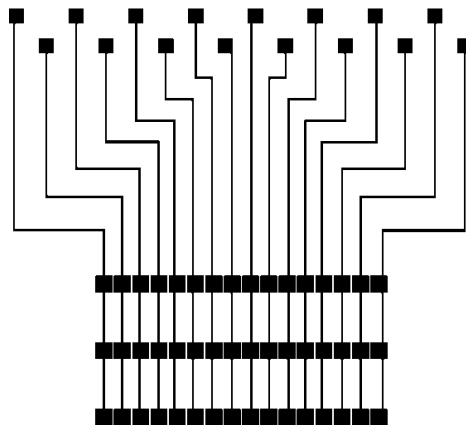


Figure 2.1: The pattern of the control electrode for the base plate of the parallel-plate EWOD devices.

To form the base plate of the device, this design was printed on the cellulose acetate substrate. The printing process and the heat treatment of the inks, PP/T20, Ag, and Ag/IPA for the three types of devices followed the same procedures described previously. A layer of Parylene-C (Specialty Coating Systems, Indianapolis, US) dielectric material (thickness $\sim 3.2 \mu\text{m}$) was deposited on top of the electrodes using Parylene deposition system (SCS Labcoater® 2, Specialty Coating Systems,

Indianapolis, US). Detailed procedures on the Parylene-C deposition method are described in the next section. Adhesive tape was used to cover the contact pad region of the base plate before the deposition of the dielectric material. A final layer of *Cytop*® (Asahi Glass Co., Ltd.) hydrophobic surface was spin coated (LabSpin6, SUSS MicroTec, Garching, Germany) onto the plate at 1500 rpm for 30 s and cured at temperature of 110 °C for one hour.

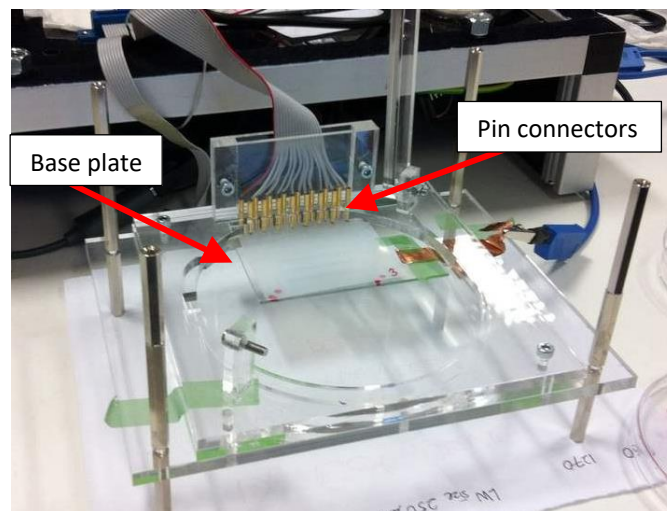


Figure 2.2: The PMMA frame used to hold the EWOD device in place. Only the base plate is mounted in this figure and it is connected to the control electronics (not shown here) by 16 spring-loaded pin connectors.

The printed base plate was assembled with a grounded cover plate made of a *Cytop*®-coated silicon wafer (p-type, <100>, 1-10 Ω cm) to form a parallel-plate device. The gap between the base and cover plates was 380 μ m using plastic substrate as the spacer. The following will describe the supporting frame, electronics, and software used in this investigation, which were not constructed or developed by the author. A custom made poly(methyl methacrylate) (PMMA) frame was employed to secure the EWOD plates in place. **Figure 2.2** shows the set-up of the PMMA frame with the base plate mounted on it. Spring-loaded pins were used to connect the base plate with a USB powered compact electronics. The electronics was able to control

independently all 16 electrodes using a 1 kHz sine wave signal with voltage that can be adjusted up to 225 V_{RMS} . The operation of the EWOD device is controlled using a bespoke software interface [177] via a computer. 5 μ l of deionised (DI) water was used to evaluate the linear transportation of droplet in the parallel-plate EWOD devices.

2.2.1.7 Parylene-C deposition method

Parylene is a linear chain polymer composed of benzene rings with two methylene groups instead of hydrogen atoms at the opposite end of the rings (chemical structure shown in the **Figure 2.3**). This polymer has several variants, for this study, Type C or Parylene-C was used in which one of the hydrogen atoms on the ring is substituted with a chlorine atom. Parylene-C has the lower permeability to gas and moisture, while having the higher dielectric constant among the other Parylene variants [178, 179].

The deposition process using the Parylene deposition system (SCS *Labcoater*® 2), depicted in the **Figure 2.3** starts with the vaporising of the dimer precursor under vacuum at a temperature of circa 175 °C for Parylene-C. The dimer vapour is then further heated in the furnace at a much higher temperature, 690 °C to pyrolyse the dimer into its monomeric form. The monomer is finally deposited and polymerised as a thin transparent film at ambient temperature, which is an advantage of this method as it allows for a wide selection of substrates to be applied [179]. Approximately 4 g of the Parylene-C dimer material in powder form was loaded into the vaporiser to produce a dielectric layer thickness of ~3.2 μ m on both the silicon wafer and ITO coated glass slide substrates.

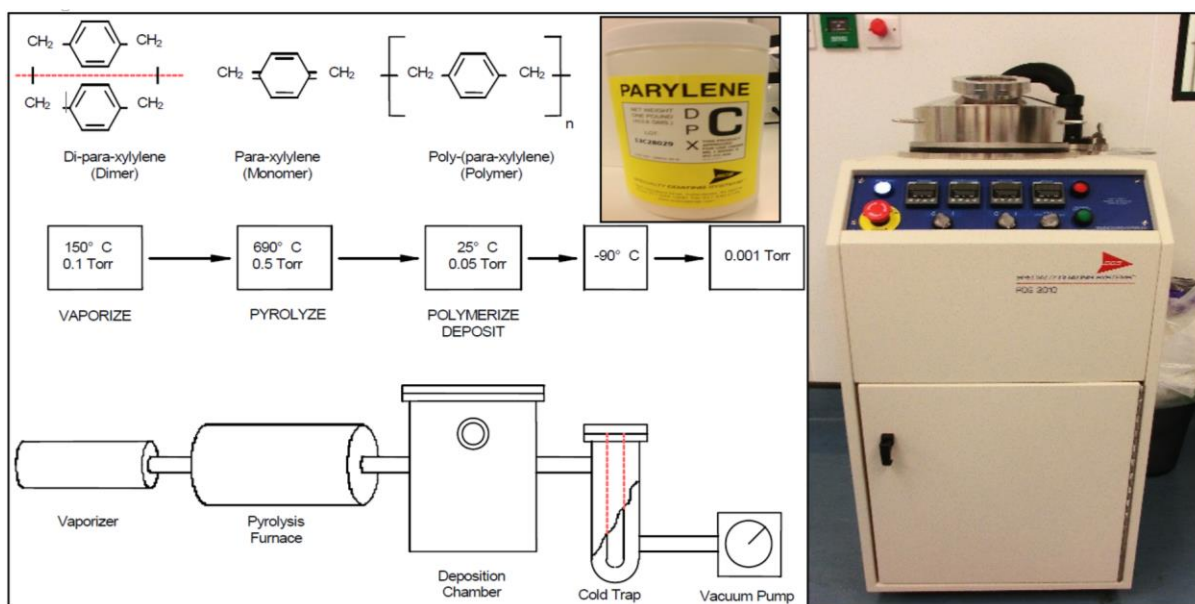


Figure 2.3: Parylene deposition system. (Top left) The chemical structure of Parylene dimer, monomer, and polymer. (Middle and bottom left) The Parylene deposition process. It begins in the vaporiser where the solid dimer is turned into gas under vacuum and temperature of 175 °C for Parylene-C, then the gas is split into monomer inside the pyrolysis furnace at temperature of 690 °C and finally deposited as a thin film inside the deposition chamber at ambient temperature [179]. (Right) The SCS Labcoater® 2 Parylene Deposition System equipment.

2.2.2 Continuity and reliability of the printed tracks

One of the key parameters of EWOD electrodes is conductivity; poor conductivity in narrow tracks can cause voltage loss due to high resistance or unwanted Joule heating [61]. To evaluate the capability of the inkjet printer to deposit continuous thus conductive narrow tracks, a test pattern was designed as shown in **Figure 2.4**. The vertical and horizontal tracks in this pattern are 10 mm in nominal length with varying nominal width from 10 µm up to 250 µm.

The continuity of the tracks for four different types of ink: PP, PP/T20, Ag, and Ag/IPA are summarised in **Table 2.1**. For each combination of ink and treatment, the test pattern shown in **Figure 2.4** were printed three times. The reported results in **Table 1.1** are the best performing sample out of the printed samples. The effect of

plasma treatment on the required minimum nominal track width to produce continuous and conductive tracks for each type of ink was investigated.

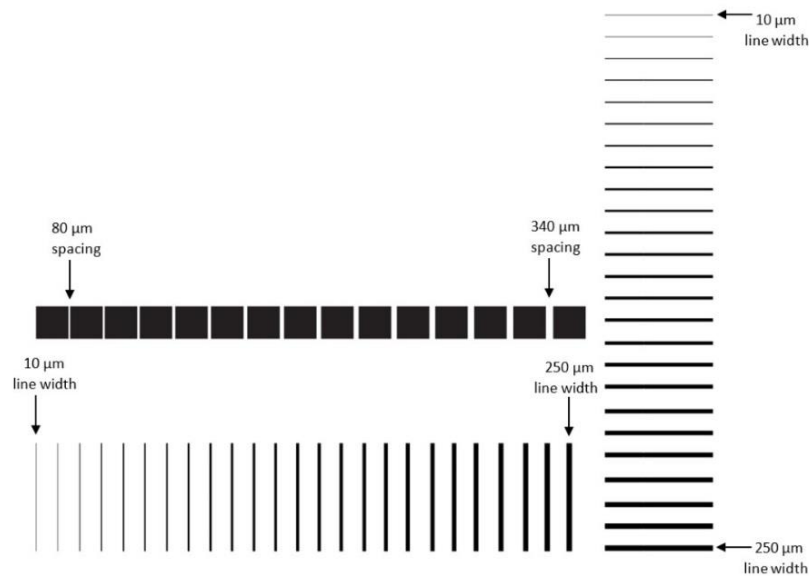


Figure 2.4: Test pattern to determine the minimum allowable track width and electrode spacing. The smallest width of the track is 10 µm and the largest width is 250 µm. For the electrode spacing, the smallest gap is 80 µm and the largest gap is 340 µm.

For Ag/IPA ink, it was found during initial evaluation that there was no improvement in the conductivity between the narrow tracks printed on untreated and plasma-treated substrates so no treatment was used in the subsequent testing. The printer is capable of printing tracks as narrow as 10 µm visually but an actual electrical conductivity can only be measured with wider tracks. Without any treatments to the substrate, the minimum nominal width for tracks to be conductive for both the PP and PP/T20 inks is 250 µm. When plasma treatment is introduced, the minimum track

width required to produce conductive tracks reduced to between 30 μm to 50 μm for both types of PEDOT:PSS inks.

Table 2.1: The minimum nominal track width required to produce measurable electrical conductivity for different type of inks and substrate treatment.

| Type of ink | Plasma treatment | Number of printing layer | Line direction | Minimum line width with electrical conductivity (μm) | |
|--|-----------------------------|--------------------------|----------------|---|-----|
| PEDOT:PSS (PP) | None | 1 | Horizontal | > 250 | |
| | | | Vertical | > 250 | |
| | 50 W 120 s | | Horizontal | 40 | |
| | | | Vertical | 40 | |
| PEDOT:PSS added with DI water, glycerol, and Tween 20 (PP/T20) | None | | Horizontal | 250 | |
| | | | Vertical | > 250 | |
| | 10 W 10 s | | Horizontal | 30 | |
| | | | Vertical | 50 | |
| Silver (Ag) | None | 2 | Horizontal | 250 | |
| | | 3 | | 20 | |
| | | 2 | Vertical | > 250 | |
| | | 3 | | 90 | |
| | | 30 W 60 s | 1 | Horizontal | 250 |
| | | | 2 | | 70 |
| | 3 | | 20 | | |
| | 1 | | Vertical | 250 | |
| | 2 | | | 120 | |
| | 3 | | | 10 | |
| | 1.6 Silver : 1 IPA (Ag/IPA) | None | 2 | Horizontal | 60 |
| | | | 3 | | 20 |
| 2 | | | Vertical | 40 | |
| 3 | | | | 40 | |

The Ag ink needed at least 250 μm track width and two printing passes to produce conductive tracks when the substrate was untreated. The minimum requirement for track width reduced when the number of printing passes is increased to three layers or when plasma treatment is included. Plasma treatment can help produce conductive tracks with only one layer of printing but this can only be achieved using a minimum of 250 μm track width. The Ag/IPA ink has demonstrated good conductivity without the need of any substrate treatments. The minimum track width to be able to print conductive tracks with this ink are between 20 μm to 60 μm after two or three printing passes.

The conductivity of inkjet-printed electrode is highly dependent on the ink's surface tension, the surface energy of the substrate, and the substrate roughness [149]. It is evident from the results that plasma treatment improves the connectivity between the deposited ink droplets for the PP, PP/T20, and Ag inks significantly. The track conductivity relies on the interconnectivity between the ink droplets; the larger the size of the ink droplets on the substrate upon impact, the higher the probability of ink droplets to be connected with each other. The wetting and the size of the ink droplets increase with the surface energy of the substrate. This investigation however, used polymer substrates which have low surface energy, which the plasma treatment helps increase; but nonetheless it complicated the process of producing conductive tracks on this substrate.

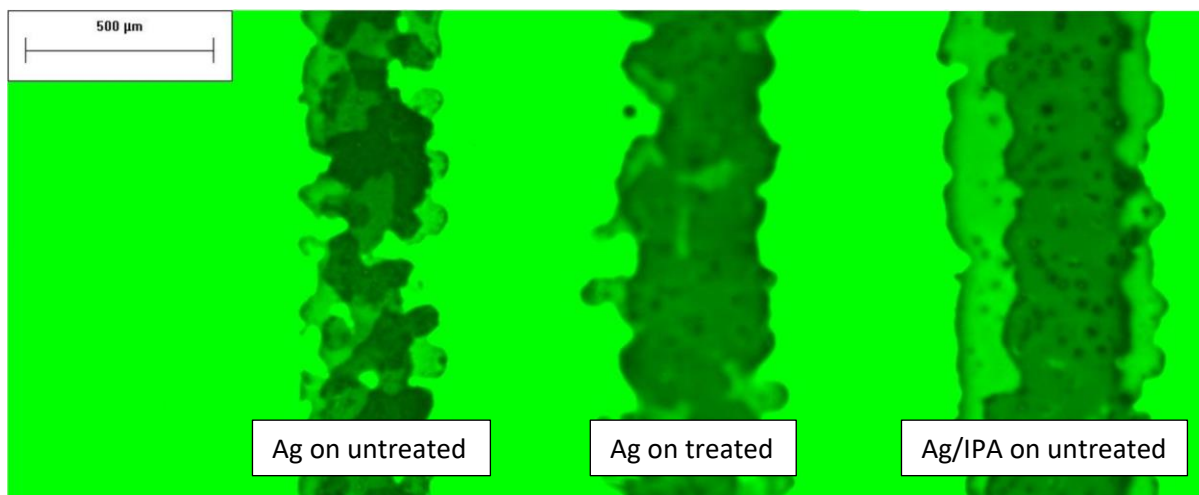


Figure 2.5: The left and middle tracks are made of Ag ink while the right track is made of Ag/IPA ink. The left and right tracks were printed on untreated substrate while the middle track was printed on substrate treated at 30 W for 60 s. All tracks were printed in two layers.

Figure 2.5 compares the difference between tracks printed on treated and untreated substrates, and between inks with different values of surface tension. The track in the left of figure is Ag ink printed in two layers on untreated PA substrate. It can be seen that the droplets that constitute the track are not fully interconnected, which causes poor conductivity. The droplets spreading and the connectivity between them improve when the substrate surface energy is increased by plasma treatment prior to printing as shown by the track in the middle of **Figure 2.5**.

In addition to increasing the substrate surface energy, the surface tension of the ink was lowered in an attempt to increase the wetting of the droplets. The surface tension of the silver ink was reduced by adding IPA while Tween 20 surfactant was added to the PEDOT:PSS ink as described previously in **Section 2.2.1.3**. The right track in **Figure 2.5** was printed using Ag/IPA ink and as can be seen the ink droplets constituting this track spread the most among the three.

From **Table 2.1**, when no substrate treatment was applied, PP/T20 ink perform slightly better than PP ink by producing continuously conductive horizontal track at 250 μm line width while no conductive tracks were produced by the PP ink. Comparing between the same numbers of printing pass for no substrate treatment condition, the Ag/IPA ink has smaller minimum nominal track width required to produce continuous tracks than the Ag ink. The maximum line width needed for the Ag/IPA ink was 40 μm (2 printing pass, vertical) while the Ag ink needed larger than 250 μm width to produce continuous vertical track with two printing pass.

It is imperative however to be careful while altering the ink surface tension because excessive modification could affect the ink performance. The Ag and PP inks are formulated by the supplier for their respective surface tension and viscosity to be compatible with the inkjet printing method. In order for the print head nozzles to be able to eject ink droplets efficiently, both the ink surface tension and viscosity need to be in a specific range (discussed in **Section 1.6.2.1**) [154, 155].

In terms of track orientation, horizontal tracks have a slightly better performance when compared with the vertical ones. Horizontal tracks were printed in parallel to the direction of print head trajectory. The adjacent ink droplets in a horizontal track are ejected immediately next to each other which allows for mutual flow connection between the two droplets since both are not dried yet. The flow between the two ink droplets improves the continuity of the tracks. It was reported elsewhere that pattern that has its longitudinal axis parallel to the printing direction, has a better conductivity than the one perpendicular to it [157]. In contrast, there is no or less mutual flow between adjacent ink droplets in vertical track as the printhead moves perpendicular to the track longitudinal direction. The second ink droplet of the two adjacent droplets

is ejected after the printhead has completed all the droplets it is required to print located on the same horizontal coordinate. By the time it reaches the next horizontal coordinate where the second ink droplet of the two adjacent droplets of the same vertical track is located, the first droplet has either nearly or fully dried.

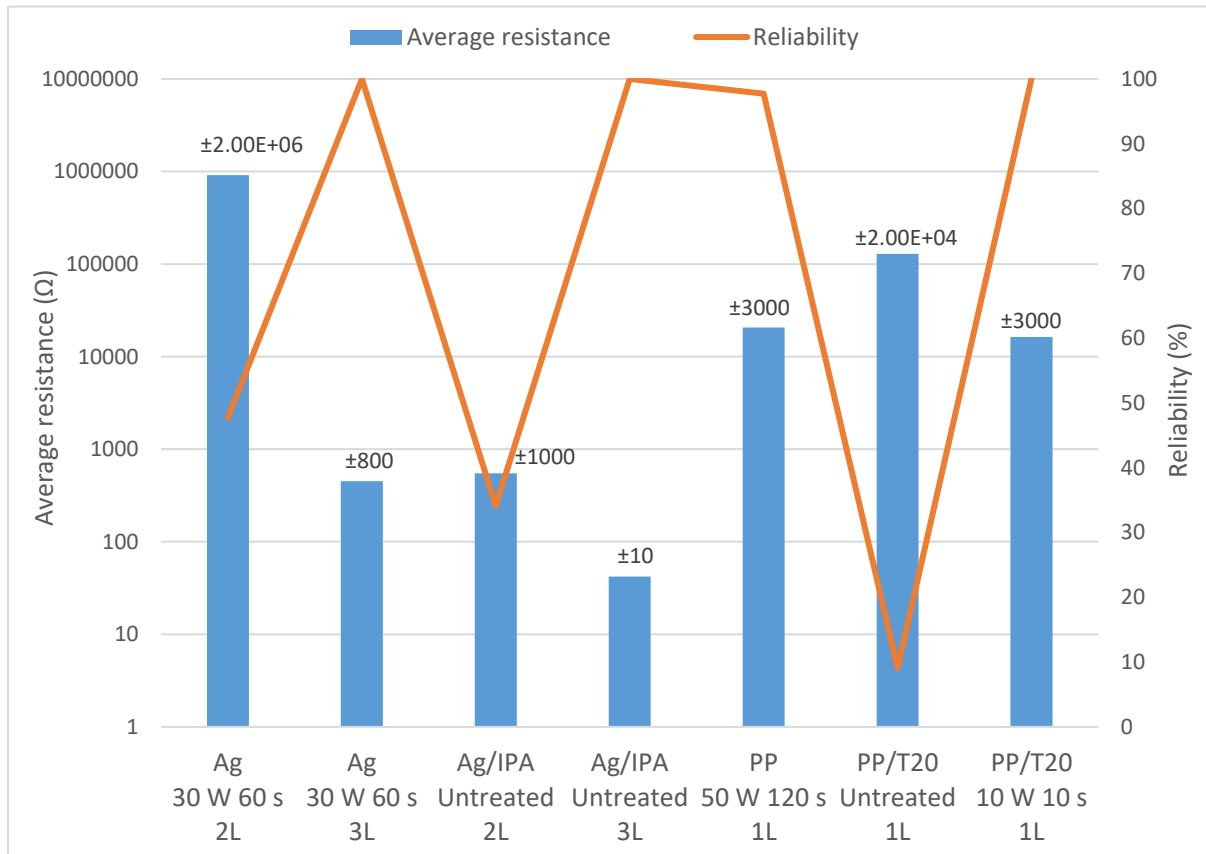


Figure 2.6: Average resistance in 15 mm long and 250 μm wide horizontal tracks and the reliability of the printing process to produce conductivity in the tracks. The standard deviations are given in the labels.

The reliability of the inkjet printer to consistently produce conductive track was investigated by printing 44 tracks (12 mm in length and 250 μm in width) for each type of the seven combinations of ink-treatment-presented in **Table 2.1**. The reliability was determined by calculating the percentage of narrow tracks that are conductive from end to end. The average resistance of the tracks and the reliability of the printing process are shown in **Figure 2.6**. The average resistance decreases and the reliability

of producing conductive tracks increases to 100% when the number of printing passes is increased from two to three layers for both types of silver ink tracks. Comparing between tracks having the same number of printing passes, the Ag/IPA ones always have lower average resistance than the Ag tracks. The two-layer Ag/IPA tracks have a massively lower average resistance of 50 Ω , compared to 100 k Ω for the Ag tracks. This indicates that Ag/IPA ink produces tracks with larger and uniform width than the Ag ink, as can be seen in the **Figure 2.5** which results in a lower average resistance. The Ag tracks have an inconsistent track width; there are regions with considerably narrower width, which cause the increase in average resistance. For the PEDOT:PSS tracks, the treated ones have lower average resistance and higher reliability than the untreated ones. The PEDOT:PSS tracks' reliability is 98% for PP ink and 100% for PP/T20 ink when treatment is introduced. To summarise, the silver ink tracks' reliability improves significantly when three printing passes are applied while PEDOT:PSS tracks' reliability increases when plasma treatment is included.

2.2.3 Minimum allowable electrode spacing

Another important feature in patterning of EWOD electrodes is the spatial resolution as large spacing between two adjacent electrodes (>150 μm) can impede droplet movement [61, 180]. The minimum allowable nominal spacing was evaluated by printing an array of square electrodes, as shown in **Figure 2.4**, 1.5 mm in nominal size with varying nominal spacing from 80 μm to 340 μm increasing in 20 μm increments. For each combination of ink and treatment, the test pattern shown in **Table 2.2** were printed at least three times. The reported results in **Table 2.2** are the best performing sample out of the printed samples. The spacing resolution was evaluated by checking for the absence of a conductive path between two adjacent electrodes with an optical

microscope and also by measuring the resistance between the electrodes using the digital multimeter. The results are presented in **Table 2.2**.

Table 2.2: *The minimum allowable spacing between electrodes for different types of ink.*

| Type of ink | Plasma treatment on substrate | Number of printing layers | Minimum nominal electrode spacing with complete separation (μm) |
|---|-------------------------------|---------------------------|--|
| PEDOT:PSS (PP) | 50 W 120 s | 1 | 220 |
| PEDOT:PSS added with glycerol and Tween 20 (PP/T20) | 10 W 10 s | | 140 |
| Silver (Ag) | 30 W 60 s | 2 | 220 |
| 1.6 Silver : 1 IPA (Ag/IPA) | None | | 200 |

For the PP/T20 electrode, the smallest allowable nominal spacing is 140 μm while for the PP and Ag electrodes it is 220 μm . The smallest allowable spacing for Ag/IPA electrode on untreated substrate is 200 μm . A small allowable nominal spacing indicates the ability of the ink to produce a high fidelity pattern. A large allowable nominal spacing will increase the length of electrode pitch (the sum of electrode size and electrode spacing) which requires a larger droplet volume for an effective EWOD actuation. It was difficult to determine accurately the minimum allowable spacing for silver electrodes as they need two printing passes. The precise manual repositioning of the substrate on the commercial printer tray for the second printing pass was difficult to achieve resulting in the misalignment of the electrode pattern as shown in **Figure 2.7**. This was exacerbated by the slight bending of polymer substrate resulting from the heat treatment required after each printing pass.



Figure 2.7: The first (blue outline) and second (yellow outline) printing pass did not align precisely which can cause overlapping between adjacent electrodes, indicated in the red-dashed circle, reducing the resolution of the inkjet printing method for silver inks.

2.2.4 Reliability of the inkjet-printed EWOD plates

In order to evaluate the reliability of the low-cost printer when producing functional plates for droplet actuation, electrode pattern as shown in **Figure 2.1** was inkjet printed on the PA substrate. The pattern consists of three rows of $1.7 \times 1.7 \text{ mm}^2$ 16 square electrodes. Each of these electrodes is connected to a corresponding contact pad located at the top of the pattern. In the pattern design, the track width is $250 \text{ }\mu\text{m}$ while the electrode spacing is $360 \text{ }\mu\text{m}$ and $320 \text{ }\mu\text{m}$ for the PP/T20 and silver plates respectively. The PP ink was excluded from this investigation and hereafter since it clogged the print head nozzles very easily, not allowing a full completion of the design printing. After printing, the connectivity between the contact pad and its corresponding electrode in the third row was evaluated by measuring the resistance using the digital multimeter. Assessment of any electrical short circuits in the pattern was performed by measuring the resistance between adjacent electrodes.

Table 2.3: Reliability of plates printed using the PP/T20 ink. The tracks' width is 250 μm while the electrode spacing is 360 μm . Only one layer of printing was applied for this ink.

| | PEDOT:PSS added with DI water, glycerol, and Tween 20 (PP/T20) Plasma treated substrate at 10 W for 10 s | | | | | |
|--|---|----|----|----|----|----|
| Plate number | 1 | 2 | 3 | 4 | 5 | 6 |
| Tracks connectivity (out of 16) | 10 | 10 | 13 | 16 | 15 | 15 |
| Electrode spacing separation (out of 15) | 15 | 4 | 6 | 15 | 15 | 14 |

Table 2.4: Reliability of plates printed using the silver inks. The tracks width is 250 μm while the electrode spacing is 320 μm . Two layers of printing were applied for this ink and 2+1 indicates two layer of printing with additional printing pass just for the tracks connecting the electrodes excluding the square electrodes.

| | Silver (Ag) Plasma treated substrate at 30 W for 60 s | | | | Silver added with IPA (Ag/IPA) Untreated substrate | | |
|--|--|----|-----|-----|---|-----|-----|
| Plate number | 1 | 2 | 3 | 4 | 1 | 2 | 3 |
| Number of printing pass | 2 | 2 | 2+1 | 2+1 | 2 | 2+1 | 2+1 |
| Tracks connectivity (out of 16) | 10 | 11 | 15 | 16 | 14 | 15 | 13 |
| Electrode spacing separation (out of 15) | 6 | 15 | 15 | 15 | 11 | 14 | 13 |

Table 2.3 and **Table 2.4** summarise the results of the printed electrode pattern reliability to produce conductive tracks and complete separation between electrodes for PP/T20 and silver inks respectively. The PP/T20 plates have produced one perfect plate (out of 6 plates) with all 16 electrodes fully connected to the contact pads and without any shorted connections between adjacent electrodes. Two plates have one

disconnected track, one plate with three disconnected tracks, and the rest have six disconnected tracks. In terms of electrode spacing, 50 percent of the PP/T20 plates do not have any shorted electrodes. One plate has only one shorted connection while the other two plates have very poor electrode separation, producing only four and six spacing with complete partition.

For the silver inks, to improve the reliability of producing functional plates, four plates were printed with additional printing pass just for the tracks excluding the square electrodes (referred to as 2+1 plates). By printing only the tracks, the problem of reduced spacing resolution due to multiple printing pass can be minimised. Without the additional printing pass, fully interconnected tracks for all 16 electrodes cannot be achieved for both types of silver plates. One fully functional plate was produced using the Ag ink while the best performing plate for Ag/IPA ink has one disconnected track and one shorted connection.

The findings in this section have demonstrated that it is difficult to achieve a plate with fully interconnected tracks and without any shorted electrodes using a low-cost 'standard' inkjet printer. Even though the results in **Sections 2.2.2** and **2.2.3** have shown that the inkjet printing method is capable of producing conductive tracks with smaller nominal width, a larger width, 250 μm was used to increase the reliability of the method. The same argument is applied for the electrode spacing where larger separations were used, 320 μm and 360 μm . Despite the precautions taken to improve the consistency of the process, there were still disconnected tracks and shorted electrodes occurring on the printed plates. Complete electrical separations between all electrodes were easier to achieve (46% of plates) than full connection in all 16 electrodes (15% of the plates). It is suspected that some of the shorted electrodes

were caused by the printer roller which inadvertently transfers or smears the ink across the substrate when in contact with the undried electrode pattern.

2.2.5 EWOD performance of the inkjet-printed parallel-plate devices

In this section, the feasibility of using the inkjet-printed silver and PEDOT:PSS as electrodes in EWOD devices was evaluated. Parallel-plate devices employing the PP/T20, Ag, and Ag/IPA inks as the control electrodes were assembled and these devices were tested for droplet transportation by actuating 5 μ l droplets of DI water. The thickness of the electrodes is $0.28 \pm 0.02 \mu\text{m}$ for the Ag/IPA device and $0.06 \pm 0.01 \mu\text{m}$ for the PP/T20 device. The nominal gap size for the Ag/IPA and PP/T20 electrode are 320 μm and 360 μm respectively but when measured after the printing process, the gap sizes reduced to $258 \pm 32 \mu\text{m}$ for the Ag/IPA and $257 \pm 56 \mu\text{m}$ for the PP/T20 device.

Both the Ag/IPA and PP/T20 devices were successful in actuating the droplet across an array of electrodes while the Ag device only managed to actuate a droplet across just one electrode and was discarded. Comparing the two functional plates, the PP/T20 device produced better reliability of droplet transportation than the Ag/IPA device. The PP/T20 device transported the droplet across all the 16 electrodes and back. In contrast, the droplet on the Ag/IPA device could only be actuated across six electrodes and back. Electrical failure, manifested by sparks can be observed in several locations on both the Ag and Ag/IPA plates. The sparks were induced by the irregularities, such as sharp points and scattered dots of ink that characterise the edges of the printed silver electrodes. The sharp points projected from the electrode edge with varying length that can reach up to 120 μm . Electrostatic charges accumulate at these sharp edges and points, increasing the electric field at these locations. As the potential between the sharp points and the edge of an adjacent

electrode becomes too high and exceeds the dielectric layer breakdown voltage, current begins to flow between the two points [118].

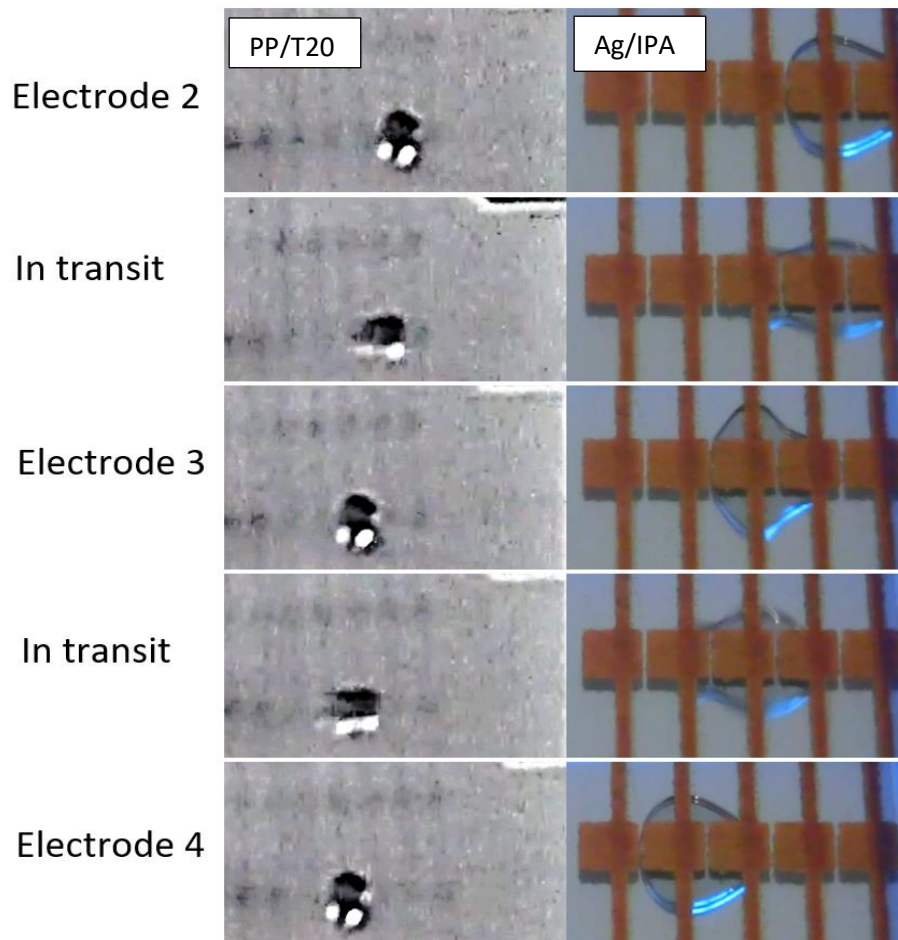


Figure 2.8: The sequence of images in the left show the droplet while in transportation (from electrode no. 2 to electrode no. 4) in the PP/T20 device while the right images is for the Ag/IPA device. The PP/T20 electrodes are harder to identify than the Ag/IPA electrodes because of the PEDOT:PSS transparency. The still images were taken from videos recorded using Canon PowerShot at 29 frame per second and camera phone Samsung Galaxy Ace 4 Neo at 25 frame per second for the Ag/IPA and PP/T20 devices respectively.

In the PP/T20 device, the droplet kept a regular rounded shape during the whole actuation event. However in the Ag/IPA device the droplet has an irregular shape (**Figure 2.8**) because the droplet contact line movement was not confined only to the activated electrodes but also affected by the thicker tracks connecting the array

of electrodes. In the PP/T20 device, these tracks are thinner than in the Ag/IPA device, so their influence on the droplet actuation appeared negligible. The tracks in the Ag/IPA device were thicker because of the three printing pass needed to ensure its reliability.

Previously, Wheeler's Digital Microfluidics group [11, 117] reported a method of patterning EWOD electrode using low-cost piezoelectric desktop inkjet printer, Epson C88+. The desktop printer is capable of producing robust EWOD devices employing 55 μm actual electrode spacing and 148 μm actual track width. The inkjet-printed EWOD devices have been successfully used to perform rubella immunoglobulin assays in a remote setting in north-western Kenya. The very promising results from Wheeler's group indicates that inexpensive inkjet printed devices can be used for real life application. This project aims to provide further technological development toward reducing the DMF devices cost by exploring alternative, inexpensive material and fabrication techniques.

In comparison with the method used in the current study, there are few advantages of the inkjet printing method presented by the Wheeler's group [117]. The Epson C88+ printer has a maximum printing resolution of 2880 \times 1440 dpi, while the printer employ in this thesis has the maximum dpi of 1200 \times 1200. The substrate used for their device was Novele™ IJ-220, a PET transparent film coated with porous coating. This substrate was specially engineered to be used with *Metalon*® silver nanoparticle ink that was also employed as the electrode material in their DMF devices. The same group [61] also developed another inkjet printing method for DMF device fabrication but this particular study used a laboratory-grade printer, Fujifilm Dimatix DMP-2800 material printer, instead of a low-cost one. The laboratory-grade

printer has the capability to vary the spacing between the ink droplets, to as little as 5 μm and also to control the ink and substrate temperature, allowing the user to alter the surface tension and thus the spreading of the ink droplet. This printer was utilised to pattern silver electrodes on paper substrate optimised for inkjet printing of electronics devices [61, 181], which is in contrast with the write-on film made of cellulose acetate substrate used in the current study.

2.2.6 Conclusions

The aim of the first section of this chapter was to investigate the feasibility of using a low-cost technique and materials that can be easily acquired to pattern EWOD electrodes. Home-grade desktop inkjet printer and transparent polymer sheets are common office supplies while conductive polymer PEDOT:PSS is lower in cost compared to conventional metal materials such as silver. The main challenge of using the proposed technique and materials is how to fully utilise their potential whilst circumventing their limitations to produce accurate and detailed features which are necessary in DMF systems. The promising result obtained with the PP/T20-ink device strongly suggests that both inkjet printing and PEDOT:PSS ink have the potential to be used as a patterning method and material for EWOD electrodes.

The desktop inkjet printer used in this study produced satisfactory electrode spacing and track width resolutions but in terms of reliability of the printing process, significant improvement is needed. The spacing resolution is however reduced when multiple printing passes are required, specifically for the silver ink. Furthermore, it is suspected that the printer's paper roller might have caused the shorts between the electrodes while rolling the substrate patterned with the wet ink droplets. Since the margin of error is very small due to the pattern being in the range of tens of

micrometres, all these issues affect the spacing resolution and the reliability of the printing method significantly.

Introduction of plasma treatment improves the printing reliability to produce fully interconnected narrow tracks by increasing the substrate surface energy, which increases the droplet's spreading. As the droplets spread more, the connectivity between droplets improves. Another method that was used to increase the droplet spreading involved lowering the ink's surface tension by adding IPA to the silver ink and surfactant to the PEDOT:PSS ink. The reproducibility of the inkjet printing process also needs to be improved as the problem of nozzles clogging when PEDOT:PSS ink is used has produced varying quality of electrode printing. Steps such as ink filtering, adding glycerol as humectant, and immediate cleaning of cartridge after usage reduce this problem. The use of laboratory-grade inkjet printer such as the Fujifilm Dimatix printer, similar to the one used in previously mentioned study [61] can eliminate, or at least minimise, some of the problems described here (discussed in the next section).

The cellulose acetate film used as substrate in this study demonstrates good performance when a plasma treatment is conducted prior to the inkjet printing process. This substrate however bends after the post-printing annealing process on the hot plate creating an uneven base plate for the EWOD device. An alternative substrate material that can withstand a temperature of 120 °C (annealing temperature for silver ink) without undergoing deformation is needed for the realisation of a reliable EWOD device. A substrate with a higher surface energy than the one used in the current study could also improve the reliability of the printing method in producing fully interconnected tracks.

2.3 Electrode patterning using Fujifilm Dimatix DMP-2850

The Fujifilm Dimatix Materials Printer DMP-2850 (Fujifilm Dimatix, Inc., Santa Clara, US) is a piezoelectric printer designed for research and development purpose especially in the field of microelectromechanical systems (MEMS) fabrication process [182]. At this point in time during the author's research project, funds became available for the Microfluidics and Micro-engineering Research Group (MMRG), University of Hertfordshire to purchase the Fujifilm Dimatix printer. This has given the opportunity for the research project to investigate the printer usability as a method to pattern EWOD electrodes. The first inkjet printing investigation reported previously in **Section 2.2** was conducted from February 2016 and lasted for about 10 months until early December 2016. The second inkjet printing investigation using the Fujifilm Dimatix printer started around July 2017.

Figure 2.9 shows the Fujifilm DMP and its cartridge. The cartridge can be filled with any type of materials including biological fluids such as cell suspension, making the printer very useful for feasibility studies with a new ink material. The printer operates like a 3D printer where the print head can move in three directions (but only in the x and y axes during printing) while the substrate remains stationary (unlike the ink jet printer used previously). Due to this capability, it can perform small-scale additive layer manufacturing, although limited to a certain thickness.

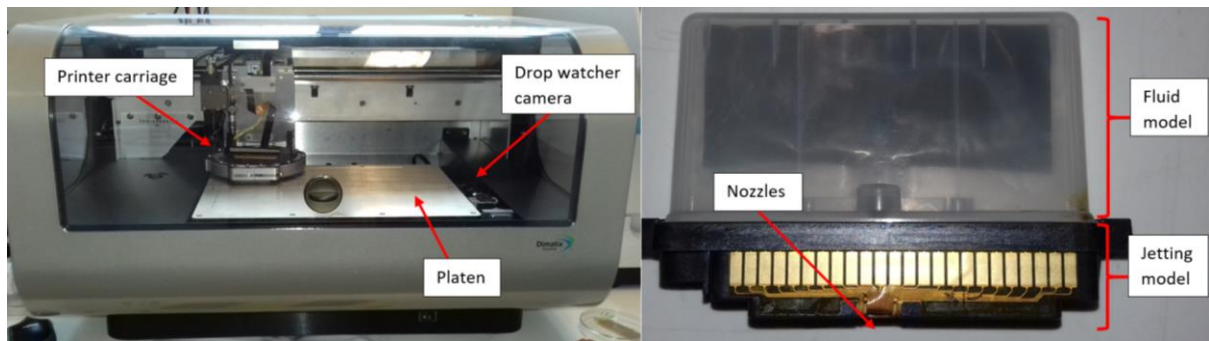


Figure 2.9: The Fujifilm Dimatix DMP-2850 printer (left). Some of the important components such as the printer carriage is shown in the figure. The printer cartridge (right) is consisted of a fluid model and a jetting module. The fluid model contains the ink while the jetting module contains the nozzles and the electrical connection to the printer.

The cartridge print height can be set from 0.25 mm up to 1.5 mm from the surface of the substrate while the maximum allowable thickness of the substrate is 25 mm. The printer also allows wide range of substrates to be used, such as glass slides and silicon wafers, unlike the ink jet printer employed in the previous section which requires the substrate to be flexible. The platen is the platform that holds the substrate using vacuum suction and it can be heated up to 60 °C in temperature [183].

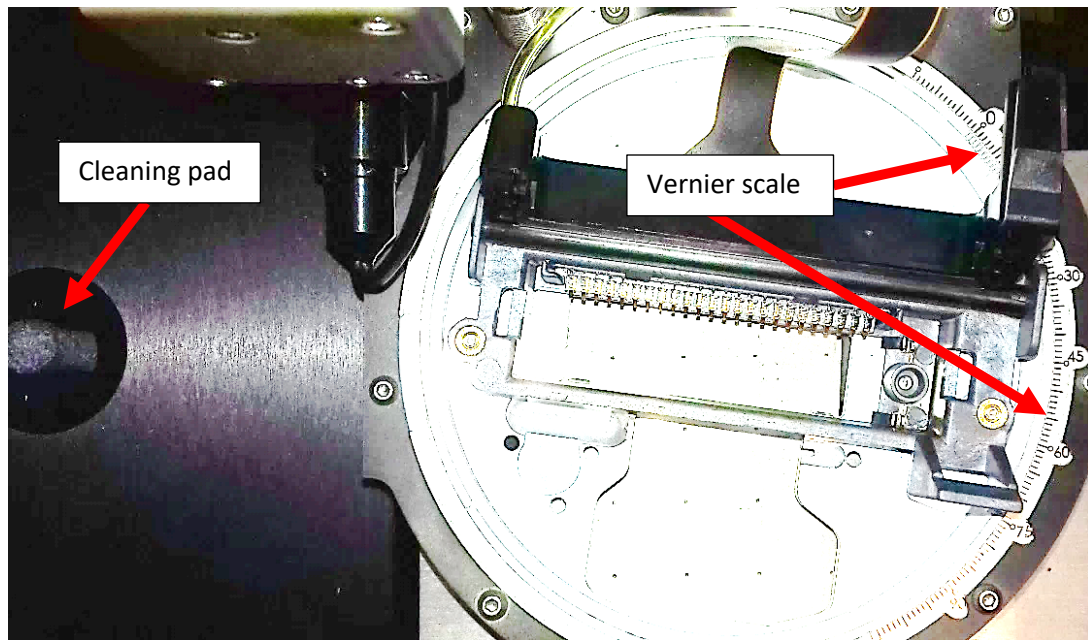


Figure 2.10: The printer cartridge carriage, without cartridge attach to it. The vernier scale is used to set the mounting angle which determine the drop spacing. The cleaning pad on the left is used to absorb ink from the nozzles during cleaning cycles.

The cartridge contains 16 nozzles. The spacing between the nozzles is 254 μm . The printing resolution or the spacing between the ink droplets is adjusted by setting the cartridge mounting angle. The printer system calculates the corresponding angle for a certain drop spacing or resolution desired by the user. The user then needs to set the mounting angle manually. **Figure 2.10** shows the Vernier scale on the carriage of the printer cartridge for the setting of the mounting angle. The highest resolution that can be employed is 5080 dpi which is 5 μm in drop spacing. The drawing of the patterns can be done using the printer's in-house software feature, *Pattern Editor*. Drawings done using other software such as Adobe Illustrator® can be uploaded in either Gerber or Bitmap (BMP) formats. The bitmap files need to be saved in the same dpi resolution as the cartridge drop spacing so that the printed pattern have the same scale as the drawing [183].

The printer also includes a *Cleaning Cycle Editor* feature for the maintenance of the cartridge nozzles. To keep the nozzles clear and functioning properly at all times, the user can set a cleaning cycle before, during, and after printing. There are three cleaning actions that can be performed: spit, purge, and blot. Spit is the firing of nozzles at a designated frequency and duration, purge is the pushing of ink fluid through the nozzles using pressure, and blot is moving the down the nozzles to make contact with a cleaning pad. The cleaning pad is shown in **Figure 2.10**. The user can decide the sequence of the cleaning actions and also the duration of each action [183].

For each type of ink, the user can determine the firing voltage, the meniscus pressure, the cartridge temperature, the maximum jetting frequency, and most importantly, the jetting waveform that will result in reliable and quality droplet ejection. A jetting waveform is the voltage signal applied to the piezoelectric (PZT) element in the nozzle. A simplified structure of the nozzle is shown in **Figure 2.11**.

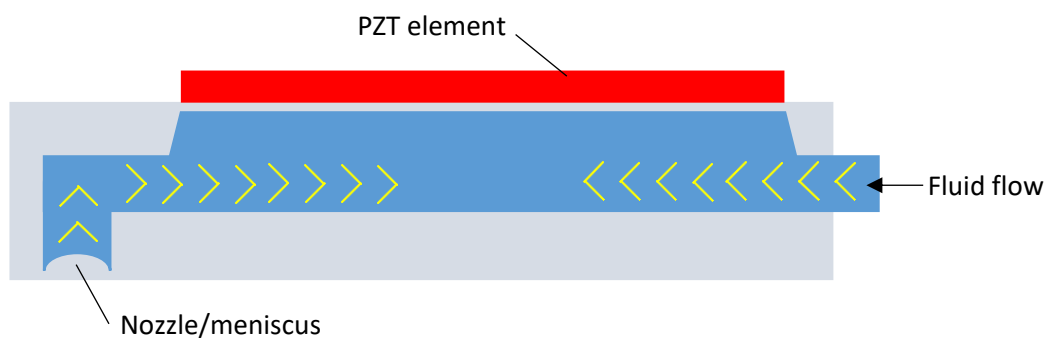


Figure 2.11: The simplified diagram of the chamber, PZT element, and the nozzle. The jetting waveform applied to the PZT element will cause its deflection and relaxation which controls the flow of the ink fluid inside the chamber. A meniscus pressure is applied to avoid the ink from flooding the nozzle while the PZT element is in its relaxation mode.

The user can determine the amplitude, the duration, and the slope of each segment in the waveform using the *Waveform Editor* in the DMP software. Using the waveform shown in **Figure 2.12** as an example, typically a waveform is composed of

four segments. In the beginning of the first segment, the PZT element is in a slightly deflected state due to the voltage applied at the end of the previous cycle. The PZT element then returns to its relaxed condition as no voltage is applied. The ink fluid is drawn into the chamber through the inlet but a meniscus pressure holds the ink from flowing through the nozzle.

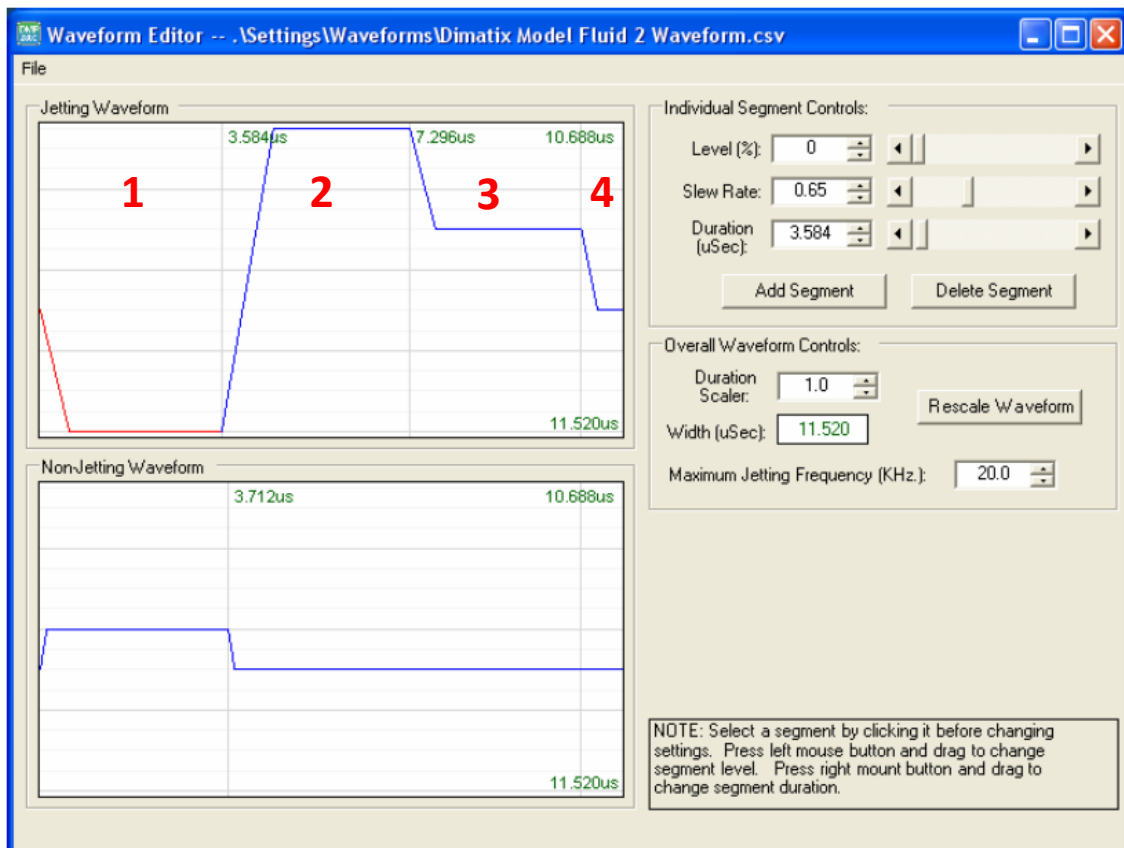


Figure 2.12: An example of jetting waveform and non-jetting waveform applied to the piezoelectric element of the DMP print head. The jetting waveform is composed of four segments. The user can edit the amplitude, the slope, and the duration of each segment in the waveform [183].

The drop ejection occurs during the second segment where the voltage is the highest resulting in the highest deflection of the PZT element. The chamber is compressed and a droplet is ejected from the nozzle. Entering the third segment, the applied voltage is lowered and the chamber decompresses slightly resulting in partial refilling of the ink. The meniscus pressure at the nozzle pulls back the ink into the

chamber, ensuring complete separation of the ejected droplet. The fourth segment is the standby phase before the next cycle starts again. Non-jetting waveform is a 'tickle pulse' sent during idle period to avoid the ink from forming a thin 'skin' layer at the nozzles due to fluid evaporation [183].

The firing voltage of each of the nozzles can be individually controlled using the DMP's software. Ink with a high viscosity needs a higher voltage and a steeper slope to be jetted from the nozzle but they can perform very well at a high jetting frequency. The viscosity of the ink can be lowered by increasing the cartridge temperature which can be adjusted up to 70 °C. High surface tension ink also needs higher voltage and steeper slope but the performance may decrease with the jetting frequency. The desired velocity of an ink droplet is 6-10 ms⁻¹. The printer software is capable of evaluating drop velocity by assessing the droplet vertical position after 100 μs using the *Drop Watcher* camera, as shown in **Figure 2.13**. The higher the firing voltage, the higher the drop velocity. The *Drop Watcher* camera also enables the user to evaluate the ink performance in real-time as parameter such as firing voltage and the shape of the waveform is being set. In addition to the *Drop Watcher* camera, the printer includes another camera system: the fiducial camera. The fiducial camera allows exploration of the substrate surface and can be used to identify different printing relevant reference points on the substrate, such as the origin point of the printing. The fiducial camera include measurement tools for measurement of features on the substrates [183].

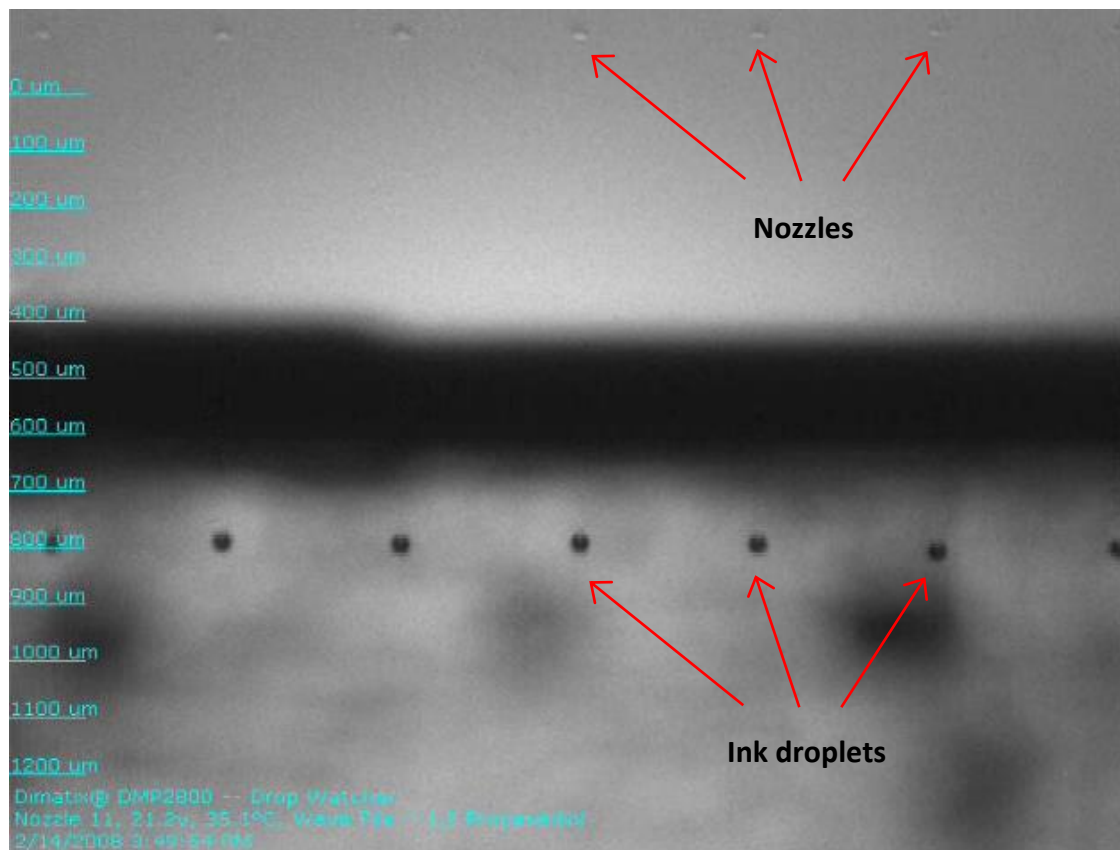


Figure 2.13: The Drop Watcher camera displays the droplet ejection from the nozzles, allowing the user to evaluate in real-time the performance of the droplet with the changing of the printing parameter. The image above shows good formation of ink droplets with no long tails or satellite drops trailing behind [183].

2.3.1 Experimental

In order to investigate the feasibility of using the Fujifilm Dimatix printer as EWOD electrodes patterning method, the capability of the printer to produce micro-feature size patterns was assessed. The conductivity of narrow tracks with varying width and electrical separation of electrode spacing with varying size patterned using the desktop printer were evaluated. Several combinations of ink and substrate were tested to determine which one was the most reliable in producing fully interconnected tracks without any shorted electrodes. The chosen ink and substrate combinations were then employed to fabricate EWOD plates for evaluation of water droplet actuation.

2.3.1.1 Conductive inks

Two types of ink material were used: conductive polymer PEDOT:PSS (739316, Sigma Aldrich, St. Louis, US) and silver (ANP silver DGP 40LT-15C, ANP Co. Ltd., Sejong, South Korea). The silver ink used previously in the HP desktop printer investigation has been discontinued by the manufacturer. The surface tension, γ of the PEDOT:PSS and ANP silver ink are 31 - 34 mNm⁻¹ and 35 - 38 mNm⁻¹ while the viscosity, η are 7 -12 mPa s and 10 -17 mPa s respectively. Two formulations of the PEDOT:PSS ink were tested: one using the ink directly from stock and the other with added DI water, glycerol, and surfactant (same as the one used for the HP desktop printer) [150] referred to as PP/T20 ink. After printing, the silver and PEDOT:PSS inks were annealed on the hot plate for about 5 minutes at temperature of 120 °C and 110 °C respectively. The temperatures used for the curing of ink are as suggested by the manufacturer and the literature [169].

2.3.1.2 The Fujifilm Dimatix DMP-2850 printer setting

Table 2.5 lists the settings used for the three types of ink employed in this investigation. Both the PP and PP/T20 inks used the same settings. The ANP silver ink was ejected at temperature of 30 – 35 °C while the PEDOT:PSS inks were ejected at ambient temperature to avoid quick drying of ink particles at the nozzles which can cause clogging. No heating of the platen was required for either paper or polymer substrates when PEDOT:PSS inks were used. The same applied to silver ink on paper substrate but when polymer substrate was used for silver ink, the platen needs to be heated to 60 °C to increase the spreading of the silver ink droplet. The PEDOT:PSS inks were ejected at a lower firing voltage than the silver ink.

Table 2.5: The printer setting applied for the silver and PEDOT:PSS inks printing

| Printer parameter | ANP silver ink | PP and PP/T20 inks |
|---|-----------------------|---------------------------|
| <i>Print height</i> | 1 mm | 1 mm |
| <i>Print head temperature</i> | 30 – 35 °C | Ambient temperature |
| <i>Platen temperature for paper substrate</i> | Ambient temperature | Ambient temperature |
| <i>Platen temperature for polymer substrate</i> | 60 °C | Ambient temperature |
| <i>Firing voltage</i> | 28 – 35 V | 18 – 25 V |
| <i>Maximum jetting frequency</i> | 5 kHz | 5 kHz |
| <i>Meniscus</i> | 3.5 inches | 3.5 inches |

If a fine resolution pattern such as in EWOD electrodes is required, a lower jetting frequency was suggested [153]. The maximum jetting frequency used was 5 kHz for all types of ink (the highest available frequency setting is 30 kHz). As reported elsewhere [153], the precision and the definition of a printed pattern also depend on the number of jetting nozzle; the fewer the jetting nozzle, the higher the precision and definition of the printed pattern [153]. For this reason, only one nozzle was used for the PEDOT:PSS inks while up to four nozzles were used for silver ink printing.

2.3.1.3 Cartridge maintenance

The cartridge was filled with 1.5 ml of the ink. All types of ink were agitated for 15 minutes in ultrasonic water bath to re-disperse the ink particles and filtered with 0.45 µm syringe filter prior to filling into the cartridge. The filtering was performed to reduce the clogging of the cartridge nozzles. While a cleaning cycle promotes a better reliability of the printing process for most types of ink, the opposite has been demonstrated for the PEDOT:PSS inks. After optimum printing parameters have been set for the PEDOT:PSS inks, the quality of the jetted droplets can be altered after running the cleaning cycle at the start of the printing process. Due to this issue, no cleaning cycles were applied before and during printing for the PEDOT:PSS inks as

the reproducibility of the jetted droplets was very poor. Cleaning was also avoided during printing to avoid any misalignment of the printed pattern as the printer carriage sometimes slightly shifted after moving to the cleaning pad. After printing, a 'spit-purge-spit' sequence was performed to keep the nozzles clear. No special maintenance step was applied for the silver ink cartridge for overnight or long term resting. As for the PEDOT:PSS ink cartridge, the PEDOT:PSS fluid module was disconnected from the jetting module and exchanged with another fluid module containing DI water. To increase the lifetime of the PEDOT:PSS ink nozzles, the cartridge was then run with a cleaning cycle of purging for 10 seconds. This was repeated several times. The jetting module was then stored immersed in a DI water bath inside a petri dish. By applying this step, the cartridge can be used for up to three weeks before all nozzles are completely clogged. The cost of one Fujifilm Dimatix cartridge is £75. Previous study [153] using PEDOT:PSS ink with the same type of printer, Fujifilm Dimatix reported an average printer cartridge lifetime of only two days despite various measures being taken such as cleaning cycles to avoid the clogging of nozzles: so the maintenance schedule appears to be highly effective.

2.3.1.4 Types of substrate and surface treatment

Five types of substrate were employed (**Table 2.6**); three were paper substrates while the other two were polyethylene terephthalate (PET), one is from unidentified manufacturer (identified as hPET) and the other one uses the brand name *Melinex*[®], polymer substrates. One of the paper substrate is PEL P60 (PP60), a specialised paper for inkjet printing of electronic circuits, and the other two paper substrates are Mitsubishi's resin-coated (MRC) paper and HP's 'Advanced' (HPA), both used as high quality photographic paper. The MRC paper is laminated with polyethylene. Both of

the hPET and *Melinex*® substrates are treated on both surfaces to promote ink and coating adhesion for medical and electronics applications.

Table 2.6: Substrates employed in the Fujifilm Dimatix DMP-2850 printer investigation with the required surface treatment.

| Types of substrate | Substrate name | Surface treatment |
|--------------------|--|---|
| Paper | PEL P60 (PP60) (Printed Electronics Ltd, Staffordshire, UK) | None |
| | Mitsubishi resin-coated paper, RC-3GR120 (MRC) (Mitsubishi Paper Mills Ltd, Japan) | None |
| | HP Advanced photo paper (HPA) (HP Inc. California, US) | None |
| PET polymer | Hydrophilic PET (hPET) | None |
| | <i>Melinex</i> ® 506 (HiFi Industrial Film®, Hertfordshire, UK) | None for ANP silver ink but platen heated to 60 °C during printing. UV/ozone treatment (15 min) for PP ink. |

Upon the first printing trial using the silver ink, all the substrates led to satisfactory track conductivity without the need of any surface treatment. For the PP ink, UV/ozone treatment was required for the *Melinex*® substrate. This substrate was treated for 15 minutes using a UV/ozone cleaner (Novascan Technologies Inc., Iowa, US). None of these substrates were heated during printing except for *Melinex*® which was heated to 60 °C but only when silver ink was used. Platen heating was avoided especially while printing PEDOT:PSS inks as it promotes drying of the ink at the nozzles which can cause clogging.

2.3.1.5 Conductivity measurements of the printed pattern

The conductivity measurements of the electrode patterns and tracks deposited using the inkjet printer were conducted using a digital multimeter.

2.3.1.6 Contact angle measurements

Static contact angle of 10 μl of DI water on the substrates listed in **Table 2.6** was measured to evaluate the wettability or spreading of the droplet on these substrates. The measurement was made using Theta Lite optical tensiometer (Biolin Scientific, Gothenburg, Sweden) with the droplet images recorded at 1.3 frame per second (fps) and were analysed by *One Attension* software (the Theta Lite system's software).

2.3.1.7 Fabrication of EWOD plates and evaluation of droplet actuation in the parallel-plate EWOD devices

Parallel-plate EWOD devices (design shown in **Figure 1.5**) employing electrodes patterned using the Fujifilm DMP-2850 printer were assembled to further validate the method. There were seven types (listed in **Table 2.9**) of EWOD devices fabricated using different combination of ink and substrate. The design of the control electrode is shown in **Figure 2.1**. It comprises three rows of 16 square electrodes, 1.7 mm in size with the corresponding contact pads for connection with the electronics located at the top of the design. To form the base plate of the device, this design was printed on the chosen substrate. A layer of Parylene-C dielectric material (thickness $\sim 3.2 \mu\text{m}$) was deposited on top of the electrodes using the Parylene deposition system. Adhesive tape was used to cover the contact pad region of the base plate before the deposition of the dielectric material. A final layer of *Cytop*[®] hydrophobic surface was spin coated onto the plate at 1500 rpm for 30 s and cured at temperature of 110 °C for one hour.

The printed base plate was assembled with a grounded cover plate made of an ITO-coated glass slide (Diamond Coatings, West Midlands, UK) deposited with *Cytop*[®] hydrophobic layer to form a parallel plate device. The gap between the base and cover plates, the PMMA frame holding the EWOD plates (**Figure 2.2**), and the drive electronics to control the droplet movement were the same as the ones employed

in **Section 2.2.1.6**. 5 μl of deionised (DI) water was used to evaluate the linear transportation of droplets in the parallel-plate EWOD devices. Droplet movement was recorded using a *Canon PowerShot* (Canon, Tokyo, Japan) camera at 240 fps. The displacement and velocity of the droplet on the EWOD devices were evaluated using image analysis software (Tracker, Video Analysis and Modelling Tool, Douglas Brown, California, US). This software tracks the position of a point in a frame-by-frame basis and capable of both kinematic and kinetic analyses.

2.3.2 Drop spacing and electrical conductivity of the printed tracks

In the previous HP printer investigation where the drop spacing is a constant parameter, the ink properties were altered and the substrates were treated in order to achieve conductive tracks. These methods were tedious and time consuming. Using the Fujifilm DMP-2850, instead of modifying the fluid-substrate interaction, track conductivity was accomplished by decreasing the drop spacing. A few printing trials were made for each combination of ink and substrate to determine the optimum drop spacing that produce conductive tracks. The smaller the drop spacing the higher the connectivity between the ink droplets. While track conductivity is desired, it is also important to take into consideration the time taken to print a pattern which is also depending on the drop spacing. The smaller the drop spacing the longer it needs to complete the pattern printing. For comparison, to print the pattern shown in **Figure 2.1** using PEDOT:PSS ink with only one nozzle employed, it took about 45 minutes to complete if 30 μm drop spacing was used and up to 3 hours if the drop spacing was 15 μm . The silver ink printing took a shorter time to complete than PEDOT:PSS inks as more than one jetting nozzles were used.

CA measurements of a DI water droplet sitting on all the substrates were conducted to evaluate the spreading of the droplets on the different types of substrate

employed in this study (results shown in **Figure 2.14**). Apart from the ink drop spacing, the conductivity of the tracks also depends on the wettability or spreading of the droplet on the substrate. The wetting of a droplet on a substrate is closely related to its contact angle where the lower the droplet CA the higher the wettability and the spreading of the ink droplet [184, 185]. The increase in the droplet spreading will in turn increase the droplet contact area with the substrate surface [186]. The possibility of the overlapping between two adjacent ejected ink droplets is higher when the droplet contact area is large thus improving the connectivity between the droplets and the electrical conductivity of the tracks. The droplet CA can also be decreased by increasing the substrate surface temperature as has been demonstrated previously [187] but in this measurement, the substrate temperatures were kept at a constant ambient temperature. From **Figure 2.14**, the DI water droplet has the lowest CA with 9.8° on the hPET substrate indicating the highest droplet spreading among the substrates while the lowest CA with 74° was recorded on the MRC paper substrate.

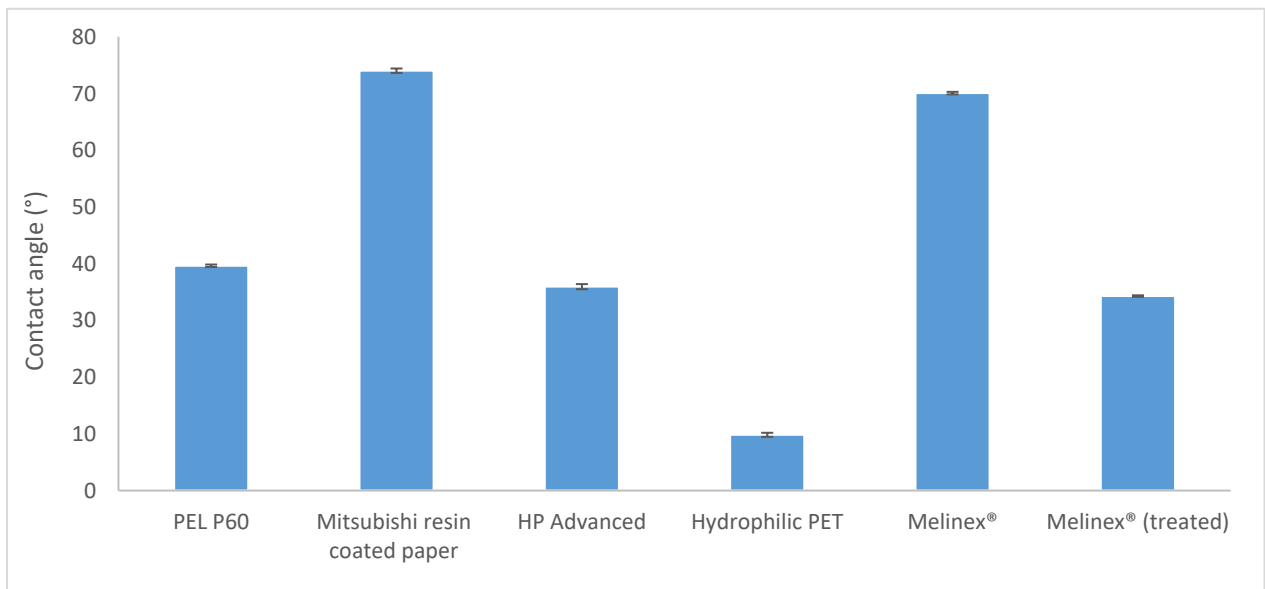


Figure 2.14: Contact angle measurements of DI water droplet on the substrates employed in this investigation.

Table 2.7: Droplet spacing used for printing of the silver and PEDOT:PSS inks on different types of substrate. Electrical resistance and the minimum track width for different combination of ink and substrate.

| Type of ink | Type of substrate | Droplet spacing/ resolution in dpi | Line direction | Electrical resistance (Ω) of track (nominal size of 10 mm x 250 μ m) | Minimum nominal track width with electrical conductivity (μ m) | |
|-------------|-------------------------------------|--|---------------------|---|---|----|
| ANP silver | PEL P60 | 20 μ m /1270 dpi | Horizontal | 4 \pm 1 | 10 | |
| | | | Vertical | 2.7 \pm 0.4 | 10 | |
| | Mitsubishi resin coated paper (MRC) | 20 μ m /1270 dpi | Horizontal | 3 \pm 1 | 10 | |
| | | | Vertical | 2.2 \pm 0.2 | 10 | |
| | HP Advanced (HPA) | 20 μ m /1270 dpi | Horizontal | 5 \pm 1 | 10 | |
| | | | Vertical | 5.5 \pm 0.5 | 10 | |
| | <i>Melinex</i> [®] | 50 μ m /508 dpi | Horizontal | 50 \pm 6 | 10 | |
| | | | Vertical | 158 \pm 20 | 10 | |
| PP/T20 | PEL P60 | 15 μ m / 1693 dpi | Horizontal | 6 M \pm 1 M | 40 | |
| | | | Vertical | 7 M \pm 3 M | 60 | |
| | Mitsubishi resin coated paper (MRC) | 15 μ m / 1693 dpi | Horizontal | 17 M \pm 2 M | 240 | |
| | | | Vertical | - | >250 | |
| | HP Advanced (HPA) | 15 μ m / 1693 dpi | Horizontal | 9.0 M \pm 0.1 M | 10 | |
| | | | Vertical | 6.0 M \pm 0.6 M | 10 | |
| | Hydrophilic PET (hPET) | 30 μ m /847 dpi | Horizontal | 7 k \pm 2 k | 10 | |
| | | | Vertical | 7 k \pm 2 k | 10 | |
| | PP | <i>Melinex</i> [®] (UV/ozone treated) | 30 μ m /847 dpi | Horizontal | 9 k \pm 1 k | 10 |
| | | | | Vertical | 16 k \pm 4 k | 10 |

A similar test pattern to the one used in the HP printer investigation (**Figure 2.4**) was printed on the various types of substrate using the three different inks to evaluate the track width required to produce conductive tracks. For each combination of ink and substrate, the test pattern shown in **Figure 2.4** were printed three times. The vertical and horizontal tracks in this pattern are 10 mm in nominal length with varying nominal width from 10 μm up to 250 μm .

Table 2.7 reports the drop spacing employed to print the track pattern for nine ink-substrate combinations. On all the three paper substrates, the drop spacing for silver ink is 20 μm while on *Melinex*[®] substrate the drop spacing is larger with 50 μm . The *Melinex*[®] substrate has a larger drop spacing even though it has a higher CA (70°) than two of the paper substrate (CA of 34° and 36°) because of the heating applied to the platen. The platen temperature was raised to 60 °C for the silver ink printing on *Melinex*[®] and this has decreased the surface tension of the ink thus improving the spreading of the droplet on the substrate. Without the platen heating, the silver ink droplets pooled together into larger droplets on the polymer substrate, causing disconnections in the electrode pattern (shown in **Figure 2.15**). In terms of minimum track width with electrical conductivity, all the silver tracks regardless of the substrate type were conductive at 10 μm width.

Similar to silver ink, the results for PP/T20 show that the paper substrates (PEL P60, MRC, HPA) needed a smaller drop spacing (15 μm) than the polymer substrate (30 μm) to produce conductive tracks. The results for the PP/T20 ink are consistent with the CA measurement where the substrates with high CA have poor track conductivity. MRC paper, which have the highest CA (74°) produces the poorest conductivity, requiring the track to be 250 μm wide or more to be conductive. As reported in **Table 2.7**, all the paper substrates (PEL P60, MRC, HPA) have very high

resistance in the range of 6-17 M Ω compared to only 6.5-7.3 k Ω for tracks on hPET substrate. Both the HPA paper and hPET substrates are capable of producing track conductivity at 10 μ m width.

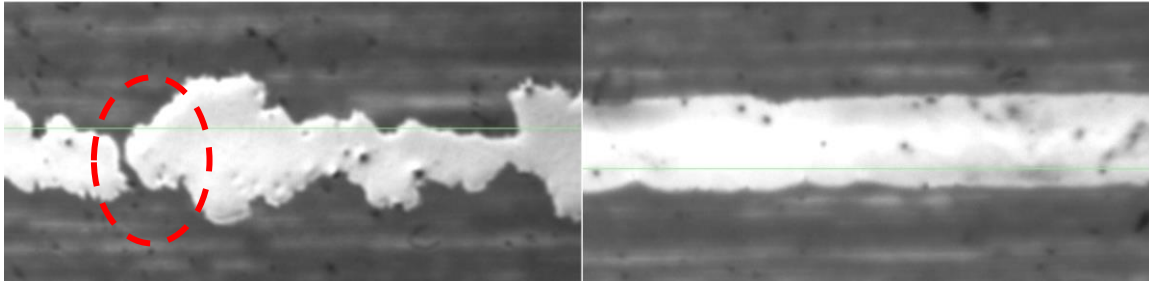


Figure 2.15: The left image shows a silver track printed on Melinex® substrate without any heat applied to the platen and the right image is a silver track printed on the same substrate while the platen temperature was raised to 60 °C. There is a disconnection (shown in the red circle) in the left track due the non-uniform spreading of the silver ink when the substrate was not heated.

For the PP ink only one substrate was tested, the Melinex® treated with UV/ozone for 15 minutes. Paper substrates were excluded as they have been demonstrated to produce poor track conductivity using the PP/T20 ink. Melinex® was chosen over hPET as the former composition can be identified if optimisation is required in the future. The first trial of the PP ink on the Melinex® without any treatment did not produce conductive tracks even at a very small drop spacing. This however improved when UV/ozone treatment is introduced. The CA made on the substrate before and after treatment gave the following readings 70° and 34° respectively, indicating increase in the droplet spreading. On the treated Melinex®, drop spacing of 30 μ m requires minimum nominal track width of 10 μ m to produce conductive tracks.

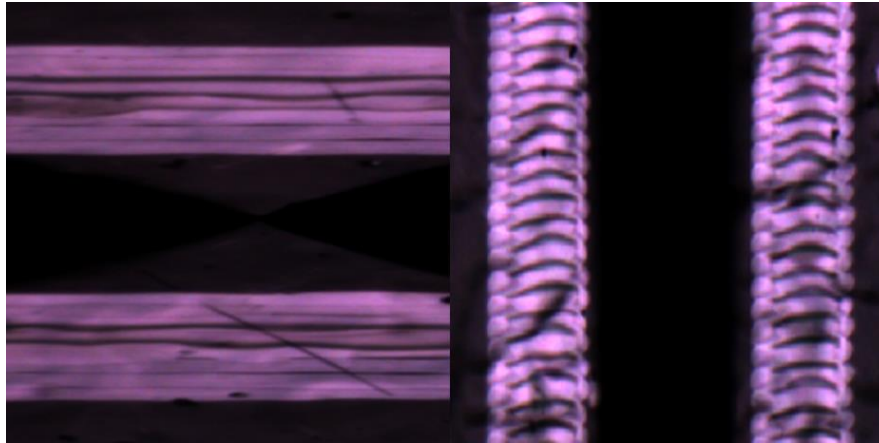


Figure 2.16: PP/T20 tracks on PP60 paper substrate using 15 μm drop spacing. The left tracks are horizontal tracks, printed parallel to the printing direction while the tracks in the right are vertical tracks, printed in perpendicular direction to the printing direction.

Comparing between the silver and PEDOT:PSS inks, the conductive polymer tracks have higher resistance than the silver ones. The PEDOT:PSS inks also require smaller drop spacing than the silver ink to produce conductive tracks. Though no surface tension measurement were made, it suspected that the PEDOT:PSS inks have a higher surface tension than the silver ink based on the drop spacing requirement. The silver ink also performs better on the paper substrates which have demonstrated high CA measurements such as the MRC paper. In terms of direction of track, the horizontal tracks have a slightly better performance than the vertical track, especially for the PP/T20 on MRC paper. **Figure 2.16** shows the different in the formation between the two types of track. The horizontal tracks, printed in the same direction with the printer carriage movement display a laminar structure while the vertical tracks, printed in the perpendicular direction of the carriage movement exhibit a 'stacked coins' pattern. The laminar pattern is more reliable in producing conductive and continuous track than the stacked coins pattern as a 'missing' coin due to clogging of one nozzle can causes a cut in the track.

2.3.3 Minimum allowable nominal electrode spacing to produce electrical separation

The minimum allowable nominal spacing was evaluated by printing an array of square electrodes (**Figure 2.4**), 1.5 mm in size with varying nominal spacing from 80 μm – 340 μm (20 μm increment). The spacing resolution was evaluated by checking the absence of conductive path between two adjacent electrodes under the optical microscope and by measuring if there were any conductivity between the electrodes using a digital multimeter. The results are presented in **Table 2.8**.

Table 2.8: The minimum allowable spacing between electrodes for different combination of ink and substrate.

| Types of ink | Types of substrate | Droplet spacing/resolution in dpi | Spacing direction | Minimum nominal electrode spacing to produce electrical separation (μm) | |
|--------------|-------------------------------------|-----------------------------------|---------------------------|--|-----|
| ANP silver | PEL P60 | 20 μm /1270 dpi | Horizontal | 80 | |
| | | | Vertical | 80 | |
| | Mitsubishi resin-coated paper (MRC) | 20 μm /1270 dpi | Horizontal | 80 | |
| | | | Vertical | 80 | |
| | HP Advanced (HPA) | 20 μm /1270 dpi | Horizontal | 80 | |
| | | | Vertical | 80 | |
| | Melinex® | 50 μm /508 dpi | Horizontal | 180 | |
| | | | Vertical | 120 | |
| PP/T20 | PEL P60 | 15 μm / 1693 dpi | Horizontal | 120 | |
| | | | Vertical | 160 | |
| | Mitsubishi resin-coated paper (MRC) | 15 μm / 1693 dpi | Horizontal | 100 | |
| | | | Vertical | 80 | |
| | HP Advanced (HPA) | 15 μm / 1693 dpi | Horizontal | 140 | |
| | | | Vertical | 200 | |
| | Hydrophilic PET (hPET) | 30 μm /847 dpi | Horizontal | 100 | |
| | | | Vertical | 80 | |
| | PP | Melinex® (UV/ozone treated) | 30 μm /847 dpi | Horizontal | 80 |
| | | | | Vertical | 120 |

Silver-on-paper electrodes are capable of producing complete separation between two adjacent electrodes using nominal spacing of 80 μm . Other combinations of ink and substrate that require small nominal electrode spacing (80 μm) are PP/T20 on hPET, PP/T20 on MRC paper, and PP on *Melinex*[®]. These combinations have minimum allowable electrode spacing between nominal values of 80 μm and 120 μm . The ink-substrate combination with a small minimum allowable spacing indicates a robust and reliable interaction between the fluid ink and the substrate. These findings were used as a guide in designing the EWOD electrodes pattern for plates fabricated in the next section.

2.3.4 EWOD performance of the printed base plate

Seven different ink-substrate combinations were employed to fabricate seven types of EWOD device to validate their feasibility as EWOD components. Each type of device was tested for linear transportation of a 2.5 μl DI water droplet. Two examples of the devices are shown in **Figure 2.17**. **Table 2.9** summarises the EWOD performance of the devices. Only one plate for each type of substrate was fabricated for silver ink. Two plates were fabricated for each type of substrate for PEDOT:PSS inks. The results in **Table 2.9** represent the best performing plate out of the three plates. The electrodes size is 1.7 mm in all of the devices.

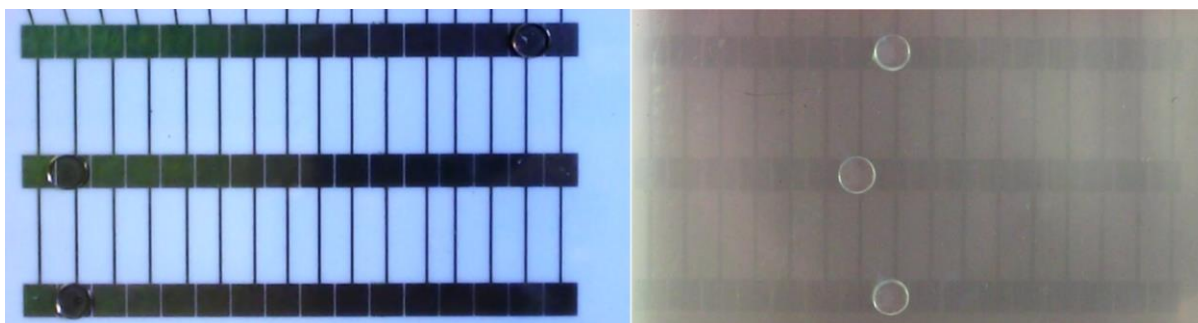


Figure 2.17: The silver-on-HPA (left) and the PP/T20-on-hPET devices.

Table 2.9: EWOD performance of devices made from the inkjet-printed base plate.

| Type of ink | Type of substrate and resolution | Plate design | | Droplet transportation performance | |
|-------------|---|---------------------|---------------------------|--|---|
| | | Nominal track width | Nominal electrode spacing | Voltage to instigate movement across one electrode | Voltage for reliable actuation across 3 and more electrodes |
| ANP Silver | PEL P60 1270 dpi | 100 μm | 100 μm | 75 V_{RMS} | 5 electrodes at 105 V_{RMS} |
| | HP Advanced (HPA) 1270 dpi | 100 μm | 100 μm | 75 V_{RMS} | All 16 electrodes at 105 V_{RMS} |
| | Mitsubishi resin coated paper (MRC) 1270 dpi | 100 μm | 100 μm | 75 V_{RMS} | 10 electrodes at 90 V_{RMS} |
| PP/T20 | PEL P60 1693 dpi 2 layers of printing for the track pattern | 140 μm | 220 μm | 75 V_{RMS} | 7 electrodes at 195 V_{RMS} |
| | HP Advanced (HPA) 1693 dpi 2 layers of printing for the track pattern | 100 μm | 220 μm | 225 V_{RMS} | Droplet not movable across more than one electrode |
| | Hydrophilic PET (hPET) 847 dpi | 200 μm | 200 μm | 75 V_{RMS} | All 16 electrodes at 105 V_{RMS} |
| PP | Melinex® (UV/ozone treated) | 200 μm | 200 μm | 75 V_{RMS} | All 16 electrodes at 120 V_{RMS} |

In **Table 2.9**, two types of voltage performance are reported; one is the minimum voltage required to instigate droplet movement to the next electrode and the other one is the minimum voltage required to move the droplet reliably across at least three electrodes. The assessment was performed by increasing the voltage from 0 V_{RMS} with an increment of 25 V_{RMS} each time until observation of the droplet movement was made.

For silver devices, the HPA paper type has the best performance by successfully actuating a DI water droplet across all 16 electrodes at 105 V_{RMS} . The *silver-on-MRC* device is capable of moving a droplet at a lower voltage, 90 V_{RMS} , but only across 10 electrodes. The *silver-on-PP60* can only move a droplet across five electrodes using 105 V_{RMS} but this device might have a better performance if not for an issue during its fabrication. Some of the contact pads became non-conductive during the process and the problem is discussed in the next section. All of the silver devices are capable of moving droplet across one electrode at 75 V_{RMS} .

The *PP/T20-on-hPET* and *PP-on-Melinex*® devices demonstrated the best performance by reliably actuating a droplet across all 16 electrodes at 105 V_{RMS} and 120 V_{RMS} respectively. These good performances were displayed on both plates fabricated for both types of device, showing promising reliability and reproducibility of the ink and substrate combinations. A DI water droplet was actuated across seven electrodes on the *PP/T20-on-PP60* device while no droplets could be actuated across more than one electrode on the *PP/T20-on-HPA* device. All of the PEDOT:PSS devices were capable of moving the droplet to the next electrode at 75 V except for the *PP/T20-on-HPA* device which required 225 V_{RMS} .

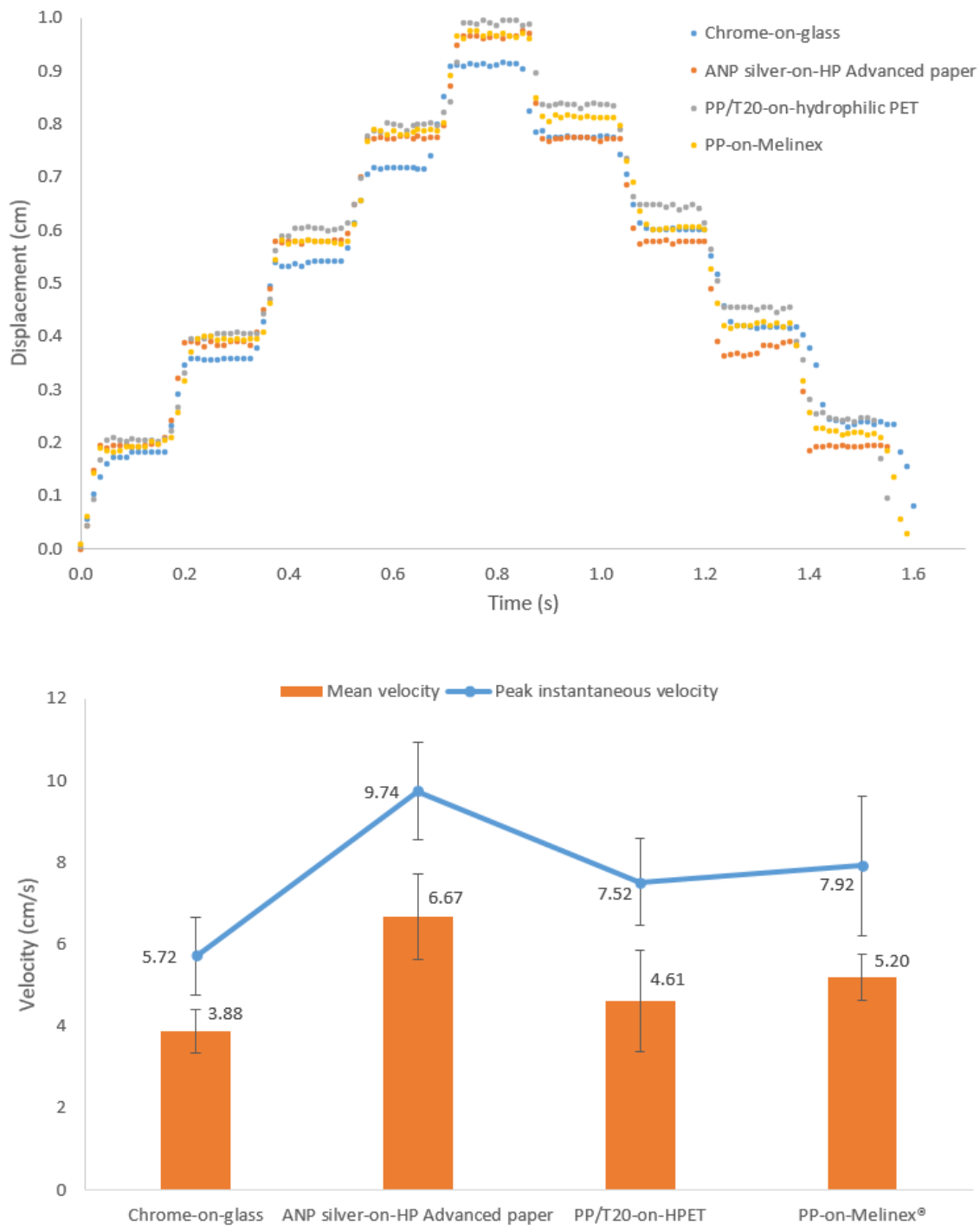


Figure 2.18: The displacement and velocity of water droplets across five electrodes and back to the original position in four EWOD devices. One of the device is a chrome-on-glass device with the electrodes fabricated using photolithography method. The other three are inkjet-printed devices. The water droplets were actuated using 150 V and 100 ms pulse signal.

The displacement and instantaneous velocity of 2.5 μl water droplets moving in the inkjet-printed EWOD devices were analysed by tracking the position of the leading edge of the droplet during transportation. The results are presented in **Figure 2.18** and the reported values are the average of five measurements. Only devices capable of moving a droplet across all 16 electrodes were evaluated: *silver-on-HPA*, *PP/T20-on-hPET*, and *PP-on-Melinex®*. Their performances were compared with a chrome-on-glass device, where the electrodes were fabricated using the standard physical vapour deposition, photolithography and etching methods. The displacement and velocity were assessed traversing five electrodes and returning to the original position. The droplet's movements in all the devices were actuated using a 150 V_{RMS} and 100 ms pulse. The inkjet-printed devices showed a better performance than the chrome-on-glass device by demonstrating a higher instantaneous velocity indicating a lower contact line friction in the inkjet-printed devices. The highest instantaneous velocity was recorded by *silver-on-HPA* device with 9.74 cm/s followed by the *PP-on-Melinex®* device with 7.92 cm/s, the *PP/T20-on-hPET* with 7.52 cm/s, and finally the chrome-on-glass with 5.72 cm/s. As the velocity graphs display, the instantaneous velocity peaked once during each transportation of the droplet between two electrodes. The peak instantaneous velocity occurred during the elongation phase of the droplet during which the leading edge of the droplet displaced the farthest from the previous position. The peak instantaneous velocity for the chrome-on-glass device is consistently the lowest for every single transfer compared to the other devices.

The highest mean velocity was recorded by the *silver-on-HPA* devices with 6.67 cm s^{-1} , followed by the *PP-on-Melinex®* with 5.20 cm/s and the *PP/T20-on-hPET* with 4.61 cm s^{-1} . The mean velocity for the chrome-on-glass device is 3.88 cm s^{-1} . The chrome-on-glass device has a slightly lower mean velocity even though the same

pulse was applied because of the longer distance that droplet have to cover in the inkjet-printed devices. All the devices have the same electrode size with 1.7 mm but the electrode spacing were varied, with the chrome-on-glass having the smallest spacing, 60 μm . The inkjet-printed device nominal spacing were between 100 μm to 200 μm .

2.3.5 Process details and problems encountered during fabrication of EWOD plates

There are some process details that need to be acknowledged during the fabrication of the EWOD plates. One of them has already been mentioned where the *silver-on-PP60* plate's, contact pads became non-conductive after *Cytop*® hydrophobic material was spin coated onto the base plate. The contact pads need to be masked with a PET adhesive tape during the *Cytop*® deposition process to avoid this issue which occurred only on this type of substrate.

All of the paper and polymer substrates need to be held at the edges with glass slides whenever curing on the hot plate is required. This step is especially important for HPA paper as this substrate deformed significantly with the application of heat. For the printing of silver ink on MRC paper, a longer curing time of about ten minutes, more than the suggested 5 minutes by the ink manufacturer is required. Adjacent electrodes will not separate electrically if the ink does not fully dry even though there is no obvious ink connection visually.

Other than the process details mentioned above, there were also some problems and issues encountered during the fabrication process of the EWOD plates. The printing of PP/T20-on-paper plates was very time consuming, taking about six to seven hours just to print one plate because of the low jetting frequency and only one nozzle was being used. The low jetting frequency setting and few number of working

nozzles were employed to increase the precision and accuracy of the printed pattern [153]. In addition, more than one printing pass was needed to pattern the tracks in order to ensure reliable conductivity from the contact pads to all the corresponding electrodes.

While the PP/T20 ink was preferred over the PP ink for the HP printer, this was the opposite for the Fujifilm DMP-2850 printer. With the same rigorous steps applied to both ink cartridges to prevent clogging, they both have the same lifetime of about three weeks. For the PP/T20 ink, after three days of use, it was very difficult to reproduce consistent droplet ejection compared to when the ink cartridge was newly refilled. The droplet ejection of the PP/T20 ink became more unstable (misdirected jets and clogging) with time, which could be due to the precipitation of the glycerol component of the ink. It was possible to agitate the ink inside the cartridge but this would only induce bubble formation which can occlude the nozzles. This was not a problem with the previous HP printer as only a small amount (85 μ l) was filled each time into the cartridge. **Table 2.10** summarises all the problems met during the fabrication process of the inkjet-printed devices.

Table 2.10: Summary of the problems in fabrication of the inkjet-printed EWOD base plates.

| Type of ink | Type of substrate and resolution | Issues and problems encountered during plate fabrication |
|-------------|---|---|
| Silver | PEL P60 1270 dpi | Spin coating of <i>Cytop</i> ® hydrophobic material directly on top of the electrodes made the contact pads non-conductive. |
| | HP Advanced 1270 dpi | The substrate bended significantly during curing on hot plate. |
| | Mitsubishi resin coated paper 1270 dpi | The substrate bended with application of heat. The silver ink dried very slowly on this substrate so it need very long curing time. Electrodes will not separate electrically if the ink does not fully dry even though there is no obvious ink connection visually. |
| PP/T20 | PEL P60 1693 dpi | PEDOT:PSS inks on paper substrates required more than one printing pass to make sure all the tracks were fully connected from the contact pads to all the corresponding electrodes. This increased the printing time significantly as the PEDOT:PSS ink was printed at low jetting frequency, using only one nozzle and very small drop spacing. The PEDOT:PSS cartridge clogged easily and required time consuming maintenance. |
| | HP Advanced 1693 dpi | |
| | Hydrophilic PET 847 dpi | The PEDOT:PSS cartridge clogged easily and required time consuming maintenance. The substrate bended with application of heat |
| PP | <i>Melinex</i> ® 847 dpi | The PEDOT:PSS cartridge clogged easily and require time consuming maintenance. |

2.3.6 Conclusions

The aim of the second section of this chapter was to investigate the feasibility of using Fujifilm Dimatix, a laboratory-grade inkjet printer to pattern EWOD electrodes. In this investigation, the inkjet printing of silver on paper substrate and PEDOT:PSS on polymer substrate have been proven to be a robust and reliable process that have the potential to be widely applied in EWOD device fabrication. The reliability of the printer

to produce fully interconnected narrow tracks is dependent on the printing resolution or spacing of the ink droplets; the smaller the drop spacing, the higher the connectivity between the ink droplets which improves the narrow tracks conductivity. Several types of ink-substrate combination were evaluated and three combinations were found to produce encouraging results for both track conductivity and electrode spacing: *silver-on-HPA*, *PP/T20-on-hPET*, and *PP-on-Melinex®*. EWOD devices fabricated using these combinations are capable of actuating DI water droplets reliably back and forth across 16 electrodes with performance comparable to the standard chrome-on-glass device suggesting their high potential to be used as materials for EWOD substrate and electrodes.

The reliability of the Fujifilm Dimatix printing process is very much influenced by the stability of the ink. The ANP silver ink used in this study has demonstrated consistent jetting quality and easy to control, without any serious clogging problem. The jetting of PEDOT:PSS ink is more difficult to reproduce, making it a bit problematic if a relatively large pattern is required. Problems such as misdirected jets, unmatched drop velocities, and missing nozzles could happen in the middle of printing. To reduce the risk of damaging the pattern during printing, only one nozzle is used for PEDOT:PSS ink.

In this chapter, two types of inkjet printing equipment have been tested, a commercial desktop printer (HP) and a specialised laboratory printer (Fujifilm Dimatix). The laboratory Fujifilm Dimatix printer has the superior performance in terms of spatial resolution in addition to having easier ink management. The use of laboratory inkjet printer such as the Fujifilm Dimatix printer eliminates and minimises some of the problems encountered with the HP desktop printer. One of the most important advantage of using the Fujifilm Dimatix printer is the no loss of layer alignment (if no

processing is required in between printing layers) with multiple printing layers. Even if a process is required in between printing passes, the Dimatix allows easy, precise realignment of the substrate as demonstrated later in **Section 4.2.1.2**. The problem of ink smearing due to printer roller encountered during the HP desktop printer investigation is also eliminated as the Fujifilm Dimatix printer operates by moving the cartridge in two-axis like a 3D printer.

Unlike the desktop printer which only allows the use of a flexible flat substrate, the laboratory printer allows for a wide range of substrate to be printed. Another advantage of using the Fujifilm Dimatix printer is the capability to modify the viscosity and the surface tension of the ink by increasing the temperature of the cartridge. During the HP desktop printer investigation, this was done by changing the formulation of the ink which is more of a trial and error process and also riskier as it could affect the jetting performance of the ink. The fluid-substrate interaction can also be improved by applying heat to the platen using the Fujifilm Dimatix printer. The connectivity of the ink was also very dependent on the substrate plasma treatment in the HP printer investigation. Using the Fujifilm Dimatix printer, the connectivity of ink droplet is still depending on the surface treatment to some extent, particularly the *Melinex*® substrate but mostly it can be done by controlling the drop spacing. The Fujifilm Dimatix printer also allows for accurate realignment of the substrate after removing it for post processing like heat treatment.

While the outcome in this project has shown that the Fujifilm Dimatix printer has a more reliable printing process than the commercial HP desktop printer, Wheeler's Digital Microfluidics group [11, 117] has reported a robust portable EWOD device fabricated using another type of low-cost commercial printer, Epson C88+. This device has successfully performed rubella immunoglobulin assays in a remote setting in

north-western Kenya. The Epson C88+ printer is a piezoelectric desktop printer, capable of producing 55 μm actual electrode spacing and 148 μm actual track width. In comparison with the method used in the current study, the Epson C88+ printer has a maximum printing resolution of 2880 \times 1440 dpi, while the commercial HP printer employed in this thesis has the maximum dpi of 1200 \times 1200. The substrate used for their device was Novele™ IJ-220, a PET transparent film specially engineered to be used with *Metalon*® silver nanoparticle ink that was also employed as the electrode material in their DMF devices [117]. Whilst the use of commercial, low-cost printer such as demonstrated by the Wheeler's group is certainly advantageous to produce simple pattern, using multi-material printer such as the Fujifilm Dimatix has several advantage such as allowing precise alignment of multi-layered ink pattern and being able to print thick, rigid substrate, which can't be processed through a commercial printer.

The proposed inkjet printing method has the advantage of comprising fewer fabrication steps than the photolithography method. The inkjet printing technique combines the material deposition and patterning steps by directly depositing the electrode onto the substrate in the form of the desired pattern. The most important advantage of the inkjet printing method is the lower fabrication cost than the photolithography, as it does not require expensive clean-room equipment. The use of inexpensive substrates (photographic papers and PET films) and conductive polymer, PEDOT:PSS also contribute significantly to the reduction in the EWOD device fabrication cost. Based on the advantages stated above, the Fujifilm Dimatix printer using PEDOT:PSS ink and PET substrate have been chosen as the electrode patterning method and materials for the fabrication of EWOD devices in Chapter 3 and Chapter 4.

3 Off-the-shelf products as alternative low-cost component materials in DMF device

3.1 Introduction

This chapter explores the potential of using readily available consumer products as the alternative to conventional materials for dielectric and hydrophobic components of EWOD device. As discussed previously, there are certain challenges that need to be addressed before DMF technology can become widespread and one of these is the high fabrication cost of DMF devices. A few previous studies [20, 118, 119] have employed off-the-shelf products as the EWOD dielectric and hydrophobic components. Realising the potential of utilising off-the-shelf materials, several products were chosen for a preliminary study of their usability as inexpensive substitutes for EWOD components and the findings are reported in this chapter.

In this preliminary study, only one electrowetting property of the off-the-shelf products was investigated, the contact angle (CA) reversibility of the product surfaces after an electrowetting cycle. The reversibility of a droplet CA on a surface after an electrowetting cycle implies low CA hysteresis [188]. CA hysteresis increases the threshold voltage requirement and decreases the droplet velocity [188]. Furthermore, the CA reversibility also indicates no failure mechanisms such as formation of pin holes or dielectric breakdown occurs in the dielectric and hydrophobic layers [22]. Two component materials of the EWOD device were investigated, namely the dielectric and hydrophobic layers; accordingly, the first two sections in this chapter correspond to the type of component material, the dielectric (**Section 3.2**) and the hydrophobic materials (**Section 3.3**). Only one product, either from the dielectric or hydrophobic investigations, was chosen for detailed investigation based on the result of the

preliminary studies and the results are presented in the final section (**Section 3.4**) in this chapter.

3.2 Preliminary study on dielectric materials

As discussed in detail in **Section 1.4**, the dielectric layer provides the capacitance required to accumulate the electrostatic energy used to actuate a droplet in the EWOD device. Ideally, a promising candidate for an EWOD device's dielectric material should have a high dielectric constant to provide large CA change (based on the Young-Lippmann equation), and high dielectric strength so as to prevent breakdown when high voltage is employed. Parylene polymer has been used extensively as dielectric material in EWOD applications due to its relatively high dielectric constant and good dielectric strength [111].

Other types of dielectric material that have been reported in EWOD devices include *Teflon AF*TM [99, 102], *Cytop*[®] [111], silicon dioxide [92, 99, 102], and PDMS [107, 112]. Some of these materials, including Parylene, are expensive or require high-end laboratory equipment for their deposition process or both, which results in high ultimate production cost. In response to this, several consumer products (**Table 3.1**) are investigated in this section as low-cost substitutes for the conventional materials. In addition to being inexpensive, these materials could imply simpler fabrication methods.

All the products listed in **Table 3.1** are used as a finishing layer that can be applied on wood, metal, plastics, and ceramics to seal and protect the surfaces from external stimuli such as weather, temperature, water, corrosion, and extreme pH. Upon deposition, the substance of the materials begins to dry and harden into a durable layer which provides protection to the surface underneath. Apart from the protection purpose, they are also used to enhance the surface appearance by giving

it for example, a glossy or matt look. Two of these products, *Blackfriar* varnish and *Rust-Oleum® Polyurethane Finish* contain polyurethane (PU), a type of synthetic organic polymer as their main ingredient. PU is widely used as a finishing layer due to its high durability to intensive mechanical wear and its glossy appearance for aesthetic purposes [189].

Table 3.1: List of commercially available dielectric materials for the EWOD investigation.

| Dielectric material | Manufacturer | Application | Components (content %) | Price |
|--|--------------------------------------|---|--|------------------|
| <i>Blackfriar Polyurethane Varnish</i> (BF) | Blackfriar Paints, County Durham, UK | Wooden surfaces | 1. Naphtha (petroleum) hydrotreated heavy (10-25), 2. Distillates (petroleum) hydrotreated light, kerosene – unspecified (10-25), 3. Silicon dioxide (5-10), 4. Cobalt neodecanoate (<1), 5. Ethyl methyl ketoxime (<1) | £24.68 per litre |
| <i>Rust-Oleum® Crystal Clear</i> (RO-CC) | Rust Oleum® Corp., County Durham, UK | Wood, metal, plastics, ceramics, and painted surfaces | 1. Liquefied petroleum gas (10-30), 2. Xylene (10-30), 3. Butane (10-30), 4. Butyl acetate (5-10), 5. Isobutane (5-10), 6. Solvent naphtha light aromatic (1-5), 7. White spirit (1-5), 8. 1,2,4-trimethylbenzene (1-5), 9. Cumene (<1), 10. Mesitylene (<1) | £23.73 per litre |
| <i>Rust-Oleum® Polyurethane Finish</i> (RO-PU) | Rust Oleum® Corp., County Durham, UK | Wood, metal, painted surfaces | NA | £23.73 per litre |

PU is synthesised through the reaction between a di- or polyisocyanate and a di- or polyol [190]. The mechanical properties of PU vary widely depending on, but not limited to, the chemical structure of the reactants used in its synthesis, the degree of polymer cross-linking, and the molecular weight of the polyol [190]. Due to its wide and varied formulations, the dielectric constant of PU can be tailored as required by the desired application, which makes PU a very good candidate as an EWOD component material.

In commercial applications, PU is not normally selected for its dielectric properties. Polyurethane foam however has been used by General Plastics Manufacturing Company, US as the construction material for radomes (environmental protection cover for antennas) due to its low dielectric loss (dissipation of electrical energy through heating when an alternating voltage, the electric field component of an electromagnetic wave in this case, is applied) and its dielectric constant properties as a function of radio frequency [191-193]. Lorenzini et al. [194] have investigated the dielectric constant of several types of PU for application as capacitors, an application with similarities to our requirement. The PU materials were synthesised by reacting five different types of diol with 2,4-toluene diisocyanate with the measured dielectric constants for the fabricated thin film polyurethane (200-400 nm in thickness) ranged between 4.09 and 13.8.

3.2.1 Methodology

For each type of dielectric material, its feasibility as EWOD component was first determined by characterising the CA evolution of a DI water droplet sitting on its surface as a function of applied voltage. If the CA of the water droplet was found to be reversible after voltage application, further investigation was conducted by employing the material in the fabrication of an EWOD plate. The EWOD plate was used to

evaluate whether actual droplet transportation could be demonstrated in a device employing the commercial material. It should be noted, that the investigation conducted in this section does not attempt to measure the dielectric constant and dielectric strength of the proposed commercial dielectric materials as it is not the objective of this investigation to determine the dielectric properties of each of the material but rather to identify which of these materials have the potential for further development as EWOD component material and what can be done to improve their performance.

3.2.1.1 Preparation of dielectric material samples

Three types of commercial dielectric material were investigated in this study: *Blackfriar Polyurethane Varnish* (BF), *Rust-Oleum® Polyurethane Finish* (RO-PU), and *Rust-Oleum® Crystal Clear* (RO-CC). All the dielectric material samples were coated with a *Cytop®* (Asahi Glass Co., Ltd.) hydrophobic surface. The materials are supplied in liquid form inside aerosol cans except for BF which is a varnish in a metal container. The deposition methods used for each material are listed in **Table 3.2**. For each type of surface, two types of sample were prepared: a one-layer sample and two-layer sample in order to study the effect of dielectric thickness on the electrowetting cycle.

All the surfaces prepared for this investigation used silicon wafer (p-type, <100>, 1-10 $\Omega\cdot\text{cm}$) (Pi-Kem Ltd, Staffordshire, UK) as the substrate. The RO-CC and RO-PU materials were deposited onto the substrate using two methods; aerosol spraying which is the suggested method by the manufacturer, and spin coating method. The BF varnish requires an applicator such as a roller or a brush for its deposition. The BF varnish was applied using a rubber squeegee, with the blade size of 15 cm used for car windows cleaning. About 1 ml of the BF varnish was poured onto

the silicon wafer and the squeegee was used to distribute the substance evenly by applying uniform pressure across the surface area. Excess substance was removed and the surface was left to dry at ambient temperature. For the two-layer sample, a second layer was applied after 2 hours of drying. Spin coating was not attempted for the BF varnish as the material is too viscous to produce a thin film desired for electrowetting. The spin coating method however might be compatible with the BF varnish if dilution could be done to the material by adding solvent to it. Due to time limitation, further investigation has not been conducted to experiment with the dilution and spin coating of the BF varnish material.

Table 3.2: Fabrication method for commercial dielectric materials

| Dielectric material | Deposition method suggested by manufacturer | Fabrication technique | Number of layers | Curing time and temperature |
|--|---|-----------------------|------------------|--|
| <i>Blackfriar Polyurethane Varnish (BF)</i> | Brush and roller | Squeegee | 1 and 2 | 24 hours at ambient temperature |
| <i>Rust-Oleum® Polyurethane Finish (RO-PU)</i> | Aerosol spraying | Aerosol spraying | 1 and 2 | 24 hours at ambient temperature |
| | | Spin coating | 1 and 2 | 1 hour on hot plate at temperature of 100 °C |
| <i>Rust-Oleum® Crystal Clear (RO-CC)</i> | Aerosol spraying | Aerosol spraying | 1 and 2 | 24 hours at ambient temperature |
| | | Spin coating | 1 and 2 | 1 hour on hot plate at temperature of 100 °C |

Spin coating of the dielectric materials was performed using a spin coater (LabSpin6, SUSS MicroTec) set to 1500 rpm for 30 s. Afterward, the samples were

cured on hot plate for one hour at 100°C. The spraying method was conducted using standard manufacturer's procedures; the bottle can was shaken vigorously for 1 minute prior to spraying. The nozzle was placed about 30 cm from the surface while spraying was performed by moving the can back and forth in a steady motion. For the two-layer sample, a second layer was applied two minutes after the first layer. The surfaces were left afterward for curing for 24 hours at ambient temperature. After the dielectric layers had completely dried, a layer of Cytop® was spin-coated on top of them at 1500 rpm for 30 s and cured for 30 minutes at 140°C.

3.2.1.2 Contact angle measurements

The measurement of the CA variation with the applied DC voltage was performed using a Theta Lite optical tensiometer (Biolin Scientific, Gothenburg, Sweden). The droplet images were recorded at 1.3 fps and were analysed by *One Attension* software (the Theta Lite system's software). **Figure 3.1** shows the setup used for the CA measurement. A positive bias was applied via a platinum wire to a 20 µl of DI water droplet sitting on the dielectric sample coated with *Cytop*® implemented on a silicon substrate.

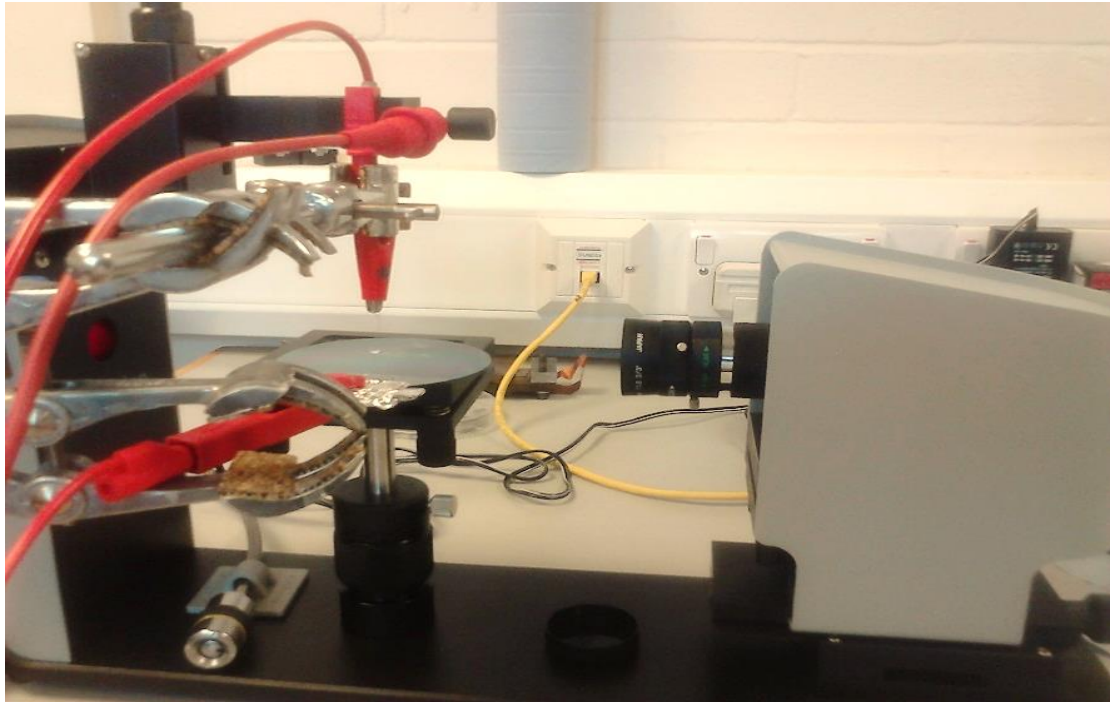


Figure 3.1: *Experimental set up for the CA measurement using optical tensiometer. The droplet was connected to the positive output terminal of the power supply via a wire while the silicon wafer was connected to the negative output terminal.*

The voltage was varied between 0 V and 250 V using a DC power supply (Digimess) and the CA change was identified at three important levels: the initial CA at 0 V, the CA at a maximum voltage of 250 V, and the final CA when the voltage was returned to zero. The voltage was increased to the maximum voltage of 250 V in approximately 20 seconds and left at the maximum level for about 10 seconds before returning to the initial value. It took 45 seconds for the voltage to return to zero voltage. The duration of one hysteresis cycle (from 0 V to maximum value and back to 0 V) was 75 seconds. The hysteresis cycle was repeated a minimum of three times ($n=3$) for each sample. Every run was performed with a fresh droplet on a different surface location.

3.2.1.3 Surface characterisation

The same samples as the ones used for the CA measurements were used for the surface characterisation. The dielectric layer's thickness and surface roughness were evaluated using the stylus surface profilometer, AlphaStep® D-500 (KLA Tencor, California, US).

3.2.1.4 Design and fabrication of EWOD plates and actuation of DI water droplet

To further investigate the feasibility of the commercial products as potential EWOD device components, EWOD plates employing these materials as dielectric layers were fabricated for demonstration of linear droplet transportation. The parallel-plate configuration (**Figure 1.5**) was used in this investigation. The design of the EWOD plates comprises three rows of 16 electrodes array as shown in **Figure 3.2**. The nominal size of each square electrode is 1.7 mm with 200 μm nominal inter-electrode spacing. As a reminder, the nominal size is defined as the size of the electrode or pattern in the CAD file, not the measured size of the inkjet-printed electrode. The electrodes of the plates were made of PEDOT:PSS ink (Sigma Aldrich, St. Louis, US) patterned on a hydrophilic polyethylene terephthalate (PET) substrate using inkjet printing technique (Fujifilm Dimatix DMP-2850). The inkjet printing method employed to pattern the electrodes is similar to the one discussed in **Section 2.3.1**.

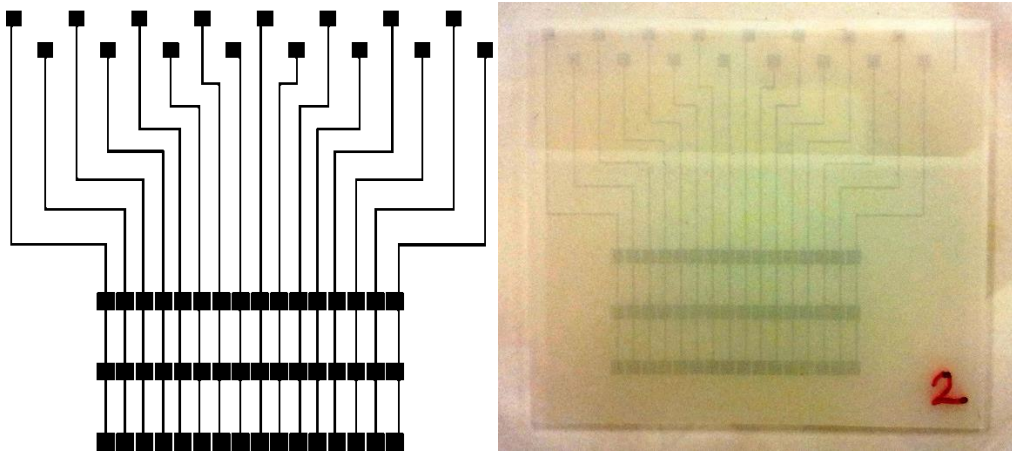


Figure 3.2: The design of electrode pattern for the EWOD plates comprises three rows of 16 square electrodes, 1.7 mm in nominal size with 200 μm nominal inter-electrode spacing (left), and the actual inkjet-printed plate made of PEDOT:PSS electrode on PET substrate (right).

For each dielectric surface that demonstrated suitable electrowetting performance, two actuation plates were prepared using an identical deposition method as per during the preparation of the CA measurements samples. EWOD plates employing conventional Parylene-C (Specialty Coating Systems) were also fabricated for comparison purpose. The Parylene-C deposition method has been described in detail in **Section 2.2.1.7**. The thickness of the Parylene-C dielectric layer was $\sim 3.2 \mu\text{m}$. The cover plate (ITO-coated glass slide, Diamond Coatings, West Midlands, UK), the gap between the base and cover plates, the drive electronics, and the PMMA frame to hold the EWOD securely in place are similar to the ones described in **Section 2.2.1.6**.

3.2.2 Contact angle measurements

All but one of the prepared samples exhibited hydrophobicity with initial CA of more than 90° for DI water droplet (**Table 3.3**). The one surface that has CA less than 90° was the spin-coated RO-CC surface with CA of 88.66° . This surface possibly needed more than one layer of *Cytop*[®] to produce CA larger than 90° . For the electrowetting

hysteresis measurement, the same sample was used despite the low initial CA since number of *Cytop*® layers is one of the control variables in the experiment. The highest CA is demonstrated by the two-layer BF and the one-layer spray-coated RO-CC surfaces with CA of 112°. For spray-coated surfaces, the one-layer samples always have higher CAs than the two-layer samples.

For all types of dielectric material, the two-layer samples have a higher thickness than the one-layer sample. The measured thicknesses of the BF surfaces are 0.53 μm and 8.96 μm for one layer and two layers respectively. The very large difference in the thickness between the two-layer and one-layer samples is believed to be due to the change in the surface roughness of the sample after the first application of the BF material onto the silicon wafer. The single-coated BF average surface roughness is $0.15 \pm 0.03 \mu\text{m}$ while the silicon wafer surface is very smooth with average roughness of $0.054 \pm 0.007 \mu\text{m}$. The first coating was much thinner as the BF material flows easily on the smooth silicon wafer surface and it was easier to remove the excessive material using the squeegee. For the two-layer sample, the distribution of the material on the surface after the first layer was dried was not as smooth as the first time as the surface has now become coarser. For both the RO-CC and RO-PU materials, the spin-coated samples have the lower thickness than the spray-coated samples regardless of the number of spray coating layer.

Table 3.3: Initial CA, electrowetting hysteresis, and average thickness of the dielectric materials samples

| Dielectric material | Number of coating & fabrication technique | Initial CA at 0 V (°) | Lowest CA at 250 V (°) | Final CA back at 0 V (°) | Electrowetting hysteresis (°) | Electrowetting number at 150 V | Average thickness (µm) |
|--|--|------------------------------|-------------------------------|---------------------------------|--------------------------------------|---------------------------------------|-------------------------------|
| <i>Blackfriar Polyurethane varnish</i> (BF) | 1-layer squeegee | 107 ± 3 | 78 ± 3 | 78 ± 2 | Irreversible | - | 0.5 ± 0.2 |
| | 2-layer squeegee | 112 ± 2 | 64 ± 5 | 108 ± 5 | 4 ± 5 | 0.49 | 9 ± 1 |
| <i>Rust Oleum® Crystal Clear</i> (RO-CC) | 1-layer spray-coated | 112 ± 1 | 70 ± 3 | 105 ± 4 | 6 ± 4 | 0.38 | 26 ± 4 |
| | 2-layer spray-coated | 106 ± 2 | 89 ± 3 | 100 ± 1 | 7 ± 2 | 0.09 | 56 ± 7 |
| | 1-layer spin-coated | 88.7 ± 0.8 | 69.3 ± 0.6 | 69.3 ± 0.2 | Irreversible | - | 4.6 ± 0.3 |
| <i>Rust Oleum® Polyurethane Finish</i> (RO-PU) | 1-layer spray-coated | 110.3 ± 0.9 | 70 ± 2 | 86 ± 4 | 25 ± 3 | 0.39 | 40 ± 10 |
| | 2-layer spray-coated | 105 ± 2 | 79 ± 5 | 97 ± 2 | 7.1 ± 0.8 | 0.08 | 71 ± 3 |
| | 1-layer spin-coated | 105 ± 2 | 98 ± 1 | 98 ± 1 | Irreversible | - | 1.83 ± 0.03 |

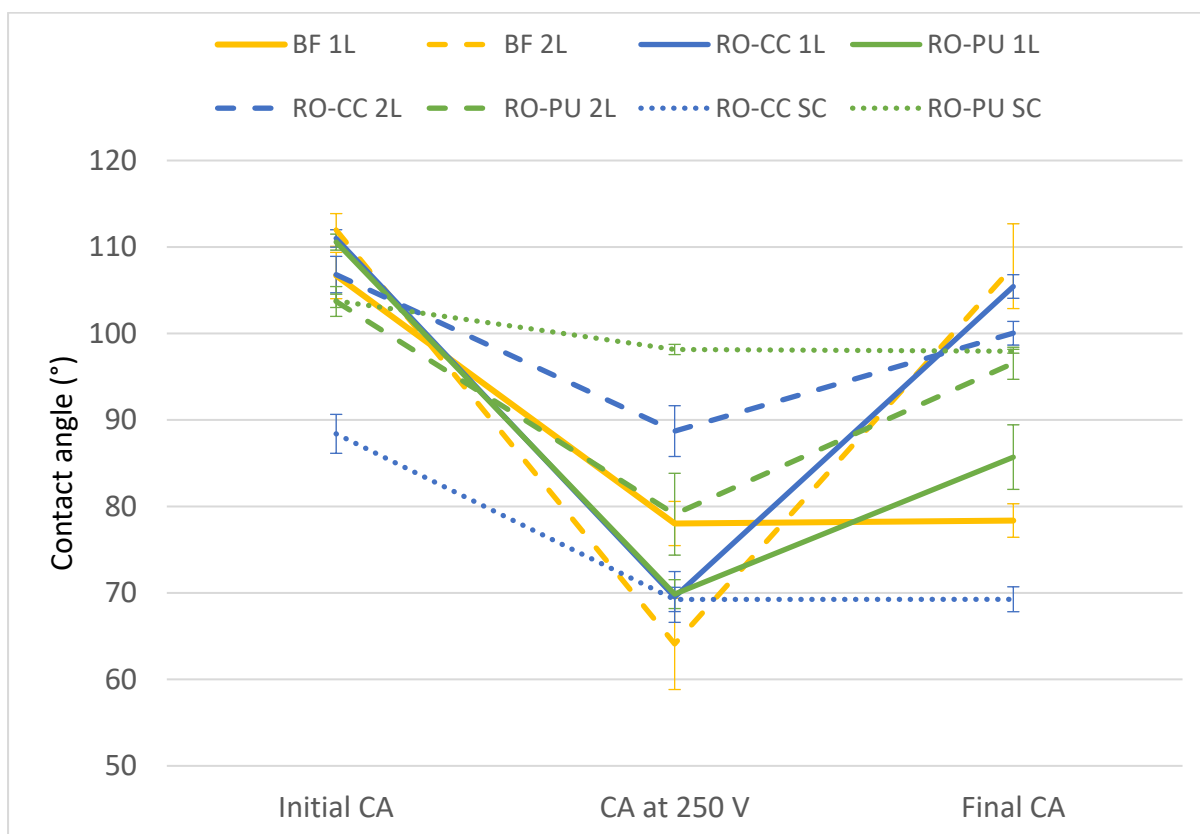


Figure 3.3: The electrowetting behaviour of the BF (yellow lines), RO-CC (blue lines), and RO-PU (green lines) dielectric materials. The solid lines represent the one-layer squeegee and spray-coated samples of the BF and both RO-CC and RO-PU materials respectively. The dashed lines represent the two-layer squeegee and spray-coated samples of the BF and both RO-CC and RO-PU materials respectively. The small dotted lines represent the spin-coated samples which underwent electrolysis once voltage is applied across the droplet.

During the electrowetting cycle, CA at three voltage levels were recorded; the initial CA when the DC voltage was 0 V, the lowest CA which occurred at 250 V, and the final CA when the DC voltage was returned to 0 V. All three dielectric materials have demonstrated CA reversibility after voltage application of 250 V depending on their deposition method (**Table 3.3**). **Figure 3.3** shows the electrowetting performance of the BF material samples. The two-layer BF varnish sample demonstrates CA reversibility with a low hysteresis of 4° and a wide range of CA modulation with 48°.

These results are comparable to the more conventional dielectric material, Parylene-C with 3.2 μm thickness employing the same *Cytop*® hydrophobic surface described in **Section 3.4.3**. The one-layer BF varnish however fails to display the same reversibility; it is believed that the insulating layer underwent failure due to the presence of pinholes in the dielectric layer. Bubbles formation can be observed due to electrolysis as electric current pass through the DI water droplet (**Figure 3.4**).

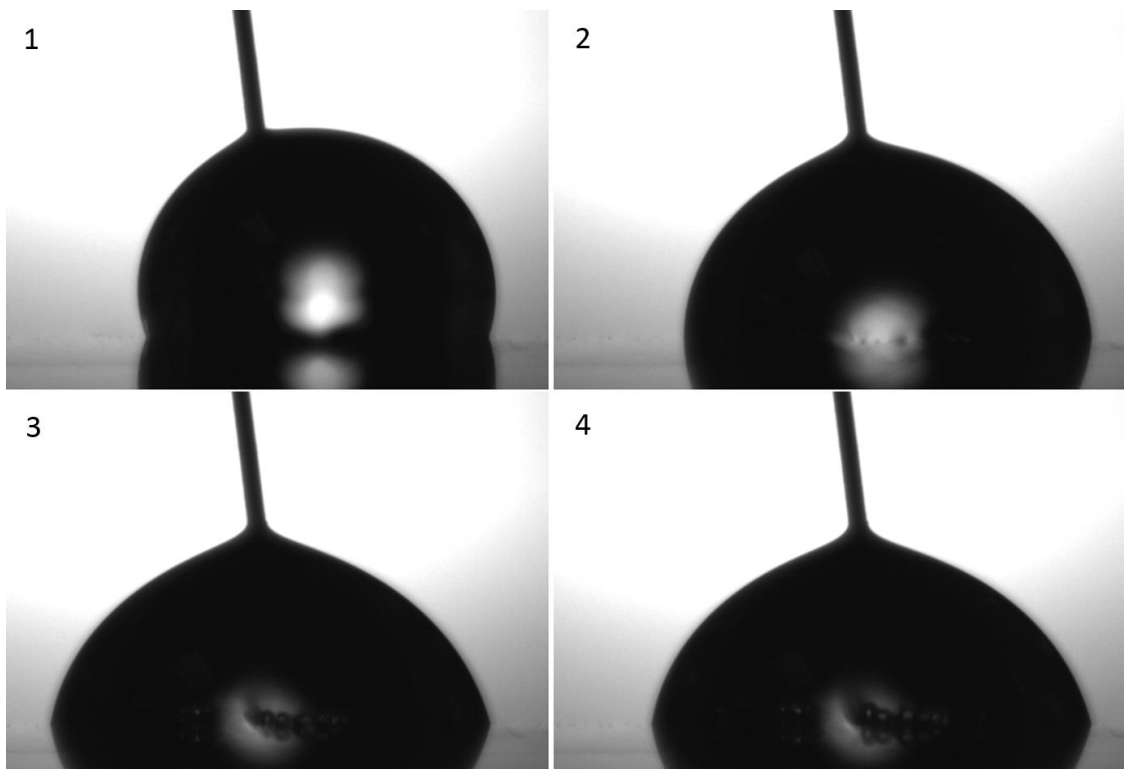


Figure 3.4: Bubble formation due to dielectric layer failure in one-layer Blackfriar varnish sample. The first figure shows the initial condition of a DI water droplet before any voltage was applied. In the second figure, tiny bubbles started to form during the voltage application. The relatively thin insulating layer of the BF sample underwent breakdown, causing electrolysis of the water as current ran through it. The third and the fourth figures illustrate the bubbles progressive formation as the voltage was increased to the maximum value of 250 V.

Figure 3.3 also shows the electrowetting behaviour of the dielectric materials other than the BF varnish. The one-layer RO-CC has the best electrowetting

reversibility performance out of all the spray-coated surfaces with low hysteresis of 6° and achieving the lowest CA with 70° occurring during the 250 V maximum DC voltage. The two-layer RO-CC also has quite a low hysteresis with 7° but the CA modulation is narrower than the one-layer with 89° being the lowest CA reached at maximum DC voltage. The narrower CA modulation is due to the thicker insulating layer for the two-layer RO-CC with 56 μm compared to 26 μm for the one-layer sample.

Similar to the spray-coated RO-CC samples, the spray-coated RO-PU samples also exhibit reversibility on both the one-layer and two-layer surfaces albeit with higher hysteresis especially for the one-layer sample (25°). In contrast with the spray-coated surfaces, both the spin coated RO-CC and RO-PU surfaces do not exhibit electrowetting reversibility. The spin-coated samples of both RO-CC and RO-PU have pinhole defects in the dielectric layers causing bubbles generation during the electrowetting cycle. For all types of materials, several successive spin-coated layers or another deposition method that can produce a thicker dielectric layer would be desirable to prevent failure probably due to pinholes or dielectric layer breakdown. However the layer should not be too thick so that the electrowetting performance and the voltage requirement for EWOD are affected.

The electrowetting number $\left(\frac{\epsilon_0 \epsilon_r}{2 \gamma_{lg} d} V^2\right)$ at 150 V was calculated for all the surfaces with electrowetting reversibility and the results are shown in **Table 3.3**. This dimensionless number, which originated from the Young-Lippmann equation is used as an indicator of the efficiency of the electrowetting mechanism at the respected DC voltage level. Based on the calculated values, two-layer RO-PU is the least efficient at 150 V with the lowest electrowetting number of 0.08 followed by two-layer RO-CC with

0.09. The two-layer BF surface has the highest number with 0.49, while one-layer RO-PU and one-layer RO-CC numbers are 0.39 and 0.38 respectively.

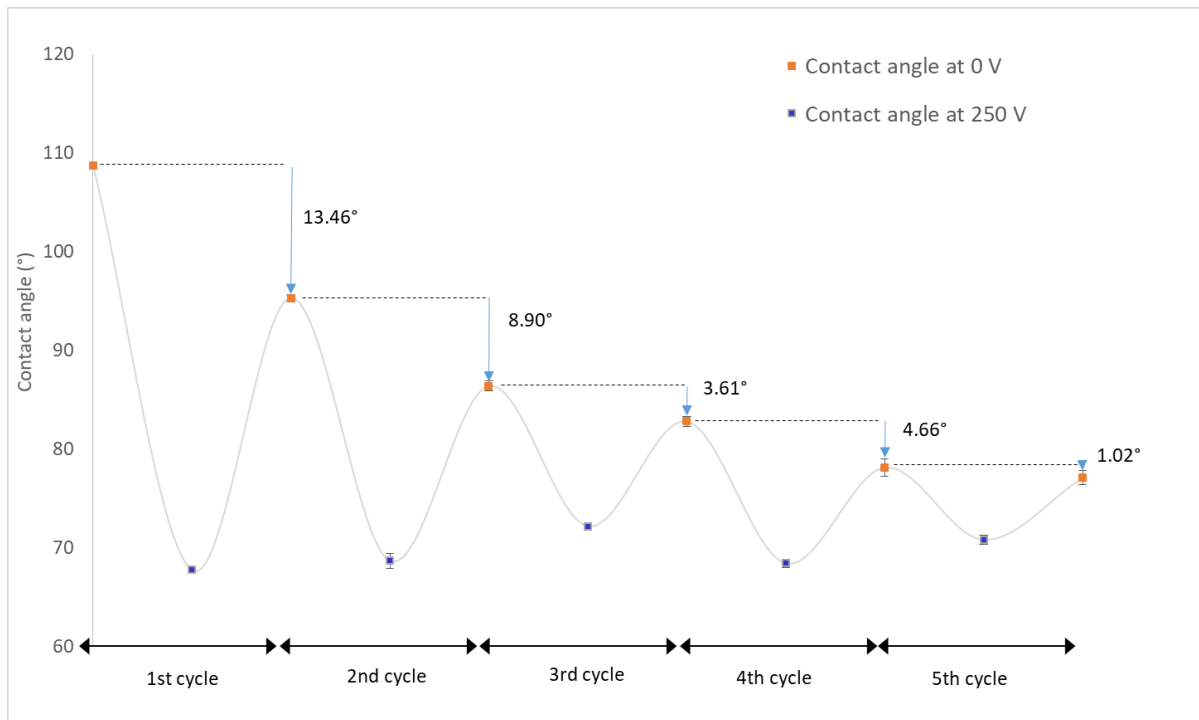


Figure 3.5: Evolution of contact angle of one-layer spray-coated RO-PU during repeated cycle of electrowetting.

The CA measurement for the one-layer RO-PU surface with repeated electrowetting cycles of five times was presented in **Figure 3.5**. As can be seen from the figure, the CA at 0 V after completing a cycle decreases after each cycle. After the fifth cycle, the initial CA of 109° reduced to 77°. The hysteresis (the difference in CA at the start of new cycle with the value in the previous cycle) decreases as the repetition of electrowetting progresses. The CA modulation also decreases as the repetition increases with only about 7° change in CA was induced during the 5th cycle. The CA at 250 V for each cycles were fairly constant with values ranged between 68° to 71°.

3.2.3 Droplet actuation

The three types of dielectric surfaces that have shown electrowetting reversibility were selected as the dielectric component in the fabrication of EWOD plates for droplet transportation. The surfaces are: one-layer spray-coated RO-CC, one-layer spray-coated RO-PU, and two-layer BF applied using squeegee. Two plates were fabricated for each type of surface. EWOD plates employing conventional dielectric material, Parylene-C were also fabricated as a reference.

For the RO-PU material, one-layer sample was chosen for fabrication despite having the higher hysteresis than the two-layer sample as the one-layer has the higher efficiency of electrowetting at 150 V (higher electrowetting number) than the two-layer surface. The two-layer sample generated only 6° change in CA compared to 22° for the one-layer sample. Another reason to use one-layer RO-PU instead of the two-layer is the inconsistency of the spraying technique which make it difficult to produce uniform and consistent thicknesses each time. It is safer to apply only one layer just in case a thicker layer might have been deposited if two spray coating is applied thus increasing the operating voltage requirement beyond 225 V_{RMS} . The operating voltage for the demonstration of droplet actuation is limited to maximum voltage of 225 V_{RMS} .

Table 3.4: Droplet transportation performance of EWOD plates with difference types of dielectric layer

| Dielectric material | Number of fabricated plate and observations | Voltage to instigate droplet movement to the next electrode | Lowest voltage for reliable actuation across three or more electrodes (minimum of 3 cycles of back and forth) |
|--|---|---|---|
| Parylene-C | 2 – Both capable of moving droplet | 75 V _{RMS} | All 16 electrodes at 105 V _{RMS} |
| Blackfriar polyurethane varnish (two-layer squeegee applied) | 2 – Both plates not functional | - | - |
| Rust-Oleum® Crystal Clear (one-layer spray-coated) | 2 – Only one functional plate | 150 V _{RMS} | 4 electrodes at 180 V _{RMS} |
| Rust-Oleum® Polyurethane Finish (one-layer spray-coated) | 2 – Both capable of moving droplet. | 150 V _{RMS} | 3 electrodes at 165 V _{RMS} and 8 electrodes at 180 V _{RMS} |

Table 3.4 summarises the results of linear droplet actuation in the EWOD devices employing different types of dielectric material. The lowest voltage for reliable actuation across three or more electrodes, back and forth for minimum of three cycles, was identified for each type of device. Both the Parylene-C devices are capable of actuating droplets across all of their 16 electrodes. A minimum actuation voltage of 75 V_{RMS} is required to initiate droplet movement to the next electrode while 105 V_{RMS} is required to actuate the droplet across all 16 electrodes reliably. Out of the three types of device fabricated using the commercial dielectric materials, only BF devices are not capable of demonstrating any sort of droplet movement across their electrodes.

The RO-PU plates have the best performance amongst the commercial dielectric plates. Reliable droplet actuation across eight electrodes at 180 V was

achieved in one of the RO-PU plates. The RO-CC are capable of moving a droplet across four electrodes at $180 V_{RMS}$ and $225 V_{RMS}$. The main problem with all the commercial dielectric plates is layer thickness non-uniformity causing varying voltage requirement to actuate the droplet across the plate surface. The non-functional area on the plates could be due to the layer being too thick, thus requiring a higher voltage to actuate the droplet. Additionally, there is still a chance that defects could occur on the inkjet-printed plates even though particular care has been taken throughout the printing process.

3.2.4 Conclusions

The aim of this investigation is to study the potential of using commercial products as dielectric component in EWOD devices. Three products have been identified and their feasibility was initially investigated by evaluating the electrowetting reversibility of these dielectrics. The results of the investigation have implied that the key to the commercial dielectric layer electrowetting reversibility is the material together with its deposition method. Electrowetting reversibility is highly influenced by the thickness of the dielectric layer which in turn depends on the method used to deposit the dielectric materials. A thicker layer is desired to avoid failure due to pinholes which cause electrolysis of the droplet when voltage is applied. However, the thickness should not be too thick or it will affect the EWOD performance by increasing the voltage requirement to induce CA change [99, 102].

The dielectric materials with a deposition method that produced good reversibility were investigated further to evaluate their capability of moving droplets across electrodes as part of an EWOD device. All three materials have shown potential to be used as dielectric component in EWOD devices but future investigations are necessary to determine the dielectric strength of each material. If the intention is to

employ this material as a reliable and robust component in EWOD application, it is imperative to know the breakdown voltage and the corresponding dielectric thickness of a dielectric material before the full incorporation can happen. It should be noted that the investigation conducted in this section does not attempt to measure the dielectric constant and dielectric strength of the proposed commercial dielectric materials. It is not the objective of this investigation to determine the dielectric properties of each of the materials but rather to identify which of these materials have the potential for further development as EWOD component material and what can be done to improve their performance.

Another significant challenge in using commercial materials is to find a deposition technique that can produce homogenous layer of uniform thickness across the substrate. Manual techniques such as spraying and squeegee rely on the operator's skills to produce good quality surfaces. It is difficult to control the amount of substance applied to the substrate in both the aerosol spraying and squeegee methods. For the spraying method, the amount of substance deposited onto the substrate depends on how much pressure is applied to the button and how long the button is pushed. For the BF varnish material, the thickness depends on how much pressure is applied to flatten the surface and remove the excess material using the squeegee.

To minimise the variance in the amount of material deposited between the different types of dielectric materials when spray-coated, a trial or practise run was conducted first to familiarise the operator with the spraying method. The same practise run was applied for the squeegee method to attempt consistent thickness across the sample surface. It is favourable if these materials can be adapted to a more reliable and robust method using equipment such as spin coater to reduce error causes by

human operator. Spin coating method is a good option to produce homogenous and uniform dielectric layer. Apart from that, the use of automated spray coating method [195] can eliminate the dependency on the operator's skill to produce a layer with uniform thickness. For future investigation beyond this preliminary study, it is suggested that the spin coating method is employed again for the RO-PU and RO-CC materials but with more than one deposition layer to produce a higher thickness to prevent failure due to pinholes formation or breakdown of the dielectric layer.

Many studies have been conducted previously to find the best material for EWOD dielectric layer. While some materials might have high dielectric constant, for example, aluminium oxide (9.5) [114] and tantalum pentoxide (20-25) [115, 116], the fabrication process however requires expensive equipment and the process is very time consuming. Some studies attempt to overcome this by using low-cost material such as SU-8 [15, 113] and PDMS [107, 112]. These materials however pose another challenge which is the formation of pinholes in the layer [22]. Cheap commercial materials such as *Saran*[™] wrap [20] and parafilm [118] have also been employed in some devices but their robustness and reliability have not been proven yet. As reported previously, Parylene-C is relatively inexpensive when compared to some of the other dielectric materials (e.g. tantalum pentoxide, barium strontium titanate) while having a very reliable electrowetting performance, e.g. low hysteresis and high CA modulation [111]. Since no satisfactory material has been identified from this investigation, Parylene-C will be used for the rest of the study presented in this thesis.

3.3 Preliminary study on superhydrophobic and hydrophobic materials

As discussed in detail in **Section 1.5** hydrophobic material functions as both insulating layer and actuating surface in EWOD device application. A good candidate for actuating surface in EWOD device needs to have high hydrophobicity which is defined

by the CA of a water droplet sitting on the surface. As a reminder, a surface is considered hydrophobic if the CA is more than 90° and superhydrophobic if the CA is more than 150° [78]. Eight commercial superhydrophobic and hydrophobic products have been selected as listed in **Table 3.5**.

Table 3.5: List of superhydrophobic and hydrophobic materials.

| Super hydrophobic/hydrophobic material | Manufacturer | Application | Deposition method suggested by manufacturer | Components (Weight %) | Price |
|--|---|---|---|---|--------------------|
| <i>crep protect</i> (CP) | Crep protect, UK | Shoes (suede, nubuck, canvas) | Aerosol spraying | NA | £49.95 – per litre |
| <i>Drywired®</i> Defense Super Hydrophobic Spray (DW-SH) | Drywired®, Los Angeles, California, USA | Satellite dishes, radars, radomes, ground microwave systems, antennae, wind farms | Aerosol spraying | Solvent naphtha (petroleum, light aliphatic, 0-75), naphtha (petroleum, hydrotreated light, 0-75), fluorocarbons (15), propane (10) | £156 – per litre |
| <i>Drywired®</i> 101X A4 series liquid nanocoating (DW-A4) | Drywired®, Los Angeles, California, USA | Fluidic components, medical devices, electronic circuit | Dip/Spray/Roll | Methyl nonafluoroisobutyl ether (35-50), methyl nonafluorobutyl ether (35-50), fluoroacrylate (0.1-30) | £166 – per litre |
| <i>Drywired®</i> 101X 6 series liquid nanocoating (DW-6) | Drywired®, Los Angeles, California, USA | Fluidic components, medical devices, electronic circuit | Dip/Spray/Roll | Methyl nonafluoroisobutyl ether (35-50), methyl nonafluorobutyl ether (35-50), fluoroacrylate (0.1-30) | £739 – per litre |
| G5 water repellent coating (G5) | Gtechniq Ltd, Towcester, UK | Glass and perspex | Cloth wiping, spin coating, spraying | NA | £99.80 – per litre |
| <i>Nanotol</i> (NT) | CeNano GmbH & Co. KG, Dorfen, Germany | Automobile, glass, plastic, metal, marble, leather, wood | Spraying | NA | £107 – per litre |
| <i>NeverWet®</i> top coating (TNW) | Rust-Oleum® Corporation, Illinois, USA | Metal, concrete, wood surfaces | Aerosol spraying | Top coat: Acetone (75), LPG (25), silicones & siloxanes, dimethyl-, reaction product with silica (5) | £29.30 – per litre |
| <i>Rain-X®</i> (RX) | ITW Global Brands, Texas, USA | Glass, plastic | Aerosol spraying, spraying, cloth wiping | Ethanol (30-60), acetone (10-30), isopropanol (10-30) | £34.95 – per litre |

*NA – not available

Two superhydrophobic materials were investigated, the *Drywired®* superhydrophobic (DW-SH) and *NeverWet®* top coating (TNW) sprays. The *NeverWet®* product is comprised of two coating materials: a base coat and a top coat,

but for this preliminary study only the top coat spray will be applied as the actuating surface. The DW-SH is used to protect radio communication devices such as satellite dishes and antennas while the TNW can be applied to many types surfaces such as metal, concrete, and wood among others. Two of the hydrophobic materials from the same manufacturer as DW-SH, *Drywired*® 101X A4 series (DW-A4) and *Drywired*® 101X 6 series (DW-6) are applied in fluidic components and electronic circuit as protective layer. The other three materials: *Nanotol* (NT), *Rain-X*® (RX), and G5 coating (G5) are used on glass surfaces as water repellent. Another product, *crep protect* (CP) is marketed specifically as a footwear protection spray.

All of these products contain chemical compounds such as hydrocarbons which are non-polar molecules that repel water (a polar molecule) to produce the surface's hydrophobicity [196]. In hydrocarbons, dispersion interactions (between induced dipoles and instantaneous dipoles), which is a type of Van Der Waals forces, dominate the molecules interaction. Water on the other hand interacts by forming hydrogen bonds [197, 198]. When a hydrocarbon containing surface is in contact with the water molecules, it disrupts the network of water hydrogen bonds due to its disability to form new bonds with the hydrogen molecules. The water molecules reorient tangentially to the hydrocarbon surface to maximise the hydrogen bonds between the molecules which forms a 'cage'-like structure around the hydrocarbon surface. This phenomenon is the cause of the hydrophobicity effect in hydrocarbon molecules when in contact with water molecules [197, 198]. For the DW-SH and TNW superhydrophobic products, other elements such as fluorocarbon nanoparticles are incorporated to make them superhydrophobic. The nanoparticles' function is to introduce nanostructures to the surface, which reduce the contact area between the water droplet and the surface, thus increasing the droplet CA.

3.3.1 Methodology

Similarly to the investigation on the commercial dielectric materials, the utility of these superhydrophobic/hydrophobic (SH/H) materials as EWOD device materials was first evaluated by measuring the CA change with applied voltage. Once the electrowetting reversibility of these surfaces was established, the ones displaying good CA reversibility were then used to fabricate EWOD plates to test their capability to actuate a droplet.

3.3.1.1 Preparation of the superhydrophobic/hydrophobic surfaces

Silicon wafers were used as the substrate for the SH/H samples prepared for the evaluation of the surface electrowetting reversibility. The eight SH/H materials and the methods used for their deposition are listed **Table 3.6**. All of the products are supplied as solutions except for DW-SH, TNW and CP which are contained inside an aerosol can. Before the deposition of the SH/H materials, a $\sim 3.2 \mu\text{m}$ layer of dielectric material, Parylene-C, was deposited onto the substrate.

Table 3.6: Deposition method for the commercial superhydrophobic and hydrophobic materials.

| Superhydrophobic/hydrophobic materials | Deposition method suggested by the manufacturer | Deposition method | Curing time and temperature |
|--|---|-------------------------------|-----------------------------|
| <i>crep protect</i> (CP) | Aerosol spray | Spin coating | 100 °C for 15 minutes |
| <i>Drywired</i> ® 101X A4 series (DW-A4) | Dip, spray, spin, flow, or syringe coat | Spin coating | 60 °C for 10 minutes |
| <i>Drywired</i> ® 101X 6 series (DW-6) | Dip, spray, spin, flow, or syringe coat | Spin coating | 60 °C for 10 minutes |
| <i>Drywired</i> ® superhydrophobic (DW-SH) | Aerosol spray – two coatings | Aerosol spray - two coatings | Left to rest for 2 hours |
| G5 water repellent (G5) | Wipe using cloth | Spin coat Wipe using cloth | 100 °C for 15 minutes |
| <i>Nanotol</i> (NT) | Wipe using cloth | Spin coating | 100 °C for 15 minutes |
| <i>NeverWet</i> ® top coat (TNW) | Aerosol spray – two coatings | Aerosol spray – two coatings | Left to rest for 2 hours |
| <i>Rain-X</i> ® (RX) | Wipe using cloth | Spin coating | 100 °C for 15 minutes |

To ensure homogeneity and uniformity of the SH/H layer thicknesses, most of the materials were deposited using spin coater set to 1500 rpm for 30 s. The spin-coating method however was found to be an unsuitable deposition method for the superhydrophobic materials. The spin coating techniques employed for the volatile superhydrophobic solution produce different microstructure from the spray-coated surface as can be seen in **Figure 3.6**. The spin-coated surface displays congregation of the nanoparticles in the solution into striations or ridge-like structures in the size range of hundreds of microns oriented in the radial direction. It has been proposed that striations formed during spin coating of a volatile solution were due to depletion of the substance thickness at the surface caused by solvent evaporation [199]. The viscous forces opposing the flow of the solution due to the rotational motion of the substrate increase as the solution-layer becomes thinner during the spin coating process. The spray-coated surface meanwhile present a homogenous distribution of microstructures. Due to this reason, spin coating was not used as the deposition

method for the superhydrophobic materials and only one method of deposition was applied, the spraying method.

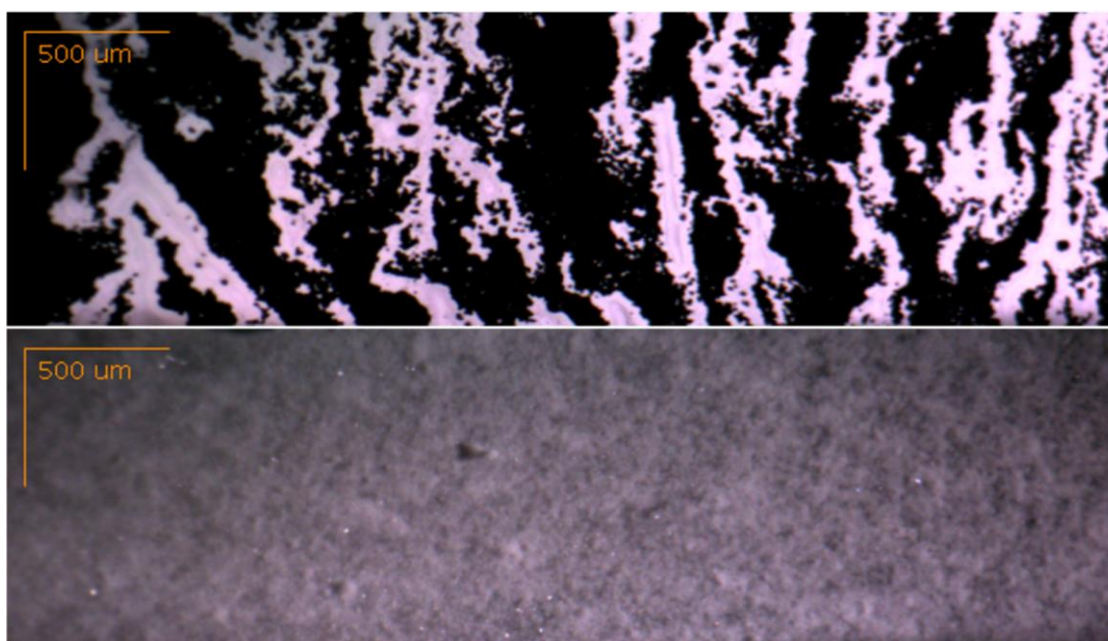


Figure 3.6: *Different in microstructures between the spin-coated (above) and spray-coated (below) for Drywired® superhydrophobic material. Striations can be seen in the spin-coated surface due to solvent evaporation of the volatile superhydrophobic solution while the spray-coated surface exhibits a more homogenous microstructure.*

Apart from the spin coating method, another technique was employed with the G5 product, wiping using a cloth which is the method suggested by the manufacturer. A lint-free cloth was used to apply the G5 material on to the substrate in a circular motion. For the spin-coated samples, the samples were dried on a hot plate for 15 minutes at 100 °C to remove any excess aqueous solution, if no curing instructions were given by the manufacturer. The DW-A4 and DW-6 samples were cured 10 minutes at temperature of 60 °C as specified by the manufacturer. For the spray-coated DW-SH and TNW samples, the aerosol can was shaken vigorously for 1 minute prior to spraying. The nozzle was placed about 30 cm from the surface while spraying was performed by moving the can back and forth in a steady motion. The

second layer was applied two minutes after application of the first layer. The samples were then left for drying at ambient temperature for two hours.

3.3.1.2 Contact angle measurements

The electrowetting behaviour of the SH/H materials was investigated by evaluating the CA changes of a DI water droplet using an optical tensiometer when 250 V DC voltage was applied to the droplet. The droplet images were recorded at 1.3 fps and were analysed by One Attension software. The setup used for the CA measurement was the same as described in **Section 3.2.1.2**.

3.3.1.3 Surface characterisation

The samples used for the CA measurements were also used for the characterisation of their surfaces. The SH/H layer thickness and surface roughness were evaluated using a stylus surface profilometer, *AlphaStep® D-500* (KLA Tencor).

3.3.1.4 Design and fabrication of EWOD plates and actuation of water droplets

To further validate the feasibility of the SH/H materials as EWOD device components, EWOD plates employing these materials as their actuating surface were fabricated for demonstration of linear droplet transportation. The parallel-plate configuration was used in this investigation. The design of the EWOD plates comprises three rows of 16 electrodes array as shown in **Figure 3.7**. The nominal size of each square electrode is 1.7 mm with a 200 μm nominal inter-electrode spacing. The electrodes of the plates were made of PEDOT:PSS ink patterned on hydrophilic PET substrate using Fujifilm Dimatix inkjet printing technique. The full description of the inkjet printing method used for the electrode patterning is available in **Section 2.3.1**.

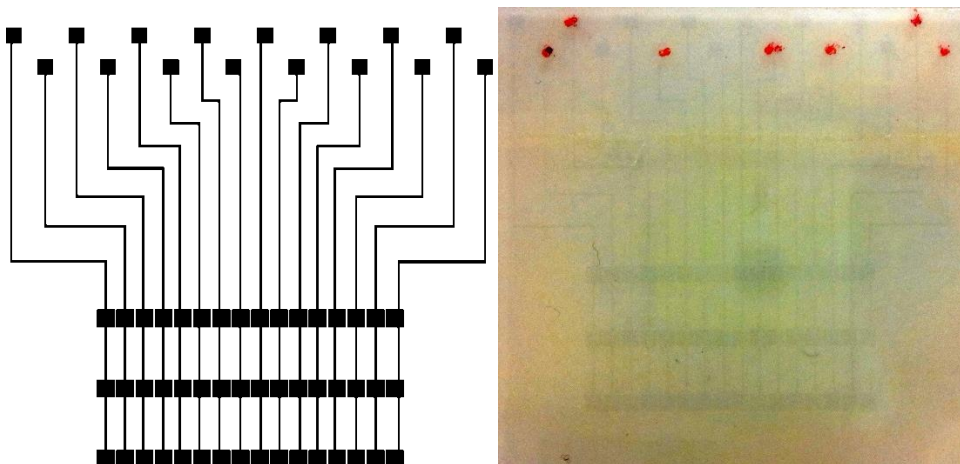


Figure 3.7: The EWOD plate employing superhydrophobic/hydrophobic materials for the evaluation of droplet transportation. The electrode design pattern comprising three rows of 16 square electrodes, 1.7 mm in nominal size with 200 μm nominal inter-electrode gap (left), and the actual inkjet-printed plate made of PEDOT:PSS electrode on PET substrate (right). This plate employed Rain-X as its actuating surface. The red dots are markers to help aligning the contact pads with the pin connectors since the PEDOT:PSS ink is transparent.

A layer of Parylene-C dielectric material with thickness of $\sim 3.2 \mu\text{m}$ was deposited on top of the patterned electrodes using Parylene deposition system. For the SH/H surfaces, the same deposition methods used during the preparation of the CA measurements samples were applied here. The SH/H materials were deposited on both the base and the cover plates. An ITO-coated glass slide was used as the cover plate. EWOD plates employing conventional Cytop[®] hydrophobic material were also fabricated for reference purposes. Cytop[®] was spin-coated at 1500 rpm for 30 s and cured at temperature of 140 $^{\circ}\text{C}$ for 30 minutes. The gap between the base and cover plates, the drive electronics, and the PMMA frame to hold the EWOD securely in place are all similar to that described in **Section 2.2.1.6**.

3.3.2 Contact angle measurements

Seven surfaces displayed hydrophobicity with initial CAs of more than 90 $^{\circ}$ (**Table 3.7**) while two surfaces, the spray-coated DW-SH and spray-coated TNW, demonstrated

superhydrophobicity with CA of 162° and 171° respectively. Using the surface profilometer, both of the superhydrophobic surfaces, the DW-SH and TNW have high surface roughness, $1.8\ \mu\text{m}$ and $0.6\ \mu\text{m}$ respectively due to the presence of microstructures on their surfaces. The cloth-wiped G5 also has a high surface roughness ($1.1\ \mu\text{m}$) because of its micro-textured surface resulting from the lint-free cloth used to apply the substance. This is in contrast with the spin-coated G5 sample, which has a very smooth surface. There is no relationship however found between the average surface roughness with the CA of the commercial hydrophobic surfaces [200, 201].

Table 3.7: Summary of contact angle measurements of the SH/H materials.

| Superhydrophobic/ hydrophobic materials (deposition method) | Average surface roughness (nm) | Initial CA at 0 V (°) | CA at 250 V (°) | Final CA back at 0 V (°) | Electrowet ting hysteresis (°) | CA modulation (°) |
|--|---|-----------------------------|-----------------------|-----------------------------------|---|-------------------------|
| <i>crep protect</i> (CP) (spin coating) | 80 ± 20 | 109 ± 4 | 79 ± 8 | 92 ± 2 | 17 ± 4 | 30 ± 10 |
| <i>Drywired</i> ® 101X A4 series (DW-A4) (spin coating) | 35 ± 2 | 108 ± 5 | 90 ± 1 | 88.6 ± 0.5 | 20 ± 5 | 18 ± 6 |
| <i>Drywired</i> ® 101X 6 series (DW-6) (spin coating) | 268 ± 20 | 118 | 90 | 87 | 31 | 28 |
| <i>Drywired</i> ® superhydrophobic (DW-SH) (spraying - two coatings) | 1774 ± 200 | 162 ± 5 | 124 ± 8 | 147 ± 3 | 16 ± 7 | 38 ± 12 |
| G5 (applied using cloth) | 1119 ± 900 | 107.3 ± 0.5 | 54 ± 2 | 104 ± 2 | 4 ± 2 | 53 ± 2 |
| G5 (spin coating) | 4.0 ± 0.3 | 109 ± 1 | 95 ± 3 | 93 ± 2 | 16 ± 3 | 14 ± 3 |
| <i>Nanotol</i> (NT) (spin coating) | 26 ± 4 | 108 ± 2 | 84 ± 2 | 88 ± 4 | 20 ± 4 | 24 ± 3 |
| <i>NeverWet</i> ® top coat (TNW) (spraying-two coatings) | 570 ± 400 | 171 ± 3 | 99 ± 4 | 134 ± 5 | 37 ± 2 | 72 ± 4 |
| <i>Rain-X</i> (RX) (spin coating) | 4.1 ± 0.2 | 104 ± 2 | 69 ± 1 | 93 ± 5 | 11 ± 6 | 35 ± 2 |

From **Figure 3.8** five surfaces display partial electrowetting reversibility out of the nine surfaces after maximum DC voltage application of 250 V: the spin-coated CP, the spin-coated RX, the spray-coated DW-SH, the spray-coated TNW, and the G5 applied using cloth. All the four surfaces however have high hysteresis between 11° to 37° except for the G5 surface which has quite low hysteresis with 4°. The CA modulation for the reversible surfaces range between 30° - 72° with the spray-coated TNW having the largest CA modulation. Both of the superhydrophobic spray-coated surfaces, the DW-SH and TNW are partially reversible, exhibiting similar mechanisms

of droplet transitioning from being on top of the nanostructures (Cassie-Baxter state) to partial impalement into the nanostructures (Wenzel state) once voltage is applied. When the voltage is removed, the energy required to return to its initial state is too high so the droplet remains impaled on the nanostructures [130].

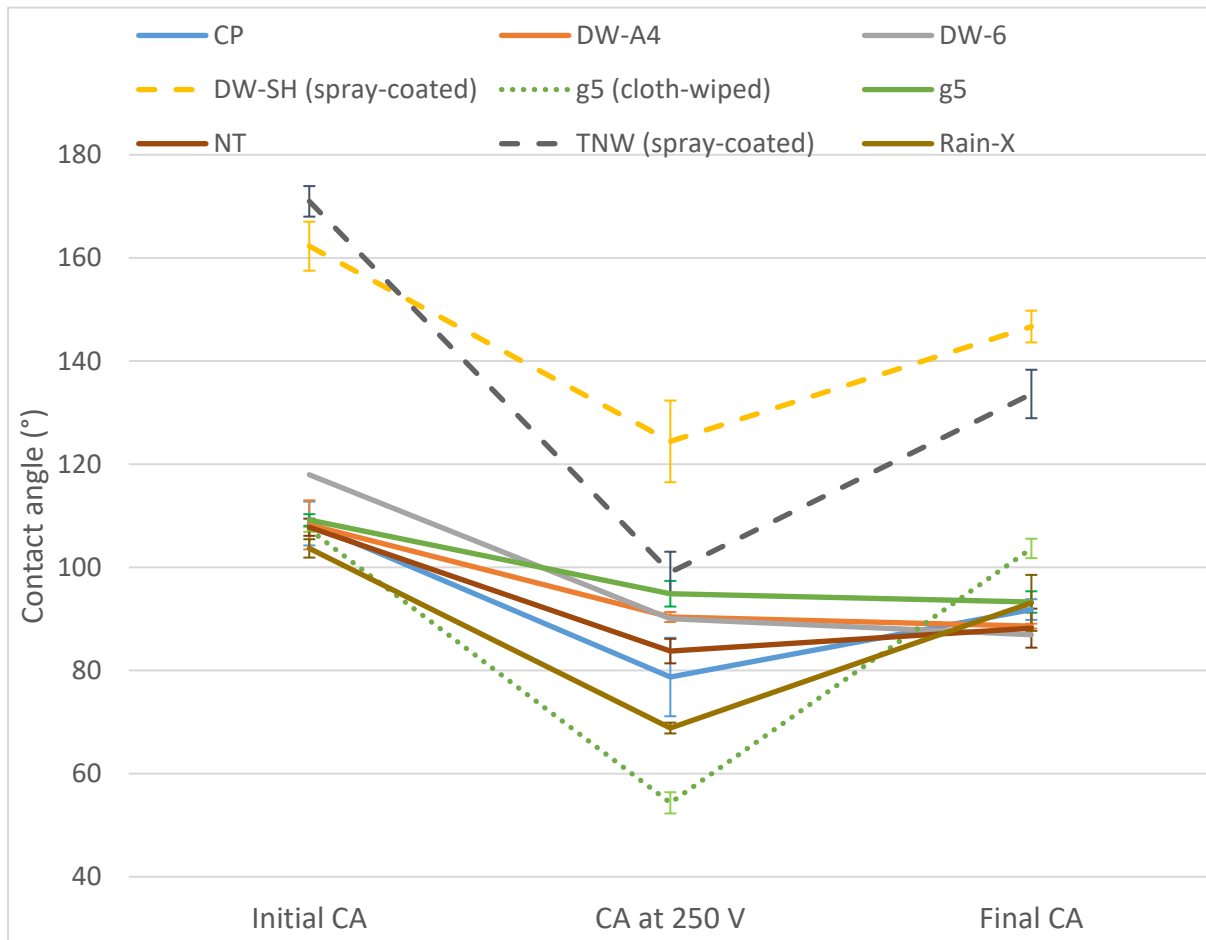


Figure 3.8: The changes in CA when 250 V of DC voltage is applied across a 20 μ l of DI water sitting on the superhydrophobic/hydrophobic surfaces. The solid lines represent the spin-coated surfaces, the dashed line represent spray-coated surface, and the dotted line represent surface deposited using cloth.

The irreversibility of the other hydrophobic surfaces could be due charge trapping inside the SH/H layer. Irreversibility due to charge trapping is a topic that is still not fully understood but there are studies [82, 202] reporting that charges can be trapped in the insulating layer causing the droplet to remain wetted even after the

voltage is removed. Further investigations such as that by Verheijen & Prins [82] would be needed to validate if charge trapping did occur on the surfaces of the investigated hydrophobic materials. **Table 3.7** summarises the findings of the CA measurement of the different types of SH/H materials.

3.3.3 Droplet actuation

Based on the findings of electrowetting reversibility investigation in the previous section, five types of surfaces were selected to be employed in the fabrication of the EWOD plates. These surfaces were: the spin-coated CP, the spin-coated RX, the spray-coated DW-SH, the spray-coated TNW, and G5 applied using cloth. EWOD plates employing conventional *Cytop*® hydrophobic surface were also fabricated for reference purposes. All the plates including the *Cytop*® ones have the same characteristics in terms of the type of substrate (PET polymer), the electrode design, and the dielectric material (~3.2 µm layer of Parylene-C).

Table 3.8 summarises the findings on the linear droplet actuation evaluation of the EWOD devices employing different types of SH/H material. The lowest voltage for reliable actuation across three or more electrodes, back and forth for a minimum of three cycles, was identified for each type of device. Both of the *Cytop*® devices are capable of actuating droplets across all of their 16 electrodes. For the *Cytop*® devices the minimum voltage needed to instigate droplet movement across just one electrode is 75 V_{RMS} . To actuate the droplet across all 16 electrode reliably, a minimum voltage of 105 V_{RMS} is required.

Only one of the plates employing commercial SH/H materials, the spray-coated TNW device is capable of demonstrating droplet movement across more than two electrodes. The TNW device moved a droplet across seven electrodes at 210 V_{RMS}

actuation voltage. The second best performing device is the *Rain-X*® device by moving droplet across two electrodes using 165 V_{RMS} . Previously, Abdelgawad [180] reported fabricating low-cost EWOD plates employing *Rain-X*® as the actuating surface. *Rain-X*® was deposited onto *Saran*™ wrap (the dielectric layer) using spin coating method. The device was capable of moving droplets but the actuation voltage was very high at 800 V_{RMS} (18 kHz).

Table 3.8: Droplet transportation performance of EWOD plates with difference types of dielectric layer

| Superhydrophobic/hydrophobic material - fabrication method | Number of plate fabricated and observations | Voltage to instigate droplet movement to the next electrode | Lowest voltage for reliable actuation across three or more electrodes (minimum of 3 cycles of back and forth) |
|--|---|---|---|
| <i>Cytop</i> ® - spin coated | 2 – Both capable of moving droplet | 75 V_{RMS} | All 16 electrodes at 105 V_{RMS} |
| <i>crep protect</i> (CP) – spin-coated | 2 – Both managed to move droplet across only one electrode | 225 V_{RMS} | - |
| <i>Drywired</i> ® superhydrophobic (DW-SH) – spray-coated | 2 – Both plates not functional | - | - |
| G5 - applied using cloth | 1 | 195 V_{RMS} | - |
| <i>NeverWet</i> ® top coat – spray-coated | 1 | 180 V_{RMS} | 7 electrodes at 210 V_{RMS} |
| <i>Rain-X</i> ® (RX) – spin-coated | 2 – Both plates can actuate droplet across only one to two electrodes | 165 V_{RMS} | - |

Neither of the spray-coated DW-SH devices were functional while the G5 device could only move a droplet across one electrode using 195 V_{RMS} . For these devices, the droplets stuck to a location most of the time. The high surface roughness

exhibited by these devices surfaces inhibits droplet movement across the electrodes as the droplet impales into the microstructures once the voltage is applied. Additionally, the poor performance of these devices could also be contributed to by defects that might occur in the inkjet-printed electrodes and tracks despite considerable care having been taken during the printing process. There could also be other contributing factors such as charging and degradation of the SH/H layer which needs further investigation for confirmation.

3.3.4 Conclusions

The objective of this investigation is to find potential commercial hydrophobic surfaces as substitute to conventional and expensive materials for application in EWOD device. Eight superhydrophobic/hydrophobic products have been investigated, and five showed electrowetting reversibility after 250 V DC voltage application. However the promising results for the electrowetting reversibility investigation did not continue to the next investigation, as all candidates performed poorly except for the TNW surface in droplet actuation evaluation. Out of all the hydrophobic candidates, the TNW material has the most potential to be employed in EWOD device as it was the only surface capable of moving a droplet across more than three electrodes. The top coating of *NeverWet*® superhydrophobic material is a fascinating material that is worth looking into for further development. Apart from being compatible with EWOD actuation, this material also possess superhydrophobic characteristics which can be used as a strategy to overcome the biofouling problem (discussed in **Section 1.5.1**). For this reason, the *NeverWet*® product has been chosen for detailed investigation in the next section.

3.4 Superhydrophobic NeverWet top coating material as EWOD actuating surface

Previous section reports the results of the preliminary study on feasibility of using superhydrophobic and hydrophobic materials as EWOD actuating surface. One of the superhydrophobic material, top coating of *NeverWet*® product have demonstrated a very encouraging result in terms of its surface electrowetting reversibility and droplet actuation. As suggested by previous studies [9, 15], superhydrophobic surfaces have the capability to prevent biofouling problems, due to the adsorption of biomolecules to the device actuating surface. The problem of biofouling hinders the implementation of 'real-world' assays that require high concentrations of biomolecules in EWOD devices.

Superhydrophobic surfaces reduce biofouling by exploiting their self-cleaning property [9, 15] where an almost frictionless movement of water droplets can be observed [128, 129]. The direct contact between liquid droplet and superhydrophobic surface is minimised due to the high CA (larger than 150°) which reduces the droplet contact area with the surface [128, 129]. On account of this characteristic, this thesis proposes the application of superhydrophobic material as a substitute to the conventional hydrophobic surface to address the biofouling issue. Whilst well suited to EWOD operation, the implementation of a superhydrophobic surface increases the cost and complexity of the fabrication process [9]. The use of commercial products such as the *NeverWet*® (NW) superhydrophobic spray, manufactured by *Rust-Oleum*®, (Illinois, US), employed in the previous section provides an alternative to conventional expensive materials and fabrication techniques. The aim of this section is to investigate further the electrowetting properties of the NW material, beyond its surface reversibility that has been demonstrated in **Section 3.3.2**. To demonstrate the capability of the NW material as an anti-biofouling surface, this section also reports

investigation of the NW surface's biofouling rate. The results from this section and **Section 4.4** have been published in *RSC Advances* journal: *Latip, E. A., Coudron, L., McDonnell, M. B., Johnston, I. D., McCluskey, D. K., Day, R., & Tracey, M. C. (2017). Protein droplet actuation on superhydrophobic surfaces: a new approach toward anti-biofouling electrowetting systems. RSC Advances, 7(78), 49633-49648.*

3.4.1 Experimental

Three studies were conducted to investigate the suitability of the NW material as both the EWOD actuating and anti-biofouling surface. The first study concerned the measurement of the CA evolution with change in applied DC voltage in order to observe the electrowetting reversibility of the surface using protein-laden droplets. Once the electrowetting capability of the surface with protein-laden droplets was established, the second study investigating the impact of voltage magnitude and duration on protein adsorption rate on the surface was conducted. Indirect evaluation of protein adsorption via its effect on superhydrophobicity was performed by measuring the roll-off angle required to move a droplet after an electrowetting cycle. The third investigation, also evaluating the biofouling rate, was performed by direct measurement of the amount of adsorbed protein on the superhydrophobic surface by means of fluorescence optical imaging. The results of these three studies are compared to performance on Cytosol®.

3.4.1.1 Types of substrates and deposition of dielectric layer

Two types of substrate were used, 1) silicon wafer (p-type, <100>, 1-10 Ω -cm) for the CA and roll-off angle measurements and 2) indium tin oxide (ITO) coated glass slides for the direct measurement of biofouling rate due to its compatibility with the optical fluorescence measurement. All the substrates were coated with a $\sim 3.2 \mu\text{m}$ layer of Parylene-C.

3.4.1.2 Hydrophobic and superhydrophobic surface preparation

After coating the substrates with Parylene-C, the next step is to deposit a layer of superhydrophobic or hydrophobic material. Three surfaces were prepared for the investigation: one hydrophobic, coated with *Cytop*[®] and two superhydrophobic, coated using two different approaches based on the commercial product *NeverWet*[®] (*Rust-Oleum*[®] Corp., Illinois, US). **Figure 3.9** summarises the process of preparing the three surfaces.

For the hydrophobic surface, *Cytop*[®] was spin coated on top of the Parylene-C layer at 1500 rpm for 30 s and then baked at 140 °C for 30 minutes. The NW product is comprised of two coating materials: a base coat and a top coat. The base coat consists of liquefied petroleum gas, aliphatic hydrocarbon, n-butyl acetate, methyl isobutyl ketone, methyl acetate, ethyl acetate, and polypropylene while the top coat contains acetone, propane, n-butane and dimethyl siloxane (reaction product with silica) [203].

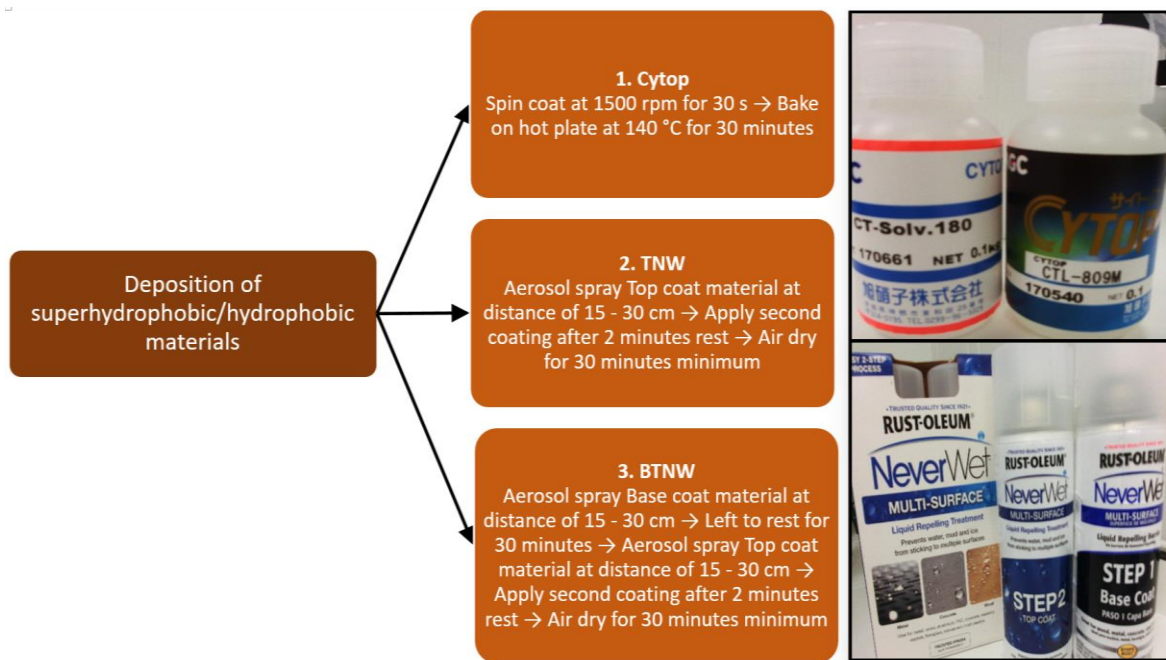


Figure 3.9: Preparation steps of the three types of superhydrophobic/hydrophobic surfaces for CA angle and roll-off angle measurements. All three surfaces were deposited with Parylene C dielectric layer before coated with either Cytop®, TNW, or BTNW. (Top right) The Cytop® hydrophobic material and its solvent; (bottom right) the Top coat and Base coat materials of the NW superhydrophobic product.

Two superhydrophobic surfaces, identified as BTNW and TNW were implemented. The BTNW surface was prepared by applying both the base coat and top coat materials while the TNW surface consists of only the top coat material. As specified by the manufacturer's instructions, both base and top coat layers were aerosol sprayed between 15 cm and 30 cm from the substrate. For the BTNW surface, one coating of the base coat material was applied and then left for rest for 30 minutes before the application of the top coat material. Two coatings of the top coat material were then applied with a 2-minute interval between them. The surface was allowed to dry at ambient room temperature for a minimum of 30 minutes before use. The preparation for the TNW surface was the same as the BTNW surface, but excluded the base coat material application step.

3.4.1.3 Surface characterisation

The surface's microstructure's were characterised using a scanning electron microscope (SEM) (JCM 5700, JEOL, US). The superhydrophobic, hydrophobic and dielectric layer thickness and surface roughness were evaluated using a stylus surface profilometer (AlphaStep® D-500, KLA Tencor).

3.4.1.4 Contact angle measurements

The measurement of CA variation with the applied DC voltage was performed using a Theta Lite optical tensiometer. The droplet images were recorded at 1.3 fps and were analysed by *One Attension* software. **Figure 3.1** shows the setup used for the CA measurement. A positive bias was applied via a platinum wire to a droplet sitting on the superhydrophobic or hydrophobic surface implemented on a silicon substrate. No surface treatment has been applied to the platinum wire. The voltage was varied between 0 V and 250 V using a DC power supply and the CA evolution was identified with every 10 V increment. Once the maximum voltage of 250 V was reached, the voltage was returned back to zero in 10 V decrements. It took approximately 5 s to change from one voltage level to the next, and once the desired voltage was reached, the voltage stayed at that level for 10 s. The total duration for each 10 V interval was 15 s. Since there were 51 voltage level (zero to 250 V and back to zero with 10 V increment), the total duration of the electrowetting cycle was 765 s.

Four types of droplet solution were employed: deionised (DI) water ($0.1 \mu\text{S cm}^{-1}$ at $25 \text{ }^\circ\text{C}$) and aqueous solutions of ovalbumin from chicken egg white (lyophilised powder, $\geq 98\%$, Sigma Aldrich, St. Louis, US) solution at three concentrations (0.01 mg ml^{-1} , 0.1 mg ml^{-1} , 1 mg ml^{-1}). The ovalbumin solutions were used as simulants of typical protein samples used in bioassays [204] (with a wide concentration range). The hysteresis cycle was repeated for a minimum of three times ($n=3$) for each

solution on three types of surface: *Cytop*®, TNW, and BTNW. To avoid the possibility of charge trapping [82] and protein adsorption effects, every run was performed with a fresh droplet on a fresh surface location on the wafer or slide.

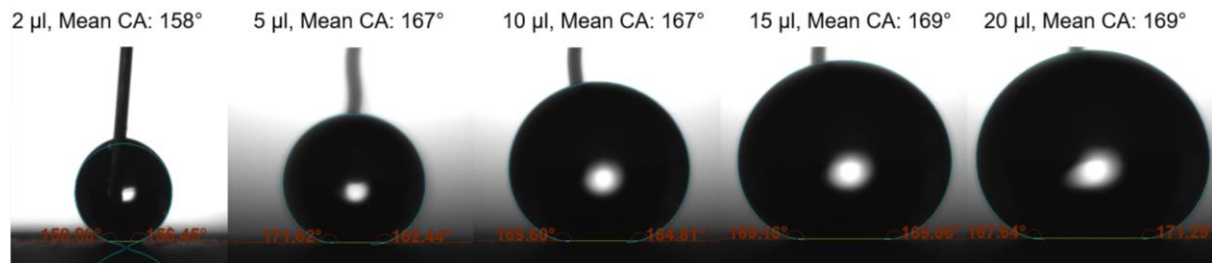


Figure 3.10: Effect of droplet volume on the CA measurement for superhydrophobic surface. The droplets in the figure are DI water sitting on TNW superhydrophobic surface. There is a large difference in the mean CA (more than 10°) between the 2 μl and 15 μl droplets while the difference between the 5 μl and 20 μl droplets is quite small ($\pm 2^\circ$ to $\pm 3^\circ$).

The volume of droplet used for measurement was 20 μl. A previous study [205] proposed using small droplet volumes (below 5 μl) for CA measurement on a superhydrophobic surface to prevent underestimation of the CA due to gravity deforming the droplet profile. The capillary length, $\lambda = \sqrt{\frac{\gamma}{\rho g}}$ (γ is surface tension, ρ is the liquid density, and g is the gravitational acceleration) is a number which describes the influence of the surface tension and the gravity forces for a given liquid [206]. The smaller the capillary length of a liquid the higher the influence of the gravity forces on the droplet, for example, a droplet with small capillary length sitting on surface is flattened due to gravity [207, 208]. The capillary length of water is 2.73 mm which is relatively high when compared to the other liquids such as diiodomethane with 1.25 mm [208, 209]. The volume used in this study is 20 ul, which roughly correspond to a droplet radius of 1.68 mm using a spherical approximation for the droplet shape. At this volume, the radius of the droplet being in the same order of magnitude as the

capillary length of water, gravity is expected to have an impact on the shape albeit a very marginal one [205, 207].

However, it was demonstrated during the experiments reported here that due to the inclusion of the wire for the voltage application, the opposite actually occurred resulting in underestimation of CA (by more than 10°) for droplets below $5\ \mu\text{l}$ as shown in **Figure 3.10**. Due to the adhesive forces between the droplet and the wire and the high superhydrophobicity of the surface, droplets with low volume tend to stick to the wire and in extreme cases were actually suspended above the surface. This altered their shape rather significantly, this was particularly true for droplets with high protein concentration. The small volume droplets were also more affected by evaporation which could influence the CA measurement due to the relatively long duration (765 s) of the experiment. However, the difference in CA between the $5\ \mu\text{l}$ and $20\ \mu\text{l}$ droplets was $\pm 2^\circ$ to $\pm 3^\circ$, which is relatively insignificant. Therefore, despite the CA being slightly affected by gravity, $20\ \mu\text{l}$ droplets were employed for the measurements to minimise altered shape and evaporation effects.

3.4.1.5 Roll-off angle measurements

The roll-off angle measurements were conducted as an indirect evaluation of how voltage magnitude and its duration affect protein adsorption on the hydrophobic and superhydrophobic surfaces. BTNW was excluded from this and subsequent studies due to its poor electrowetting performance exhibited during the CA measurements. The roll-off angle measurement was performed by measuring the required tilting angle of the silicon substrate to cause a $20\ \mu\text{l}$ droplet to roll-off from its resting position. Half of the silicon substrate was positioned on top of a static reference surface while the other half was attached to a small laboratory jack. Before positioning the silicon substrate at the centre, the reference surface and the jack were ensured to be on the

same level. The silicon wafer was then gradually tilted by lowering the jack slowly until the droplet begins to roll-off the surface. A bubble protractor was used to measure the tilt angle between the silicon substrate and the jack surface.

This process was repeated a minimum of three times ($n=3$) for each of the DI water and ovalbumin (0.01 mg ml^{-1} , 0.1 mg ml^{-1} , and 1 mg ml^{-1}) droplet solutions on two types of surface: *Cytop*® and TNW. To investigate the effect of applied DC voltage magnitude and its duration on the roll-off angle, the droplets underwent a hysteresis cycle with varying value of maximum DC voltage and duration prior to measurement. Maximum DC voltage of either 0 V, 150 V or 250 V were applied to the droplets with two different duration of either 75 s or 765 s. The 75 s was used to represent the effect of short exposure to protein on the surfaces biofouling rate while 765 s was for the long duration. For the short duration, similar to the procedure in **Section 3.2.1.2**, it took 20 s to increase the voltage from zero to the maximum value, and the voltage stayed at the level for 10 s, before returning to zero voltage which took another 45 s. The method of voltage increment from zero to the maximum value for the 765 s duration was performed similarly to the one described in CA measurement.

3.4.1.6 Evaluation of the biofouling rate

Apart from the roll-off angle measurements, direct measurement of the amount of protein adsorbed onto the surface was also conducted using optical fluorescence imaging to investigate the effect of voltage magnitude and its duration on adsorption of protein on EWOD surfaces. Two types of surface were employed: *Cytop*® and TNW, deposited onto ITO coated glass substrates. The solution used for the $20 \mu\text{l}$ droplets was fluorescent dye-labelled human plasma fibrinogen, Alexa Fluor™ 647 conjugate (ThermoFisher Scientific, Massachusetts, US) at 0.1 mg ml^{-1} . The droplets were subjected to the same hysteresis cycle as the one described in the roll-off angle

measurements section with a maximum DC voltage of either 0 V, 150 V or 250 V applied with a duration of either 75 s or 765 s. After the exposure of the surface to the protein-laden droplet, the droplet was then removed and followed by a cleaning step to remove any residue of protein molecules that had not adsorbed onto the surface. This step was performed twice by pipetting a droplet of DI water at the same location as the previous 'preconditioning' fibrinogen droplet. Finally, the biofouling rate was quantified by measuring the mean fluorescence intensity of the resulting spots on the surfaces after their contact with the energised droplets. A GenePix 4000B microarray scanner (Molecular Devices, California, US) was used for the measurement while the image acquisition and analysis was performed using the GenePixR Pro 7 Acquisition and Analysis Microarray software (Molecular Devices, San Jose, US).

3.4.2 Surface characterisation

There are two key properties of a superhydrophobic surface: the material's chemical composition and its surface topography [133]. For both of the NW surfaces, TNW and BTNW, they are superhydrophobic due to their hydrocarbon and silicone contents combined with their surface microstructures as shown in the SEM images of **Figure 3.11** [203]. BTNW and TNW display two distinctive features at the macroscale ($\times 40$ magnification); asperities in the size range of hundreds of micrometres (**Figure 3.11 a**) are observed in the BTNW while smaller ones, in the range of tens of micrometres (**Figure 3.11 d**) are found in the TNW surface. Filler-particles are assumed to be incorporated into the *NeverWet*® base and top coating compositions to create surface texture [210] similar to the morphology that can be found on naturally occurring superhydrophobic surfaces such as Lotus leaves or butterfly wings.

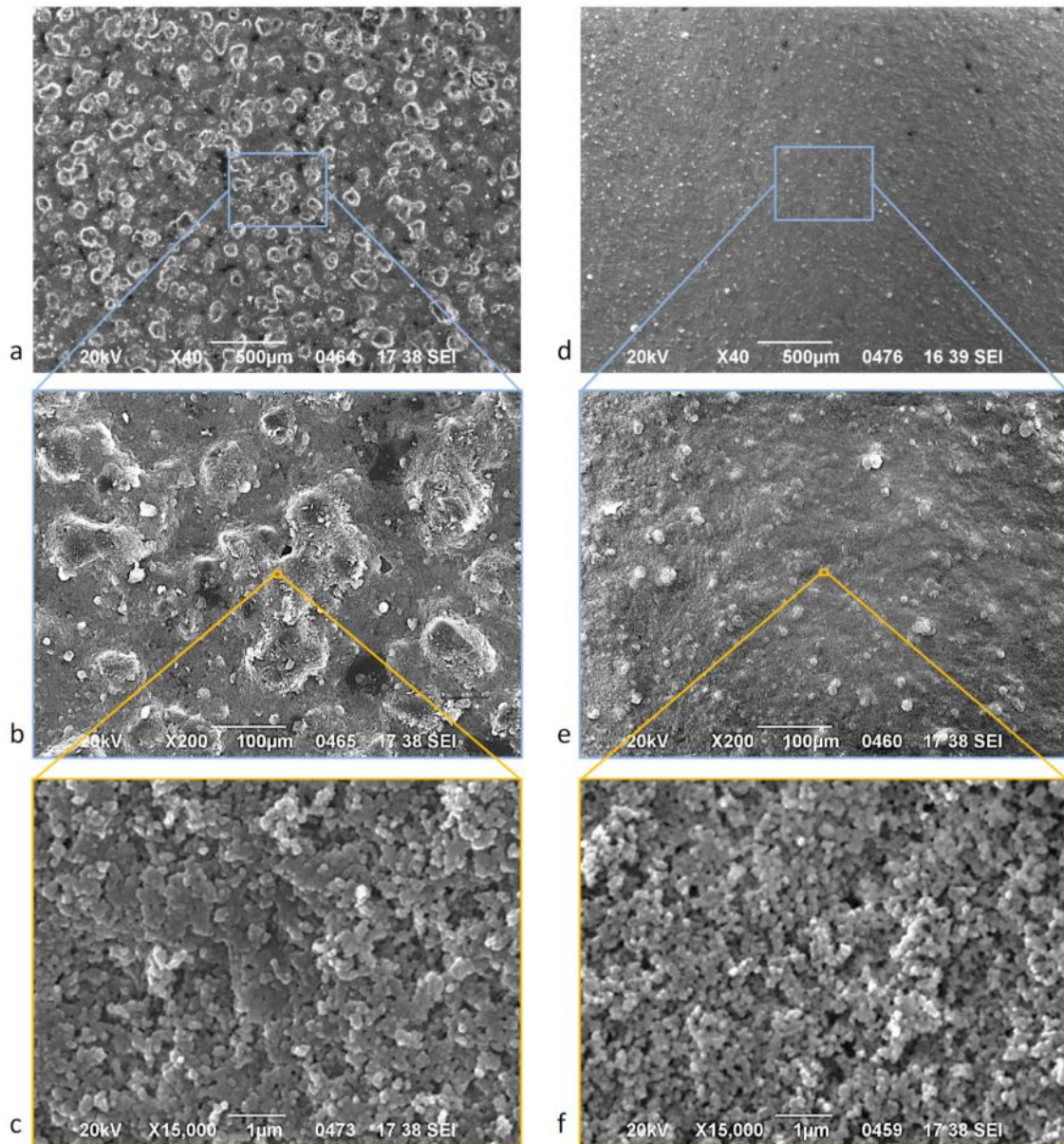


Figure 3.11: SEM microstructure images of BTNW (left) and TNW (right) superhydrophobic surfaces at different magnifications (increasing from top to bottom); $\times 40$ (a and d), $\times 200$ (b and e), and $\times 15,000$ (c and f).

Images with higher magnification ($\times 200$) (**Figure 3.11** b and e) reveal the spherical nature of the asperities found in previous images (**Figure 3.11** a and d), corroborating the plausible presence of filler-particles. The macroscale asperities are in turn characterised by smaller nanostructures as can be seen when the images are further magnified at $\times 15,000$ (**Figure 3.11** c and f). These nanoscale structures, which probably originate from the silicone derivative [203] in the formulation of top coating

material, are very similar in shape and size (approximately 100 nm typical diameter) for both BTNW and TNW surfaces. The shared BTNW and TNW characteristic of having both micro and nanoscale structure is similar to what has been described previously [129] in order for a surface to exhibit superhydrophobic properties.

The measured surface roughness of the surfaces assessed using the stylus profilometer are consistent with the SEM observations. The roughness was measured at three different locations on the sample by scanning the stylus of the profilometer across a length of 5 mm. BTNW, which displays substantial asperities in the images, has the highest roughness with $R_a = 6 \pm 2 \mu\text{m}$ whereas TNW roughness is lower by one order of magnitude with $R_a = 0.6 \pm 0.2 \mu\text{m}$. *Cytop*® has the smoothest surface with roughness of $R_a = 0.007 \pm 0.003 \mu\text{m}$. The thickness of each type of surface was measured using the stylus profilometer and BTNW again has the highest thickness of $23 \mu\text{m}$ while TNW's thickness is approximately 20 times lower than that of BTNW. Based on the Young-Lippman equation, it is expected that the voltage requirement for the BTNW surface will be higher compared to the other two surfaces due to its higher thickness.

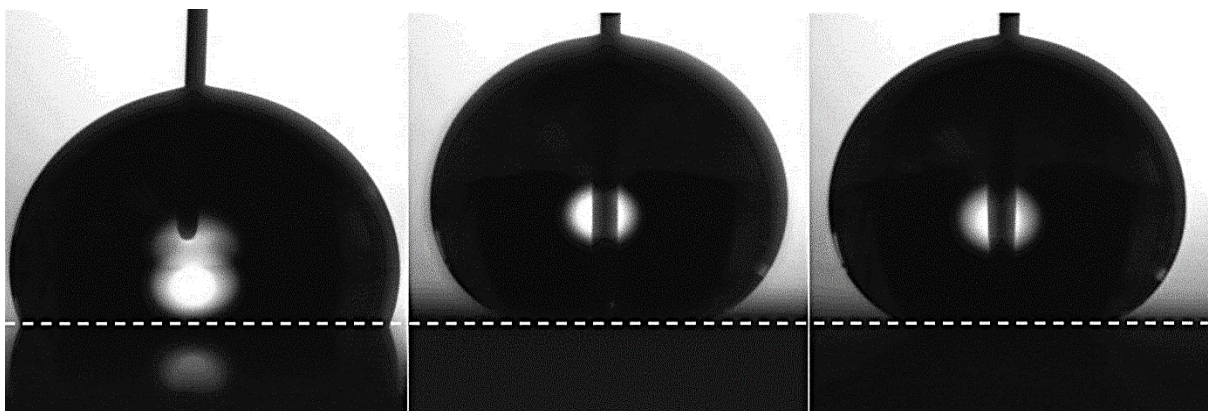


Figure 3.12: Droplets of DI water on *Cytop*® (left), BTNW (middle), and TNW (right) surfaces. The images were captured using the optical tensiometer. The baseline for the estimation of the CA is represented by the dash line.

The superhydrophobic or hydrophobic properties of the surfaces were verified by introducing DI water droplets of equal volume onto each surface. The resulting CA profiles are shown in **Figure 3.12**, both BTNW and TNW display very high CA (higher than 150°) indicating their superhydrophobicity. While still exhibiting good water repellency, *Cytop*® demonstrates a lower CA, of approximately 110°. The rather significant difference in the surface roughness between BTNW and TNW does not seem to affect the superhydrophobic property of the surfaces.

3.4.3 Contact angle measurements

This study does not intend to investigate the effect of liquid-gas surface tension, γ_{lg} on the droplet CA, θ , but its influence is noted based on the Young's equation. The liquid-gas surface tension, γ_{lg} was not measured but a previous study [211] demonstrated that γ_{lg} decreases with increasing protein concentration and this in turn affects the CA values. The capillary length of protein solution is also expected to be lower than the water as the surface tension decreases and also due to the increase in the solution density due to the ovalbumin loading [206].

There are differences in the initial CA of the different droplet solutions (DI water, 0.01, 0.1 and 1 mg ml⁻¹ ovalbumin) sitting on the same type of surface before the start of hysteresis cycle. *Cytop*® is most affected by the protein concentration with the initial CA varying between 97° and 110°; the initial CA values decreasing with the increase in the protein concentration. This is followed by BTNW with measurements ranging between 161° and 171° while TNW has the least noticeable variation between 168° and 171°. These variations are shown in **Figure 3.13**. Among the three surfaces, TNW allows for the widest range of CA modulation for all types of droplet solution. The CA of DI water changes by 72°, from the highest initial CA of 171° to the lowest of 99° on TNW while on *Cytop*® the decrease is by 33° from 110° to 77°. BTNW demonstrates the lowest CA modulation with a decrease of only 23° from its initial CA value after the application of 250 V maximum DC voltage.

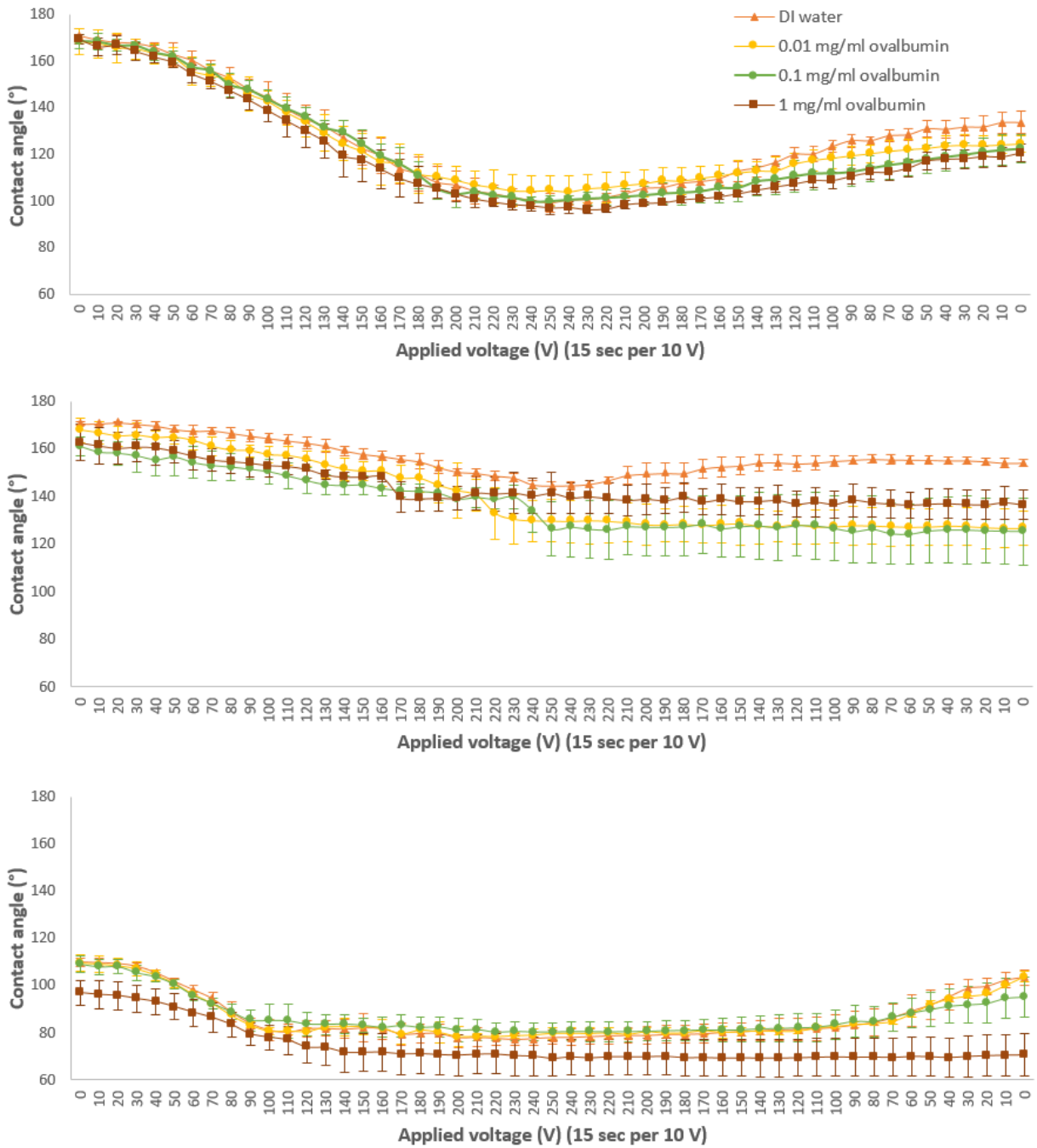


Figure 3.13: Contact angle changes with applied DC voltage for different droplet solutions on three types of surface: TNW (top), BTNW (middle), and Cytop® (bottom). Note that left to right, the plots are from zero to maximum voltage and back to zero voltage – for clarity this is an ‘unfolded’ hysteresis curve plot.

Electrowetting reversibility is an important property for an actuating surface because it influences the ability of a droplet to move across the surface by means of EWOD force. This property is particularly important for a superhydrophobic surface since the droplet can be wedged and impaled between the micro and nanostructures, thus hindering the droplet's motion by increasing the energy required to move the droplet forward [128]. The electrowetting response of all the droplet solutions on the three different surfaces by applying DC voltage between 0 V to 250 V are presented in two figures, **Figure 3.13** and **Figure 3.14**. Both are plots of contact angle against applied DC voltage derived from the same data where **Figure 3.13** compares the CA changes between different types of solution on the same surface while **Figure 3.14** compares the CA changes between different surfaces using the same solution. On the TNW surface, all types of droplet solutions demonstrate partial reversibility with moderate hysteresis. DI water displays the lowest hysteresis with 37° followed by the protein solutions with increasing concentrations. TNW has the advantage of being the only surface that displays reversibility for 1 mg ml⁻¹ ovalbumin after a long duration hysteresis cycle. On the *Cytop*® surface, all types of solution are partially reversible except for 1 mg ml⁻¹ ovalbumin. Conversely, only DI water shows reversibility on the BTNW surface. It has also been found that increase in protein concentration increases the hysteresis on both *Cytop*® and TNW surfaces but the effect is more pronounced on *Cytop*®.

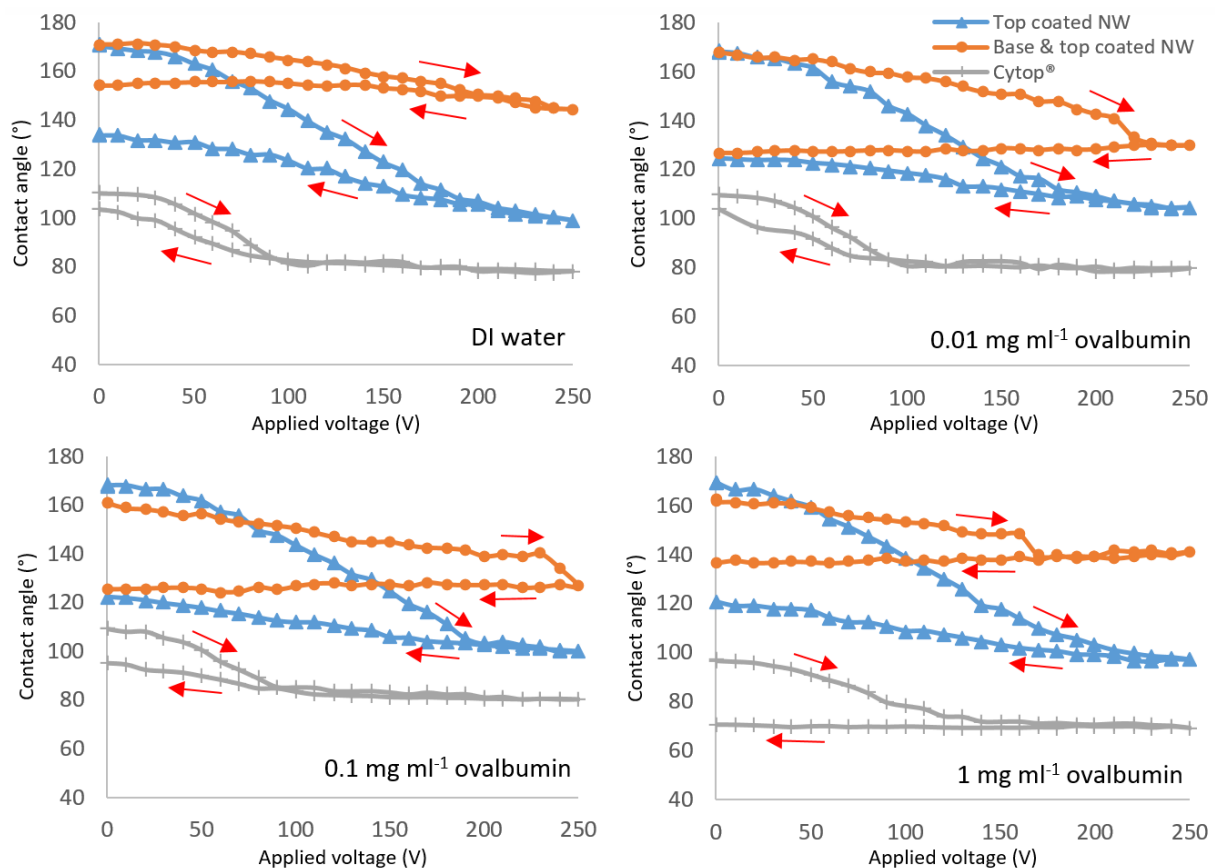


Figure 3.14: Electrowetting hysteresis curves for different droplet solutions (clockwise from top left) DI water, 0.01, 1, and 0.1 mg ml⁻¹ ovalbumin on three types of surface: TNW (blue triangles), BTNW (orange circles) and Cytop® (grey crosses). Each curve starts at the higher initial point and the difference between the initial and the final CA is the hysteresis. Red arrows indicate the increasing or the decreasing voltage segment of the curve.

Figure 3.14 shows the electrowetting hysteresis plots (derived from the same data for **Figure 3.13**) for all types of solution on the three surfaces. Of the three surfaces, *Cytop*® exhibits the lowest hysteresis for all types of solution. The higher hysteresis measured on TNW compared to *Cytop*® is believed to be caused by the impalement of droplets on the nanostructures of the surface. The droplet sits on top of the nanostructure in a state called Cassie-Baxter when no voltage is applied at the beginning of the hysteresis cycle. Once the voltage is increased and reaches a certain level, the droplet starts to transition into the Wenzel state where part of the droplet is

impaled by the nanostructures. The energy required for the droplet to return to its initial Cassie-Baxter state is generally unachievably high (depending on parameters such as dimensions of the nanostructures [130]). This leads to the higher value of hysteresis on TNW as part of the droplet remains impaled in the nanostructure even after the voltage is removed. As the hysteresis curves indicate, although most of the droplet solutions are partially reversible on TNW, the high initial CA could not be attained again.

Table 3.9: Summary of the CA measurement results.

| Type of surface | Type of droplet Solution | Initial CA(°) | Lowest CA at 250 V (°) | Final CA(°) | EWH (°) | CA modulation range (°) | Reversibility |
|----------------------------|--------------------------|---------------|------------------------|--------------|---------------|-------------------------|---------------|
| TOP COATED NEVERWET | DI water | 171 ± 3 | 99 ± 4 | 134 ± 5 | 37 ± 2 | 72 ± 4 | Partial |
| | 0.01 mg/ml ovalbumin | 168 ± 6 | 104 ± 7 | 124 ± 4 | 44 ± 9 | 64 ± 7 | Partial |
| | 0.1 mg/ml ovalbumin | 168 ± 3 | 100 ± 2 | 122 ± 6 | 46 ± 4 | 69 ± 2 | Partial |
| | 1 mg/ml ovalbumin | 169 ± 2 | 96 ± 3 | 121 ± 4 | 49 ± 5 | 73 ± 2 | Partial |
| BASE & TOP COATED NEVERWET | DI water | 170.7 ± 0.6 | 145 ± 2 | 154 ± 1 | 17 ± 2 | 26 ± 2 | Partial |
| | 0.01 mg/ml ovalbumin | 168 ± 5 | 127 ± 9 | 127 ± 7 | 41 ± 1 0 | - | No |
| | 0.1 mg/ml ovalbumin | 161 ± 4 | 125 ± 10 | 125 ± 1 0 | 36 ± 1 0 | - | No |
| | 1 mg/ml ovalbumin | 163 ± 8 | 137 ± 9 | 136 ± 6 | 26 ± 2 | - | No |
| Cytop® | DI water | 110 ± 2 | 77 ± 2 | 104 ± 3 | 7 ± 4 | 33 ± 5 | Partial |
| | 0.01 mg/ml ovalbumin | 110 ± 3 | 78 ± 1 | 104 ± 2 | 5.8 ± 0 .3 | 31 ± 2 | Partial |
| | 0.1 mg/ml ovalbumin | 109 ± 3 | 80 ± 4 | 95 ± 9 | 14 ± 1 0 | 29 ± 5 | Partial |
| | 1 mg/ml ovalbumin | 97 ± 5 | 69 ± 8 | 71 ± 9 | 26 ± 1 0 | - | No |

* (-) indicates no CA modulation range since the surface is irreversible.

Cytop® displays almost fully reversible performance with a low hysteresis value is due to its very flat surface. However the higher hysteresis values of TNW than Cytop® have been demonstrated not to decrease the EWOD actuation

performance of the device as presented by the results in **Section 4.4.2**. Considering BTNW, it is suggested that the same explanation of irreversible transition of states from Cassie-Baxter to Wenzel is responsible for the non-reversibility of all the droplet solutions except for DI water. Since microscopic observation shows that BTNW has the larger asperities than TNW, it is reasonable to predict that this surface will require higher energy to return to its initial state. A previous study [130] achieved complete reversibility, from approximately 130° back to 160° after application of 190 V_{TRMS} on a superhydrophobic surface with a 20 µm high silicon nanowire structure. The authors found that the reversibility decreased with increasing voltage magnitude, increasing nanostructure height and decreasing nanostructure density. The full results of this sections' CA measurement are summarised in **Table 3.9**.

3.4.4 Electrowetting-number of the surfaces

Based on the fitting of the Young-Lippmann equation to the experimental data below saturation angle, the electrowetting numbers $(\frac{\epsilon_0 \epsilon_r}{2 \gamma_{lg} d} V^2)$ give values in reasonable agreement with theoretical values. The fittings are shown in **Figure 3.15** and the data used to plot the graphs are the same for **Figure 3.13** and **Figure 3.14** but taking only the CA changes induced during the increasing DC voltage segment of the electrowetting cycle. For example, using the following values of Parylene-C dielectric constant, ϵ_r , 3.15, permittivity of free space, ϵ_0 , 8.8542×10^{-12} F m⁻¹, DI water-air surface tension, γ_{lg} , 72 mN m⁻¹ [212] and insulating layer thickness, d , 3.2 µm, the theoretical electrowetting number is given by $6.05 \times 10^{-5} \times V^2$ which is relatively close to the fitting value for the DI water on *Cytop*® of $5 \times 10^{-5} \times V^2$ (as estimated from the experimental data). However these fittings do not take into consideration the roughness of the surfaces which also affects the electrowetting mechanism especially for superhydrophobic surfaces. Models proposed by Hebertson et al. [134] and Torkelli

[213] do take into account the nanostructures' geometry, however these approaches have not been employed in this study as their approximations need further parameters including the nanostructures' height and diameter which were not measured.

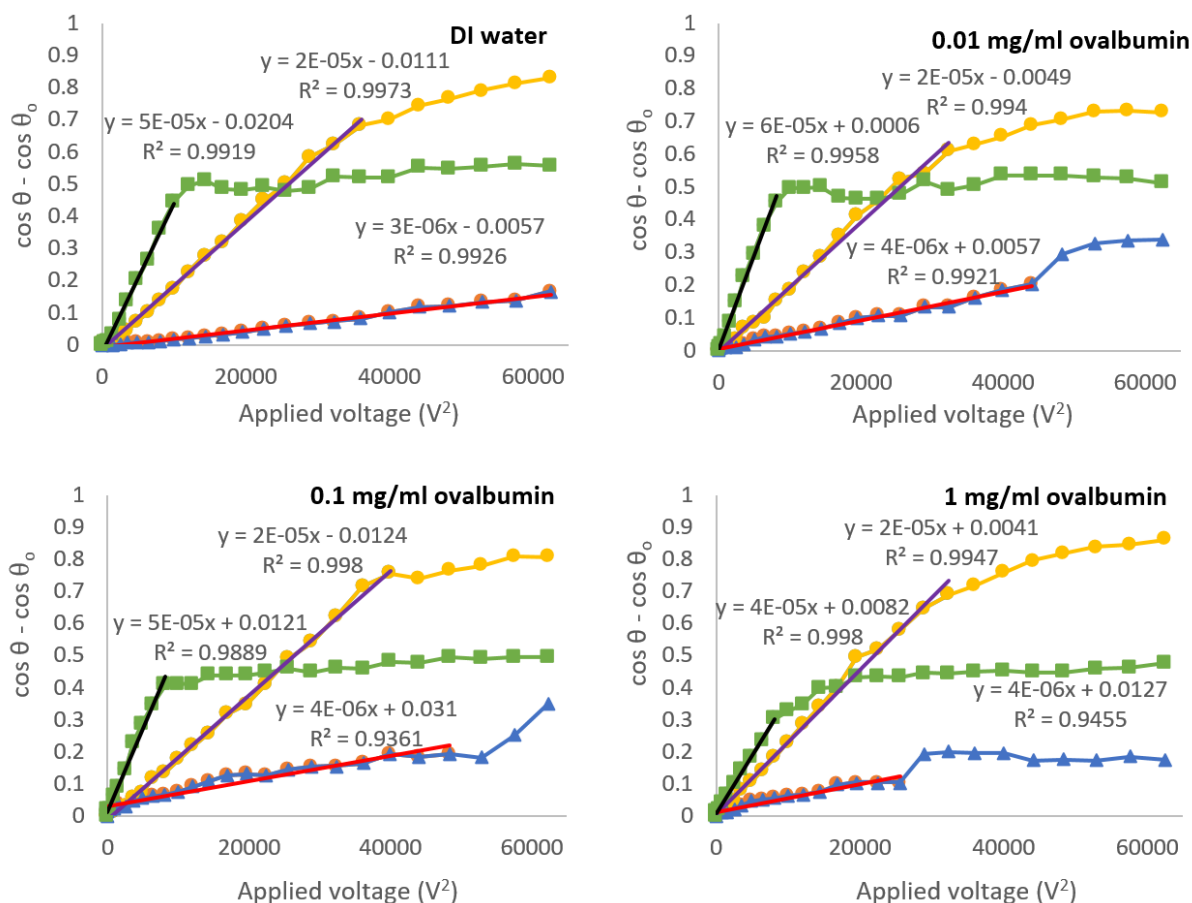


Figure 3.15: Fittings of Young-Lippmann equation for experimental data below saturation point (clockwise from top left) DI water, 0.01, 1, and 0.1 mg ml⁻¹ ovalbumin on different types of surface. Square markers for Cytop®, round markers for TNW, triangle markers for BTNW, and straight lines for Young-Lippmann fittings.

The electrowetting number can be related to the efficiency of the electrowetting mechanism; according to the fittings, BTNW is the least efficient of the three surfaces with the lowest values for all solutions (approximately $3 \times 10^{-6} \times V^2$ to $4 \times 10^{-6} \times V^2$). TNW's electrowetting number is in the same order as Cytop® albeit with a lower value, $2 \times 10^{-5} \times V^2$. The differences in the electrowetting number between the surfaces are believed to be contributed to by the different thicknesses of the hydrophobic and

superhydrophobic layers. *Cytop*® is very thin with a thickness in the range of tens of nanometers while TNW's thickness is approximately 1 μm . BTNW is very thick (circa 25 μm) which greatly affects the electrowetting force, hence resulting in the lowest electrowetting number. There are no significant differences in the electrowetting number between the different types of solution on the same type of surface as there are only small variations in their values of liquid-gas surface tension. However *Cytop*® efficiency reduced a little for 1 mg ml^{-1} ovalbumin which could be due to the stickiness of the high protein concentration solution to the surface.

3.4.5 Effect of maximum DC voltage magnitude on CA reversibility and hysteresis on TNW surface

Further investigation was conducted to evaluate the impact of maximum DC voltage magnitude on the reversibility of droplet solutions on the TNW surface. The hysteresis cycle was repeated for all types of solution on the TNW surface but the maximum voltage was reduced from 250 V to 150 V. The time taken for each electrowetting cycle was 775 seconds with 10 V change per 25 seconds. The total duration of the electrowetting cycle was kept as close as possible to the 765 used for the cycle with maximum DC voltage of 250 V where the voltage change was 10 V per 15 seconds. In the electrowetting cycle for 150 V maximum DC voltage, the voltage change was 10 V per 25 seconds so that it would be easy to be consistent in adjusting the knob of the voltage source for every voltage increase.

The results are summarised in **Figure 3.16** and **Figure 3.17**. Complete reversibility is still not achievable but the hysteresis is observed to reduce by almost 27% for both 0.01 mg ml^{-1} and 1 mg ml^{-1} ovalbumin solutions. However the decrease is not as significant for DI water. Due to the lower voltage, the CA modulation range also reduced by approximately 14°. The maximum allowable voltage for complete

reversibility on a TNW surface was also evaluated. All types of solution have a maximum allowable voltage between 45 V and 50 V. Application of DC voltage above this level results in CA hysteresis larger than 0.5° .

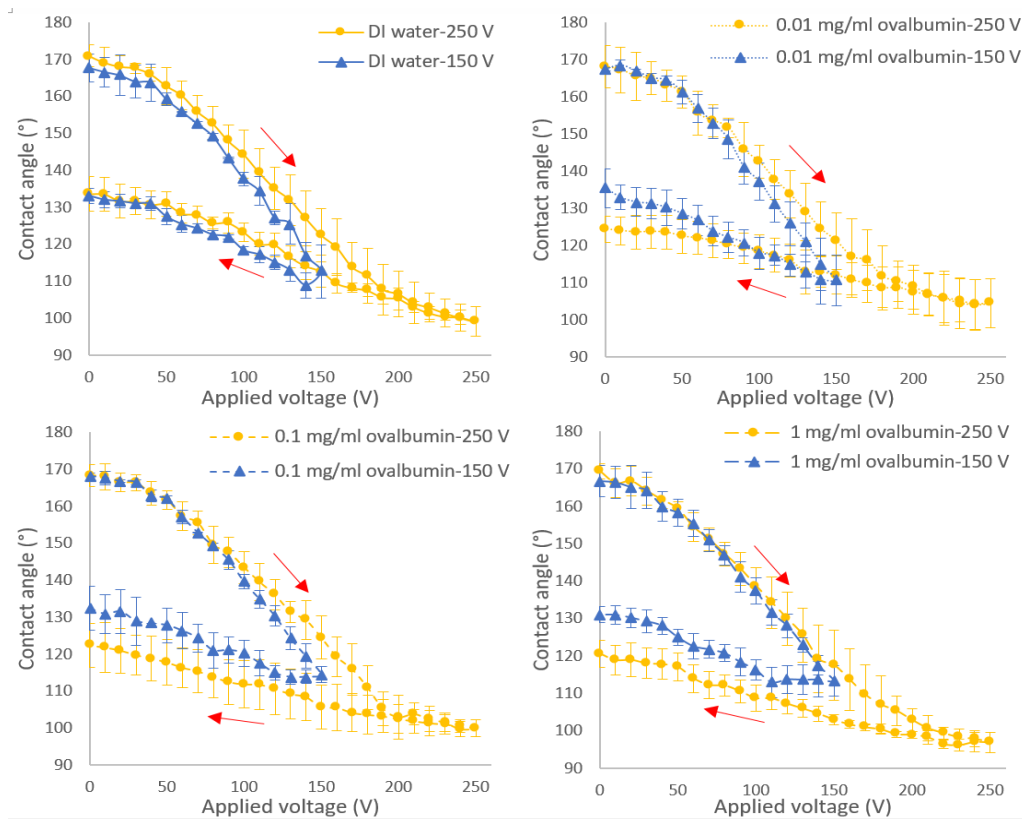


Figure 3.16: Electrowetting hysteresis curves for different droplet solutions (clockwise from top left) DI water, 0.01, 1, and 0.1 mg/ml ovalbumin on TNW surface comparing between 150 V and 250 V maximum voltage. Each curve starts at the higher initial point and the difference between the initial and the final CA is the hysteresis.

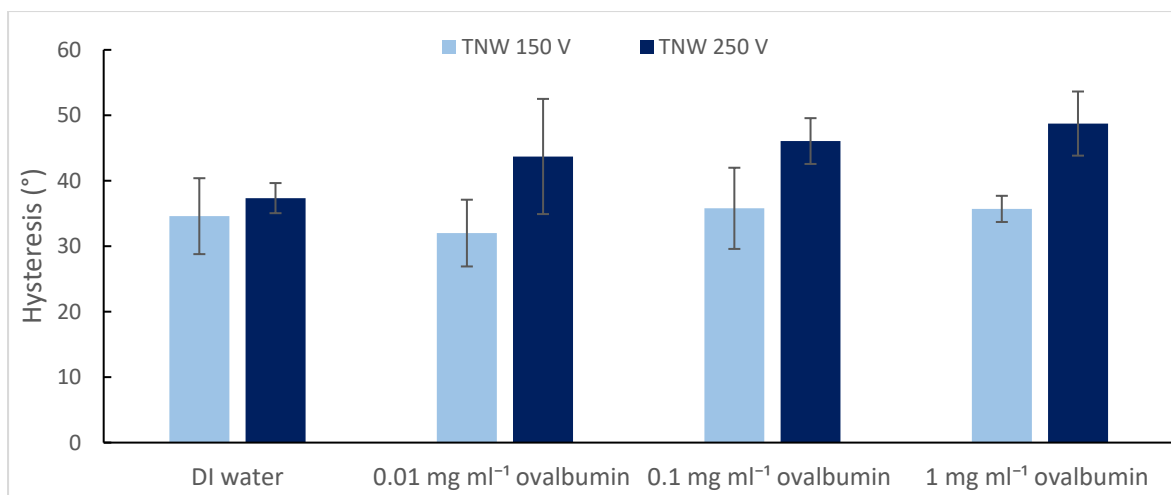


Figure 3.17: Hysteresis of different solutions on TNW for 150 V and 250 V maximum applied voltage (column graphs) and on Cytop® for long and short duration application of 250 V (line graphs).

3.4.6 Effect of maximum DC voltage duration on CA reversibility and hysteresis on Cytop® surface

Figure 3.18 presents investigation of the effect of maximum DC voltage duration on CA reversibility and hysteresis of Cytop®. The hysteresis cycle was repeated on Cytop® for all types of solution with the same maximum DC voltage of 250 V but using a shorter energisation cycle, reduced from 765 s to 75 s. It is observed that the hysteresis is reduced, especially for the higher protein concentration solutions, which suggests their predisposition to adsorption resulting in the surface biofouling. The non-reversibility of 1 mg ml⁻¹ ovalbumin droplets previously observed during the long hysteresis cycle did not reoccur with the shorter cycle. This finding indicates that when in prolonged contact with protein solution, Cytop® is more prone to biofouling compared to TNW. Since some immunoassay protocols involve a long incubation times this would increase the risk of biofouling if Cytop® was to be employed as the actuating surface.

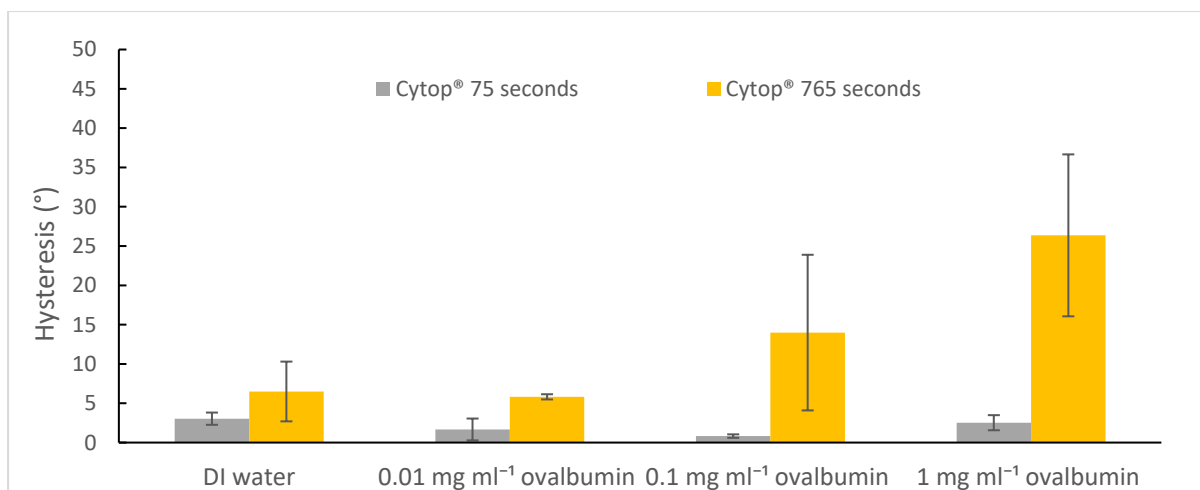


Figure 3.18: Hysteresis of different solutions on TNW for 150 V and 250 V maximum applied voltage (column graphs) and on Cytop® for long and short duration application of 250 V (line graphs).

The results from this investigation also suggest that the higher the protein concentration, the more impact the duration of voltage application has on CA reversibility and hysteresis. This finding is consistent with a previous study [214] which suggested that protein adsorption on a surface is a highly time dependent process. Unlike the present thesis, this previous study was conducted without any voltage application to the protein droplets.

3.4.7 Saturation angle of the surfaces

The Young-Lippmann equation can be used to predict the changes in CA as a function of voltage before the saturation angle is reached. Beyond the saturation angle, further increment of voltage will not produce any reduction in the CA. As suggested by studies [82-85], saturation angle lies approximately between 60° - 80° for any electrowetting systems. The complete physical mechanism of this phenomenon has not been fully described yet, but from the perspective of the electromechanical model of EWOD, saturation angle occurs when equilibrium is reached between the electrostatic and surface tension forces [9].

The saturation angle for *Cytop*® occur at approximately 100 V DC voltage for all types of solution and is estimated between 69° and 80° which is within the suggested range [82-85]. Meanwhile on TNW surface, the saturation points for all types of solutions could probably decrease further if the voltage was increased more than 250 V. The same could be said for DI water on BTNW as the CA measurement has not reached constant value yet. The rate of CA changes for all types of solution on TNW surface however began to decrease as they approached 220 V to less than 1° per 10 V. It is fair then to assume that the saturation angles for TNW surface would not be much lower than the lowest CAs induced which were between 96° and 104°.

These higher values than the 60° to 80° limit proposed by the literature may be due to the current study's employment of DC voltage rather than AC voltage combined with the long duration of voltage application before reaching the saturation angle [85]. Studies [84, 85] have demonstrated that CA saturation is highly time dependent; a longer time scale could cause the system to have a higher saturation angle thus never reaching the complete saturation. This is due to the reduction of the electrowetting force when electric field at the liquid-solid interface is attenuated by the charging of the dielectric layer [83]. This effect was confirmed when experiments were repeated to investigate the effect of maximum voltage duration on the CA reversibility and hysteresis; it was found that the saturation angles for the *Cytop*® surface decreased to values between 60° and 77° from the previously measured between 69° and 80° when the voltage duration was reduced from 765 seconds to 75 seconds. Another factor that could influence saturation angle, as suggested by Chevalliot et al. [85] is the type of hydrophobic material. *Cytop*® was found to have a higher saturation

angle (by 10°) than *FluoroPeI*TM under the same electrowetting condition. In this study, it appears that TNW promotes dielectric charging more than *Cytop*[®] does as is evident by its higher saturation angles [83].

Apart from being non-reversible for all types of solution other than DI water, BTNW surface also induced the lowest CA changes at 250 V with the values do not vary significantly from the initial CA value, particularly for 1 mg ml⁻¹ ovalbumin where it varied by only 26°. It is believed that, as the Top Coat material was found to be promoting dielectric charging in TNW, BTNW will also suffer the same problem since the BTNW layer includes the same Top Coat material. This problem is compounded by the fact that BTNW has a very high thickness due to the Base Coat material which further reduces its electrowetting performance. BTNW's high saturation angle due to charge trapping [82, 83] together with the irreversibility of protein solution droplets on BTNW resulted in a decision to exclude this surface from subsequent studies.

3.4.8 Roll-off angle measurements

Indirect measurements of the effect of DC voltage magnitude and its duration on protein adsorption rate were conducted by evaluating the tilting angle required for the TNW and *Cytop*[®] surfaces to roll-off a 20 µL droplet from its resting position. Roll-off angle is used as it directly corresponds with how much force is required to overcome the static friction force to move the droplet on the surface [127]. Accordingly it is a good indicator of how much protein has adsorbed onto the surface based on the magnitude of the force required to instigate the rolling off of the droplet. It is expected that the roll-off angle for the protein solution would be higher than the DI water due to higher pinning force

exhibit by protein solution as previously demonstrated by another study [215]. The pinning force at the contact line is attributed to the mechanical heterogeneities, such as surface roughness and asperities, and chemical heterogeneities (e.g. change in surface chemical groups) on the substrate surface [216]. As reported by Choi & Kim (2009), when a protein solution droplet is evaporated on a surface, it has been found that the droplet contact diameter does not change with time indicating a very strong pinning force at the contact line [215]. It is suggested that protein adsorption has occurred on the surface thus increasing the chemical hysteresis of the surface. The liquid-solid interface after the wetting has been changed compared to the one before wetting as the adsorbed protein molecules on the surface have changed the chemical composition of the surface [216].

Wenzel state is the condition where a droplet sitting on a superhydrophobic surface is impaled into the nanostructures. As reported elsewhere [128, 207], this state is described by complex relationship between the liquid pressure at interface and Wenzel roughness parameter which depends on the periodicity of roughness, real surface area, apparent surface area. All these parameters were not measured in this study to predict whether the nanostructures on the TNW can cause impalement. However, we believe that the impalement occurred due to the rather high hysteresis on the TNW surface even though the CA is reversible.

The roll-off angle was evaluated after the droplet underwent application of either 150 V or 250 V DC voltage for durations of 75 s and 765 s, according to the specific measurement. The roll-off angle was also evaluated for droplets

under the condition where no voltage is applied. For this condition, two durations were used: immediately after it was pipetted on the surface and after a resting period of 765 s.

Table 3.10: The roll-off angles for different types of solution on TNW and Cytop® surfaces

| Types of solution | Roll-off angle on Top Coat NW [°] | | | | | |
|------------------------------------|-----------------------------------|-------------|--------------|---------------|--------------|---------------|
| | 0 V | 0 V (765 s) | 150 V (75 s) | 150 V (765 s) | 250 V (75 s) | 250 V (765 s) |
| DI water | <1 | <1 | <1 | <1 | 2-4 | 4 |
| 0.01 mg ml ⁻¹ ovalbumin | <1 | 3 | 4-5 | 10 | 4 | 16-24 |
| 0.1 mg ml ⁻¹ ovalbumin | <1 | 3 | 3 | 9 | 10 | 20-53 |
| 1 mg ml ⁻¹ ovalbumin | <1 | 3 | 4 | 9 | 10 | 20-33 |
| Types of solution | Roll-off angle on Cytop® [°] | | | | | |
| | 0 V | 0 V (765 s) | 150 V (75 s) | 150 V (765 s) | 250 V (75 s) | 250 V (765 s) |
| DI water | 20 | 20 | 17-20 | 19-21 | 16-21 | 17 - 30 |
| 0.01 mg ml ⁻¹ ovalbumin | 24-45 | >90 | 32-38 | >90 | 27-28 | >90 |
| 0.1 mg ml ⁻¹ ovalbumin | 33-50 | >90 | 45 | >90 | 33-35 | >90 |
| 1 mg ml ⁻¹ ovalbumin | >90 | >90 | >90 | >90 | >90 | >90 |

As shown by **Table 3.10**, all concentrations of droplet solution roll-off very easily on TNW with angles ranging from less than 1° to 3° when the no voltage condition is applied regardless of the durations. The same low angles are observed for DI water on TNW when the droplets were applied with 150 V for both durations of 75 s and 765 s. The roll-off angles increase slightly for DI water when the voltage is increased to 250 V but the difference is insignificant between 75 s and 765 s under the same voltage. The slight increase for higher

voltage could be contributed to by the impalement of the droplets into the TNW nanostructures. DI water behaves similarly on *Cytop*® as on TNW where the roll-off angle is not influenced significantly by the variations in both voltage magnitude and duration. However the roll-off angles are higher on *Cytop*® ranging from 16°-30° compared to a value of only < 1° to 4° on TNW.

For the protein solution droplets, the roll-off angle on TNW increases with the increase in voltage duration indicating molecular adsorption from the protein solutions to the surface. The effect of the long voltage duration on the increase of roll-off angle is reinforced by the increase in the voltage as evident with the significant increase in roll-off angle when both 250 V and a long duration of 765 s are employed. The roll-off angles for all ovalbumin concentrations on TNW for other droplet conditions are generally low (less than 10°). Comparing the droplet solutions, there are considerable increases between the DI water and the protein solutions. There are however no substantial variations between different concentrations of protein solution for all droplet settings. In general, the increase in the roll-off angle can be ascribed to two factors: firstly, impalement of the droplet on to the TNW nanostructures and secondly, adsorption of protein molecules to the surface. For the first factor, the roll-off angle increases due to the higher energy required to move the droplet once the transition from Cassie-Baxter state to Wenzel state occurs. The second factor plays vital role when solutions with high protein concentration are used and the effect becomes more pronounced when both extended duration and high magnitude of voltage is employed.

On *Cytop*®, the roll-off angle generally increases with the voltage duration and the ovalbumin concentration. This surface demonstrates a very high roll-off angle of more than 90° for all concentrations of protein solution when the duration is 765 s regardless of the magnitude of the voltage. The stickiest

solution is 1 mg ml⁻¹ ovalbumin for which roll-off angles on *Cytop*® are larger than 90° for all settings including that without any voltage application or resting period. This finding reveals how predisposed *Cytop*® is to protein adsorption when high concentration protein solutions are used and the condition is further exacerbated by a prolonged duration of contact. Comparing the two surfaces, TNW always displays lower roll-off angles than *Cytop*® for all types of solution and settings implying a considerably lower biofouling rate on its surface.

Contact angle hysteresis (CAH) plays a major role in influencing the behavior of a droplet sitting on a tilted substrate where its value is the difference between the advancing CA, θ_{adv} (the CA on the downhill side) and the receding CA, θ_{rec} (the CA on the downhill side) [217]. The higher the CAH, the higher the pinning force and energy barrier required to move the contact line thus the higher the required roll-off angle of a droplet on a tilted surface [216, 217]. Measurement of CAH was not conducted but it is anticipated that the CAH for TNW would be very low especially when no voltage is applied beforehand, as evidenced by the very low roll-off angles (less than 1°). Roll-off angle can reflect the CAH value when the droplet is in Cassie-Baxter state [129]. CAH contributes greatly to the static friction force of a droplet on a solid substrate as given by the following **equation (3.1)** and **(equation (3.2))** [129]:

$$(3.1) \quad F_f = 2\gamma_{lg}w (\cos \theta_{adv} - \cos \theta_{rec})$$

$$(3.2) \quad \approx -4\gamma_{lg} w \sin \theta_c \sin \left(\frac{\Delta\theta}{2} \right)$$

where F_f is the static friction force, w is the droplet width, θ_{adv} is the advancing CA, θ_{rec} is the receding CA, θ_c is the static CA, and $\Delta\theta$ is the CAH. The low CAH on TNW reduces the driving force required to overcome the static friction force, thus causing

the low roll-off angles. However the roll-off angle on TNW increases once voltage is applied, indicating that a higher driving force is needed to overcome the pinning of the droplet to the surface. Based on the above equation, the static friction force is also influenced by the static CA. As presented previously, TNW has the advantage of having a higher static CA ($168^\circ - 171^\circ$ at 0 V; $121^\circ - 134^\circ$ after 765 s of 250 V) for all types of solutions when compared to *Cytop*[®] ($97^\circ - 110^\circ$ at 0 V; $71^\circ - 104^\circ$ after 765 s of 250 V) which will reduce the magnitude of the static friction force. Therefore in most cases the lower roll-off angles demonstrated by TNW compared to *Cytop*[®] are in agreement with these hypotheses where the droplets require lower driving force on TNW than on *Cytop*[®] to instigate movement.

Work of adhesion, W , represents the work done to separate a droplet from a solid substrate [218]. The same conclusion that higher force is required to move a droplet on the *Cytop*[®] than the TNW surface can also be reached if the work of adhesion of DI water droplets ($\gamma_{lg} = 72 \text{ mN m}^{-1}$) [212] on both surfaces is calculated using Young-Dupré **equation (3.3)** [219]:

$$(3.3) \quad W = \gamma_{lg} (1 + \cos \theta_c)$$

Again, the work of adhesion values calculated both at rest (0 V applied) and after application of 250 V for the 765 s duration are the highest for *Cytop*[®] ($W_{\text{Cytop}^\circledast}|_{0 \text{ V}} = 47.37 \text{ mN m}^{-1}$ at rest and $W_{\text{Cytop}^\circledast}|_{250 \text{ V}} = 55.19 \text{ mN m}^{-1}$ after 250 V) as compared to that calculated for TNW ($W_{\text{TNW}}|_{0 \text{ V}} = 0.89 \text{ mN m}^{-1}$ at rest and $W_{\text{TNW}}|_{250 \text{ V}} = 22.33 \text{ mN m}^{-1}$) showing that more energy is required to detach and move droplets from *Cytop*[®] than from TNW surfaces.

3.4.9 Biofouling rate evaluation

To further validate the results of the roll-off angle measurements, a direct measurement of the effect of voltage magnitude and its duration on protein adsorption rate was conducted. Both *Cytop*® and TNW surfaces were prepared on glass slides instead of silicon substrates and 0.1 mg ml⁻¹ fluorescent-tagged Alexa Fluor 647 fibrinogen was used as the droplet solution. The droplets were subjected to exactly the same conditions (voltage of 0 V, 150 V, or 250 V for both 75 s and 765 s) as described in the roll-off angle measurements. Following the exposure of the *Cytop*® and TNW surfaces to the 20 µl fibrinogen droplets, the glass slides were evaluated for the mean (the raw scanner data is an image with a droplet extending over multiple pixels, the mean of which is calculated) fluorescence intensity of the resulting adsorbed protein-labelled spots. An example of a glass slide with the resulting spots due to the adsorption of protein-labelled molecules to TNW surface is shown **Figure 3.19**. The results of the mean fluorescence intensity are shown in the same figure.

Comparing the results in **Figure 3.19** with those of **Table 3.10** for roll-off angle measurements, there is a consistency of higher roll-off angle values and higher fluorescence intensity on the *Cytop*® than the TNW surface. Higher fluorescence intensity indicates a higher level of biofouling and as can be seen from the graph the differences in the intensity between *Cytop*® and TNW for all settings are very significant. For the *Cytop*® surface, protein adsorption does not appear to be affected substantially by the maximum voltage magnitude but has a strong dependency on the voltage duration. On TNW surface, the fluorescence intensity is very low for all voltages under 250 V regardless of the voltage duration. The protein adsorption however doubled for the 75 s case and increased four times for the 765 s case when 250 V was applied on TNW. Again, this result is closely matched with the roll-off angle

measurement for 0.1 mg ml^{-1} ovalbumin on the same surface. The findings of the direct evaluation of protein adsorption further corroborate the suggestion of this study that superhydrophobic surfaces can reduce the amount of biofouling compared to conventional hydrophobic surfaces such as *Cytop*®.

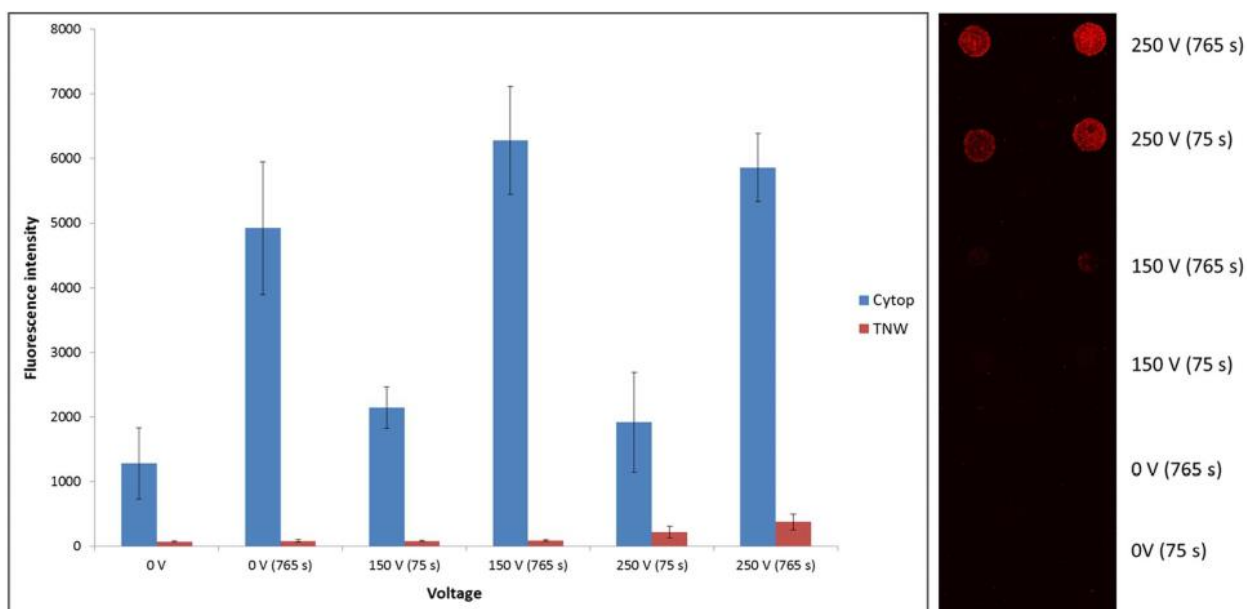


Figure 3.19: Biofouling rate of Alexa Fluor 647 human fibrinogen on *Cytop*® and TNW surfaces (Left) Mean fluorescence intensity of 0.1 mg ml^{-1} fluorescent-tagged fibrinogen after different electrowetting treatments. (Right) The fluorescence image of the TNW surface after exposure to the 0.1 mg ml^{-1} fluorescent-tagged fibrinogen where protein adsorption is indicated by the red spots [220].

3.4.10 Conclusions

Off-the-shelf products offer an alternative to the expensive conventional materials and techniques used for the fabrication of EWOD devices. The first part of this chapter explored the potential of using commercial polyurethane materials as the EWOD dielectric component while the subsequent section examined commercial superhydrophobic and hydrophobic materials as the actuating surface component. While the outcomes of these sections do not solve the problem of the EWOD plate's high production cost, their results provide insight concerning products worthy of further

investigation and in which direction development might go (e.g. improvement of deposition techniques or improvement in material composition) if future development is pursued.

These investigations found that two products, Rust-Oleum Polyurethane (RO-PU) and NeverWet top coating (TNW) have the potential to be employed as substitutes for the dielectric and actuating surface components of a low-cost disposable EWOD device, respectively. For the RO-PU material, improvement is needed in its fabrication process before it can be employed reliably in a device. The spraying method has been used to deposit the dielectric layer but this method has the drawback of producing layer with non-uniform thickness as it relies on the skill and consistency of the operator. This is problematic during droplet actuation as it causes different voltage requirement across the EWOD device surface. It is suggested that a thicker layer of the commercial dielectric materials is employed in future investigation by depositing more than one successive spin-coated layers to avoid failure due to pinholes as has been demonstrated earlier. Another available option is by employing automated spraying method instead of doing it manually so that the amount of deposited material can be controlled precisely.

The TNW superhydrophobic materials have demonstrated good electrowetting reversibility and capability to actuate a droplet across more than five electrodes reliably. The superhydrophobicity of the material is an added benefit since a previous study [15] has reported superhydrophobic surface as a self-cleaning surface which can be used as an approach to tackle the protein adsorption problem. While TNW has demonstrated a good electrowetting performance, another component of the *NeverWet®* product, the BTNW is irreversible and promotes charge trapping as indicated by its very high saturation angle. Due to these reasons, within this study, the

TNW product has been selected for detailed investigations of its electrowetting behaviour and response to protein-laden droplets.

In terms of electrowetting hysteresis, the TNW has a higher hysteresis than *Cytop*® surface due to the impalement of a droplet into the surface nanostructures. This higher hysteresis however does not affect the capability of the surface to transport droplet as has been shown in **Section 3.3.3** and later in **Section 4.4.2**. A very promising result has been achieved in terms of the TNW surface response when exposed to droplet with high concentration of ovalbumin protein. The TNW has shown minimal protein adsorption by demonstrating a low roll-off angle for 1 mg/ml ovalbumin applied with voltage up to 250 V for the long duration of 765 s. In contrast, a droplet with the same concentration of ovalbumin, but without any voltage application and exposed only for a very short time adheres to the *Cytop*® surface, requiring a very high force to remove it from the surface.

This finding is further corroborated by fluorescence measurement of both the TNW and *Cytop*® surfaces after exposure to protein-laden droplets under the same settings described in the roll-off angle measurements. The TNW again displays the lowest protein adhesion between the two surfaces by having a lower fluorescence intensity in all settings compared to the *Cytop*® surface. In the following chapter, the TNW product feasibility as an actual component of EWOD device is investigated by employing the TNW material as the actuating surface to linearly transfer a few types of protein-laden droplet. The devices tested for this purpose were fabricated using the conventional methods and materials for the substrate, electrode, and dielectric components; only the actuating surface employs an alternative material.

The next chapter also aims to explore the prospect of using the inkjet printing technique described in Chapter 2 to fabricate a more elaborate EWOD device. For this new objective, despite the very encouraging results reported in this chapter for off-the-shelf materials, Parylene-C and *Cytop*® have been selected as the dielectric and hydrophobic materials respectively due to their robustness and the reproducibility of the materials' fabrication process, which are harder to achieve with the low-cost commercial products that have been tested so far. By doing so, efforts can be focused upon new device topology challenges based upon the most mature dielectric and hydrophobic materials available. As can be seen from droplet actuation results in **Sections 3.2.3** and **3.3.3**, whilst promising, the devices built using combination of the inkjet-printed PEDOT:PSS electrodes on PET substrate and the commercial dielectric and superhydrophobic products do not produce devices that are currently capable of transporting droplet across all electrodes. To avoid the same problem in the devices fabricated in the next chapter, conventional dielectric and hydrophobic materials are used for the inkjet-printed devices.

4 Application prospect of the low-cost EWOD devices

4.1 Introduction

The previous two chapters investigated the feasibility of using alternative methods and materials for the fabrication of EWOD devices. Inkjet printing of conductive polymer ink on polymer substrate has shown reliability in producing functional EWOD devices while the commercial superhydrophobic surface is capable of actuating droplet across its surface and has shown very low surface contamination for droplets with high protein concentration. The aim of this chapter is to present EWOD devices with elaborated and more complicated design and/or functions using the methods and materials that have been investigated so far. To test the usability of the selected materials and methods, three types of EWOD devices have been fabricated: a three-dimensional (3D) 4×4 electrode array device, a magnetic micro-immunoassay device and a superhydrophobic anti-biofouling device.

The first device is proposed as a method to overcome the topological limitation of EWOD electrode array size, usually restricted to $N \times 3$ due to the difficulty of interconnection between the inner electrodes and the contact pads [115]. The second device was built specifically as a proof of principle that the proposed inkjet-printed device is capable of performing an immunoassay, a biochemical test to detect the presence of an 'analyte' (e.g. protein antigen or antibody) in a sample [71]. Apart from transporting droplets, this device is also capable of performing particle separation by means of magnetic manipulation. The electrodes in these two types of EWOD device were made of conductive polymer ink patterned using a laboratory-grade printer, Fujifilm Dimatix printer on a polymer substrate. The final and third device is made of chrome-on-glass electrodes while commercial superhydrophobic material is used as the actuating surface to demonstrate the ability of the surface to transport a highly

concentrated protein droplet. The following sections report the fabrication and performance of the aforementioned EWOD devices that could be targeted at lab-on-chip applications.

4.2 Three-dimensional 4 × 4 electrode array EWOD device

Design for EWOD devices is usually constrained to a $N \times 3$ size due to the limited means to connect driving electrodes located in the middle of an electrode array with their corresponding contact pads [115]. Generally, the tracks to link the inner electrodes with the contact pads are patterned between the electrode spacing [139]. The spacing between two adjacent electrodes is however very narrow and usually can only fit one track depending on the type of patterning method used. The largest reported inter-electrode spacing (without interdigitated microstructures included in the design) where the droplet was able to move efficiently in an EWOD device without any impediment is 150 μm [180].

An EWOD device with a large electrode array of 5×8 has been constructed previously using complementary metal-oxide-semiconductor (CMOS) compatible fabrication technology [115]. The device was built using multi-level metallisation approach, creating a two-level aluminium structure with the lower level used for the tracks between the inner electrodes and the contact pads. Similar to the other clean-room technology, the device fabrication using this method is costly as it requires expensive equipment and materials [20, 21].

Another strategy to construct a large electrode array in EWOD device is by using a PCB substrate, as demonstrated by Gong & Kim [139]. They fabricated a four layers 8×8 EWOD device by lapping epoxy woven layers with patterned copper layers where each layers are connected by vias with copper-plated walls. This device

however requires a very high actuation voltage of 500 V and to reduce the voltage to below 100 V a post processing comprised of wet etching and re-deposition and re-patterning of the electrodes are necessary to reduce the trenches that impeded the droplet movement [139]. A third approach utilises a large programmable array of thin film transistors (TFT) normally used in liquid crystal displays (LCD) as the EWOD electrodes [221]. The electrode array size is 64 × 64 with the size of each element is 210 μm. The fabrication of the TFT backplane is however a proprietary technology that is difficult to access.

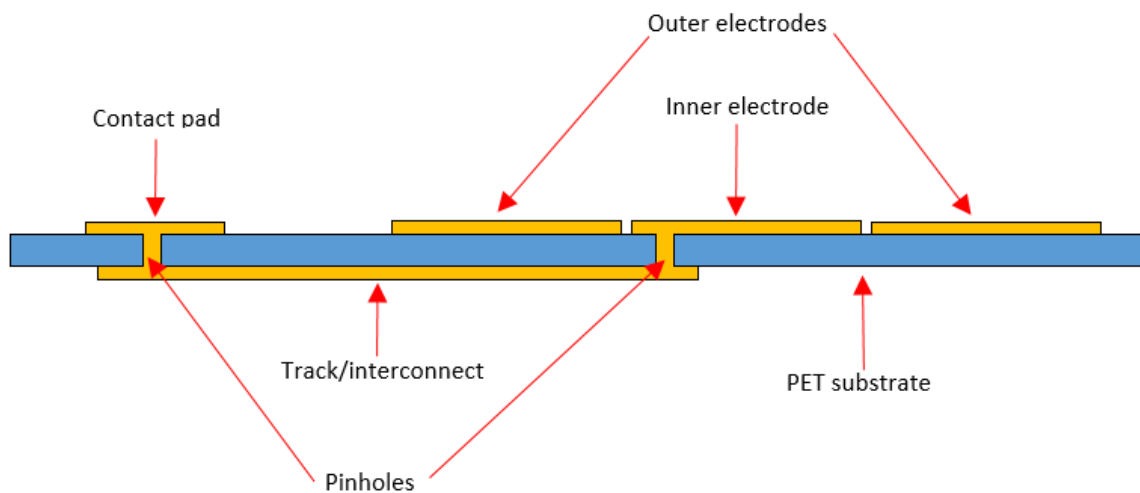


Figure 4.1: Side view of the simplified 3D 4 × 4 electrode array device structure. The yellow component represents the inkjet-printed conductive ink while the blue component is the PET substrate. In this structure, both sides of the substrate, top and bottom surfaces are deposited with the ink to form the interconnection between the inner electrode and the contact pad. Pinholes are fabricated at the relevant contact pad and inner electrode to connect between the top surface electrode and contact pad with the bottom surface track.

If the inkjet printing method and the ink-substrate combinations investigated in Chapter 2 of this thesis were to be employed for the patterning of a large size electrode array, it would be challenging to pattern even just one track between the electrode spacing due to the track relatively large width (more than 150 μm). To overcome this

problem, a 3D electrode interconnection as shown in **Figure 4.1** is suggested. Instead of patterning the conductive layer only on one side of the substrate, both sides are used. For the hard-to-reach inner electrodes, the tracks connecting them to the contact pads are printed on the bottom side of the substrate. Pinholes are drilled into the substrate before the printing process so that the ink will cover the pinholes and thus linking the relevant top surface contact pads and electrodes with the bottom surface tracks.

4.2.1 Design and fabrication of the 3D 4 × 4 electrode array devices

The design of the 3D 4 × 4 electrode array is shown in **Figure 4.2**. The first and second images show the pattern printed on the top and bottom surfaces of the substrate respectively. Since both sides of the substrate are used for electrode pattern printing, the top side and the bottom side patterns need to be aligned correctly. The two squares on the top left and top right in each image are markers used for alignment of the substrate on the printer platen before the start of a printing pass. A white A4 paper printed with the same square markers is taped on the platen so that the markers on the substrate can be aligned to the ones on the paper. The third image illustrates the location of the pinholes on the substrate. The pinholes are aligned using the same method by laser cutting the same markers to the substrate. Finally, the fourth image is the superposed images of the top and bottom patterns and the laser-cut pinholes. The nominal width of the tracks is 150 μm while the nominal inter-electrode gap is 180 μm. Two electrode nominal sizes were used to fabricate the device, 1.7 mm and 2.0 mm. Nominal size is defined as the size of the electrode or pattern in the CAD file, not the measured size of the inkjet-printed electrode. The patterns were drawn using

Adobe Illustrator®, then converted into bitmap images with 847 dpi resolution before transferred to the Fujifilm Dimatix DMP-2850 printer.

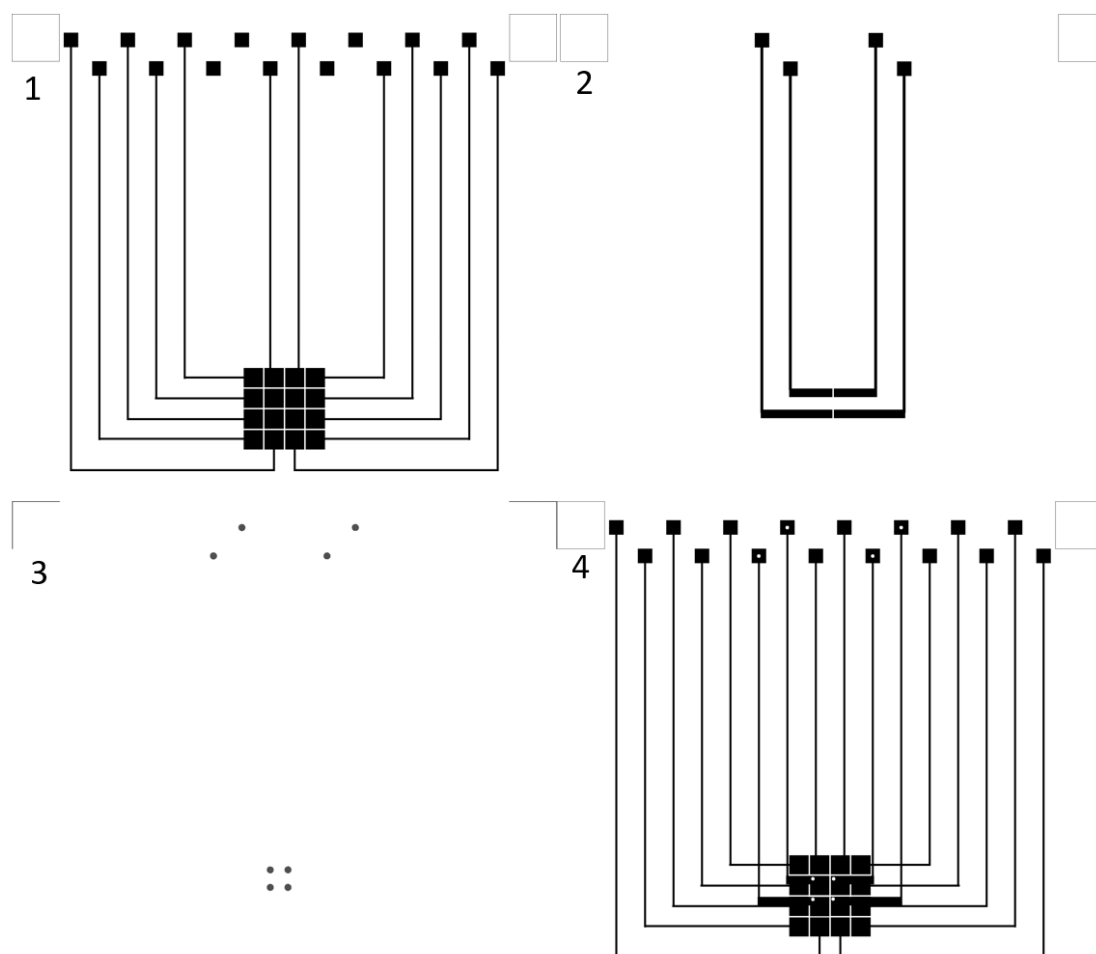


Figure 4.2: The design of the 3D 4 × 4 electrode array. The first and second images are the top and bottom pattern respectively. The squares at the top corners in each image are the markers for alignment on the printer platen. The third image shows the location of the laser-cut pinholes. The pinholes size is exaggerated here for illustration purpose wherein the actual drawing the size is 10um (the smallest possible dot size for the laser cutter software). The last image is the superposition of the top, bottom, and the laser-cut pinholes images.

4.2.1.1 Printer setting and types of ink and substrate

The Fujifilm Dimatix DMP-2850, previously described in details in **Section 2.3**, was used to pattern the EWOD electrodes. PET polymer, *Melinex*® was used as substrate for the base plate. Two types of ink, silver and PEDOT:PSS (PP) were tested for

compatibility with the proposed 3D design of the plate. The printer settings used for both types of ink were the same as in **Section 2.3.1**. Only one nozzle was used for printing. The firing voltages were between 18 V to 25 V for PP and between 28 V to 35 V for silver. The platen temperatures were set to ambient temperature for PP while for silver ink it was 60 °C. No heating was applied to PP ink but the silver ink was heated to 30 °C to 35 °C. The substrate was treated with UV/ozone radiation for 15 minutes for PP ink printing while no treatment was required for silver ink.

To ensure that electrical connection is established between the contact pads and the inner electrodes, the top surface electrode pattern and the bottom surface electrode pattern must be contiguous through the pinhole. Therefore, it is critical for the ink droplets to be able to coat the inside surface/wall of the pinholes so that the top and bottom surfaces are connected. Silver ink was first tested but it has been found that this ink is not capable of fully coating the inside surface of the pinholes. A total of nine printing passes (five over the top surface and four over the bottom surface) over the same pinholes did not produce a connective path between the top and the bottom surfaces. For the PP ink, it was demonstrated that only one printing pass over the top surface and another pass over the bottom surface was sufficient to establish the desired electrical connection between the two surfaces. In the subsequent sections, only PP ink was used for the fabrication of the 3D 4 × 4 electrode array device.

4.2.1.2 The fabrication process of the base plate

Figure 4.3 describes the process flow of the creation of the 3D 4 × 4 electrode array base plate. It begins by laser cutting the pinholes including the square markers (as shown in **Figure 4.2**) into the substrate using laser cutter (Trotec Speedy 300, Marchtrenk, Austria). After drilling, the substrate top surface is cleaned using

compressed air to remove any dust and large particles before being treated with UV/ozone cleaner (Novascan PSD, Iowa, US) for 15 minutes.

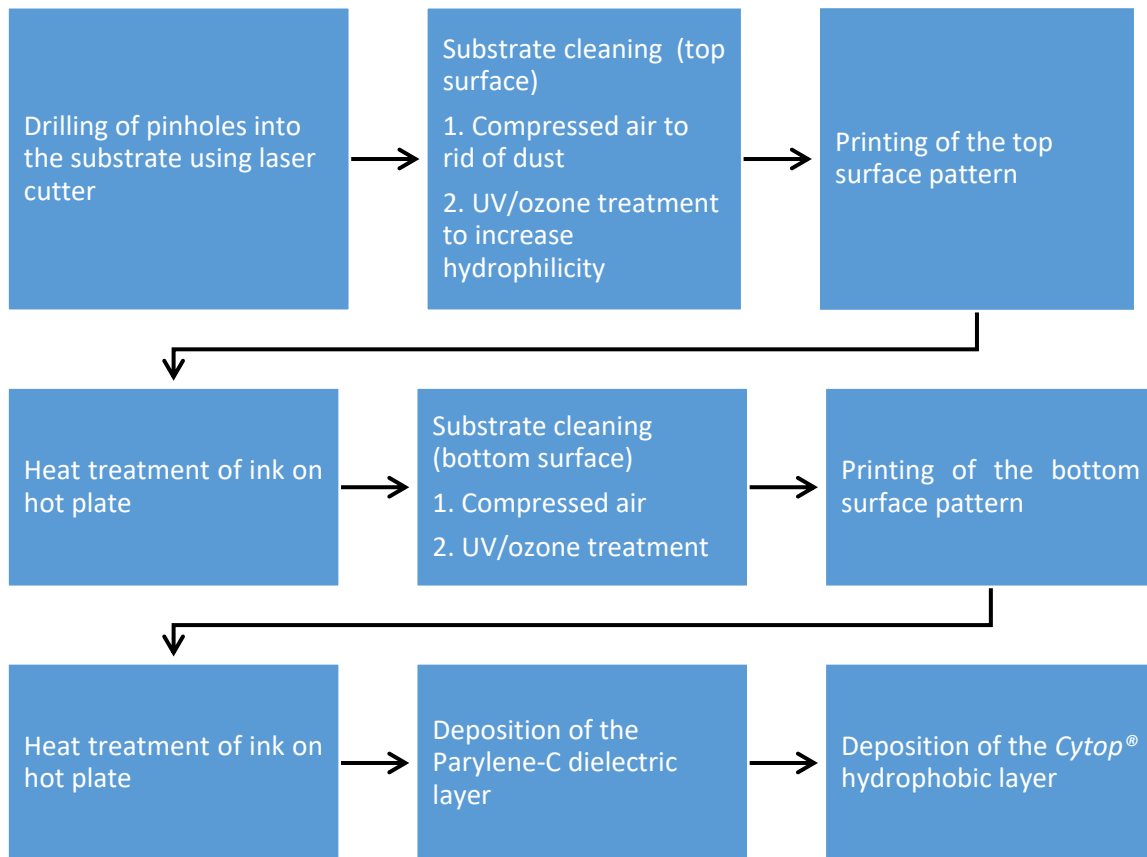


Figure 4.3: The process flow of the 3D 4 × 4 electrode array device base plate fabrication.

Prior to the printing process, a white A4 paper sheet displaying the printed square alignment markers is taped to the printer platen. This is used as a guide to position the substrate on the platen for each printing pass by aligning the laser-cut square markers with the ones on the white A4 paper. The top pattern is printed onto the substrate, followed by a heat treatment on the hot plate at 110 °C for 5 minutes. Before the start of the bottom pattern printing, the backside surface of the substrate is cleaned and treated as previously with compressed air and UV/ozone. The substrate is then heat treated again at 110 °C for 5 minutes after the printing is completed. Parylene-C, as the dielectric layer and *Cytop*®, as the hydrophobic layer, were then

deposited as described in **Sections 2.2.1.7** and **3.3.1.1** respectively. The thickness of the dielectric layer was approximately 6.0 μm .

4.2.1.3 Assembly of the 3D 4 x 4 electrode array device

The printed base plate was assembled with a grounded cover plate made of an ITO-coated glass slide to form a parallel-plate device. A layer of *Cytop*® was deposited on top of the ITO-coated glass slide as the hydrophobic layer. The gaps between the base and cover plates were 380 μm for the 1.7 mm electrode and 130 μm for the 2.0 mm electrode respectively using plastic substrates as the spacer. The smaller gap for the larger electrode size is to ensure the volume of droplet overlap the next electrode. This is to facilitate actuation as the employed electrode design does not incorporate the interdigitated border as previously used in other studies [62, 222]. Different thickness of spacer were used for the different electrode sizes to keep the volume of droplet used for transportation constant. A custom made poly(methyl methacrylate) (PMMA) frame was employed to secure the EWOD plates in place. The setup was similar to **Figure 2.2**. Spring-loaded pins were used to connect the base plate with USB powered compact electronics. The electronics was able to control independently all 16 electrodes using 1 kHz sine wave with voltage that can be adjusted up to 225 V_{RMS} . 5 μl of deionised (DI) water was used to evaluate the transportation of droplet in the parallel-plate EWOD devices.

4.2.2 Vias fabrication

The presence of large particles or any heterogeneity on the actuating surface of an EWOD device could impede droplet movement [223]. To avoid this problem, the vias in the 3D 4 x 4 electrode array device need to be as small as possible while large enough to allow the ink droplet to flow through them. Prior to the decision of using laser cutting as the method to fabricate the micro-size vias, attempts were made using

two other methods: a bench drill press and manually piercing the substrate using a pin. The benchtop drill press bit size was 0.25 mm while the pin diameter was 0.34 mm. However the holes produced using these two methods were too big with diameters of more than 0.35 mm. For the pin method, not all of the substrate material was removed. This altered the contour and the planarity of the substrate near the vias, causing the ink droplets to spill and deviate from the intended pattern after being jetted onto the substrate.

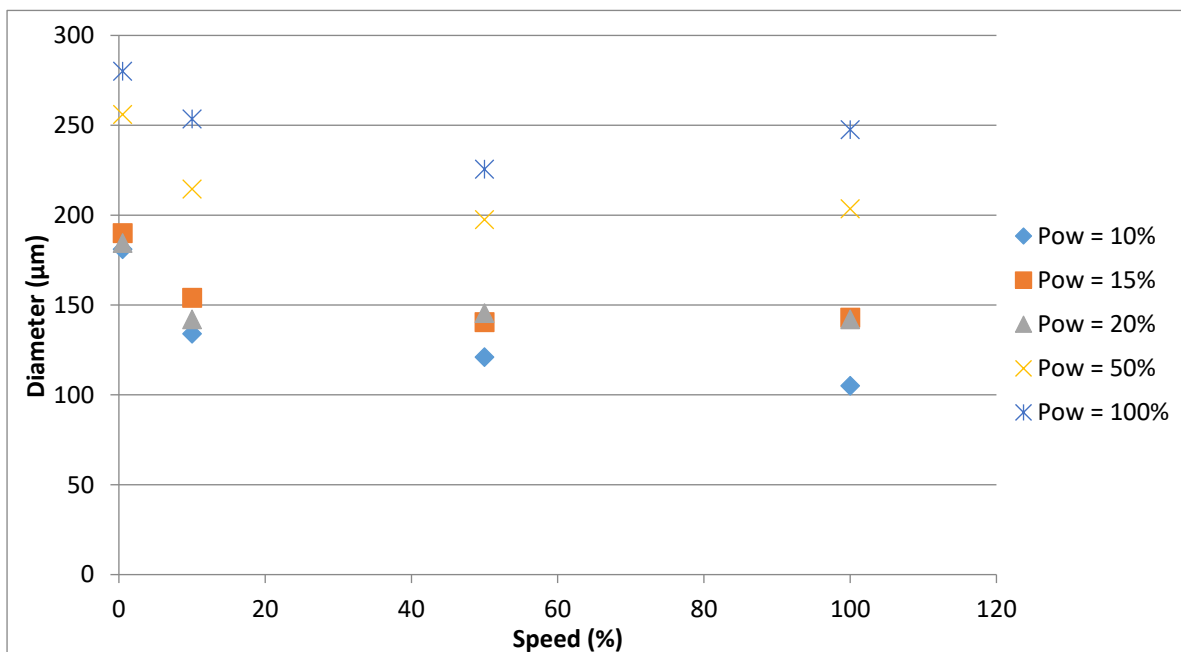


Figure 4.4: The effect of laser power and speed on the diameter of via. Five laser power levels, 10%, 15%, 20%, 50%, and 100% were used while for the cutting speed, four settings were used, 0.5%, 10%, 50%, and 100%. The diameter decreased as the laser speed increased and the laser power decreased.

The laser cutter produced the smallest via out of the three methods. A brief investigation was conducted to determine which laser cutter settings produced vias with the smallest diameter. The depth of the laser engraving is varied by controlling two parameters: the laser power and the cutting speed. Both parameters are adjustable from 0% to 100%. The smallest possible dots that can be illustrated using

the Adobe Illustrator® software, 0.01 mm in size were drawn and exported to the laser cutter. **Figure 4.4** presents the relationship between the size of the via with the speed and power setting of the laser cutter. The diameter of the pin holes were measured using the fiducial camera and measurement tool available in the Fujifilm Dimatix printer software. The smallest diameter, 105 μm was produced using 10% of laser power and 100% speed. The via diameter decreased with increasing laser cutting speed and decreased with reduced laser power. The largest diameter, 280 μm was fabricated using 100% power and 0.5% speed. Using 10% power or lower with the highest speed of 100% can produce smaller via diameters albeit rather unreliably, with occurrences of incomplete ‘blind’ holes. For the fabrication of the final 3D 4 \times 4 electrode array device that was successful in transporting droplet across the inner electrodes, the setting of 15% power and 100% speed which resulted in average diameter of 143 μm was used to fabricate the vias. **Figure 4.5** shows a via fabricated using the laser-cut method where the resulting hole has lips surrounding it.

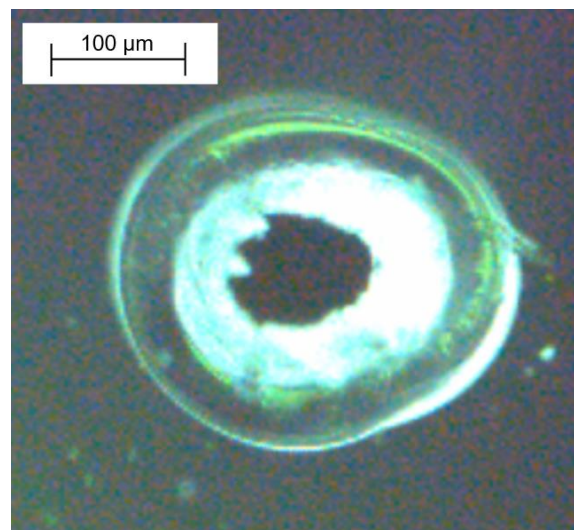


Figure 4.5: A via fabricated with laser cutter using 10% power and 100% speed. The average diameter of the hole where the substrate is fully removed is 105 μm and the average diameter including the lips around the hole is 270 μm .

Apart from the via size, another aspect that could affect the performance of the 3D 4 × 4 electrode array device is the position of the via on the inner electrode. To determine at which position the via has the least effect on the droplet movement, two via locations were tested; one is in the centre of the electrode and another one is on the top left corner of the electrode.

4.2.3 Electrode characterisation and identification

Table 4.1 reports the characteristics of the inkjet-printed PEDOT:PSS electrodes in the 3D 4 × 4 array device. Two electrode sizes were employed, 1.7 mm and 2.0 mm to study the effect of the ratio of the via size to the electrode size on the droplet actuation performance. The measured average size did not deviate too much from the intended dimension. The electrode spacing applied in the CAD is 180 µm resulting in actual spacing between 137 µm and 144 µm in the inkjet-printed device. The measured average track widths are 149 µm and 181 µm for vertical and horizontal tracks respectively with 150 µm being the nominal size. **Figure 4.6** shows the number identification for each of the electrodes in the 4 × 4 electrode array from 1 to 16. The inner electrodes are identified as number 6, 7, 10, and 11.

Table 4.1: The nominal and measured size of the inkjet-printed PEDOT:PSS electrodes in the 3D 4 × 4 electrode array device.

| | Nominal size | Average measured size | |
|-------------------------|--------------|-----------------------|---------------|
| | | Horizontal (µm) | Vertical (µm) |
| Electrode size | 1.7 mm | 1744 ± 20 | 1716 ± 20 |
| | 2.0 mm | 2060 ± 20 | 2040 ± 9 |
| Electrode spacing width | 180 µm | 144 ± 5 | 137 ± 7 |
| Track width | 150 µm | 181 ± 9 | 149 ± 5 |

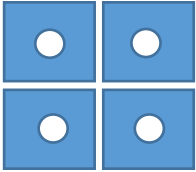
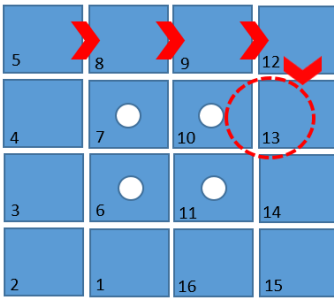
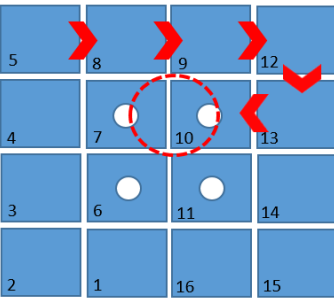
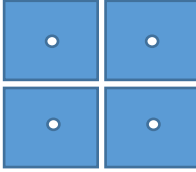
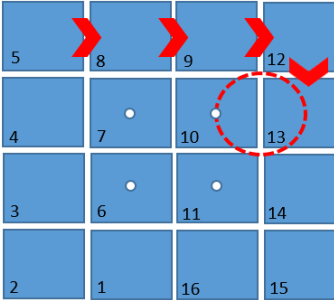
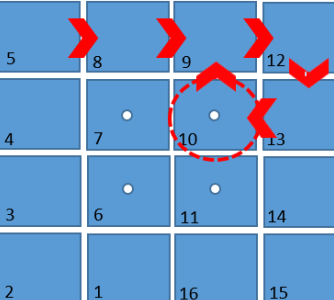
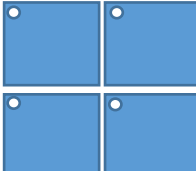
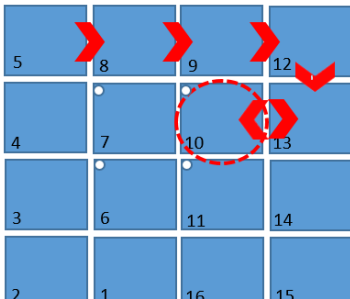
| | | | |
|---|---|----|----|
| 5 | 8 | 9 | 12 |
| 4 | 7 | 10 | 13 |
| 3 | 6 | 11 | 14 |
| 2 | 1 | 16 | 15 |

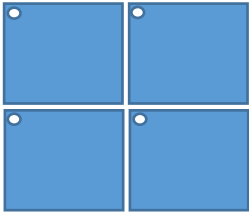
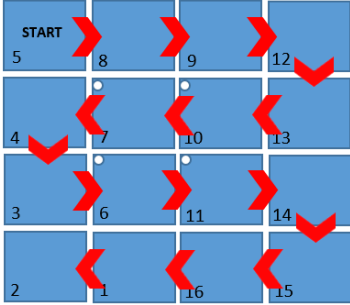
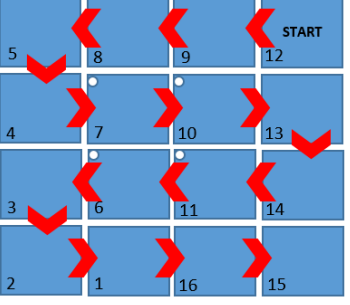
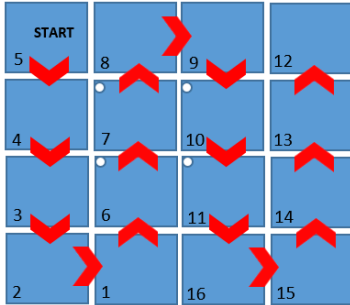
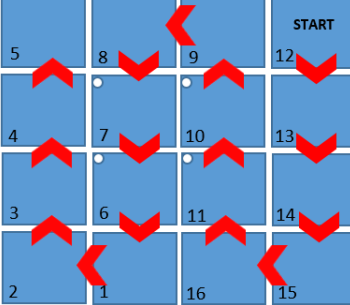
Figure 4.6: The identification number for the 16 electrodes in the 3D 4 × 4 electrode array device.

4.2.4 Droplet transportation across vias in 3D 4 × 4 electrode array device

Four configurations differing in electrode size, via size, and via position on the electrode were fabricated to demonstrate which one was capable of transporting 2.5 μ l of droplet across the inner electrodes. The first three configurations have the electrode size of 1.7 mm while the final one has the size of 2.0 mm. **Table 4.2** summarises the results of the droplet transportation across the electrodes in the 3D 4 × 4 array device for the different types of configuration. The electrical connections for all 16 electrodes on the plate were checked before droplet actuation was conducted and found to be all well-connected to the contact pads. This step was conducted on all plates used for droplet actuation

Table 4.2: Summary of the droplet movement in the 3D 4 × 4 array device for different types of configuration. The first column represent the design employed for the four inner electrodes while the second column depict the droplet transportation across the 3D 4 × 4 array device. The red dashed circles represent the position where the droplet became stuck in each device.

| Device configuration | Droplet movement | |
|---|--|---|
|  <p>Electrode size: 1.7 mm Via size: 225 μm Via location: Centre</p> | <p>Voltage: 150 V_{RMS}</p>  <p>Sequence: 5-8-9-12-13-10-7-4-3-6-11-14-15-16-1-2-3-4</p> | <p>Voltage: 225 V_{RMS}</p>  <p>Sequence: 5-8-9-12-13-10-7-4-3-6-11-14-15-16-1-2-3-4</p> |
|  <p>Electrode size: 1.7 mm Via size: 110 μm Via location: Centre</p> | <p>Voltage: 150 V_{RMS}</p>  <p>Sequence: 5-8-9-12-13-10-7-4-3-6-11-14-15-16-1-2-3-4</p> | <p>Voltage: 225 V_{RMS}</p>  <p>Sequence: 5-8-9-12-13-10-7-4-3-6-11-14-15-16-1-2-3-4</p> |
|  <p>Electrode size: 1.7 mm Via size: 126 μm Via location: Left corner</p> | <p>Voltage: 150 V_{RMS} and 225 V_{RMS}</p>  <p>Sequence: 5-8-9-12-13-10-7-4-3-6-11-14-15-16-1-2-3-4</p> | |

| Device configuration | Droplet movement | |
|---|---|--|
|  <p data-bbox="204 517 411 685">Electrode size: 2.0 mm Via size: 137 μm Via location: Left corner</p> | <p data-bbox="491 271 715 297">Voltage: 150 V_{RMS}</p>  <p data-bbox="491 613 778 712">Sequence: 5-8-9-12-13-10-7-4-3-6-11-14-15-16-1-2-3-4</p> | <p data-bbox="970 271 1193 297">Voltage: 150 V_{RMS}</p>  <p data-bbox="970 613 1257 712">Sequence: 12-9-8-5-4-7-10-13-14-11-6-3-2-1-16-15-14-13</p> |
| | <p data-bbox="491 757 715 784">Voltage: 150 V_{RMS}</p>  <p data-bbox="491 1099 794 1198">Sequence: 5-4-3-2-1-6-7-8-9-10-11-16-15-14-13-12-9-8</p> | <p data-bbox="970 757 1193 784">Voltage: 150 V_{RMS}</p>  <p data-bbox="970 1099 1273 1198">Sequence: 12-13-14-15-16-11-10-9-8-7-6-1-2-3-4-5-8-9</p> |

The first configuration's via is positioned at the centre of the electrodes. It has the largest via diameter with 225 μm (laser power: 100%, speed: 8%). Activating the electrodes using 100 ms pulse signal at 150 V_{RMS} (1 kHz), the droplet was able to move efficiently until it reached the first inner electrode. Setting the electrode activation sequence as following: 5-8-9-12-13-10-7 (illustrated in **Table 4.2**), the droplet became stuck between electrode 13 and 10 where 10 was an inner electrode with a via on it. Increasing the voltage to 225 V_{RMS}, the droplet was able to move across electrode 10 but stopped again, now between electrode 7 and 10.

The droplet has difficulty to move across the inner electrodes because of the diminishing electrostatic force in this region. The presence of a via which is a non-conductive area reduces the total capacitive energy to drive the droplet forward to the

inner electrode. The electrostatic force generated on an activated electrode is represented by the following **equation (4.1)**:

$$(4.1) \quad F_{electrostatic} = \frac{w \epsilon_0 \epsilon_r}{2d} V^2$$

where ϵ_0 is the relative permittivity, ϵ_r is the insulating layer dielectric constant, d is the insulating layer thickness, w is the width of the electrode, and V is the applied voltage [93].

The droplet was able to move across the first inner electrode when the electrostatic force was increased by using a higher voltage of 225 V_{RMS}. However, beyond this point, the droplet stopped again and was now trapped between two inner electrodes. It is believed that apart from reducing the electrostatic energy, the heterogeneity caused by the presence of the via on the actuating surface also creates a pinning force that trapped the droplet from moving forward. Stuck between two inner electrodes, not only was the electrostatic force to move the droplet forward reduced, but the droplet also needed to overcome pinning force originating from the via of the first electrode. The sequence of droplet movement onto the first inner electrode and then got stuck in between two inner electrodes is shown in **Figure 4.7**. From the figure, the droplet was positioned on electrode 13 initially. The second image shows the droplet was able to move onto the first inner electrode 10. The third image shows the droplet elongated when the next electrode 7 was activated. However, It can be seen that the trailing edge or contact line of the droplet is pinned to the via in electrode 10, preventing it from moving completely onto electrode 7, the second inner electrode. The droplet was trapped in between two electrodes due to contact line pinning by the via.

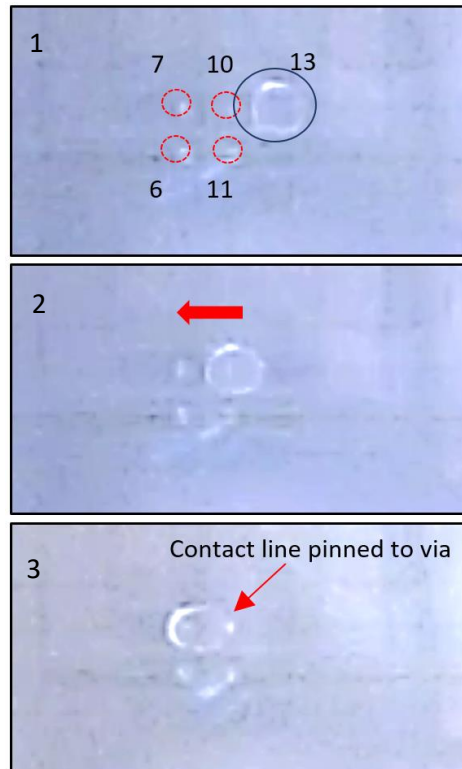


Figure 4.7: Droplet movement across inner electrodes, from electrode 13 to electrode 7 using $225 V_{RMS}$ in the first configuration. There are four inner electrodes with the vias located in the middle of each electrodes. In the first image, the droplet is indicated in the blue circle while the four vias are indicated inside the dashed red circles. The red arrow indicates the direction of droplet movement.

The second configuration in which the vias are also located at the centre of the electrodes but with a smaller diameter ($110 \mu\text{m}$) has the same problem where the droplet stopped in between electrodes 13 and 10 when $150 V_{RMS}$ of actuation voltage was used. When the voltage was increased to $225 V_{RMS}$, the droplet was able to move onto electrode 10 but still could not overcome the pinning force to move onto the next inner electrode 7: a similar problem to the first configuration. The droplet however was able to move back to electrode 9 (without a via and located next to electrode 10) when the sequence of electrode activation repeated itself. This indicates that the electrostatic force generated in the electrode without via on it is great enough to

overcome the pinning force created by the smaller diameter via. The smaller the via diameter, the smaller the pinning force trapping the droplet onto it.

The third configuration has similar via size as the second one but located at the left corner of the electrode. In this configuration, the droplet was able to move onto the inner electrode 10 without the need of using high voltage of 225 V_{RMS}. The droplet however was still incapable of moving beyond electrode 10 and increasing the voltage to 225 V_{RMS} did not resolve the problem. The droplet oscillated between electrode 10 and 13 when the sequence of electrode activation repeated itself. The final configuration is similar to the third configuration but the electrode size is larger with 2.0 mm in size. This configuration is able to move the droplet across all the inner electrodes in any direction using 150 V_{RMS}. This demonstrates that by using a larger electrode size relative to the via size, it mitigates the effect of the pinning force while increasing the electrostatic force as the size of the electrode increased.

The mechanism of the pinning force caused by the via is not well understood but it is hypothesised that its existence is due to the difference in the wettability between the via region and its surrounding as suggested by Pit et al. [224]. The pinning force as described by Pit et al. [224] is given by the following **equation (4.2)**:

$$(4.2) \quad F_{pin} = \gamma_{lg} (\cos \theta_{philic} - \cos \theta_{phobic}) \cdot w_p$$

where γ_{lg} is the liquid-gas surface tension, w_p is the width of the via region, θ_{philic} and θ_{phobic} are the Young's angles on the via surface and the deactivated electrode surface respectively. Based on this equation, the pinning force increases with the width of the via area and the difference between the Young's angle of the hydrophilic and hydrophobic areas. It is suggested that the via region has become more hydrophilic

than its surrounding once an inner electrode is deactivated after a voltage application. Further investigations would be needed to confirm the exact mechanism of the pinning force.

Table 4.3: Droplet actuation performance of the device using the fourth configuration.

| Voltage | Observation |
|----------------------|--|
| 90 V _{RMS} | Droplet moved across one electrode, needed more than 10 retries |
| 105 V _{RMS} | Droplet moved across two electrodes |
| 120 V _{RMS} | One full cycle and stopped one short of electrode before completing the second cycle |
| 135 V _{RMS} | Droplet stopped at the 12 th electrode after completing the third cycle |
| 150 V _{RMS} | Droplet completed full 50 cycles |



Figure 4.8: Droplet movement across inner electrodes, from electrode 6 to electrode 11. There are four inner electrodes with the vias located on the top left corner of each electrodes. In the first image, the droplet is indicated in the blue circle while the four vias are indicated inside the dashed red circles. Initially, the droplet was positioned on electrode 6 (the bottom left electrode of the four inner electrodes). The second image shows the elongation of the droplet during its transportation to the next electrode as electrode 11 was activated. The red arrow indicates the direction of droplet movement. The third image shows the droplet in its final position, on electrode 11.

Table 4.3 summarises the droplet transportation performance of the successful 3D 4 × 4 electrode array device employing the fourth configuration. The device requires at least 120 V_{RMS} actuation voltage to transport droplets across more than two electrodes reliably. However using this voltage, the droplet was able to complete only about two cycles of movement across all 16 electrodes (an additional three electrodes to return to the starting point). Increasing the voltage to 150 V_{RMS}, the

droplet was able to complete all 50 cycles. **Figure 4.8** shows the sequence of a droplet while in transportation between two inner electrodes with vias.

4.2.5 Conclusions

The aim of this section is to present novel integration possibilities offered by the use of inkjet printing of PEDOT:PSS electrodes on flexible polymer substrate where a method to construct an EWOD device with a large electrode array size (larger than 3 × 3) has been introduced. The large electrode array device was fabricated by utilising both sides of the substrate for electrode printing. In combination with laser-cut vias, the double-sided printing provides a mean to connect the contact pads with the hard-to-reach inner electrodes. The 3D 4 × 4 device demonstrated to an initial level in this study employed low-cost fabrication methods such as inkjet printing and laser cutting which are more accessible compared to the standard clean-room equipment. Based on the investigations in the previous chapter, the electrode and substrate materials used for the device were PEDOT:PSS and *Melinex*® respectively.

The 3D 4 × 4 electrode array device has successfully transported water droplet across all its 16 electrodes, proving the feasibility of connecting different level of conductive layers through vias. The key to the connectivity between the different level of layers is the ink coverage on the inside surface of the vias. It has been demonstrated that silver ink does not provide good ink coverage on the inside surface of the vias fabricated on the *Melinex*® substrate even after several printing passes. The PEDOT:PSS ink required only one printing pass on each surface to make the two connected to each other. Another challenge in the fabrication process was to determine the inner electrode and via design that can transport the droplet across the inner electrode surface with the via in it. The vias introduce heterogeneity to the actuating surface and cause impediment to the droplet movement. A few designs were

tested and the successful one employed a large electrode size (2.0 mm) with a very small via diameter (<140 μm). This indicates that a large ratio of the electrode size to the via size is required to mitigate the pinning effect of the via while increasing the electrostatic force to move the droplet forward at the same time.

The advantage of employing an EWOD device with a large electrode array size is the increase in the functional area of the device, making it possible to run multiple parallel assays thus increasing the throughput. The method proposed in this study is not only useful for EWOD application but is also applicable for other electronic devices employing multilevel connectivity on a single substrate.

4.3 Magnetic micro-immunoassay EWOD device

The previous section demonstrated the system integration prospects offered by the use of inkjet printing of conductive polymer ink on flexible polymer substrates. In this section, we will present another promising example of the technology by fabricating EWOD devices targeting real-world applications such as biochemical assays. In this section, the inkjet-printed EWOD plates will be employed in a pre-existing magnetic micro-immunoassay DMF platform (described in the next section). Inkjet-printed DMF devices capable of performing immunoassays have been produced before [11, 61, 117, 143] using silver, and paper and polymer as the electrode and substrate respectively. Inkjet-printed devices employing electrodes made of PEDOT:PSS conductive polymer is lower in cost [158] and might provide a better optical signal detection due to its transparency as demonstrated later in **Section 4.3.7**. The aim of this section is to prove the feasibility of inkjet-printed PP-on-*Melinex*[®] device as a platform for executing immunoassays. In order to do this, inkjet-printed *PP-on-Melinex*[®] devices were fabricated and droplet manipulation operations essential to the success and effectiveness of an immunoassay were performed on these devices.

A brief introduction to immunoassays is available in **Section 1.2.3.1**. A simplified ELISA type immunoassay for the detection of immunoglobulin G (IgG) antibody using Protein A/G-coated magnetic beads was selected as the test to be conducted on the EWOD device. Immunoglobulins are glycoproteins produced by plasma cells to bind with pathogens such as viruses and bacteria while Protein A/G is a recombinant protein that is capable of binding to IgG antibody [225]. Magnetic beads have been employed previously in EWOD-based DMF systems as carrier particles in heterogeneous immunoassay [12, 13, 60, 62], DNA sequencing [226-228], and polymerase chain reaction (PCR) [69] applications. Heterogeneous immunoassay is an assay method which involves the separation of the bound antibody-antigen complex from the unbound particles [71]. By employing magnetic beads as the antibody or antigen carrier, the bound complex can be separated from the unbound particles using magnetic force. While the magnetic particles are pinned down by magnetic force, the droplet containing the unbound particles is moved forward using EWOD actuation thus separating them from the antibody-antigen complex [43].

4.3.1 EWOD-based DMF magnetic immunoassay platform

The EWOD-based fully integrated DMF platform (**Figure 4.9**) employed to perform the magnetic micro-immunoassay was developed by the Microfluidics and Micro-engineering Research Group (MMRG), University of Hertfordshire (UH) [229]. The platform is contained inside a black box, also acting as a Faraday cage to shield it from both unwanted electromagnetic fields and stray light during signal detection. The chemiluminescent signal of the immunoassay is measured using an integrated photodiode (S9270 photodiode, Hamamatsu, Japan).

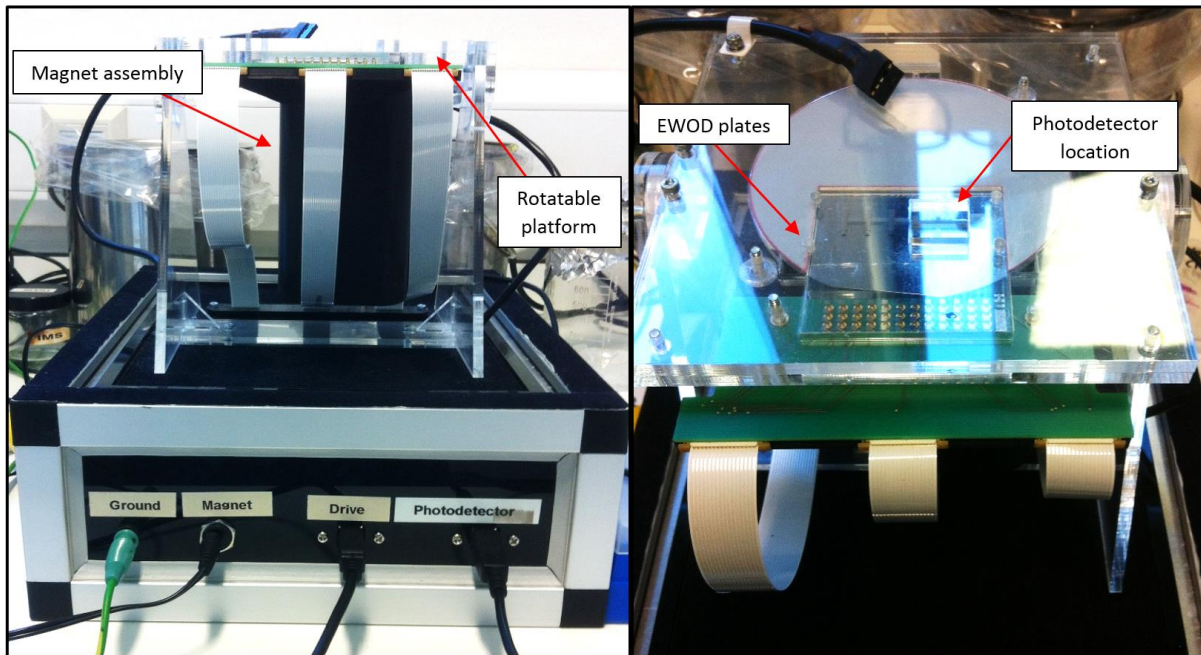


Figure 4.9: Front view (left) and top view (right) of the EWOD-based DMF magnetic immunoassay platform developed by the UH's MMRG. The images show the system without the black box cover and also without the photodetector connected to it. The magnet assembly for the magnetic beads separation operation is contained in the 3D-printed black cylinder located below the EWOD plates.

This system contains an automated permanent magnet which can be engaged or disengaged to trap the magnetic beads at a specific location on the EWOD plates for separation from supernatant. The N42 cylindrical magnet (25 mm in diameter and 10 mm in height), enclosed inside a 3D-printed case is positioned below the EWOD plates during droplet operation and is movable in the vertical direction. A PMMA structural frame that can be rotated 180° is used to hold the assembly of EWOD plates. Spring-loaded pogo pins for electrical connection of the drive electronics to the EWOD base plate are built into the frame. The base plate can be connected to the electronics by simply slotting it underneath the pins. A lid that can be clamped and unclamped is used to secure the assembly of plates in place. The 3D-printed cylinder case containing the permanent magnet is fixed to the removable lid.

The drive electronics, which consists of a stack of two USB-powered PCBs is responsible for the voltage drive of the system, PC communication, channel switching, and capacitive feedback measurement system. The operating voltage (1 kHz analogue sine wave) ranging from 0 V to 225 V_{RMS} is regulated by a Microchip 18F45K22 microcontroller. The whole operation of the DMF platform is controlled using a bespoke software interface [230] via a computer.

4.3.2 Design and fabrication of magnetic micro-immunoassay EWOD plates

The parallel-plate configuration was used for the magnetic micro-immunoassay EWOD device. **Figure 4.10** shows the pre-existing design of EWOD base plates used for the magnetic-micro-immunoassay. The design was redrawn using Adobe Illustrator® (Adobe Inc., San Jose, US) so that it can be adapted for the inkjet printing process. The electrode spacing was changed to 280 µm from the original 60 µm based on findings in Chapter 2. The EWOD plate is composed of 47 square electrodes each independently addressed by contact pads located at the top of the design in the figure. The nominal size of the electrode is 1.7 mm and one larger electrode with the nominal size of 5 mm is used as waste reservoir for the separated supernatant. A region of eight electrodes are designated as the mixing and incubation region of the immunoassay. For the separation step of the magnetic beads, the magnet assembly is aligned at a prescribed location on the EWOD plates. The photodetector is positioned at the centre of the mixing and incubation region to allow for precise and maximum detection of the luminescent signal. All these regions are indicated in **Figure 4.10**.

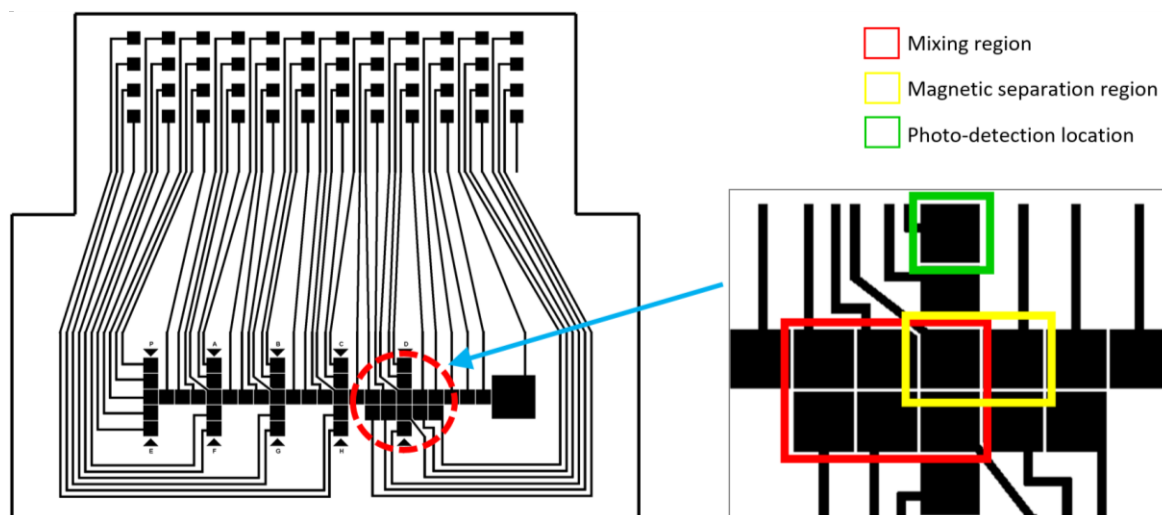


Figure 4.10: The design of the assay plate contains 47 electrodes. The size of the control electrode is 1.7 mm and the reservoir electrode size is 5 mm. The enlarged inset shows the mixing region and the locations of magnetic separation and photodetection.

4.3.2.1 Printer setting and types of ink and substrate

The EWOD electrodes pattern was inkjet-printed on PET polymer substrate, *Melinex*®, using the Fujifilm Dimatix DMP-2850 previously described in details in **Section 2.3**. PP conductive polymer was used as the ink material. The printer settings used for the ink were the same as in **Section 2.3.1.2**. The firing voltage were between 18 V to 25 V with only one nozzle was used. Both the ink and the platen temperatures were set to ambient temperature. The substrate was treated with UV/ozone radiation for 15 minutes prior to printing.

4.3.2.2 The fabrication process of the base plate and assembly of the device

A layer of Parylene-C with a thickness of 6.0 μm was deposited onto the substrate, following the process described in **Section 2.2.1.7**. A layer of *Cytop*® hydrophobic surface was then spin coated at 1500 rpm for 30 s and cured at 140 °C for 30 minutes. The printed base plate was assembled with a cover plate made of a silicon wafer to form a parallel-plate device. A layer of *Cytop*® was deposited on top of the silicon

wafer as the hydrophobic layer. The gap between the base and cover plates was 380 μm using plastic substrates as the spacer.

4.3.2.3 Reagents and samples of the micro-immunoassay

The buffer solution used for the immunoassay was diluted HEPES (4-(2-hydroxyethyl)-piperazine-1-ethanesulfonic acid, N-(2-Hydroxyethyl)piperazine-N'-(2-ethanesulfonic acid) hemi-sodium salt pH 7.5 (Sigma Aldrich, St. Louis, US) into DI water to form a 100 mM solution at a pH of 7.5. TweenTM 80 (Surfact-AmpsTM Detergent Solution, ThermoFisher Scientific, Massachusetts, US) surfactant with a concentration of 0.01% v/v was added to the HEPES buffer solution.

The magnetic particles used was PierceTM Protein A/G magnetic beads (ThermoFisher Scientific, Massachusetts, US) supplied by the manufacturer at 10 mg/ml, 1 ml in water containing 0.05% sodium azide. The magnetic beads' mean diameter is 1 μm and they have a binding capacity of 55-85 μg of IgG per mg of bead. For usage in the immunoassay, the beads were prepared by separating them from supernatant using a permanent magnet. The beads were then washed three times in HEPES buffer before re-suspending them at concentration of 2.0 mg/ml. The antibody used was Goat anti-rabbit IgG secondary antibody conjugated with HRP enzyme (ThermoFisher Scientific, Massachusetts, US) supplied at 0.01 mg/ml. For the immunoassay, the antibody was diluted to 2 $\mu\text{g}/\text{ml}$ with the HEPES buffer solution. The substrate employed for reaction with the HRP enzyme was luminol (SuperSignalTM ELISA Femto Substrate, ThermoFisher Scientific, Massachusetts, US). The luminol was prepared by adding equal amount of stable peroxide to the luminol/enhancer solution.

4.3.3 Protocol of the direct ELISA

The process flow of the magnetic micro-immunoassay implemented on the fabricated inkjet-printed PP EWOD device is shown in **Figure 4.11**. The process consisted of a sequence of separation, resuspension and mixing of the magnetic beads within 2.5 μ l droplets. The process starts with the separation of the magnetic particles coated with the Protein A/G from the buffer solution. This is performed by engaging the permanent magnet under the EWOD plate to hold the magnetic beads in a specific location while the supernatant droplet is moved towards the waste reservoir.

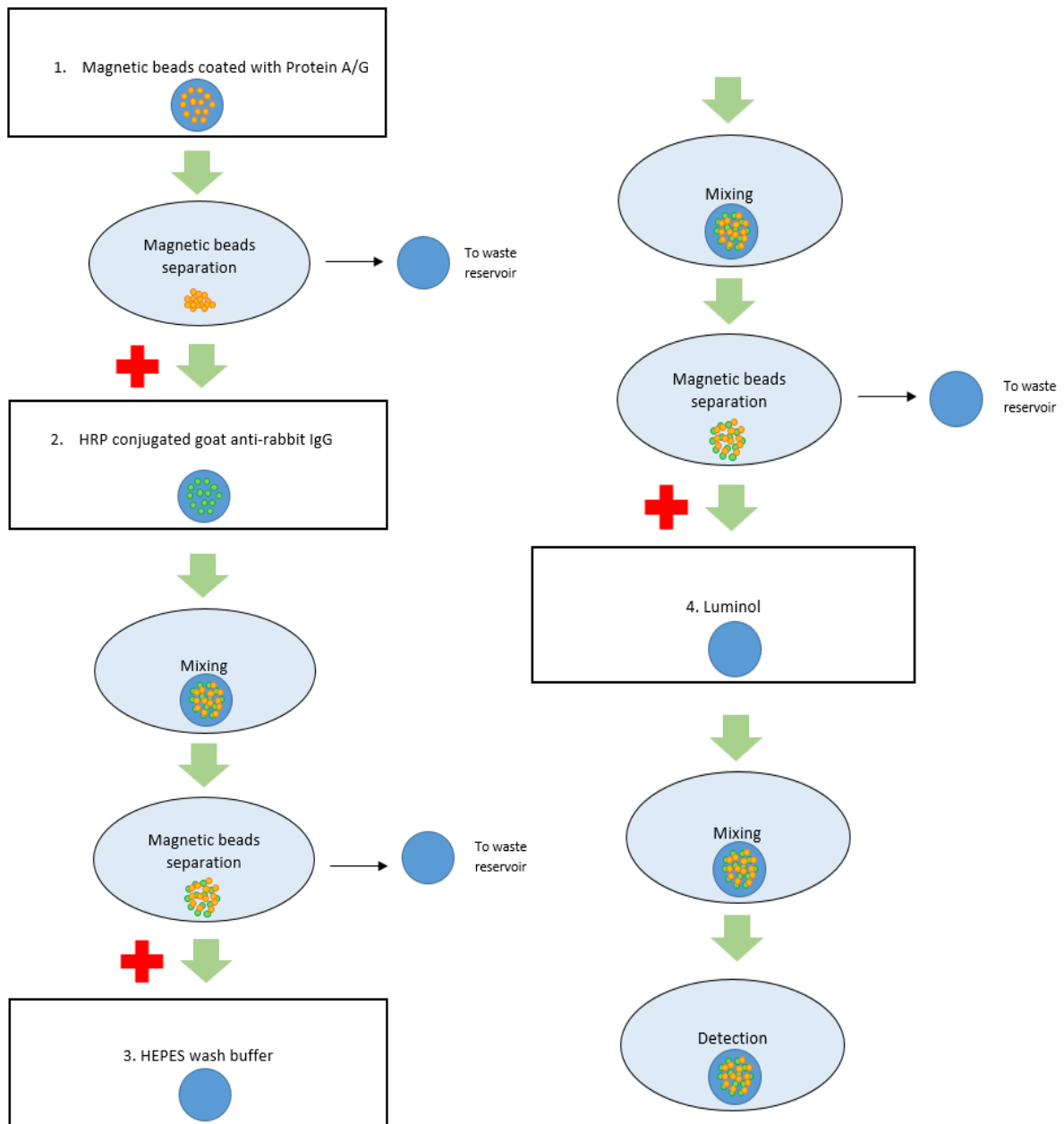


Figure 4.11: Flow process of the micro-immunoassay antibody antigen.

The next step is the collection of the magnetic beads by the HRP conjugated anti-rabbit IgG droplet. After the bead collection, the droplet is moved around in a circular manner (in the designated region shown in **Figure 4.10**) to allow for mixing and incubation for a period of time. The next sequence of separation and recollection is to wash away the unbound IgG particles using HEPES buffer. After the washing step, the final recollection of the beads is by the luminol droplet to trigger the light

generation for the chemiluminescent signal detection. The droplet is finally moved to the photodetector location for light measurement.

4.3.4 Reliability of the inkjet-printing method to fabricate immunoassay plate

The results from **Section 2.3** have demonstrated that the Fujifilm Dimatix printer is a reliable method for patterning PP as EWOD electrodes. In this chapter however, it has been found that its reliability decreases with the increase in size and complexity of the electrode pattern. The larger the size of the electrode pattern, the longer the duration of the printing which increases the risk of the PP ink droplet to becoming more inconsistent causing problems such as misdirected jets and clogging of nozzles. Comparing the previous pattern used in Chapter 2 (**Figure 2.1**) with the one in **Figure 4.10**, the latter has a more complex design and has a larger size with 72 mm × 58 mm while the former size is 52 mm × 45 mm. On average, only one out of the six printed plates was usable while the rest had defects in the printed pattern in critical locations such as the magnetic separation site. Even with the usable ones, connection defects were observed and no plates were found to be fully functional albeit comprising of enough usable electrodes for the following tests.

4.3.5 Separation of magnetic beads

Figure 4.12 depicts the sequence of magnetic beads separation from the supernatant that has been conducted on the inkjet-printed PP EWOD device. The magnetic beads-laden droplet is first actuated to the separation site. The magnet is then moved up, parallel against the silicon cover plate, causing the beads to gather at the magnetic field line with the highest strength. After ten seconds, all the beads are clustered together and forced into a concentrated pellet by the action of the droplet surface tension. While the magnet is still engaged, holding the beads in place, the supernatant droplet is moved away towards waste reservoir using EWOD force. The last image in

the figure shows the complete detachment of the beads from the supernatant as the next electrode is activated. The inkjet-printed EWOD plate has demonstrated successful and reliable separation of the magnetic beads from the supernatant, which is a very important step in a heterogeneous immunoassay.

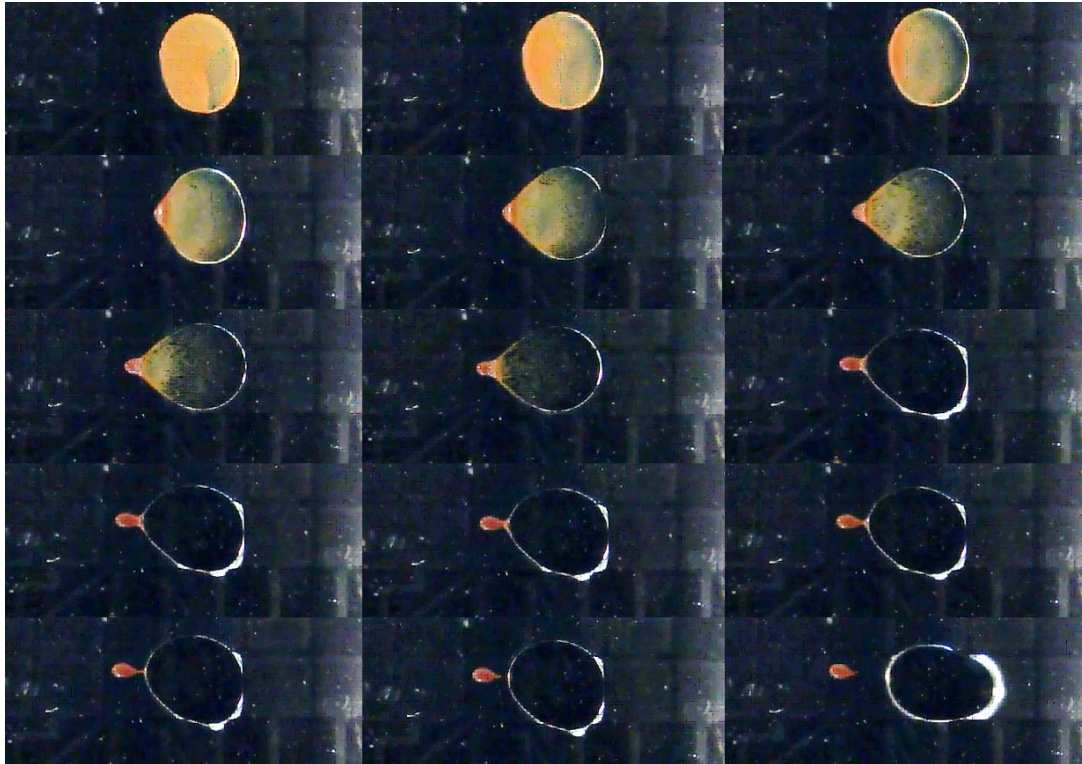


Figure 4.12: The images show the sequence of events during the separation of the magnetic beads from the supernatant. In the first image, the magnet is already engaged below the plate and the beads started moving towards the location with the highest magnetic field. The beads begin to cluster together into a pellet after some time. The last two images show the beads pellet is finally detached from the supernatant as the next electrode is activated.

4.3.6 Mixing of magnetic beads and droplet

Resuspension of separated magnetic beads with droplet solution has been demonstrated efficiently in the inkjet-printed PP EWOD device, as can be seen in **Figure 4.13**. The first two images show the buffer droplet before and after the merging with the separated beads pellet. After the merging, the beads-laden droplet is moved around in an almost circular manner to promote diffusion of the beads within the

droplet. For the mixing steps during the immunoassay, the droplet is moved around for 18 cycles, equivalent to incubation time of 66.5 seconds for the mixing between the Protein A/G-coated beads and the HRP-conjugated IgG antibody droplet.

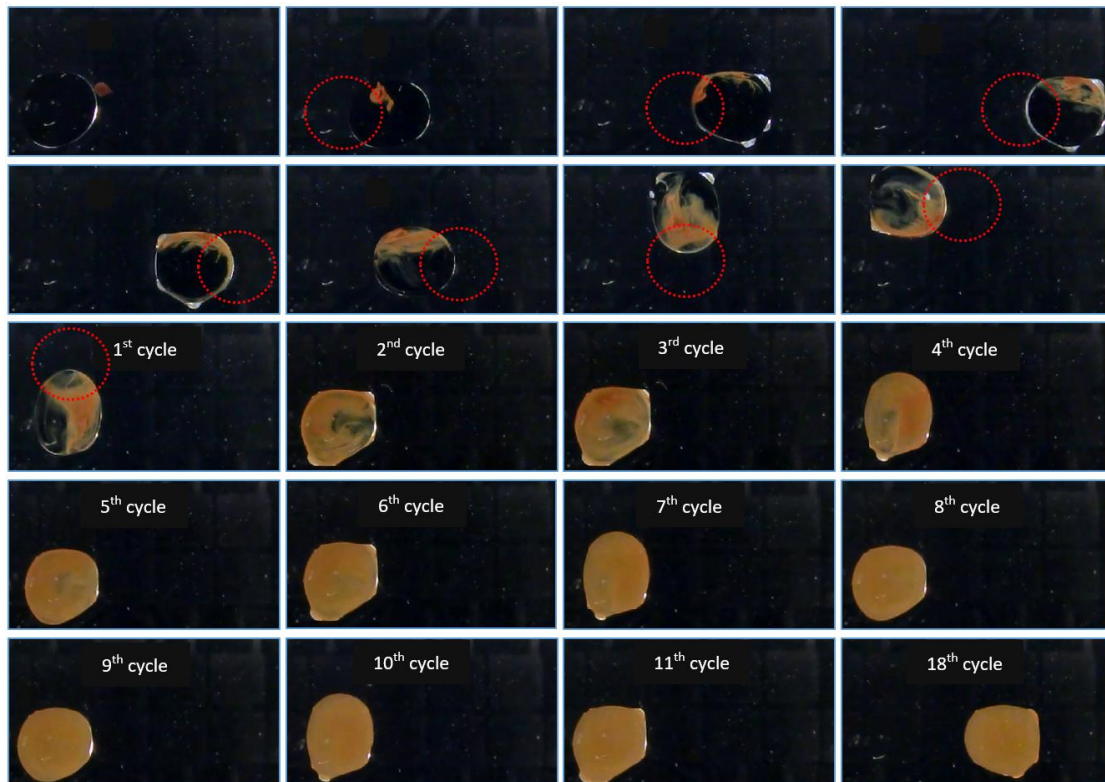


Figure 4.13: The sequence of events during merging and mixing between the magnetic beads and a droplet solution. The first image shows the droplet and the pellet of separated magnetic beads right before the merging happened. The red-dotted circles represent the previous positions of the droplet. The first two rows of images show the sequence of electrode activation during the mixing operation. The third, fourth, and fifth rows images display the condition of the droplet at the end of a mixing cycle.

From visual observation of **Figure 4.13**, uniform mixing of the beads within the droplet seems to occur after the 8th cycle of the circular movement. To confirm this, pixel intensity analysis was conducted for each of the droplet images representing each cycle using a free online dCode Image Histogram [231] software. Every pixels in the images were assigned their grayscale values, from 0 to 255, based on the

frequency of luminance in each pixel and the software then computed the frequency of each grayscale intensity. The results were plotted into histogram shown in **Figure 4.14**. From the histogram, the final cycle which is represented by the 18th image has significant pixel frequency at intensity range of 98 to 127. The images started to converge to this range starting at 7th cycle and matched rather closely at the 10th cycle indicating uniform beads concentration across the droplet after the 10th cycle.

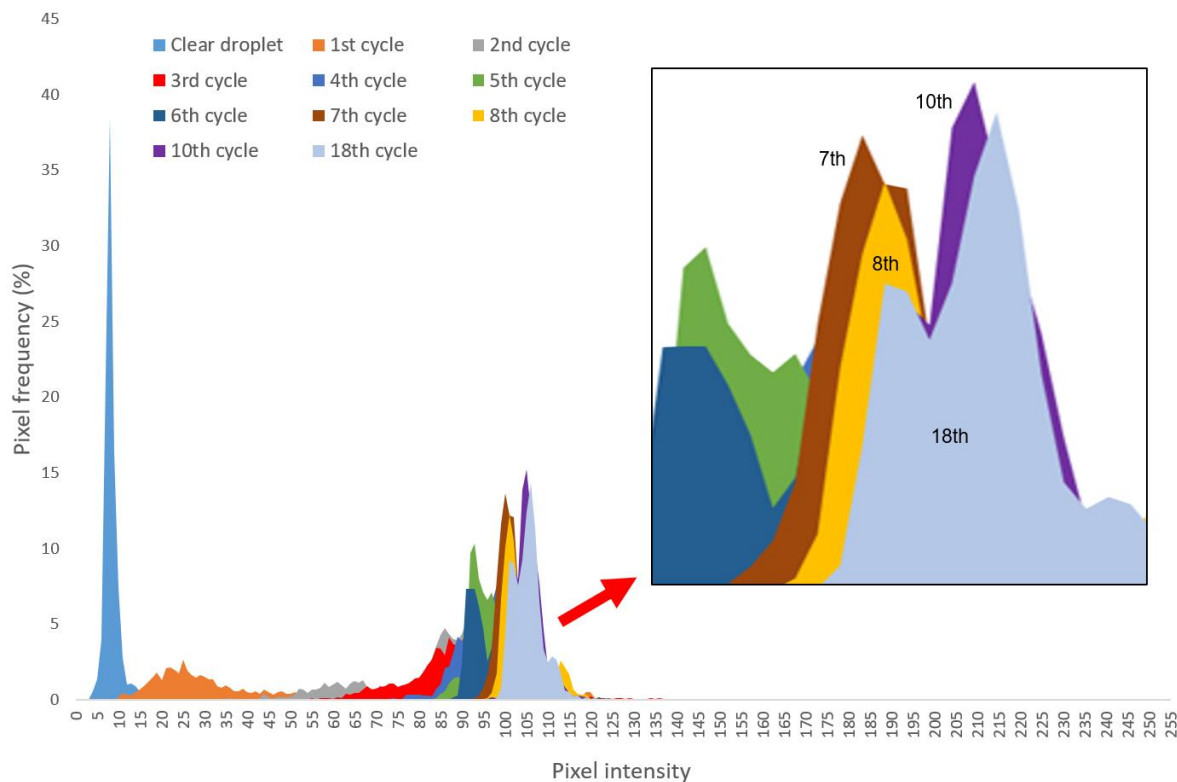


Figure 4.14: The intensity histogram of the droplet image for each cycle. The 10th cycle image pixel intensity closely matched with the 18th cycle image indicating well-mixed droplet after the 10th cycle.

4.3.7 Photodetection of the immunoassay

The results from the photodetection of the IgG immunoassay ran using 2 mg/ml of Protein A/G-coated magnetic beads and 2 µg/ml of HRP-conjugated IgG antibody are displayed in **Figure 4.15**. The results of the immunoassay performed using the inkjet-printed PP EWOD plate are compared with signals obtained using chrome-on-glass EWOD plate. The purpose of conducting the photodetection was not to prove the

efficiency of the immunoassay process but to demonstrate the device's capability to retrieve the signal produced by the immunoassay. A blank control sample was not run in this initial investigation. The reference chrome-on-glass plate was fabricated using photolithography method and coated with the same thickness of Parylene-C, ~6 μm , and a final layer of Cytop® hydrophobic material. It has the same design as shown in **Figure 4.10**, with the same electrode size of 1.7 mm but the electrode spacing is smaller with 60 μm . The chrome electrodes are filled with a grid design to make them semi-transparent. The protocol of the immunoassay run on the chrome-on-glass plate was the same as that performed on the *PP-on-Melinex*® plate.

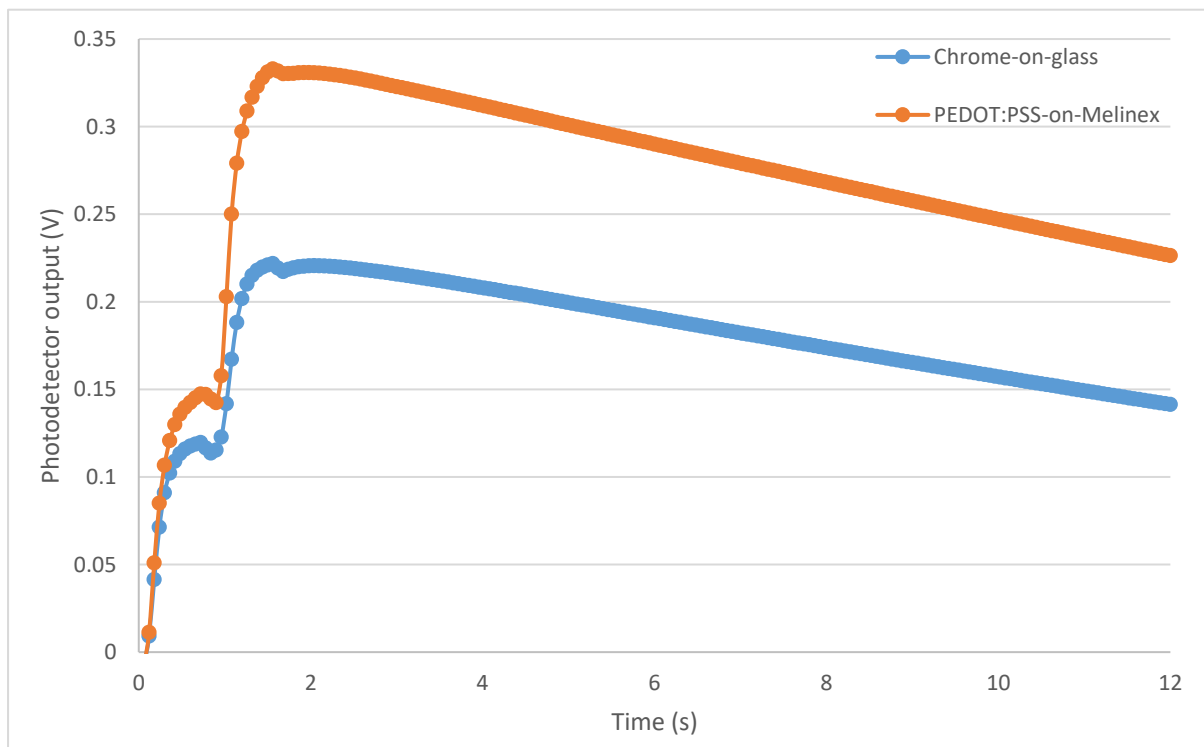


Figure 4.15: Signals from the *PEDOT:PSS-on-Melinex*® and chrome-on-glass devices using 2 mg/ml of Protein A/G-coated magnetic beads and 2 $\mu\text{g}/\text{ml}$ of HRP-conjugated IgG antibody.

The signals obtained from both types of plate increase significantly in the first 1.6 seconds as the droplets moved across two electrodes towards the signal detection location. The highest photodetector responses were recorded for both types of plate

once the droplets reached the signal detection location; the maximum response for the *PP-on-Melinex*® was 0.33 V while the maximum response for the chrome-on-glass plate is 0.22 V. There was a significant difference between the two maximum photodetector signals even though the same concentrations of Protein A/G (2 mg/ml) and HRP-conjugated IgG antibody (2 µg/ml) were used in the immunoassays.

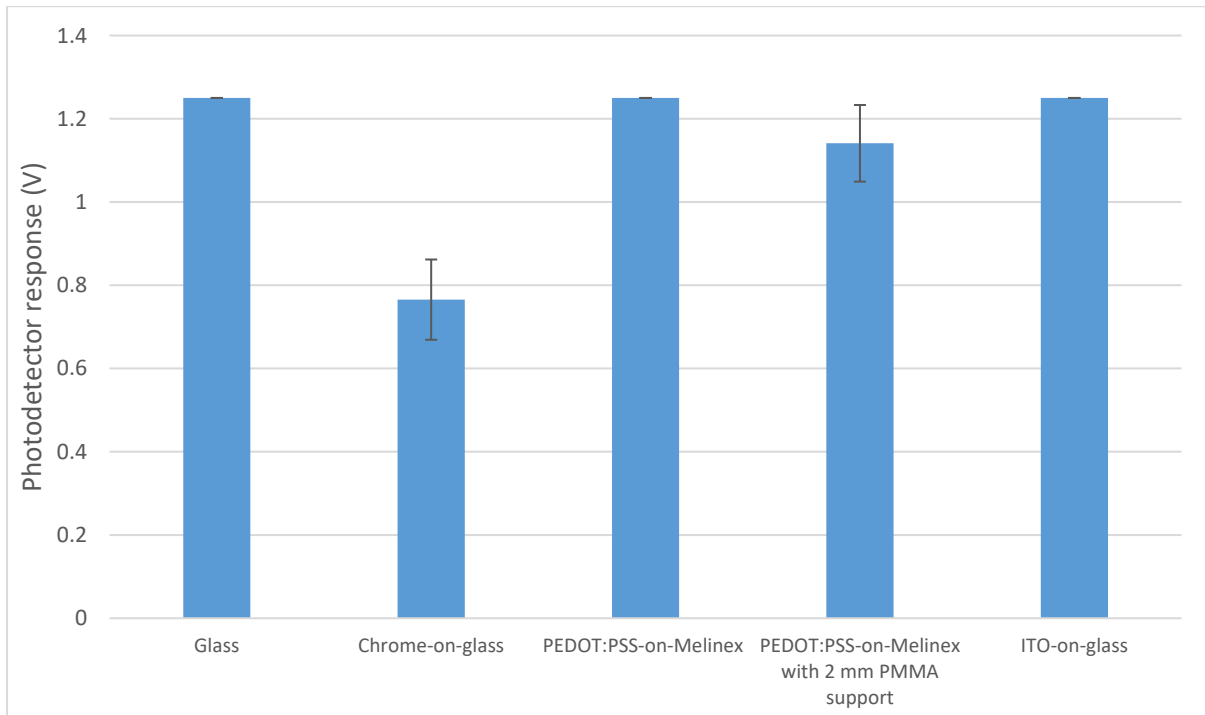


Figure 4.16: The photodetector signals produced by a 5 µl of 0.5 µg/ml HRP-conjugated IgG droplet added with luminol sitting on different types of electrode and substrate.

The *PP-on-Melinex*® plate recorded a higher response due to the higher transparency of the PEDOT:PSS electrode than the grid-patterned chrome electrode which is only semi-transparent. A simple experiment was conducted to measure the difference in the chemiluminescent signal between different types of electrodes and substrates with a fully transparent glass slide as the reference. Signal produced by a 5 µl of HRP-conjugated IgG antibody (0.5 µg/ml) droplet added with luminol sitting on five different types of substrate: glass (without any electrode pattern), *chrome-on-*

glass, *ITO-on-glass*, *PP-on-Melinex*[®], and *PP-on-Melinex*[®] with 2 mm thickness PMMA support were recorded. The *PP-on-Melinex*[®] with the PMMA support was tested because that is the setup used in the magnetic immunoassay platform. The detected chemiluminescent signals for the different types of substrate are presented in **Figure 4.16**. Three types of substrate; glass, *ITO-on-glass*, and *PP-on-Melinex*[®] recorded the highest signal with 1.25 V followed by *PP-on-Melinex*[®] with PMMA support (1.14 V), and finally chrome-on-glass with the lowest signal (0.77 V). This result indicates that the *PP-on-Melinex*[®] device has transparency as high as a glass slide and *ITO-on-glass* which is the standard transparent electrode in optoelectronic devices [232]. The high transparency of the *PP-on-Melinex*[®] device could improve the accuracy of optical signal measurement in EWOD devices.

4.3.8 Conclusions

The magnetic immunoassay device fabricated using the inkjet-printed PEDOT:PSS electrodes was capable of performing magnetic separation and resuspension of magnetic beads successfully as separate operations. The separation and the resuspension of the magnetic beads are two very important components in a heterogeneous immunoassay. By performing these two steps efficiently, the inkjet-printed device has demonstrated its potential to be employed in future applications. The photodetection of the chemiluminescent signal generated by the immunoassay has also been conducted. It has been demonstrated that the signal acquired from the PEDOT:PSS-on-*Melinex*[®] device was higher than the signal from the chrome-on-glass device using the same concentrations of antibody and antigen. The PEDOT:PSS-on-*Melinex*[®] device has been found to have transparency similar to glass slide which is beneficial optical sensing devices.

During the fabrication of the PEDOT:PSS immunoassay plates, it has been found that the inkjet printing process of the PEDOT:PSS ink decreases in reliability as the size and complexity of the electrodes increase. The unreliability of the PEDOT:PSS printing process to fabricate the relatively large immunoassay plate is the main reason why a simplified assay was employed in this investigation. To avoid this problem, if PEDOT:PSS electrodes were to be employed in an EWOD device in the future, it is suggested that a very simple design with minimised underutilised electrodes is used to reduce the size of the pattern.

In the first two sections of this chapter, we have explored some promising applications of inkjet-printed PEDOT:PSS electrodes investigated in Chapter 2 as EWOD device component. The next section will discuss the prospect of applying the commercial product investigated in Chapter 3 as the anti-biofouling and actuating surface of EWOD device.

4.4 Superhydrophobic NeverWet top coating as EWOD anti-biofouling surface

Based on the results of the CA measurements (**Section 3.4.1.4**), the roll-off angle measurements (**Section 3.4.1.5**), and the biofouling rate evaluation (**Section 3.4.1.6**), the top coating *NeverWet*[®] (TNW) superhydrophobic surface has shown considerable promise as an EWOD actuating surface. Accordingly, the aim of this section is to further investigate TNW's applicability as an EWOD device's, superhydrophobic surface to perform fundamental 'unit' EWOD device operations such as droplet transportation, merging, mixing, and splitting.

This section reports the realisation of a low-cost superhydrophobic EWOD device, the approach taken by this thesis to overcome the biofouling problem. Employing the TNW superhydrophobic material as the EWOD surface offers

significant advantages: reduction of biofouling compared to hydrophobic surfaces such as *Cytop*®, low material cost (*NeverWet*® is approximately 20 times cheaper than *Cytop*®), a simpler fabrication process compared to the nanofabrication techniques of the superhydrophobic surfaces presented in previous studies [130-135], and finally the realisation of a parallel-plate device with a passive/ungrounded cover plate.

4.4.1 Design, fabrication and testing of superhydrophobic EWOD device

Two types of EWOD device were fabricated for the investigation, a single-plate device and a parallel-plate device. For the assembly of both types of superhydrophobic device, base plates previously used by the UH's MMRG for unrelated EWOD tests were recycled for use. Before employment in the investigation, the plates were cleaned using laboratory detergent (Decon labs™ Neutracon), followed by IPA and DI water. They were blow dried using compressed air afterward. **Figure 4.17** shows the design of the base plate. The glass photomask plates implementing the design were supplied by Compugraphics International (Glenrothes, Scotland). It constitutes of ten rows of sixteen independently controlled chrome electrodes patterned on a glass substrate. The size of each square electrode is 1.7 mm with a 60 µm inter-electrode spacing. These were then post-processed at UH by depositing a 3.2 µm layer of Parylene-C over the glass and chrome electrodes.

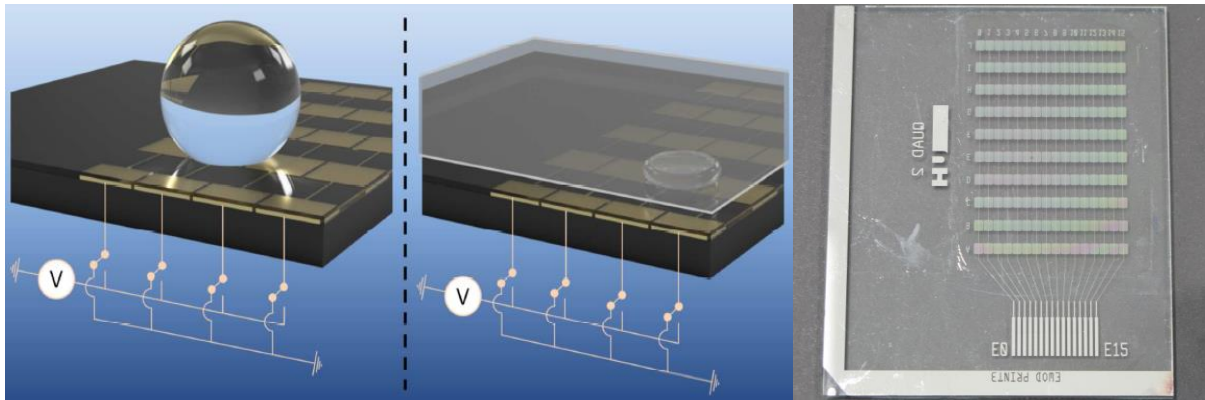


Figure 4.17: Designs of the superhydrophobic EWOD device, (left) single-plate configuration, (middle) parallel-plate configuration. (Right) The base plate of the superhydrophobic EWOD device was made of glass with ten rows of sixteen chromium control electrodes. Each electrode in the same column is electrically connected by thin chromium lines [220].

For the parallel-plate device, a 4-inch silicon wafer was used as the cover plate and the gap between the base and cover plates was set to $380\ \mu\text{m}$ using a laser-cut plastic substrate as the spacer. There were two configurations for the cover plate: grounded and ungrounded. The typical configuration for an EWOD device is the grounded one but interestingly it was found unintentionally that the ungrounded cover plate configuration is possible if a superhydrophobic surface is employed; thus both configurations were tested. This is a novel observation and is discussed more in the next section. TNW was employed as the superhydrophobic layer of both the base and cover plates and the same method described in **Section 3.4.1.2** for the superhydrophobic surface preparation was applied.

For merging and mixing droplet operations, a different base plate design than that employed for the linear droplet transportation was used and the tests were conducted only in the parallel-plate superhydrophobic EWOD device. The base plate for these operations was previously employed by the UH's MMRG as part of a project funded by the Defence Science and Technology Laboratory, UK. The demonstration

of the operations occurred on a region of a 2×5 electrode array. The cover plate was ITO-coated glass while the other parameters of the device assembly such as the layer thicknesses and electrode dimensions were the same as those implemented in the linear transportation device.

The PMMA frame and the driving electronics employed were the same as those described in **Section 2.2.1.6**. Two different implementations of driving electronics were used for the linear transportation of droplets. Initially, tests were conducted using plates compatible with 16 channels driving electronics but eventually the plates became defective due to wear and tear of frequent use. Another type of plate which has exactly the same design (electrode size, inter-electrode gap, gap spacing, and thicknesses of layers) was employed for the linear transportation. These plates are however compatible with another driving electronics with 48 channels and different design of contact pads. For signals with the same pulse rate applied to the control electrodes during the droplet actuation, there is a bit delay in the second electronics as can be seen in the graphs representing the droplets displacement in **Figure 4.18**.

For the linear transportation of droplets, four types of droplet solution were used: DI water, 0.1 mg ml^{-1} fibrinogen (Alexa Fluor™ 647 conjugate, ThermoFisher Scientific, Massachusetts, US), 1 and 10 mg ml^{-1} ovalbumin (Sigma Aldrich, St. Louis, US). For the merging and mixing operations, red dyed aqueous solution at 5 mg ml^{-1} was prepared using New Coccine dye (Sigma Aldrich, St. Louis, US). Droplet movement was recorded using a ScopeTek (Hangzhou Scopetek Opto-Electric Co., Ltd.) microscope camera at 30 fps. The displacement and velocity of the droplets on the EWOD devices were evaluated using image analysis software (Tracker, Video Analysis and Modelling Tool, Douglas Brown, California, US).

4.4.2 Linear transportation of droplet

The linear transportation of droplets were tested using two types of superhydrophobic device, single-plate and parallel-plate employing four types of droplet solution. For the parallel-plate device, two configurations were applied: the commonly employed grounded cover plate and ungrounded cover plate. The volume of droplet were 35 μ l and 5 μ l for the single-plate and parallel-plate devices respectively. The droplet was actuated in a cycle across seven electrodes and back to the initial position (a 21.1 mm path in total) by activating the electrodes individually in sequence using 150 V_{RMS} (1 kHz) and a 100 ms pulse rate.

Table 4.4: The peak and mean velocities of different types of solution in the parallel-plate (grounded and ungrounded) and single-plate superhydrophobic EWOD devices.

| | Parallel-plate (ungrounded) | | Parallel-plate (grounded) | | | Single-plate | | | |
|-----------------------------|-----------------------------|-------------------|---------------------------|-------------------|----------------------|--------------|-------------------|--------------------|----------------------|
| | DI water | 1 mg/ml ovalbumin | DI water | 1 mg/ml ovalbumin | 0.1 mg/ml fibrinogen | DI water | 1 mg/ml ovalbumin | 10 mg/ml ovalbumin | 0.1 mg/ml fibrinogen |
| Peak velocity (cm/s) | 2.3 ± 0.2 | 1.6 ± 0.1 | 2.6 ± 0.3 | 1.5 ± 0.1 | 2.5 ± 0.4 | 1.8 ± 0.2 | 1.6 ± 0.2 | 2.2 ± 0.2 | 1.4 ± 0.2 |
| Mean velocity (cm/s) | 2.8 ± 0.7 | 2.4 ± 0.8 | 4 ± 1 | 2.3 ± 0.7 | 3 ± 1 | 1.4 ± 0.2 | 1.3 ± 0.1 | 1.4 ± 0.3 | 1.0 ± 0.3 |

The measured displacement and velocity of the droplets for both single-plate and parallel-plate devices are shown in **Table 4.4** and **Figure 4.18**. The reported values are the average of five measurements. Depending on the driving electronics, the droplet solutions took between approximately 1.7 s and 2.6 s to complete one cycle with varying instantaneous velocity. The highest mean velocity (average velocity across one electrode) was recorded with DI water at

4 cm s⁻¹ in the parallel-plate grounded device while the highest peak instantaneous velocity was also recorded with DI water at 2.6 cm s⁻¹ in the parallel-plate with grounded cover plate configuration. The differences between the average and instantaneous velocities (comparing between droplets employing the same driving electronics) are rather small and they are attributed to the varying quality of the individual superhydrophobic surfaces. Some plate surfaces are more uniform than others while some may have minute defects that occurred during the spraying process of device fabrication.

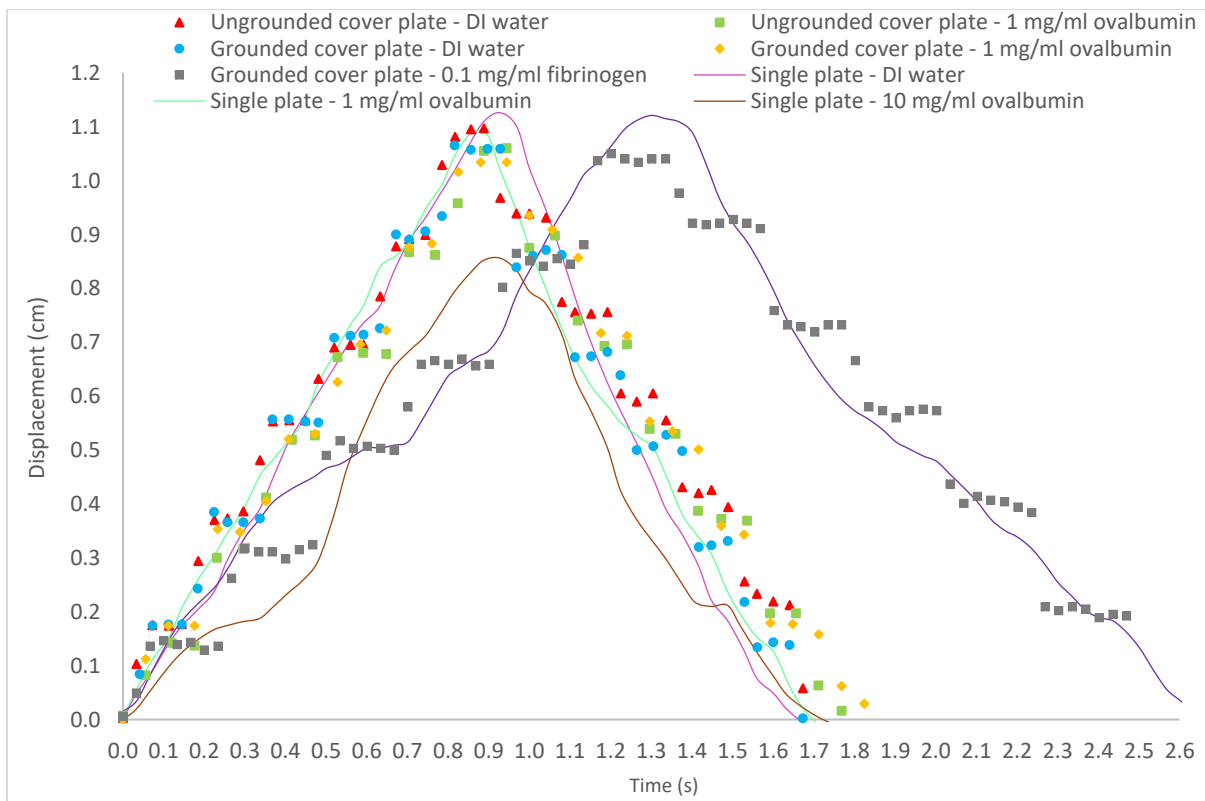


Figure 4.18: Displacements of 35 μl (single-plate) and 5 μl (parallel-plate) of DI water, ovalbumin and fibrinogen droplets for one cycle (across seven electrodes and back) using 150 V_{RMS} and 100 ms pulse rate [220].

The 10 mg ml⁻¹ ovalbumin droplet was actuated over more than two electrodes in the single-plate device whereas it only oscillated between two adjacent electrodes in the parallel-plate device. The 10 mg ml⁻¹ ovalbumin in the

single-plate device however could only move over six electrodes of the seven-electrode transportation sequence due to the adsorption of the protein molecules to the device surface.

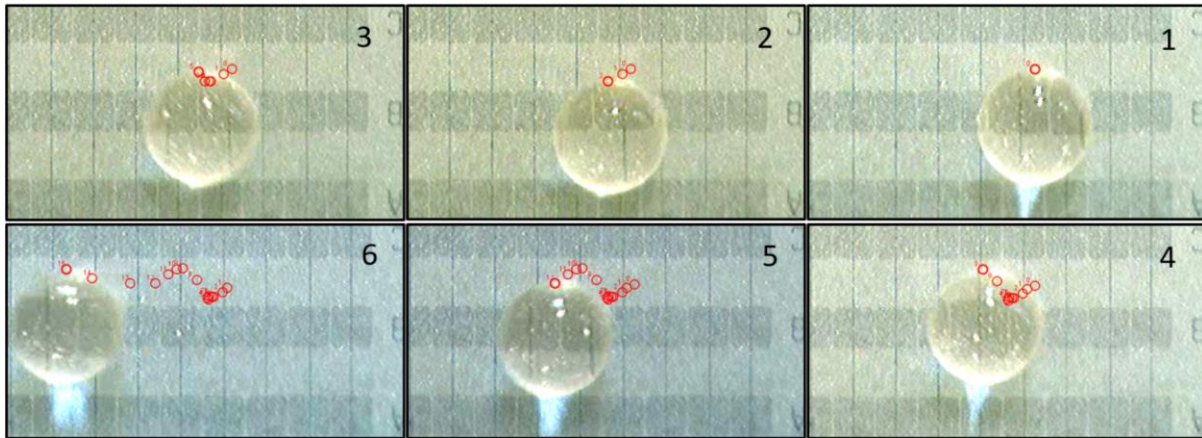


Figure 4.19: The rolling mechanism observed in droplet actuated using single-plate configuration. The droplet moves or rolls in lateral direction as indicated by the red markers which represent the previous locations of the droplet. The markers track the position of the top edge of the droplet frame by frame.

It is believed that the mechanism of droplet actuation in a single-plate superhydrophobic device does not rely solely on EWOD forces but also the rolling motion of the droplet. On the superhydrophobic actuating surface, instead of being brought to an equilibrium state after it moves to the energised adjacent electrode, the droplet continues to roll due to its rotational inertia, which is shown in **Figure 4.19**. This droplet movement is a bit difficult to control and a little unreliable due to the rolling mechanism and sometimes the droplet moves in the lateral direction or a bit further than intended. For the single-plate device, the instantaneous velocity profiles are irregular for all types of solution; some locations have higher instantaneous velocities than others due to the rolling mechanism. For example, despite not completing transiting the seven

electrodes due to stickiness, the 10 mg ml⁻¹ ovalbumin recorded quite a high peak velocity reaching up to 2.2 cm s⁻¹.

For the parallel-plate device, the measured displacements and velocities of the droplet edge (leading edge in the first half and trailing edge in the second half) for all types of solution are shown in **Table 4.4** and **Figure 4.18**. The parallel-plate device displays discrete movement since its displacement measurement is based on the droplet edge, which is not able to roll freely because of the contact line friction between the droplet and the cover plate inhibiting its momentum. This is in contrast with the single-plate configuration which displays continuous movement and gradual increase in displacement.

During energisation of each electrode in the parallel-plate device, the DI water and 0.1 mg ml⁻¹ fibrinogen droplets demonstrate higher instantaneous velocities than the 1 mg ml⁻¹ ovalbumin which could be due to the ovalbumin solution's higher viscosity. Although the effect is more significant for much higher concentration protein solutions, viscosity increases with the protein concentration [233]. It is suggested that a protein solution with high viscosity increases the resistance to droplet motion due to the increase in the viscous dissipation force; thus slowing the droplet edge from reaching its steady state [87, 90, 94-96]. However, this is just a supposition since measurement of viscosity was not performed in this study.

The ungrounded cover plate configuration was tested in the parallel-plate device. Only DI water and 1 mg ml⁻¹ ovalbumin were employed to compare the difference between the grounded and ungrounded cover plate configurations and the result is summarised in **Table 4.4**. The highest peak instantaneous

velocities for DI water droplets in grounded and ungrounded cover plate configurations are comparable at 2.6 cm s^{-1} and 2.3 cm s^{-1} respectively. The 1 mg ml^{-1} ovalbumin also has very similar maximum instantaneous velocities in grounded and ungrounded cover plate configurations; 1.5 cm s^{-1} and 1.6 cm s^{-1} respectively, although considerably lower than that of DI water. Interestingly, the results of our demonstration have shown that the typical square control electrodes design reported in [12, 13, 23, 58, 60-62, 68, 69, 92, 94, 102, 103] is also feasible for droplet transportation with an ungrounded cover plate by coating both base and cover plates with superhydrophobic material. It is believed that this configuration is viable with superhydrophobic surfaces because of the almost frictionless contact with the cover plate.

The benefit of employing the parallel-plate device with a passive cover plate is that the cover plate can accommodate other functions such as sensing devices [104] while still maintaining the droplet control advantages of two plates rather than a single-plate. Previously it has been suggested [94] that the passive cover plate setup would be unworkable if a typical square electrode design were employed because reduction of surface energy gradient once the droplet reached halfway between two electrodes would cause the droplet to stop. There are reports of parallel-plate with ungrounded cover plate [104, 109, 110] but these devices require specific design of the base plate's control electrodes. Several studies [104, 109, 110, 234] accomplished droplet transportation using an ungrounded cover plate by using actuation pads comprising 2, 4 or 6 sub-electrodes. The necessary pressure difference to move the droplet forward is achieved by applying potentials among the sub-electrodes within an actuation pad. Results of current study suggest that using superhydrophobic material

would allow the simpler-to-fabricate and address, square electrode design to be used in a functional ungrounded cover plate setup in a parallel-plate configuration.

The EWOD actuation results of the superhydrophobic device demonstrate its reliability in rapidly transporting protein-laden droplets with a performance comparable to previously reported EWOD devices for non-protein solution droplets. The superhydrophobic device is capable of transporting 0.1 mg ml^{-1} fibrinogen solution in both single-plate and parallel-plate devices which is 500 times higher than the previously reported concentration of $1.5 \text{ } \mu\text{g ml}^{-1}$ without any pluronic additives [24]. The highest concentration of ovalbumin movable in the single-plate device is 10 mg ml^{-1} while in the parallel-plate device it is 1 mg ml^{-1} . Pollack et al. [23] reported an average droplet velocity of 3 cm s^{-1} using 20 Hz pulse rate in a parallel-plate device while the superhydrophobic parallel-plate device in this study achieved the highest average velocity at 1.28 cm s^{-1} (average velocity for one cycle, back and forth across 7 electrodes) using 10 Hz pulse rate. The single-plate device droplet velocity is comparable albeit lower than Park et al.'s [105] device which reached maximum velocity of 2.5 cm s^{-1} at $150 V_{\text{RMS}}$. The superhydrophobic single-plate device's highest average velocity is 1.4 cm s^{-1} at the same actuation voltage.

4.4.3 Merging, mixing and splitting of droplets

The parallel-plate device was employed to perform merging, mixing, and splitting operations in the superhydrophobic device. Droplets of DI water and New Coccine dye, each of $5 \text{ } \mu\text{l}$ volume were merged and mixed to form a $10 \text{ } \mu\text{l}$ droplet as shown in **Figure 4.20**. The droplets were merged by moving the DI water droplet towards the

red dyed droplet, causing them to blend into one large droplet with two visibly separated regions, as can be seen occurring between $t = 0$ ms until $t = 200$ ms. After merging, the $10 \mu\text{l}$ droplet was actuated in a circular fashion across eight electrodes to induce advection for 6 seconds; this occurred from $t = 200$ ms until $t = 6200$ ms in **Figure 4.20**. From the recorded images, the droplet turned uniformly red indicating complete mixing between the two droplets at $t=5400$ ms, approximately 5 seconds (12 actuation steps at 5 Hz switching rate) after merging.

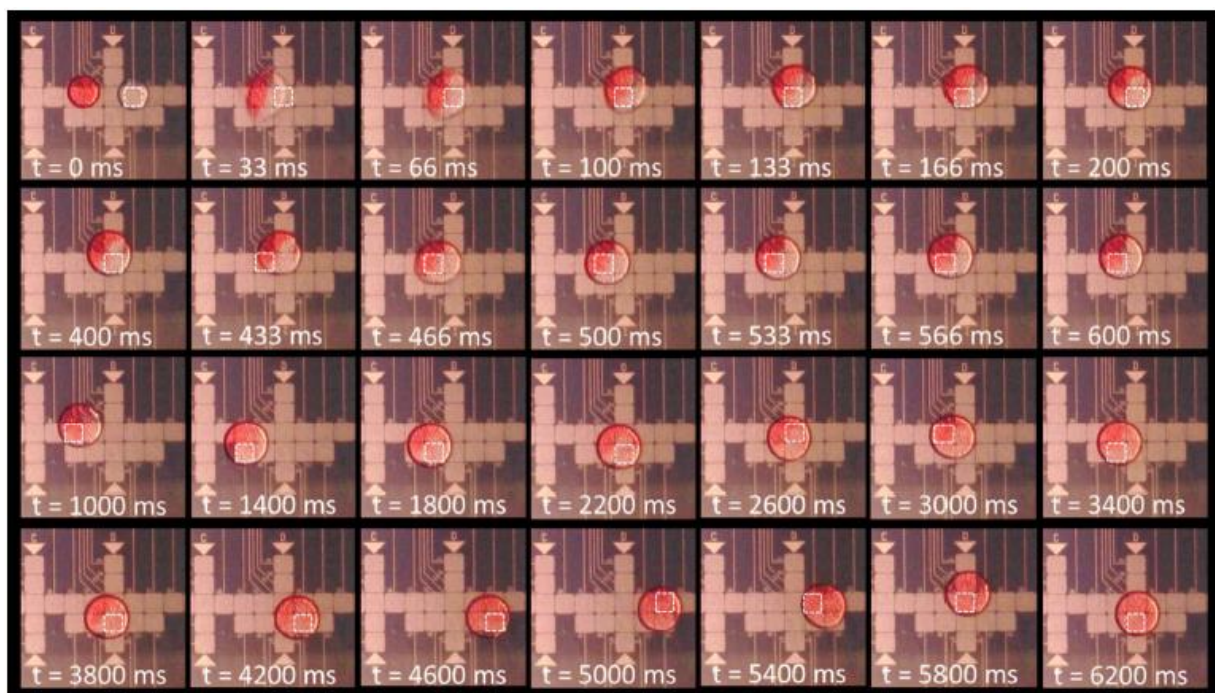


Figure 4.20: The timed video frames show the sequence of the merging of two $5 \mu\text{l}$ droplets followed by the mixing operation in the parallel-plate superhydrophobic device. One droplet is DI water while the other droplet is 5 mg ml^{-1} New Coccine dye solution (red coloured droplet). The activated electrode pad is represented with white-dash outline. The first row of images display the frame-by-frame merging of the two droplets while the second row show the stabilisation of the merged droplet by actuation to the next electrode. The third and final rows demonstrate the mixing operation which occurred by moving the droplet in a circular fashion [220].

However, attempting a splitting operation using the typical DMF method [92, 235, 236] was unsuccessful in the superhydrophobic device. It proved very difficult to produce necking of the droplet in the current investigation which is an indispensable step in the traditional method of droplet splitting. A reservoir electrode with a surface area eight times larger than the regular actuation electrodes has been employed during the investigation but necking was still not observed. Necking is a narrowing in the middle of a droplet as it elongates before splitting into two smaller droplets. Splitting requires large electrode size and small gap between the base and cover plates [237]. Due to the very high CA ($>160^\circ$) of the droplet with both base and cover plates, the superhydrophobic parallel-plate device resembles the single-plate device in which splitting is notably very challenging [9, 238, 239]. To fully evaluate the possibility of droplet splitting in a superhydrophobic device, further studies beyond the scope of this thesis would be required. Unconventional and ingenious approaches such as the implementation of a Y-junction [240] in the electrode design or the use of micro-blade splitters [241] might be needed to achieve droplet splitting in superhydrophobic device.

4.4.4 Conclusions

Three types of EWOD devices have been fabricated in this chapter to demonstrate the usability of the proposed materials and methods to produce a device capable of performing droplet operations beyond linear droplet transportation. The first two devices presented in this section were fabricated using inkjet printing of PEDOT:PSS conductive polymer ink on *Melinex*® PET substrate. The first device offers an inexpensive approach to the construction of an EWOD plate implementing a large size electrode array (larger than 3×3). The suggested method uses a laser cutting machine and an inkjet printer, which are somewhat more accessible equipment in laboratories instead that those required for classical microfabrication.

The second device was constructed to demonstrate the prospect of using the *PP-on-Melinex*® in immunoassay applications. Specific functions intrinsic to the immunoassay protocol have been conducted reliably on the inkjet-printed device. It has been found that the PEDOT:PSS electrodes present an advantage to chrome-on-glass electrodes by providing a higher transparency for a more accurate detection of optical signal. This is especially beneficial if due to the architecture of the device, the photodetection measurement has to be made through the electrodes.

The third and final device employs conventional chrome-on-glass electrodes but uses a top coating of off-the-shelf, *NeverWet*® superhydrophobic material as the actuating surface. The superhydrophobic device was fabricated to establish the anti-biofouling property of the low-cost superhydrophobic surface. Highly concentrated protein droplets have been successfully transported on the superhydrophobic device indicating minimal protein adsorption to the surface. The findings in this section have shown that the inkjet printing of PEDOT:PSS ink on polymer substrate and the TNW superhydrophobic material have significant advantages and promise when integrated into a DMF system designed to perform a specific function. Each types of device can bring further improvement to the DMF system by increasing its performance (e.g. anti-biofouling surface and higher throughput due to larger electrode array) and also by adding more functions and applications (e.g. double-sided plate and compatibility with wider range of biomolecules sample).

5 Conclusions and future works

5.1 Summary of achievements

Numerous EWOD-based DMF devices capable of performing specific functions such as heterogeneous immunoassay [12, 13, 60-63], DNA amplification [68, 69], and particle collection and detection [15] have been reported, indicating the usefulness and adaptability of the technology to various applications. However DMF technology has the drawback of having a high fabrication cost where clean-room methods such as photolithography are required in its fabrication process. Another serious shortcoming in this technology is that of biofouling which occurs on the device's actuating surface when exposed to droplet with high concentration of biomolecules: as would be the case in many real-world applications.

The aim of this project has been to develop a low-cost EWOD device employing alternative materials and methods to reduce the high fabrication cost issue. Furthermore the project also sought to overcome or minimise the surface contamination problem due to biomolecule adsorption by employing a superhydrophobic surface. Investigations conducted during the project have accomplished the following:

- In chapter 2, two types of inkjet printing technology have been investigated: a low-cost desktop printer and a laboratory-grade material printer. Both methods have produced inkjet-printed devices capable of transporting droplets across their surfaces.
- For both types of printer, the reliability and reproducibility of the inkjet printing process are highly influenced by the ink-substrate combination employed to pattern the EWOD electrodes. In addition, the desktop

printer completely relies on the substrate's surface treatment to produce fully interconnected tracks while the laboratory-grade printer can achieve this by varying the drop spacing parameter.

- In this investigation, the most reliable method to produce a printed functional EWOD device has been by employing conductive polymer PEDOT:PSS ink as the electrode material, patterned using a laboratory-grade Fujifilm Dimatix printer on polymer PET substrate, Melinex®.
- In chapter 3, several commercial dielectric and superhydrophobic/hydrophobic materials have been investigated in preliminary studies to select one material for further development. One dielectric material, *Rust-Oleum*® Polyurethane varnish, and one superhydrophobic material, the top coating component of *NeverWet*® spray, have shown the most potential by having good electrowetting reversibility and the ability to actuate droplets across their surfaces. For the detailed investigation, the superhydrophobic material has been chosen due to another prospective function as an anti-biofouling surface.
- The commercial superhydrophobic material has demonstrated minimal surface contamination after exposure to highly concentrated protein-laden droplet when compared to the conventional hydrophobic *Cytop*® surface indicating a superior anti-biofouling property.
- In chapter 4, application prospects of the methods and materials investigated in chapter 2 and chapter 3 are explored by fabricating three types of device with specific functions and/or designs. A 3D 4 × 4 electrode array device and a magnetic micro-immunoassay device have been developed using the inkjet printing of PP-on-*Melinex*® method. The

third device is a superhydrophobic device employing the conventional chrome-on-glass approach with the commercial superhydrophobic material as the actuating surface. All of the devices are capable of performing the intended functions reliably. The encouraging results promise integration of the proposed application prospects into DMF system in the future.

5.2 Future works

Whilst promising achievement has been demonstrated, further development is needed in some of the proposed methods and materials:

- The reproducibility of the inkjet printing method of the PEDOT:PSS needs improvement as the ink droplets ejected by the inkjet printer become more inconsistent as the printing time increases for large electrode patterns. This might be achieved by changing the formulation of the ink.
- The low-cost dielectric materials investigated in the preliminary study in chapter 3 have the potential to be used as the substitutes for the conventional dielectric material but a more reliable fabrication technique is needed. A method that is capable of producing a pinhole-free layer with uniform thickness is necessary before the material can be integrated into the EWOD device.
- It will be interesting to see full incorporation of the proposed techniques and designs employed in chapter 4 into one integrated DMF system, for example, the 3D 4 × 4 electrode array device implemented with a superhydrophobic actuating surface for execution of magnetic micro-immunoassay.

5.3 Conclusions

A wide implementation of DMF technology in biological and chemical assays applications could transform the way laboratory tests are conducted in the future. The promise of low-cost, robust, reconfigurable, and portable devices to perform diagnostic and bio-detection tasks could constitute a paradigm shift for civil and military protection, crop monitoring, and health care sectors among others. This project proposes an inkjet-printed PEDOT:PSS on polymer substrate DMF device to tackle one of the important challenges in the way of DMF technology rapid development and wide application: high cost of device fabrication. Although further development is needed with the PEDOT:PSS ink to improve its reproducibility with the inkjet printing technique, the proposed materials and method has shown its usability as two types of device with different designs and functions have been fabricated.

The first device, a 3D 4 × 4 electrode array device offers an alternative and low-cost method to construct an EWOD device employing a large size electrode array. Large functional area in a device can increase throughput as multiple parallel assays can be performed. Since the 3D 4 × 4 array device employs printing on both sides of the substrate, multi-level devices can also be realised. The second inkjet-printed device has shown its capability in performing tasks important to the success and efficiency of a magnetic micro-immunoassay. Another significant contribution that is presented by the magnetic micro-immunoassay device is the high visibility and transparency of the PEDOT:PSS electrodes which can enhance the sensitivity of the optical detection system. Both of the inkjet-printed devices have demonstrated high prospect to be incorporated into a fully-integrated DMF platform. They also offer the possibility of a more varied designs and formats of future EWOD devices which can cater for a wider functions and applications.

This project also suggests a low-cost approach to alleviate the biofouling problem which compromised the reliability of EWOD devices. The evaluated *NeverWet*® product has shown high potential as an anti-biofouling surface by reliably transporting highly concentrated protein droplets across its surface. Another advantage of the superhydrophobic device is its ability to employ ungrounded cover plate configuration in a parallel-plate device which allows for other functions to be incorporated into the cover plate. Hopefully, the findings in this project contribute towards the realisation of an affordable and robust DMF device in the near future that can give a positive impact to the microfluidics and biochemistry fields.

Bibliography

1. Jebrail, M.J., M.S. Bartsch, and K.D. Patel, *Digital microfluidics: a versatile tool for applications in chemistry, biology and medicine*. Lab on a Chip, 2012. **12**(14): p. 2452-2463.
2. Neethirajan, S., et al., *Microfluidics for food, agriculture and biosystems industries*. Lab on a Chip, 2011. **11**(9): p. 1574-1586.
3. Whitesides, G.M., *The origins and the future of microfluidics*. Nature, 2006. **442**(7101): p. 368-373.
4. Erickson, D. and D. Li, *Integrated microfluidic devices*. Analytica Chimica Acta, 2004. **507**(1): p. 11-26.
5. Sackmann, E.K., A.L. Fulton, and D.J. Beebe, *The present and future role of microfluidics in biomedical research*. Nature, 2014. **507**(7491): p. 181-189.
6. Fair, R.B., *Digital microfluidics: is a true lab-on-a-chip possible?* Microfluidics and Nanofluidics, 2007. **3**(3): p. 245-281.
7. Fair, R.B., et al., *Chemical and biological applications of digital-microfluidic devices*. IEEE Design & Test of Computers, 2007. **24**(1): p. 10-24.
8. St John, A. and C.P. Price, *Existing and emerging technologies for point-of-care testing*. The Clinical Biochemist Reviews, 2014. **35**(3): p. 155.
9. Choi, K., et al., *Digital microfluidics*. Annual review of analytical chemistry, 2012. **5**: p. 413-440.
10. Abdelgawad, M. and A.R. Wheeler, *The digital revolution: a new paradigm for microfluidics*. Advanced Materials, 2009. **21**(8): p. 920-925.
11. Ng, A.H., et al., *A digital microfluidic system for serological immunoassays in remote settings*. Science translational medicine, 2018. **10**(438): p. eaar6076.
12. Sista, R., et al., *Development of a digital microfluidic platform for point of care testing*. Lab on a Chip, 2008. **8**(12): p. 2091-2104.
13. Sista, R.S., et al., *Heterogeneous immunoassays using magnetic beads on a digital microfluidic platform*. Lab on a Chip, 2008. **8**(12): p. 2188-2196.
14. Bogojevic, D., et al., *A digital microfluidic method for multiplexed cell-based apoptosis assays*. Lab on a Chip, 2012. **12**(3): p. 627-634.
15. Jönsson-Niedziółka, M., et al., *EWOD driven cleaning of bioparticles on hydrophobic and superhydrophobic surfaces*. Lab on a Chip, 2011. **11**(3): p. 490-496.
16. Zhao, Y. and S.K. Cho, *Microparticle sampling by electrowetting-actuated droplet sweeping*. Lab on a Chip, 2006. **6**(1): p. 137-144.
17. Cheng, J.-T. and C.-L. Chen, *Active thermal management of on-chip hot spots using EWOD-driven droplet microfluidics*. Experiments in fluids, 2010. **49**(6): p. 1349-1357.
18. Paik, P.Y., V.K. Pamula, and K. Chakrabarty, *Adaptive cooling of integrated circuits using digital microfluidics*. IEEE transactions on very large scale integration (vlsi) systems, 2008. **16**(4): p. 432-443.
19. Peeling, R.W., et al., *Rapid tests for STIs: the way forward*. Sexually transmitted infections, 2006.
20. Abdelgawad, M. and A.R. Wheeler, *Low-cost, rapid-prototyping of digital microfluidics devices*. Microfluidics and nanofluidics, 2008. **4**(4): p. 349.
21. Jain, V., et al., *Design, fabrication and characterization of low cost printed circuit board based EWOD device for digital microfluidics applications*. Microsystem Technologies, 2017. **23**(2): p. 389-397.
22. Narasimhan, V. and S.-Y. Park, *An ion gel as a low-cost, spin-coatable, high-capacitance dielectric for electrowetting-on-dielectric (EWOD)*. Langmuir, 2015. **31**(30): p. 8512-8518.
23. Pollack, M.G., R.B. Fair, and A.D. Shenderov, *Electrowetting-based actuation of liquid droplets for microfluidic applications*. Applied Physics Letters, 2000. **77**(11): p. 1725-1726.

24. Yang, H., et al., *A world-to-chip interface for digital microfluidics*. Analytical Chemistry, 2008. **81**(3): p. 1061-1067.
25. Perry, G., et al., *Inhibiting protein biofouling using graphene oxide in droplet-based microfluidic microsystems*. Lab on a Chip, 2012. **12**(9): p. 1601-1604.
26. Gascoyne, P.R. and J.V. Vykoukal, *Dielectrophoresis-based sample handling in general-purpose programmable diagnostic instruments*. Proceedings of the IEEE, 2004. **92**(1): p. 22-42.
27. Gascoyne, P.R., et al., *Dielectrophoresis-based programmable fluidic processors*. Lab on a Chip, 2004. **4**(4): p. 299-309.
28. Beyssen, D., et al., *Microfluidic device based on surface acoustic wave*. Sensors and Actuators B: Chemical, 2006. **118**(1): p. 380-385.
29. Lehmann, U., et al., *Two-dimensional magnetic manipulation of microdroplets on a chip as a platform for bioanalytical applications*. Sensors and Actuators B: Chemical, 2006. **117**(2): p. 457-463.
30. Ohashi, T., et al., *A simple device using magnetic transportation for droplet-based PCR*. Biomedical microdevices, 2007. **9**(5): p. 695-702.
31. Pipper, J., et al., *Catching bird flu in a droplet*. Nature medicine, 2007. **13**(10): p. 1259.
32. Darhuber, A.A., et al., *Thermocapillary actuation of droplets on chemically patterned surfaces by programmable microheater arrays*. Journal of Microelectromechanical Systems, 2003. **12**(6): p. 873-879.
33. Darhuber, A.A., J.P. Valentino, and S.M. Troian, *Planar digital nanoliter dispensing system based on thermocapillary actuation*. Lab on a Chip, 2010. **10**(8): p. 1061-1071.
34. Valentino, J.P., S.M. Troian, and S. Wagner, *Microfluidic detection and analysis by integration of thermocapillary actuation with a thin-film optical waveguide*. Applied Physics Letters, 2005. **86**(18): p. 184101.
35. Pethig, R., et al., *Dielectrophoresis: a review of applications for stem cell research*. BioMed Research International, 2010. **2010**.
36. Zhang, H., H. Chang, and P. Neuzil, *DEP-on-a-chip: Dielectrophoresis applied to microfluidic platforms*. Micromachines, 2019. **10**(6): p. 423.
37. Çetin, B. and D. Li, *Dielectrophoresis in microfluidics technology*. Electrophoresis, 2011. **32**(18): p. 2410-2427.
38. Pamme, N., *Continuous flow separations in microfluidic devices*. Lab on a Chip, 2007. **7**(12): p. 1644-1659.
39. Hunt, T.P., D. Issadore, and R.M. Westervelt, *Integrated circuit/microfluidic chip to programmably trap and move cells and droplets with dielectrophoresis*. Lab on a Chip, 2008. **8**(1): p. 81-87.
40. Renaudin, A., et al., *SAW nanopump for handling droplets in view of biological applications*. Sensors and Actuators B: Chemical, 2006. **113**(1): p. 389-397.
41. Wang, Z. and J. Zhe, *Recent advances in particle and droplet manipulation for lab-on-a-chip devices based on surface acoustic waves*. Lab on a Chip, 2011. **11**(7): p. 1280-1285.
42. Guttenberg, Z., et al., *Planar chip device for PCR and hybridization with surface acoustic wave pump*. Lab on a Chip, 2005. **5**(3): p. 308-317.
43. Kokalj, T., E. Pérez-Ruiz, and J. Lammertyn, *Building bio-assays with magnetic particles on a digital microfluidic platform*. New biotechnology, 2015. **32**(5): p. 485-503.
44. Sammarco, T.S. and M.A. Burns, *Thermocapillary pumping of discrete drops in microfabricated analysis devices*. AIChE Journal, 1999. **45**(2): p. 350-366.
45. Zhao, Y.-P. and Y. Wang, *Fundamentals and applications of electrowetting*. Reviews of Adhesion and Adhesives, 2013. **1**(1): p. 114-174.
46. Mugele, F. and J.-C. Baret, *Electrowetting: from basics to applications*. Journal of Physics: Condensed Matter, 2005. **17**(28): p. R705-R774.
47. Hendriks, B., et al., *Electrowetting-based variable-focus lens for miniature systems*. Optical review, 2005. **12**(3): p. 255-259.

48. Berge, B. and J. Peseux, *Variable focal lens controlled by an external voltage: An application of electrowetting*. The European Physical Journal E, 2000. **3**(2): p. 159-163.
49. Kuiper, S. and B. Hendriks, *Variable-focus liquid lens for miniature cameras*. Applied physics letters, 2004. **85**(7): p. 1128-1130.
50. Ozbay, B.N., et al., *Three dimensional two-photon imaging of neuronal activity in freely moving mice using a miniature fiber coupled microscope with active axial-scanning*. bioRxiv, 2018: p. 226431.
51. Hayes, R.A. and B.J. Feenstra, *Video-speed electronic paper based on electrowetting*. Nature, 2003. **425**(6956): p. 383.
52. Edwards, A., et al., *Dielectrowetting: The past, present and future*. Current Opinion in Colloid & Interface Science, 2017.
53. McHale, G., C. Brown, and N. Sampara, *Voltage-induced spreading and superspreading of liquids*. Nature communications, 2013. **4**: p. 1605.
54. McHale, G., et al., *Dielectrowetting driven spreading of droplets*. Physical review letters, 2011. **107**(18): p. 186101.
55. Geng, H., et al., *Dielectrowetting manipulation for digital microfluidics: Creating, transporting, splitting, and merging of droplets*. Lab on a Chip, 2017. **17**(6): p. 1060-1068.
56. Anscombe, N., *Page turner*. Engineering & Technology, 2010. **5**(18): p. 26-29.
57. Daw, R. and J. Finkelstein, *Lab on a chip*. Nature, 2006. **442**(7101): p. 367.
58. Shih, S.C., et al., *A feedback control system for high-fidelity digital microfluidics*. Lab on a Chip, 2011. **11**(3): p. 535-540.
59. Jebrail, M.J., et al., *World-to-digital-microfluidic interface enabling extraction and purification of RNA from human whole blood*. Analytical chemistry, 2014. **86**(8): p. 3856-3862.
60. Choi, K., et al., *Automated Digital Microfluidic Platform for Magnetic-Particle-Based Immunoassays with Optimization by Design of Experiments*. Analytical Chemistry, 2013. **85**(20): p. 9638-9646.
61. Fobel, R., et al., *Paper microfluidics goes digital*. Advanced materials, 2014. **26**(18): p. 2838-2843.
62. Ng, A.H., et al., *Digital microfluidic magnetic separation for particle-based immunoassays*. Analytical chemistry, 2012. **84**(20): p. 8805-8812.
63. Wang, Y., et al., *Highly Sensitive and Automated SERS-based Immunoassay for H5N1 Detection with Digital Microfluidics*. Analytical chemistry, 2018.
64. Ng, A.H., et al., *Digital microfluidic immunocytochemistry in single cells*. Nature communications, 2015. **6**: p. 7513.
65. Jebrail, M.J. and A.R. Wheeler, *Digital microfluidic method for protein extraction by precipitation*. Analytical chemistry, 2008. **81**(1): p. 330-335.
66. Moon, H., et al. *On-chip sample preparation by electrowetting-on-dielectric digital microfluidics for matrix assisted laser desorption/ionization mass spectrometry*. in *Micro Electro Mechanical Systems, 2005. MEMS 2005. 18th IEEE International Conference on*. 2005. IEEE.
67. Zhou, J., et al., *Electrowetting-based multi-microfluidics array printing of high resolution tissue construct with embedded cells and growth factors*. Virtual and Physical Prototyping, 2007. **2**(4): p. 217-223.
68. Chang, Y.H., et al., *Integrated polymerase chain reaction chips utilizing digital microfluidics*. Biomedical Microdevices, 2006. **8**(3): p. 215-225.
69. Hua, Z.S., et al., *Multiplexed Real-Time Polymerase Chain Reaction on a Digital Microfluidic Platform*. Analytical Chemistry, 2010. **82**(6): p. 2310-2316.
70. Coelho, B.J., et al., *A Digital Microfluidics Platform for Loop-Mediated Isothermal Amplification Detection*. Sensors, 2017. **17**(11): p. 2616.
71. Wild, D., *The immunoassay handbook: theory and applications of ligand binding, ELISA and related techniques*. 2013: Newnes.

72. Sherwood, L., *Human physiology: from cells to systems*. 2015: Cengage learning.
73. Cox, K.L., et al., *Immunoassay methods*. 2014.
74. Malic, L., et al., *Integration and detection of biochemical assays in digital microfluidic LOC devices*. *Lab on a Chip*, 2010. **10**(4): p. 418-431.
75. Schwartz, J.A., J.V. Vykoukal, and P.R. Gascoyne, *Droplet-based chemistry on a programmable micro-chip*. *Lab on a Chip*, 2004. **4**(1): p. 11-17.
76. Nelson, W.C. and C.-J.C. Kim, *Droplet actuation by electrowetting-on-dielectric (EWOD): A review*. *Journal of Adhesion Science and Technology*, 2012. **26**(12-17): p. 1747-1771.
77. Serway, R. and C. Vuille, *College physics*. Vol. 1. 2012: Nelson Education.
78. Yuan, Y. and T.R. Lee, *Contact angle and wetting properties*, in *Surface science techniques*. 2013, Springer. p. 3-34.
79. Jones, T., *More about the electromechanics of electrowetting*. *Mechanics Research Communications*, 2009. **36**(1): p. 2-9.
80. Siqveland, L.M. and S. Skjaeveland, *Derivations of the Young–Laplace equation*. Unpublished research. <https://doi.org/10.13140/RG.2014.24485.5768>.
81. Berthier, J., *Micro-drops and digital microfluidics*. 2012: William Andrew.
82. Verheijen, H. and M. Prins, *Reversible electrowetting and trapping of charge: model and experiments*. *Langmuir*, 1999. **15**(20): p. 6616-6620.
83. Drygiannakis, A.I., A.G. Papatheanasiou, and A.G. Boudouvis, *On the connection between dielectric breakdown strength, trapping of charge, and contact angle saturation in electrowetting*. *Langmuir*, 2008. **25**(1): p. 147-152.
84. Quinn, A., R. Sedev, and J. Ralston, *Contact angle saturation in electrowetting*. *The journal of physical chemistry B*, 2005. **109**(13): p. 6268-6275.
85. Chevalliot, S., S. Kuiper, and J. Heikenfeld, *Experimental validation of the invariance of electrowetting contact angle saturation*. *Journal of Adhesion Science and Technology*, 2012. **26**(12-17): p. 1909-1930.
86. Mugele, F. and J. Heikenfeld, *Electrowetting: Fundamental Principles and Practical Applications*. 2018: John Wiley & Sons.
87. Gupta, R., et al., *Impact of pinning of the triple contact line on electrowetting performance*. *Langmuir*, 2011. **27**(24): p. 14923-14929.
88. Mugele, F., *Fundamental challenges in electrowetting: from equilibrium shapes to contact angle saturation and drop dynamics*. *Soft Matter*, 2009. **5**(18): p. 3377-3384.
89. Mugele, F. and J. Buehrle, *Equilibrium drop surface profiles in electric fields*. *Journal of Physics: Condensed Matter*, 2007. **19**(37): p. 375112.
90. Baird, E., P. Young, and K. Mohseni, *Electrostatic force calculation for an EWOD-actuated droplet*. *Microfluidics and Nanofluidics*, 2007. **3**(6): p. 635-644.
91. Berthier, J. and K.A. Brakke, *The physics of microdroplets*. 2012, Hoboken, New Jersey: John Wiley & Sons. xviii, 369 pages.
92. Cho, S.K., H. Moon, and C.-J. Kim, *Creating, transporting, cutting, and merging liquid droplets by electrowetting-based actuation for digital microfluidic circuits*. *Microelectromechanical Systems, Journal of*, 2003. **12**(1): p. 70-80.
93. Lee, J., et al., *Electrowetting and electrowetting-on-dielectric for microscale liquid handling*. *Sensors and Actuators A: Physical*, 2002. **95**(2): p. 259-268.
94. Ren, H., et al., *Dynamics of electro-wetting droplet transport*. *Sensors and actuators B: chemical*, 2002. **87**(1): p. 201-206.
95. Nelson, W., P. Sen, and C.-J. Kim. *Resistance of droplets sliding by EWOD actuation*. in *Solid-State Sensors, Actuators and Microsystems Conference, 2009. TRANSDUCERS 2009. International*. 2009. IEEE.
96. Bahadur, V. and S. Garimella, *An energy-based model for electrowetting-induced droplet actuation*. *Journal of Micromechanics and Microengineering*, 2006. **16**(8): p. 1494.

97. Li, H., et al., *Dynamic electrowetting and dewetting of ionic liquids at a hydrophobic solid-liquid interface*. *Langmuir*, 2013. **29**(8): p. 2631-2639.
98. Paneru, M., et al., *Static and dynamic electrowetting of an ionic liquid in a solid/liquid/liquid system*. *Journal of the American Chemical Society*, 2010. **132**(24): p. 8301-8308.
99. Saeki, F., et al., *Electrowetting on dielectrics (EWOD): reducing voltage requirements for microfluidics*. *Polym. Mater. Sci. Eng*, 2001. **85**: p. 12-13.
100. Brassard, D., et al., *Water-oil core-shell droplets for electrowetting-based digital microfluidic devices*. *Lab on a Chip*, 2008. **8**(8): p. 1342-1349.
101. Moon, H., et al., *An integrated digital microfluidic chip for multiplexed proteomic sample preparation and analysis by MALDI-MS*. *Lab on a Chip*, 2006. **6**(9): p. 1213-1219.
102. Moon, H., et al., *Low voltage electrowetting-on-dielectric*. *Journal of Applied Physics*, 2002. **92**(7): p. 4080-4087.
103. Shih, S.C., et al., *Digital microfluidics with impedance sensing for integrated cell culture and analysis*. *Biosensors and Bioelectronics*, 2013. **42**: p. 314-320.
104. Yi, U.-C. and C.-J. Kim, *Characterization of electrowetting actuation on addressable single-side coplanar electrodes*. *Journal of Micromechanics and Microengineering*, 2006. **16**(10): p. 2053.
105. Park, J.K., S.J. Lee, and K.H. Kang, *Fast and reliable droplet transport on single-plate electrowetting on dielectrics using nonfloating switching method*. *Biomicrofluidics*, 2010. **4**(2): p. 024102.
106. Ugsornrat, K., et al. *Experimental study of single-plate EWOD device for a droplet based PCR system*. in *The 8th Electrical Engineering/Electronics, Computer, Telecommunications and Information Technology (ECTI) Association of Thailand-Conference 2011*. 2011. IEEE.
107. Abdelgawad, M., et al., *All-terrain droplet actuation*. *Lab on a Chip*, 2008. **8**(5): p. 672-677.
108. Washizu, M., *Electrostatic actuation of liquid droplets for micro-reactor applications*. *Industry Applications, IEEE Transactions on*, 1998. **34**(4): p. 732-737.
109. Liu, Y.-J., et al., *DNA ligation of ultramicro volume using an EWOD microfluidic system with coplanar electrodes*. *Journal of Micromechanics and Microengineering*, 2008. **18**(4): p. 045017.
110. Yi, U.-C. and C.-J. Kim. *EWOD actuation with electrode-free cover plate*. in *Solid-State Sensors, Actuators and Microsystems, 2005. Digest of Technical Papers. TRANSDUCERS'05. The 13th International Conference on*. 2005. IEEE.
111. Liu, H., et al., *Dielectric materials for electrowetting-on-dielectric actuation*. *Microsystem technologies*, 2010. **16**(3): p. 449.
112. Karuwan, C., et al., *Electrochemical detection on electrowetting-on-dielectric digital microfluidic chip*. *Talanta*, 2011. **84**(5): p. 1384-1389.
113. Fan, S.-K., H. Yang, and W. Hsu, *Droplet-on-a-wristband: Chip-to-chip digital microfluidic interfaces between replaceable and flexible electrowetting modules*. *Lab on a Chip*, 2011. **11**(2): p. 343-347.
114. Chang, J.-h., et al., *Driving characteristics of the electrowetting-on-dielectric device using atomic-layer-deposited aluminum oxide as the dielectric*. *Microfluidics and Nanofluidics*, 2010. **8**(2): p. 269-273.
115. Li, Y., et al., *Anodic Ta₂O₅ for CMOS compatible low voltage electrowetting-on-dielectric device fabrication*. *Solid-State Electronics*, 2008. **52**(9): p. 1382-1387.
116. Lin, Y.-Y., et al., *Low voltage electrowetting-on-dielectric platform using multi-layer insulators*. *Sensors and Actuators B: Chemical*, 2010. **150**(1): p. 465-470.
117. Dixon, C., et al., *An inkjet printed, roll-coated digital microfluidic device for inexpensive, miniaturized diagnostic assays*. *Lab on a Chip*, 2016. **16**(23): p. 4560-4568.
118. Yafia, M., S. Shukla, and H. Najjaran, *Fabrication of digital microfluidic devices on flexible paper-based and rigid substrates via screen printing*. *Journal of Micromechanics and Microengineering*, 2015. **25**(5): p. 057001.

119. Abadian, A. and S. Jafarabadi-Ashtiani, *Paper-based digital microfluidics*. *Microfluidics and Nanofluidics*, 2014. **16**(5): p. 989-995.
120. Tan, X., Z. Zhou, and M.M.-C. Cheng, *Electrowetting on dielectric experiments using graphene*. *Nanotechnology*, 2012. **23**(37): p. 375501.
121. Koo, B. and C.-J. Kim, *Evaluation of repeated electrowetting on three different fluoropolymer top coatings*. *Journal of Micromechanics and Microengineering*, 2013. **23**(6): p. 067002.
122. Li, Y., et al., *Room-temperature fabrication of anodic tantalum pentoxide for low-voltage electrowetting on dielectric (EWOD)*. *Microelectromechanical Systems, Journal of*, 2008. **17**(6): p. 1481-1488.
123. Au, S.H., P. Kumar, and A.R. Wheeler, *A new angle on pluronic additives: advancing droplets and understanding in digital microfluidics*. *Langmuir*, 2011. **27**(13): p. 8586-8594.
124. Anolick, C., J.A. Hrivnak, and R.C. Wheland, *Soluble perfluoropolymers*. *Advanced Materials*, 1998. **10**(15): p. 1211-1214.
125. Yoon, J.-Y. and R.L. Garrell, *Preventing biomolecular adsorption in electrowetting-based biofluidic chips*. *Analytical Chemistry*, 2003. **75**(19): p. 5097-5102.
126. Koc, Y., et al., *Nano-scale superhydrophobicity: suppression of protein adsorption and promotion of flow-induced detachment*. *Lab on a Chip*, 2008. **8**(4): p. 582-586.
127. Mats, L., et al., *Magnetic droplet actuation on natural (Colocasia leaf) and fluorinated silica nanoparticle superhydrophobic surfaces*. *Sensors and Actuators B: Chemical*, 2015. **220**: p. 5-12.
128. Verplanck, N., et al., *Wettability switching techniques on superhydrophobic surfaces*. *Nanoscale Research Letters*, 2007. **2**(12): p. 577-596.
129. Yun, K.-S. and C.-J.C. Kim. *Low-voltage electrostatic actuation of droplet on thin superhydrophobic nanoturf*. in *Micro Electro Mechanical Systems, 2007. MEMS. IEEE 20th International Conference on*. 2007. IEEE.
130. Lapierre, F., et al., *Reversible electrowetting on superhydrophobic double-nanotextured surfaces*. *Langmuir*, 2009. **25**(11): p. 6551-6558.
131. Campbell, J.L., et al., *Electrowetting of superhydrophobic ZnO nanorods*. *Langmuir*, 2008. **24**(9): p. 5091-5098.
132. Zhou, J., et al., *Superhydrophobic ZnO for EWOD digital microfluidic device for application in micro total analysis system (μ -TAS)*. *Journal of Adhesion Science and Technology*, 2012. **26**(12-17): p. 2087-2098.
133. Verplanck, N., et al., *Reversible electrowetting on superhydrophobic silicon nanowires*. *Nano letters*, 2007. **7**(3): p. 813-817.
134. Herbertson, D.L., et al., *Electrowetting on superhydrophobic SU-8 patterned surfaces*. *Sensors and Actuators A: Physical*, 2006. **130**: p. 189-193.
135. Dhindsa, M.S., et al., *Reversible electrowetting of vertically aligned superhydrophobic carbon nanofibers*. *Langmuir*, 2006. **22**(21): p. 9030-9034.
136. Freire, S.L. and B. Tanner, *Additive-free digital microfluidics*. *Langmuir*, 2013. **29**(28): p. 9024-9030.
137. Li, Y., et al., *Room-temperature fabrication of anodic tantalum pentoxide for low-voltage electrowetting on dielectric (EWOD)*. *Journal of Microelectromechanical systems*, 2008. **17**(6): p. 1481-1488.
138. La Fontaine, B., *Lasers and Moore's law*. SPIE Professional, October, 2010: p. 20.
139. Gong, M. and C.-J. Kim. *Two-dimensional digital microfluidic system by multilayer printed circuit board*. in *Micro Electro Mechanical Systems, 2005. MEMS 2005. 18th IEEE International Conference on*. 2005. IEEE.
140. Gong, J. and C.-J. Kim, *Direct-referencing two-dimensional-array digital microfluidics using multilayer printed circuit board*. *Journal of microelectromechanical systems*, 2008. **17**(2): p. 257-264.

141. Nardecchia, M., N. Lovecchio, and P.R. Llorca. *2-D digital microfluidic system for droplet handling using Printed Circuit Board technology*. in *AISEM Annual Conference, 2015 XVIII*. 2015. IEEE.
142. Foat, T., et al., *A prototype personal aerosol sampler based on electrostatic precipitation and electrowetting-on-dielectric actuation of droplets*. *Journal of Aerosol Science*, 2016. **95**: p. 43-53.
143. Ko, H., et al., *Active Digital Microfluidic Paper Chips with Inkjet-Printed Patterned Electrodes*. *Advanced Materials*, 2014. **26**(15): p. 2335-2340.
144. Cui, Z., *Printed electronics: materials, technologies and applications*. 2016: John Wiley & Sons.
145. Suganuma, K., *Introduction to printed electronics*. Vol. 74. 2014: Springer Science & Business Media.
146. Watson, M.W., et al., *Microcontact printing-based fabrication of digital microfluidic devices*. *Analytical chemistry*, 2006. **78**(22): p. 7877-7885.
147. Xu, T., et al., *Inkjet printing of viable mammalian cells*. *Biomaterials*, 2005. **26**(1): p. 93-99.
148. Roth, E., et al., *Inkjet printing for high-throughput cell patterning*. *Biomaterials*, 2004. **25**(17): p. 3707-3715.
149. Ely, F., et al., *Patterning quality control of inkjet printed PEDOT: PSS films by wetting properties*. *Synthetic Metals*, 2011. **161**(19): p. 2129-2134.
150. Yoshioka, Y. and G.E. Jabbour, *Desktop inkjet printer as a tool to print conducting polymers*. *Synthetic metals*, 2006. **156**(11): p. 779-783.
151. Hutchings, I.M. and G.D. Martin, *Inkjet technology for digital fabrication*. 2012: John Wiley & Sons.
152. Setti, L., et al., *An amperometric glucose biosensor prototype fabricated by thermal inkjet printing*. *Biosensors and Bioelectronics*, 2005. **20**(10): p. 2019-2026.
153. Basiricò, L., *Inkjet printing of organic transistor devices*. PhD. in Electronic and Computer Engineering, University of Cagliari, 2012.
154. de Gans, B.J., P.C. Duineveld, and U.S. Schubert, *Inkjet printing of polymers: state of the art and future developments*. *Advanced materials*, 2004. **16**(3): p. 203-213.
155. Ohnesorge, W.v., *Formation of drops by nozzles and the breakup of liquid jets*. *Z. Angew. Math. Mech*, 1936. **16**(4): p. 355-358.
156. Jang, D., D. Kim, and J. Moon, *Influence of fluid physical properties on ink-jet printability*. *Langmuir*, 2009. **25**(5): p. 2629-2635.
157. Perinka, N., et al., *Preparation and Characterization of thin conductive polymer films on the base of PEDOT: PSS by ink-jet printing*. *Physics Procedia*, 2013. **44**: p. 120-129.
158. Tait, J.G., et al., *Spray coated high-conductivity PEDOT: PSS transparent electrodes for stretchable and mechanically-robust organic solar cells*. *Solar Energy Materials and Solar Cells*, 2013. **110**: p. 98-106.
159. Vacca, A., et al., *Preparation and characterisation of transparent and flexible PEDOT: PSS/PANI electrodes by ink-jet printing and electropolymerisation*. *RSC Advances*, 2015. **5**(97): p. 79600-79606.
160. Siringhaus, H., et al., *High-resolution inkjet printing of all-polymer transistor circuits*. *Science*, 2000. **290**(5499): p. 2123-2126.
161. Mannerbro, R., et al., *Inkjet printed electrochemical organic electronics*. *Synthetic metals*, 2008. **158**(13): p. 556-560.
162. Singh, A., M. Katiyar, and A. Garg, *Understanding the formation of PEDOT:PSS films by ink-jet printing for organic solar cell applications*. *RSC Advances*, 2015. **5**(96): p. 78677-78685.
163. Krebs, F.C., *Pad printing as a film forming technique for polymer solar cells*. *Solar Energy Materials and Solar Cells*, 2009. **93**(4): p. 484-490.
164. Na, S.I., et al., *Efficient and Flexible ITO-Free Organic Solar Cells Using Highly Conductive Polymer Anodes*. *Advanced Materials*, 2008. **20**(21): p. 4061-4067.

165. Lee, H.J., et al., *Negative mold transfer patterned conductive polymer electrode for flexible organic light-emitting diodes*. *Organic Electronics*, 2013. **14**(1): p. 416-422.
166. Istamboulie, G., et al., *Screen-printed poly (3, 4-ethylenedioxythiophene)(PEDOT): A new electrochemical mediator for acetylcholinesterase-based biosensors*. *Talanta*, 2010. **82**(3): p. 957-961.
167. Eom, S.H., et al., *Polymer solar cells based on inkjet-printed PEDOT: PSS layer*. *Organic Electronics*, 2009. **10**(3): p. 536-542.
168. Madou, M.J., *Manufacturing techniques for microfabrication and nanotechnology*. Vol. 2. 2011: CRC press.
169. Ramuz, M., et al., *Combined optical and electronic sensing of epithelial cells using planar organic transistors*. *Advanced Materials*, 2014. **26**(41): p. 7083-7090.
170. Forrest, S.R., *The path to ubiquitous and low-cost organic electronic appliances on plastic*. *Nature*, 2004. **428**(6986): p. 911.
171. Vazquez, G., E. Alvarez, and J.M. Navaza, *Surface tension of alcohol water+ water from 20 to 50. degree*. *C. Journal of chemical and engineering data*, 1995. **40**(3): p. 611-614.
172. Walker, S.B., B.Y. Ahn, and J.A. Lewis, *Reactive Silver Inks for High-performance Printed Electronics*. Sigma Aldrich Technical Documents.
173. Lim, T., et al., *Experimental study on spreading and evaporation of inkjet printed pico-liter droplet on a heated substrate*. *International Journal of Heat and Mass Transfer*, 2009. **52**(1-2): p. 431-441.
174. Ghahremani, H., et al., *Measuring surface tension of binary mixtures of water+ alcohols from the diffraction pattern of surface ripples*. *Der Chemica Sinica*, 2011. **2**(6): p. 212-221.
175. Park, J.-G., et al., *Interfacial and electrokinetic characterization of IPA solutions related to semiconductor wafer drying and cleaning*. *Journal of the Electrochemical society*, 2006. **153**(9): p. G811-G814.
176. Mittal, K.L., *Plasma surface modification of polymers: relevance to adhesion*. 2014: CRC Press.
177. Munro, I., *EWOD6xmasEdition*. 2014: University of Hertfordshire.
178. Specialty Coating Systems, I., *SCS Parylene Dimer*, I. Specialty Coating Systems, Editor. 2007, Specialty Coating Systems, Inc.
179. Specialty Coating Systems, I., *PDS 2010 LABCOTER™ 2 Parylene Deposition System Operator's Manual*. 2003, Specialty Coating Systems, Inc: Indianapolis. p. 153.
180. Abdelgawad, M.O.A., *Digital Microfluidics for Integration of Lab-on-a-chip Devices*. 2009.
181. Bollström, R., et al., *A multilayer coated fiber-based substrate suitable for printed functionality*. *Organic Electronics*, 2009. **10**(5): p. 1020-1023.
182. Crowley, K., et al., *Fabrication of polyaniline-based gas sensors using piezoelectric inkjet and screen printing for the detection of hydrogen sulfide*. *IEEE Sensors Journal*, 2010. **10**(9): p. 1419-1426.
183. Fujifilm Dimatix, I., *Dimatix Materials Printer DMP-2800 Series User Manual Version 1.3*. 2006: Santa Clara, California, USA.
184. Drioli, E., A. Criscuoli, and E. Curcio, *Membrane contactors: fundamentals, applications and potentialities*. Vol. 11. 2011: Elsevier.
185. Dwivedi, C., et al., *Electrospun nanofibrous scaffold as a potential carrier of antimicrobial therapeutics for diabetic wound healing and tissue regeneration*, in *Nano-and Microscale Drug Delivery Systems*. 2017, Elsevier. p. 147-164.
186. Njobuenwu, D.O., E.O. Oboho, and R.H. Gumus, *Determination of contact angle from contact area of liquid droplet spreading on solid substrate*. *Leonardo Electronic Journal of Practices and Technologies*, 2007. **10**: p. 29-38.
187. Bernardin, J.D., et al., *Contact angle temperature dependence for water droplets on practical aluminum surfaces*. *International journal of heat and mass transfer*, 1997. **40**(5): p. 1017-1033.
188. Cahill, B.P., et al., *Reversible electrowetting on silanized silicon nitride*. *Sensors and Actuators B: Chemical*, 2010. **144**(2): p. 380-386.

189. Meier-Westhues, U., *Polyurethanes: coatings, adhesives and sealants*. 2007: Vincentz Network GmbH & Co KG.
190. Sharmin, E. and F. Zafar, *Polyurethane: an introduction*, in *Polyurethane*. 2012, InTech.
191. Meyer, G.J., *Polyurethane Foam: Dielectric Materials for Use in Radomes and Other Applications*. 2015.
192. Cary, R., *Avionic radome materials*. 1974, ROYAL RADAR ESTABLISHMENT MALVERN (UNITED KINGDOM).
193. Sebastian, M.T., *Dielectric materials for wireless communication*. 2010: Elsevier.
194. Lorenzini, R., et al., *The rational design of polyurea & polyurethane dielectric materials*. *Polymer*, 2013. **54**(14): p. 3529-3533.
195. Aziz, F. and A. Ismail, *Spray coating methods for polymer solar cells fabrication: a review*. *Materials Science in Semiconductor Processing*, 2015. **39**: p. 416-425.
196. Widom, B., P. Bhimalapuram, and K. Koga, *The hydrophobic effect*. *Physical Chemistry Chemical Physics*, 2003. **5**(15): p. 3085-3093.
197. Chowdhary, J. and B.M. Ladanyi, *Hydrogen bond dynamics at the water/hydrocarbon interface*. *The Journal of Physical Chemistry B*, 2008. **113**(13): p. 4045-4053.
198. Haselmeier, R., et al., *Water dynamics near a dissolved noble gas. First direct experimental evidence for a retardation effect*. *The Journal of Physical Chemistry*, 1995. **99**(8): p. 2243-2246.
199. Birnie, D.P., *Rational solvent selection strategies to combat striation formation during spin coating of thin films*. *Journal of Materials Research*, 2001. **16**(4): p. 1145-1154.
200. Wang, S., et al. *Surface roughness effect on the hydrophobicity characteristic of operating composite insulators*. in *3rd International Conference on Electric and Electronics*. 2013. Atlantis Press.
201. Wolansky, G. and A. Marmur, *Apparent contact angles on rough surfaces: the Wenzel equation revisited*. *Colloids and Surfaces A: Physicochemical and Engineering Aspects*, 1999. **156**(1-3): p. 381-388.
202. Berry, S., J. Kedzierski, and B. Abedian, *Irreversible electrowetting on thin fluoropolymer films*. *Langmuir*, 2007. **23**(24): p. 12429-12435.
203. Rust-Oleum Corporation: Vernon Hills, I. *NeverWet Base Coat and Top Coat: MSDS No. 274234* October 19, 2015 November 26, 2015]; Available from: <http://www.rustoleum.com/MSDS/ENGLISH/274234.pdf>.
204. Song, R., Y.J. Ding, and I.B. Zotova. *Fingerprinting Ovalbumin-Simulant of protein toxins in extremely-wide frequency range*. in *Conference on Lasers and Electro-Optics*. 2010. Optical Society of America.
205. Extrand, C. and S.I. Moon, *Contact angles of liquid drops on super hydrophobic surfaces: understanding the role of flattening of drops by gravity*. *Langmuir*, 2010. **26**(22): p. 17090-17099.
206. Rapp, B.E., *Microfluidics: Modeling, Mechanics and Mathematics*. 2016: William Andrew.
207. Bottiglione, F. and G. Carbone, *An effective medium approach to predict the apparent contact angle of drops on super-hydrophobic randomly rough surfaces*. *Journal of Physics: Condensed Matter*, 2014. **27**(1): p. 015009.
208. Liu, T. and C. Kim, *Contact Angle Measurement of Small Capillary Length Liquid in Super-repelled State*. *Scientific reports*, 2017. **7**(1): p. 740-740.
209. Srinivasan, S., G.H. McKinley, and R.E. Cohen, *Assessing the accuracy of contact angle measurements for sessile drops on liquid-repellent surfaces*. *Langmuir*, 2011. **27**(22): p. 13582-13589.
210. Sikka, V.K., M. Hurley, and Z.W. Lim, *Composition and coating for hydrophobic performance*. 2015, Google Patents.
211. Tripp, B.C., J.J. Magda, and J.D. Andrade, *Adsorption of globular proteins at the air/water interface as measured via dynamic surface tension: concentration dependence, mass-transfer*

- considerations, and adsorption kinetics*. Journal of colloid and interface science, 1995. **173**(1): p. 16-27.
212. Alejandre, J., D.J. Tildesley, and G.A. Chapela, *Molecular dynamics simulation of the orthobaric densities and surface tension of water*. The Journal of chemical physics, 1995. **102**(11): p. 4574-4583.
213. Torkkeli, A., *Droplet microfluidics on a planar surface*. 2003: VTT Technical Research Centre of Finland.
214. Xu, L.-C. and C.A. Siedlecki, *Effects of surface wettability and contact time on protein adhesion to biomaterial surfaces*. Biomaterials, 2007. **28**(22): p. 3273-3283.
215. Choi, C.-H. and C.-J.C. Kim, *Droplet evaporation of pure water and protein solution on nanostructured superhydrophobic surfaces of varying heights*. Langmuir, 2009. **25**(13): p. 7561-7567.
216. Smyth, K.M., *Wetting hysteresis and droplet roll off behavior on superhydrophobic surfaces by Katherine Marie Smyth*. 2010, Massachusetts Institute of Technology.
217. Gao, L. and T.J. McCarthy, *Contact angle hysteresis explained*. Langmuir, 2006. **22**(14): p. 6234-6237.
218. Schrader, M.E., *Young-dupre revisited*. Langmuir, 1995. **11**(9): p. 3585-3589.
219. Ferraz, M., et al., *Effect of chemical composition on hydrophobicity and zeta potential of plasma sprayed HA/CaO-P 2 O 5 glass coatings*. Biomaterials, 2001. **22**(23): p. 3105-3112.
220. Latip, E.A., et al., *Protein droplet actuation on superhydrophobic surfaces: a new approach toward anti-biofouling electrowetting systems*. RSC Advances, 2017. **7**(78): p. 49633-49648.
221. Hadwen, B., et al., *Programmable large area digital microfluidic array with integrated droplet sensing for bioassays*. Lab on a Chip, 2012. **12**(18): p. 3305-3313.
222. Pollack, M.G., A.D. Shenderov, and R.B. Fair, *Electrowetting-based actuation of droplets for integrated microfluidics*. Lab on a Chip, 2002. **2**(2): p. 96-101.
223. Shirinkami, H., et al., *Improvement of droplet speed and stability in electrowetting on dielectric devices by surface polishing*. BioChip Journal, 2017. **11**(4): p. 316-321.
224. Pit, A.M., et al., *Electrode-assisted trapping and release of droplets on hydrophilic patches in a hydrophobic microchannel*. Microfluidics and nanofluidics, 2016. **20**(9): p. 123.
225. Buchwalow, I.B. and W. Böcker, *Immunohistochemistry*. Basics and Methods, 2010. **1**: p. 1-149.
226. Boles, D.J., et al., *Droplet-based pyrosequencing using digital microfluidics*. Analytical chemistry, 2011. **83**(22): p. 8439-8447.
227. Kim, H., et al., *A microfluidic DNA library preparation platform for next-generation sequencing*. PLoS One, 2013. **8**(7): p. e68988.
228. Welch, E.R.F., et al., *Picoliter DNA sequencing chemistry on an electrowetting-based digital microfluidic platform*. Biotechnology journal, 2011. **6**(2): p. 165-176.
229. Coudron, L., et al., *Fully integrated digital microfluidics platform for automated immunoassay; a versatile tool for rapid, specific detection of a wide range of pathogens*. Biosensors and Bioelectronics, 2018.
230. Munro, I., *EWOD6Snowdrop*. 2015: University of Hertfordshire.
231. dCode. *Image Histogram*. 2019 [cited 2019 28 August 2019]; Available from: <https://www.dcode.fr/image-histogram>.
232. Pang, S., et al., *Graphene as transparent electrode material for organic electronics*. 2011. **23**(25): p. 2779-2795.
233. Gonçalves, A.D., et al., *The effect of protein concentration on the viscosity of a recombinant albumin solution formulation*. RSC Advances, 2016. **6**(18): p. 15143-15154.
234. Lin, H.-C., Y.-J. Liu, and D.-J. Yao, *Core—Shell Droplets for Parallel DNA Ligation of an Ultra-Micro Volume Using an EWOD Microfluidic System*. Journal of the Association for Laboratory Automation, 2010. **15**(3): p. 210-215.

235. Song, J., et al., *A scaling model for electrowetting-on-dielectric microfluidic actuators*. *Microfluidics and Nanofluidics*, 2009. **7**(1): p. 75-89.
236. Yafia, M. and H. Najjaran, *High precision control of gap height for enhancing principal digital microfluidics operations*. *Sensors and Actuators B: Chemical*, 2013. **186**: p. 343-352.
237. Yafia, M. and H. Najjaran, *Droplet necking and morphology variations induced by changing the gap height during transport in digital microfluidic systems*. *Journal of Microelectromechanical Systems*, 2015. **24**(5): p. 1647-1658.
238. Cooney, C.G., et al., *Electrowetting droplet microfluidics on a single planar surface*. *Microfluidics and Nanofluidics*, 2006. **2**(5): p. 435-446.
239. Shih, S.C., et al., *A droplet-to-digital (D2D) microfluidic device for single cell assays*. *Lab on a Chip*, 2015. **15**(1): p. 225-236.
240. Nikapitiya, N.J.B., S.M. You, and H. Moon. *Droplet dispensing and splitting by electrowetting on dielectric digital microfluidics*. in *2014 IEEE 27th International Conference on Micro Electro Mechanical Systems (MEMS)*. 2014. IEEE.
241. Dong, C., et al., *A 3D microblade structure for precise and parallel droplet splitting on digital microfluidic chips*. *Lab on a Chip*, 2017. **17**(5): p. 896-904.

Appendix A: The HP Deskjet 1000 J110 printer setting

The printer setting was set to its maximum printing resolution by performing the following steps:

- 1) opening the printer *Properties* dialog box,
- 2) clicking the *Paper/Quality* tab,
- 3) selecting the *Photo Paper, Best Quality* from the *Media* drop-down list,
- 4) then, clicking the *Advanced* tab,
- 5) selecting *Yes* from the *Print in Max DPI* drop-down list.

Appendix B: Effect of IPA on the wetting of silver ink

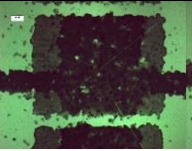
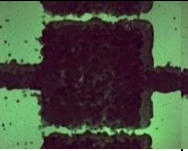
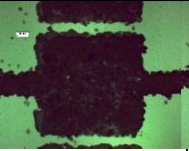
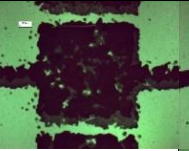
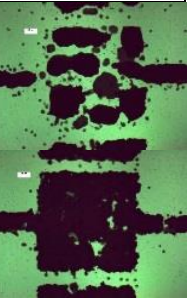
This study was conducted to determine the optimum ratio of isopropyl alcohol (IPA) to silver ink solvent to produce the best wetting of the silver ink droplet. The as-is silver ink does not produce tracks with conductivity due to the low spreading/high contact angle of the ink droplets on the cellulose acetate substrate causing non-contiguous electrode pattern. The connectivity between the ink droplets can be improved by decreasing the ink surface tension. In this study, the ink surface tension was reduced by adding IPA ($\gamma=23.3$ mN/m) to the ink ($\gamma=20-50$ mN/m).

The silver ink was added with the IPA using the following ratio (IPA:silver); 1:1, 1:1.14, 1:1.33, 1:1.6, and 1:2. To test the performance of the inks with different IPA volume percentage, pattern consisting of three rows of 16 electrodes as shown in **Figure 2.1** was printed (two printing pass) onto the cellulose acetate. Each of these electrodes is connected to a corresponding contact pad located at the top of the pattern. In the pattern design, the nominal track width is 250 μm while the nominal electrode spacing is 320 μm . After printing, the connectivity between the contact pad and its corresponding electrode in the third row was evaluated by measuring the resistance using the digital multimeter.

Table A summarises the results of the track conductivity evaluation. The 1:1.6 ratio of IPA to the silver ink has the best result by producing 14 conductive tracks out of the 16 tracks. No inks managed to produce fully interconnected tracks for all 16 electrodes. The ink with the 1:1 ratio could not be ejected from the nozzles as the ink surface tension was too low; the ink flooded the nozzles. The 100 per cent silver ink can only produce two conductive tracks, same with the 1:1.33 ink. Based on these results, the 1:1.6 ink was used for the main investigations in Chapter 2. To obtain fully

interconnected tracks for all 16 electrodes using the 1:1.6 ink, another printing pass was added so that three layers were applied for the tracks pattern.

Table A: The conductivity of the tracks for silver inks with different volume percentage of IPA

| IPA : silver ink ratio | 1 : 1 | 1 : 1.14 | 1 : 1.33 | 1 : 1.6 | 1 : 2 | 100% silver ink |
|---|--|---|---|--|---|---|
| | |  |  |  |  |  |
| Tracks connectivity (out of 16 tracks) | Ink cannot be ejected from print head, nozzles are flooded with the ink due to low surface tension | 0 | 2 | 14 | 10 | 2 |

Appendix C: Down selection of polymer transparency substrate

This study was conducted to select the most suitable polymer transparency to be used in the main investigations in Chapter 2 from several available substrates. Eight types of transparency film with different surface roughness made of cellulose acetate were evaluated. A simple 6 mm × 6 mm (nominal size) square pattern was printed on all the substrates to evaluate the conductivity of the deposited ink film. The conductivity of the film was measured using digital multimeter. **Table B** reports the average roughness of the substrates and the number of printing pass required to produce conductivity in the thin film made of silver and PP/T20 inks on the different types of cellulose acetate substrate. For the PP/T20 ink, seven out of the eight substrates are capable of producing conductive film after just one layer of printing, while the PP ink requires more than one layer of printing to attain a measurable conductivity (not reported in the table) for all eight substrates.

Table B: The conductivity of silver and PP/T20 thin films on different types of cellulose acetate substrate

| Substrate | Average roughness (nm) | Number of printing pass required to produce conductive thin film | |
|-------------|------------------------|--|-------------------------------------|
| | | Ag and Ag/IPA | PP/T20 |
| Substrate A | 57.21 | 3 | 1 |
| Substrate B | 57.70 | 2 | 1 |
| Substrate C | 39.95 | 3 | 1 |
| Substrate D | 161.14 | More than 6 | 3 |
| Substrate E | 88.14 | 2 | 1 |
| Substrate F | 4841.20 | More than 6 | 1 (very high electrical resistance) |
| Substrate G | 327.99 | More than 6 | 1 (very high electrical resistance) |
| Substrate H | 25.96 | 3 | 1 |

Five substrates allow measurable conductivity for both the Ag and Ag/IPA inks but they require multiple printing passes. Two substrates require at least two printing

pass while the other three need three printing pass to make all the silver ink droplets fully connected. There is no clear relationship between the substrate roughness and the ink conductivity. However, it can be hypothesised that above a certain value of roughness, the silver ink droplets ceased to connect with each other. Three substrates have very poor performance where no conductive films were produced for the printed silver ink even after six layers of printing. These substrates have the top three highest average roughness with values between 161 nm and 4841 nm. The two substrates which produced conductivity after two passes have average roughness of 88 nm and 58 nm respectively.

Initial trial with standard A4 paper substrate have shown no measurable conductivity for both silver inks, Ag and Ag/IPA after six printing passes while a conductive layer was produced after two layers of printing for the PP/T20 ink. Based on these preliminary findings, only one substrate, substrate E in Table B, which has produced conductive PP/T20 and silver thin films was employed for subsequent investigations on the feasibility of the inkjet printer method.

Appendix D: Effect of plasma treatment on the tracks conductivity

The previous section was conducted to shortlist the substrate to be employed in the main investigation. In that particular study, a thin film of conductive ink material was deposited by printing a small 6 mm square and the conductivity of the film was measured using digital multimeter. While this test has shown that the chosen substrate, substrate E is capable of producing conductive film for all inks without any substrate treatment, this good result is not repeatable when tracks with narrow width were printed on the substrate. To overcome this, plasma treatment was introduced in order to improve the wetting of the ink droplet on the substrate by lowering the substrate surface energy. The tracks conductivity relies on the interconnectivity between the ink droplets; thus the larger the size of the ink droplets on the substrate upon impact, the higher the probability of the ink droplets to be connected with each other. The size of the ink droplet depends on the wetting or spreading of the ink on the substrate, the higher the wetting the larger the droplet size. The wetting of droplet can be improved by increasing the substrate surface energy, which is the method used to improve the tracks conductivity in this section.

Determination of the optimum setting for the plasma treatment, specifically the power intensity and the treatment duration was conducted by testing the conductivity of the printed pattern shown in **Figure 2.1**. The substrate used in this study was substrate E, which produced the best result in the previous section. The tracks in the pattern are 250 μm in nominal width while the nominal spacing between the square electrodes are 320 μm and 360 μm for Ag and PP/T20 inks respectively. The Ag/IPA was excluded in this investigation since no significant improvements were made when plasma treatment was introduced for this type of ink.

Table C: Effect of plasma treatment on the tracks conductivity and electrode separations for PP/T20 ink. The tracks width are 250 μm while the electrode spacing are 360 μm . Only one layer of printing was applied for this ink.

| PEDOT:PSS added with Tween 20 (PP/T20) | | | | | | | |
|---|----|----|----|----|----|----|----|
| Power intensity (W) | 20 | 15 | 15 | 10 | 10 | 5 | 0 |
| Duration (seconds) | 60 | 30 | 10 | 30 | 10 | 5 | 0 |
| Electrode spacing separation (out of 15) | 0 | 0 | 12 | 2 | 15 | 15 | 13 |
| Tracks connectivity (out of 16) | 11 | 15 | 14 | 12 | 16 | 0 | 0 |

Table D: Effect of plasma treatment on the tracks conductivity and electrode separations for Ag ink. The tracks width are 250 μm while the electrode spacing are 320 μm . Two layers of printing was applied for this ink and 2+1 indicates two layer of printing with additional printing pass just for the tracks pattern without the square electrodes.

| Silver (Ag) | | | | | | | |
|--|----|----|----|----|----|-----|-----|
| Number of printing pass | 2 | 2 | 2 | 2 | 2 | 2+1 | 2+1 |
| Power intensity (W) | 40 | 30 | 30 | 30 | 0 | 30 | 0 |
| Duration (seconds) | 60 | 90 | 75 | 60 | 0 | 60 | 0 |
| Electrode spacing separation (out of 15) | 3 | 2 | 2 | 15 | 14 | 15 | 13 |
| Tracks connectivity (out of 16) | 7 | 14 | 8 | 11 | 2 | 16 | 13 |

Based on **Table C** and **Table D**, optimum treatment differs depending on the type of ink being used. For PP/T20 ink, the plasma treatment that gives the best result

is 10 W for 10 s which produced no shorted electrodes and complete connectivity for all 16 electrodes. Comparing between the untreated and treated substrates, there is significant improvement when plasma treatment is introduced. The treatment however needs to be above 5 W since no conductivity can be measured between the 16 tracks using treatment at this intensity, which is the same result for the untreated substrate. Above 5 W, there is no significant differences between the treatment settings for the tracks conductivity. As for the spacing between the electrodes, power intensity of 20 W and 15 W for 30 s resulted in shorted electrodes in all 16. The 15 W intensity however when applied in shorter duration produced 12 complete separation between spacing which is a substantial improvement.

For the Ag ink, no settings were able to produce fully interconnected tracks for all 16 electrodes using two printing pass. The best result is produced by 30 Watts of radio frequency power for 60 seconds which resulted in 11 conductive tracks and 15 electrode spacing separations. This setting does not produce connection in all 16 electrodes and to improve the connectivity, another layer of printing pass consisting of only the tracks pattern was added. By doing this, all 16 electrodes are fully connected. Plasma treatment with higher power and/or longer duration than the 30 W and 60 s resulted in more occurrences of shorted electrodes. In the main investigations conducted in Chapter 2, the plasma treatment setting used for the PP/T20 and Ag inks are 10 W 10 s and 30 W 60 s respectively.